



University of Tennessee, Knoxville

TRACE: Tennessee Research and Creative Exchange

Doctoral Dissertations

Graduate School

8-2023

Spall Characteristics of Additively Manufactured Stainless Steel

Kevin Lamb
klamb4@vols.utk.edu

Follow this and additional works at: https://trace.tennessee.edu/utk_graddiss

 Part of the [Applied Mechanics Commons](#), and the [Manufacturing Commons](#)

Recommended Citation

Lamb, Kevin, "Spall Characteristics of Additively Manufactured Stainless Steel. " PhD diss., University of Tennessee, 2023.
https://trace.tennessee.edu/utk_graddiss/8709

This Dissertation is brought to you for free and open access by the Graduate School at TRACE: Tennessee Research and Creative Exchange. It has been accepted for inclusion in Doctoral Dissertations by an authorized administrator of TRACE: Tennessee Research and Creative Exchange. For more information, please contact trace@utk.edu.

To the Graduate Council:

I am submitting herewith a dissertation written by Kevin Lamb entitled "Spall Characteristics of Additively Manufactured Stainless Steel." I have examined the final electronic copy of this dissertation for form and content and recommend that it be accepted in partial fulfillment of the requirements for the degree of Doctor of Philosophy, with a major in Mechanical Engineering.

S. S. Babu, Major Professor

We have read this dissertation and recommend its acceptance:

W. R. Hamel, Z. Z. Zhang, A. C. Stowe

Accepted for the Council:

Dixie L. Thompson

Vice Provost and Dean of the Graduate School

(Original signatures are on file with official student records.)

Spall Characteristics of Additively Manufactured Stainless Steel

A Dissertation Presented for the
Doctor of Philosophy
Degree
The University of Tennessee, Knoxville

Kevin Lamb
August 2023

ACKNOWLEDGEMENTS

I first want to acknowledge thanks to God for blessing me with all the people that have supported me throughout this journey and made this achievement possible. I want to express gratitude to my research adviser, Dr. Suresh Babu, for his guidance and assistance throughout my time at the University of Tennessee. His leadership over the last several years has been crucial to my success.

I also wish to thank my committee members Dr. Ashley Stowe, Dr. William Hamel, and Dr. Zhili Zhang for agreeing to serve on my committee and providing helpful advice towards the completion of my dissertation.

My collaborators at Georgia Institute of Technology deserve special thanks for the continued support and experimental expertise in the area of high strain-rate behavior and plate impact testing. The support from Dr. Naresh Thadhani, Dr. Joshua Kacher, Dr. Katie Koube, and Taylop Sloop was invaluable to me as a researcher.

I want to also thank my research colleagues for their individual contributions to portions of my research: Mike Boice of Y-12 for his help with sample fabrication and machine operation, Curtis Frederick of Zeiss for performing x-ray computed tomography analysis, Amy Godfrey and Michael Kohler of University of Tennessee for performing x-ray diffraction analysis, and Angela Parks of Y-12 for her help in sample preparation and optical microscope imaging.

I would like to gratefully acknowledge the funding provided for this research provided by Consolidated Nuclear Security, LLC (CNS) as accounts of work sponsored by an agency of the United States Government under Contract DE-NA-0001942.

Finally, I wish to thank my wife, Erin Lamb, as well as my kids, Hayes and Rian. Erin has been my biggest supporter and motivation, pushing me to pursue and accomplish more than I ever would have otherwise. I could not have done this without her. The curiosity of both Hayes and Rian help remind me why it is important to ask questions and never stop learning.

ABSTRACT

Additive manufacturing (AM) has rapidly transformed from a novelty technology into a growing sector of production. Much work has demonstrated the behavior of AM products under static and quasi-static loading. However, the behavior of AM materials under high strain rate loading is less understood. This research advances the fundamental knowledge of relationships between the unique aspects of AM and mechanical performance under high velocity impact loading.

This project examines AM 316L stainless steel (SS) exposed to high velocity impact, the associated shock wave propagation, and fracture as a function of orientation and internal engineered features. The research involves fabrication, characterization, plate impact testing, experiment modeling, and post-mortem analysis of SS316L samples fabricated using laser powder bed fusion (LPBF).

A build-impact orientation study and two engineered porosity were conducted. The results demonstrated that impact orientation with respect to build direction influences the extent and location of spall damage due to the relative microstructural anisotropy and collections of powder filled voids slow and weaken the progressing shock front by presenting disturbances in portions of the wave front.

A following study further utilized purposeful engineering design to control the propagation of the shock wave. The use of internal features, a capability unique to LPBF, was the primary feature of the study. This study demonstrated that a large, powder-filled void space placed within a solid sample provides damping that both slows the progression of the shock front and reduces the magnitude of the pressure stress at the rear free surface.

Overall, the results of this research demonstrate that the anisotropic properties and unique capabilities of LPBF can be leveraged to control shock wave propagation and resultant damage in SS316L. Unique aspects of this research include (1) comparing spall response of LPBF fabricated samples to shock loading applied at varying orientation, (2) the use of powder-filled engineered voids to reduce the magnitude and velocity of the shock front, along with the resulting damage, and (3) coupling the results of plate impact experiments with as-built and post-mortem sample characterization.

Table of Contents

Chapter One Introduction.....	1
Chapter Two Background	6
Historical Background.....	6
Material Properties and Microstructure of 316L Stainless Steel.....	21
Relevant Theory and Fundamentals.....	26
Relevant Literature on Research Topic	48
Conclusion	57
Chapter Three Methodology	58
Introduction.....	58
Sample Fabrication.....	59
Sample Characterization	63
Ultrasonic Testing	65
Plate Impact Testing	65
Post Impact Recovery.....	66
Presentation of Results.....	67
Chapter Four Build-Impact Orientation Study	69
Experiment.....	69
Results.....	75
Discussion	87
Summary and Conclusions:.....	93
Chapter Five Randomly Distributed Engineered Porosity Study	96
Experiment.....	96
Material Feedstock:	99
Physical Property Characterization:.....	99
Plate Impact Testing	108
Results.....	108
Discussion	119
Conclusions	127
Chapter Six Numerical Modeling.....	129
Introduction.....	129
Conclusions	144
Chapter Seven Single Engineered Void Study	146
Introduction.....	146
Modeling and Numerical Simulation	146
Experiment.....	151
Results.....	156
Discussion	160
Conclusions	163
Chapter Eight Engineering Design.....	164
Introduction.....	164
Modeling and Simulation	165
Experiment.....	174

Results.....	177
Discussion	185
Shock wave reflection and compression of powder void area	185
Conclusions	189
Chapter Nine Summary and Conclusions	190
Introduction.....	190
Summary of Results	190
Conclusions	192
Chapter Ten Recommendations and Future Work.....	194
List of References	197
Appendix.....	207
Vita.....	212

LIST OF TABLES

Table 1: Chemical Composition of AISI316L	23
Table 2: Solidification modes, Reactions, and Final Microstructure Cr/Ni ratio and solidification mode association [38]	25
Table 3: Chemical composition (weight %) of powder feedstock and build sample. AISI 316L composition shown for reference.	61
Table 4: Measured wave and moduli properties for orientation impact samples.	72
Table 5: Experiment results for each sample. Velocimetry Data and Calculated Properties.	79
Table 6: Experiment-induced damage results for each sample. Velocimetry Data Calculations and Image Analysis results	80
Table 7: Engineered porosity distribution matrix and sample ID labels	98
Table 8: Density measurements for each sample	100
Table 9: Pre-test sample characterization data.....	102
Table 10: Slope and timing information from velocimetry plots.....	110
Table 11: Experiment results for each sample. Velocimetry Data, Calculated Properties, and Image Analysis results.....	113
Table 12: Comparison of velocity rise to peak for void models and 500-1% experiment.....	136
Table 13: Peak Velocity (v_{peak}) and Arrival time ($t_{arrival}$) from simulation at locations in Figure 63.....	150
Table 14: Wave speeds for Single pore study	153
Table 15: Experiment data for Single Pore Study	157
Table 16: As-built properties of Engineered Sample.....	181

LIST OF FIGURES

Figure 1: Dynamic Aspects of Mechanical Testing [2]	2
Figure 2: Overview of AM processing principles for metallic materials. [10]	7
Figure 3: Schematic of LPBF process [23].....	7
Figure 4: Microscopic fracture example (Top). Potential energy as a function of atomic separation (Middle). Force as a function of atomic separation (Bottom). [24].....	11
Figure 5: Influence of location relative to defect on stress intensity [24]	14
Figure 6: Diagrams of stress concentration conditions. (a) Void diameter and shape. (b) Void orientation relative to stress. (c) Void collinear spacing. (d) Void consecutive spacing. [24]	17
Figure 7: Stress concentration as function of void spacing. Collinear (Left) and Consecutive (Right). [24]	17
Figure 8: Schematics of plastic zone blunting at crack tip. (a) Estimation of the crack-tip opening displacement in the plastic zone. (b) An initially sharp crack blunts with plastic deformation at the crack tip. (c) Idealized stress-strain diagram indicating yield point where material behavior transitions from elastic to plastic.	17
Figure 9: Schematics comparing quasi-static and dynamic testing.(a) Quasi-static compression test setup and deformation. (b) Quasi-static tension test setup and deformation. (c.1) Initial condition of dynamic impact test. Initial material compression driven by wave propagation. Impact causes change in sample velocity. (c.2) Final condition of dynamic impact test. Tensile force driven by wave reflection at rear free surface.....	19
Figure 10: Fe-Cr-C pseudo-binary diagram at 17% Cr [30]	23
Figure 11: Pseudobinary Fe-Cr-Ni ternary diagrams (a) Pseudobinary section of the Fe-Cr-Ni ternary diagram at 70% Fe. (b) Modified pseudobinary section of the Fe-Cr-Ni ternary diagram at 70% Fe, showing solidification modes. [30].....	23
Figure 12: Schematic of Longitudinal and Shear wave propagation (L). Example of ultrasonic transducer (R) [42].....	28
Figure 13: Schematic of shock front.....	30
Figure 14: Example u-p vs P plot for 316L. Compares Shock-Hugoniot EOS and Rayleigh Line Approximation	33
Figure 15: Example u-p vs P plot for 316L, showing "impedance matching" technique for reflection at free surface.....	33
Figure 16: Reflection of shock wave at a free surface (Left). Pressure-distance and Particle velocity-distance profiles at free surface interface (Right). [4]..	35
Figure 17: Transmission of shock wave from one material to another. (Top Left) Pressure-Particle velocity plot of high to low shock impedance transmission. (Bottom Left) Stress profile of high to low impedance transmission. (Top	

Right) Pressure-Particle velocity plot of low to high impedance transmission.	
(Bottom Right) Stress profile of low to high impedance transmission. [4]	35
Figure 18: Longitudinal elastic wave intersecting material A-B boundary, generating refracted and reflected waves. [4]	37
Figure 19: Experiment details (a) Diagram of Light Gas Gun setup for High-velocity plate impact experiments. (b) Side view schematic of flyer-target sample configuration, (c) Front view of target sample holder	39
Figure 20: Representative example (a) x-t diagram and (b) free surface velocity profile, for plate impact experiment.....	41
Figure 21: Influence of the fracture rate on the shape of spall pulse in the free surface velocity history. It follows from acoustic analysis that the rate of growth of the volume of voids dV_v/dt which is approximately equal to the expansion rate dV/dt in the unloading wave is associated with constant free surface velocity [44]	44
Figure 22: Example of interference created by surface movement [4]	47
Figure 23: Relationship between free surface velocity and signal vs time [51] ...	47
Figure 24: Comparison of stress-strain diagrams comparing quasi-static tensile behavior of samples with varied size and content of voids. Samples are compared with and without post-processing HIP treatment [71]. The general trend demonstrates a slight decrease in strength and a major decrease in ductility with increasing void size and content. The application of HIP to reduce porosity improves the performance.....	49
Figure 25: Velocity-time plot comparing different crystallographic orientations of single-crystal copper [73].....	52
Figure 26: Information on AM-Wrought-AM Rx study. (Left) Pre-test images, LOM and EBSD, (Mid) Post-shot LOM images, (Right) Velocity-time plot [5].....	55
Figure 27: Images from [78] Ti-6Al-4V study. Sample build direction and orientation (Left). Orientation between tensile loading direction and build layers (Right).	55
Figure 28: Schematic of build-impact orientations	61
Figure 29: Pre-shot characterization of as-built samples. (a) Optical image showing very small porosity resulting from build which is often lower to the pixel resolution of the image. (b) Optical micrograph of the XY plane showing etched to highlight the melt pool tracks. (c) EBSD results of the XY plane in the form of inverse pole figure (IPF) for FCC crystal show smaller grains at the boundaries of adjacent melt pool tracks as indicated. (d) SEM image showing high concentration of voids along melt pool boundaries. (e) Optical micrograph of the XZ plane showing as-built melt pool layers and varied grain shapes and lightly etching grains. (f) EBSD results of the XZ plane in the form (IPF) for FCC crystal show columnar grains and small grains near the melt pool boundary typically referred as “fish-scale” boundaries. (g) Measure of pore size distribution from many images. (h) EBSD results of the Wrought sample in the form of IPF shows the more consistent equiaxed crystal structure compared to the AM samples.	74

Figure 30: Velocimetry (v-t) data results plot. Results of shot test showing free surface velocity vs. time. (a) Plot of full data set. The blue arrows indicate the “shoulder” observed in the IP sample. The orange arrows indicate the “double hump” observed in the TT. (b) Plot showing closer inspection of initial rise times and the HEL, (c) Plot showing closer inspection of pulse duration at peak velocity.	78
Figure 31: Spall damage results from shot test.(a) Spall damage distribution. (c-e) Optical micrograph showing spall damage of (c) TT sample, (d) IP sample, and (e) Wrought sample.....	82
Figure 32: Details of MPB characteristics.(a) Optical image highlighting damage sites related to MPB and smaller ductile fracture sites for TT sample, (b) Same for IP sample, (c) SEM image showing grain structure difference above and below melt pool, (d) Example of single melt pool, (e) Example of Layer-Layer MPB, (f) Example of Track-Track MPB, and (g) Example of Combination MPB.....	84
Figure 33: Post-shot characterization of samples.(a) IP, (b) TT. (a1 and b1) Inverse pole figure (IPF) maps showing examples of spall fracture relative to grain structure. (a2 and b2) IQ map showing dark areas of strained material near spall fracture locations.	84
Figure 34: Post-shot sample X-ray computed tomography (XCT). (a) Example XCT slice of parallel sample at spall plane, (b) Spall damage distribution plot for perpendicular sample comparing XCT data with LOM data at cross-section, (c) Spall damage distribution plot for parallel sample comparing XCT data with LOM data at cross-section.....	86
Figure 35: Lagrangian x-t plots of (a) IP sample and (b) TT sample.	89
Figure 36: Porosity build defect example.(a) SEM image of void located at MPB, (b) Schematic of void at MPB subjected to IP loading, (c) Schematic of void at MPB subjected to TT loading, (d) Diagram of stress concentration relationship for void at angle relative to loading direction, indicating that the stress concentration increases as the angle relative to normal decreases. .	94
Figure 37: Details of sample fabrication. (a) STL file showing engineered voids on 0.500 mm at 5% sample, (b) Enlarged image of STL file to highlight the voids placed in the file.	98
Figure 38: Density Measurements for each sample.	100
Figure 39: Elastic wave speeds for engineered void samples. (a-c) Data points grouped by void size. (a) Longitudinal wave speed, (b) Shear wave speed, (c) Bulk wave speed. (d-f) Data points grouped by distribution percentage. (a) Longitudinal wave speed, (e) Shear wave speed, (f) Bulk wave speed.	102
Figure 40: XCT analysis of 200-5% sample. (a-c) Slice images of XY plane at three consecutive Z-layer locations, (a) Z = 1.75mm, (b) Z = 2.00mm, (c) Z = 2.25mm, (d) Plot of void fraction measured via XCT vs. Z location, (e) XCT image demonstrating measurement of engineered void within build sample.	104

Figure 41: As-built LOM images of engineered void samples. Note that the images indicate random distribution, irregular void shapes, and void volumes that reasonably meet the design goals. (a) 500-3%, (b) 200-1%, (c) 350-5%, (d) 500-5%, (e) 200-3%, (f) 350-1%.....	105
Figure 42: SEM and EBSD images of as-fabricated engineered voids.(a) 0.500 mm at 3%, (b) 0.350 mm at 5%, (c) 0.500 mm at 3%, (d) Zoomed image of (c) to highlight material at edge of void that fused with neighboring powder. (e) EBSD image of void in 0.500mm at 3%. (f) Zoomed image of (e) to highlight the grain refinement along the edge of the void.	107
Figure 43 - Velocimetry plots for Engineered void impact experiments for 1% and 3% porosity. (a) Full experiment data set. (b) Closer view of initial velocity rise region of plot. (c) Closer view of pullback region of plot.....	109
Figure 44 - Velocimetry plots for Engineered void impact experiments for 5% porosity. (a) Full experiment data set. (b) Closer view of initial velocity rise region of plot. (c) Closer view of pullback region of plot.....	110
Figure 45: Post-shot characterization of samples (a-c) Etched LOM images showing spall formation along melt pool boundaries: (a) 0.200 mm x 5%, (b) 0.350 mm x 5%, (c) 0.500 mm x 5%, (d-f) LOM images showing spall formation relative to engineered void locations: (d) 0.200 mm x 5%, (e) 0.350 mm x 5%, (f) 0.500 mm x 5%.....	115
Figure 46: XCT images and data from Engineered void samples post-mortem.(a-b) Individual 2D slices of XCT. Impact direction indicated by blue arrow. (a) 500-5%, (b) 200-5%. (c-d) Cumulative data of XZ damage locations compiled across the Y-direction. (c) 500-5%, spall damage located away from engineered voids is highlighted, (d) 200-5%, shifted spall plane is highlighted. Orange line indicates sample centerline corresponding to expected spall plane location.....	116
Figure 47: SEM image of 500-1% sample showing void collapse. Yellow boxes are 500 μ m square to indicate relative reduction in size. (a) Full sample length showing voids relative to sample mid-plane. (b) Area of suspected void collapse near the impact surface. (c) Area of suspected void collapse near the rear surface.	118
Figure 48: Post-mortem IPF images of engineered void samples,, indicating void collapse. (a) and (b) Examples in 200-5% sample, (c) Example in 200-3% sample, (d) Example in 200-1%.sample, (e) and (f) Examples in 350-5% sample. Dimension bars show the expected width of the square void. Yellow arrows note potential jetting locations. Orange arrows indicate locations of traditional spherical spall damage.	119
Figure 49: XCT images of as-built Engineered void samples.	121
Figure 50: Schematics of shock wave transmission between materials with different shock impedance.	125
Figure 51: Conceptual Lagrangian X-t diagrams showing influence of void on the wave propagation in sample. (a) Baseline, (b) Multiple 200 μ m voids, (c)	

Single 500 μm void, (d) Velocity-Time plot from experiment showing absence of plateau at peak velocity for samples with voids.....	126
Figure 52: Plots highlighting the initial compressive section that is being simulated. (a) Lagrangian x-t plot. (b) Velocimetry v-t plot.....	130
Figure 53: Baseline model details and results.(a) Simulation setup with Flyer impacting stationary target and contour plot showing progression of pressure wave. (b) Simulation result: Velocity-Time plot measured at rear-free surface. (c) Legend associated with contour plot.....	133
Figure 54: Void model details and contour plot results. (a) Partial mesh view of Empty Void approach, showing void area. (b) Partial mesh view of Bulk Continuum approach, showing void area. (c) Partial mesh view of Individual Powder Particle approach. This image is zoomed in to display the individual powder particles. (d-i) Abaqus contour plots of pressure wave distribution in samples. (d) Empty void approach at 0.3 μs , (e) Empty void approach at 0.6 μs , (f) Bulk continuum approach at 0.3 μs , (g) Bulk continuum approach at 0.6 μs , (h) Individual powder approach at 0.3 μs , (i) Individual powder approach at 0.6 μs	135
Figure 55: Velocity-time plot of Void model results. Data measured at RFS. The Empty Void and Individual Powder approaches provide very similar results.	135
Figure 56: Pressure-time contour plots of Single-void simulations. (a) 200 μm void located at center, (b) 500 μm void located at center, (c) 500 μm void shifted “UP” toward impact surface, (d) 500 μm void shifted “DOWN” toward RFS	140
Figure 57: Velocity-time profile comparison of Void size & location. Measurement location is at center of sample, directly in-line with void.....	140
Figure 58: Horizontal array void simulation details and results.	142
Figure 59: Plot of FS location vs. Velocity (at $t = 0.8 \mu\text{s}$, for Horizontal Array of Voids.....	142
Figure 60: Vertical array simulation details and contour plots of results.	144
Figure 61: Array simulation velocity-time result plot.....	144
Figure 62: Test sample configuration for Single Pore study.....	147
Figure 63: Contour plots of pressure magnitude for Baseline, 200 μm , and 500 μm void simulations. The 200 μm void presents minimal disruption to the pressure front while the 500 μm provides reflection and reduces the pressure stress magnitude in area directly in-line behind it.	149
Figure 64: Simulation results for 500 μm single pore experiment.	150
Figure 65: As-built properties of single void samples. (L) Plot of bulk sample density as function of void size. (R) Plot of elastic wave speeds as function of void size.....	153
Figure 66: XCT images of 0.500 mm Single Void sample. (a) X-Y plane slice showing center location of void. (b) X-Z plane slice showing vertical position of void. (c) X-Z plane slice showing approximate void dimensions.	153
Figure 67: Schematic of PDV and Void Layout.....	155

Figure 68: Velocity profiles for single void plate-impact experiment. (a) 200 μ m single void, (b) 350 μ m single void, (c) 500 μ m single void, and (d) Comparison of “near” probe on each to Control.....	158
Figure 69: Comparison of Simulation and Experiment results. (a) Velocity-Time plot of 200 μ m single void case. (b) Velocity-time plot of 500 μ m single void case.	159
Figure 70: Post-mortem image of 200 μ m single void sample. Complete spall fracture.	161
Figure 71: Results of Single Large Void simulation. (a) Contour plot of Pressure at time = 0.9 μ s. (b) Velocity-time plot of different locations across free surface.....	166
Figure 72: ABAQUS models of 2-D "X pattern" that represents lattice. All configurations are “Void Size” x “Member Size”. (a) 0.200 mm x 0.500 mm, (b) 0.500 mm x 0.500 mm, (c) 0.200 mm x 0.100 mm, (d) 0.500 mm x 0.100 mm.....	168
Figure 73: ABAQUS simulation results of 2-D "X pattern" that represents lattice.	168
Figure 74: CAD renderings of hexagonal honeycomb arrangements examined in this study.....	170
Figure 75: Deformation mechanisms in hexagonal honeycomb structures. (a) Isometric view showing relative orientation of applied stress. (b) Vertical configuration showing buckling of vertical member. (c) Horizontal-Side configuration showing yielding at the hinge points. (d) Horizontal-Top configuration showing combination of buckling and hinge.	173
Figure 76: Simulation results of 2-D hexagonal honeycomb designs.....	173
Figure 77: CAD renderings of target samples with hexagonal honeycomb designs.	175
Figure 78: LOM images of as-built engineered samples. Notice that the individual struts were not successfully built in any of the samples. (a) Side hex orientation, (b) Edge hex orientation, (c) Vertical hex orientation.	178
Figure 79: Etched LOM images of as-built engineered samples. (a) Side hex orientation, (b) Edge hex orientation. The hex honeycomb cells at the boundary of the insert appear to have attempted to build but did not fully form, as indicated by the outline on the zoomed images.	178
Figure 80: XCT image of as-built Vertical hex honeycomb sample. Insert indicates that the void edge has artifact of the hex cells along that boundary.	179
Figure 81: Schematics of Wave Measurement Probes.	183
Figure 82: Velocity plot of engineered sample. (a) XCT image indicating approximate location of probes. (b) Velocity-time plot from plate-impact experiment. Each probe location is shown along with CONTROL sample data for comparison.	183
Figure 83: Engineered sample velocity data comparison with simulation. (a) Blue probe location and the corresponding model location. (b) Velocity-time plot	

of the Blue probe location and the corresponding model location. (c) Black probe location and the corresponding model location. (d) Velocity-time plot of the Black probe location and the corresponding model location. (e) Red probe location and the corresponding model location. (f) Velocity-time plot of the Red probe location and the corresponding model location.	184
Figure 84: XCT image comparison of as-built and post-impact engineered sample.	186

Chapter One

Introduction

Additive manufacturing (AM) has rapidly transformed from a novelty prototyping technology into a growing sector of production across a wide range of industries. This transition has been driven by the numerous advantages of AM over traditional methods: increased complexity, design flexibility, high customization, etc. Much work has been documented in literature to demonstrate the anisotropic behavior of AM products under static and quasi-static loading conditions. However, the behavior of AM materials under high strain rate loading is not as well understood. This research attempts to advance the fundamental knowledge of the relationship between the unique aspects of AM and the mechanical performance under high velocity impact loading conditions. The scope of this project focuses on laser powder bed fusion (LPBF) fabricated 316L stainless steel (SS316L) samples subjected to high velocity plate impact spallation testing.

Dynamic forces, including those applied at very high loading rates, represent a great portion of the forces that some components are exposed to in actual conditions. Dynamic forces are time-rate-based and, thus, involve accelerating and decelerating forces. Impact, wind, and wave loads are all examples of dynamic forces. Some studies have involved evaluation of AM components under dynamic conditions. Often the mechanical properties of materials under rapid loading differ greatly from situations with forces applied more slowly [1].

The focus of this study is on the highest strain rate regime depicted in Figure 1, the shock-wave propagation that occurs at strain rates above 10^4 s^{-1} . Although information and properties obtained at slower strain rate conditions is somewhat applicable, those results are not a full predictor of the material response under more dynamic loading conditions. There are applications where understanding

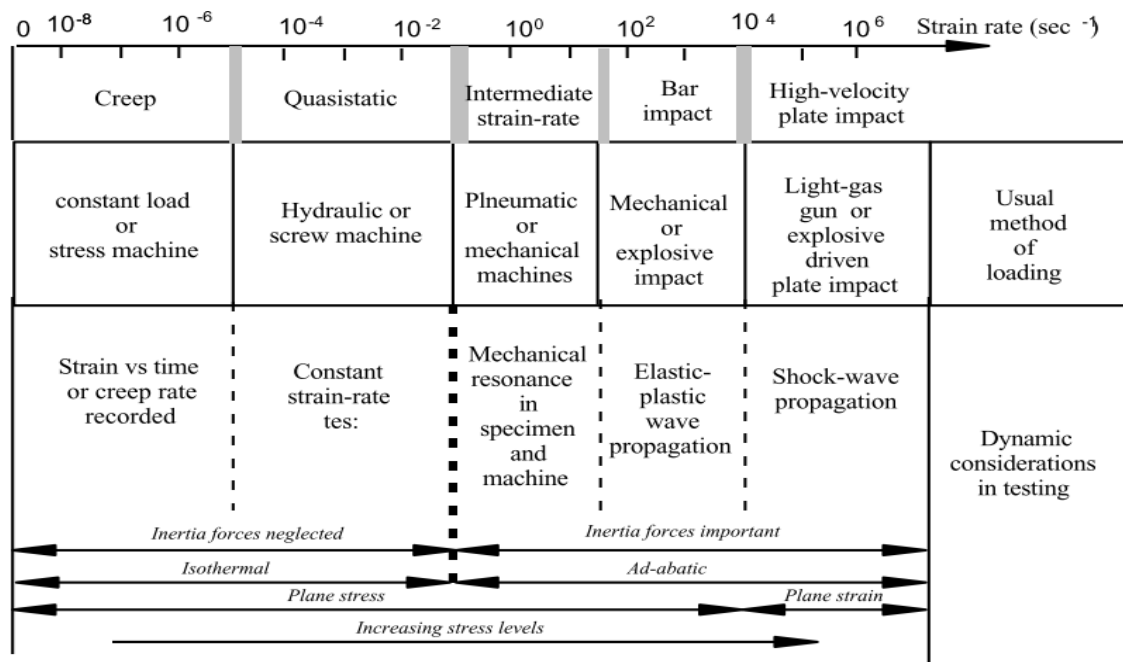


Figure 1: Dynamic Aspects of Mechanical Testing [2]

the relationships between shock wave propagation and the unique characteristics of AM materials may be of benefit in addressing future design challenges.

In general, less research has been done on material behavior in the high strain rate ($>10^4 \text{ s}^{-1}$) dynamic mechanical property regime, where the stress is applied by the material response to the shock wave propagation induced by high velocity impact. Test equipment used to quantify high strain rate (HSR) characteristics is often quite expensive, requires precise set up, and must collect data within a very short time frame (on the order of microseconds). Sample preparation is tedious, as well, since the impact surfaces must be smooth and parallel. For these reasons, fewer than 100 facilities around the world pursue HSR experiments [3]. Gas gun tests are capable of achieving strain rates in excess of 10^4 , up to 10^6 in some cases. In addition to providing increased strain rates, the sample geometry used in gas gun tests also provides information under an applied uniaxial strain that produces triaxial stress conditions (plane strain) [4], giving increased insight to the bulk material properties.

Work by Gray et al [5] compared spall behavior of wrought samples, AM as-built samples, and AM samples subjected to a post-build recrystallization heat treatment (1060°C for 1 hour under vacuum following by cooling to room temperature in 2.5 minutes by rapid argon gas quenching). The heat-treated samples developed a fully recrystallized AM microstructure whereby evidence of deposit interfaces, layer boundaries, and directional solidification normally associated with AM was replaced with a microstructure that more closely resembled the equiaxed microstructure of the wrought samples (although coarser and more varied). Spallation experiments were performed with the plate impact parallel to the build direction. The study showed damage characteristics of the recrystallized AM samples more similar to the wrought samples than the as-built AM samples, which experienced damage evolution across a wide range of locations rather than just along the spall plane of maximum tension. The damage locations appeared to preferentially occur at the build layer boundaries, leading

the authors to a “weak link” hypothesis that suggests that unconsolidated powder at some but not all of these solidification boundaries was the driving factor.

Elsewhere, literature has shown that AM materials exhibit very directionally dependent texture. It has also been demonstrated in similar anisotropic materials that crystal orientation influences both the material wave properties and the dynamic spall response [6-8]. The collection of these previous works contributes to the hypothesis that the spall behavior of AM materials will be controlled, to some degree, by the relative orientation of the applied impact stress. However, these works did not address the influence of initial defect distribution or crystallographic texture on the spall response of the AM samples.

Therein lies the motivation for this research. The project examines the behavior of AM 316L SS when exposed to high velocity impact, the associated shock wave propagation, and the resistance to fracture under these conditions. The material response as a function of orientation will be examined, along with the influence of internal engineered porosity (a design tool unique to AM).

This thesis will address the primary research question: How can the unique attributes and capabilities of AM be used to control shock wave propagation (by reducing the wave’s velocity and magnitude) and influence the material’s associated resistance to impact damage?

Hypothesis 1: Impact orientation with respect to build direction will influence the wave properties, spall strength, and associated damage evolution in AM SS316L.

Hypothesis 2: Purposeful internal voids will influence the wave properties, the spall strength, and the associated damage evolution in AM 316L SS samples with powder filled void spaces that are engineered using the input design file.

This project involves fabrication, sample characterization, plate impact spallation testing, and post-mortem analysis of 316L stainless-steel (SS) samples fabricated using LPBF. The samples were characterized both before and after the gas gun impact experiments. The pre-test characterization consisted of bulk density measurements, ultrasound wave speed measurements, moduli calculations and microstructure characterization. Non-destructive evaluations

were performed on each tested sample, and analysis requiring cross-section was done on representative section from the same printed sample specimen. The post-test characterization was performed on soft-recovered samples collected after the experiment and consisted primarily of cross-section analysis.

Plate impact experiments were performed using the single-stage light-gas gun at the Georgia Institute of Technology. The basic operation of the gas gun test involves impacting a thin target plate with a high velocity flyer plate (ranging from 200-1000 m/s). The resulting failure process is related to nucleation, growth, and coalescence of microvoids and microcracks as the geometry of the sample and flyer plate is designed to generate a tension plane near the center of the sample. Using photon Doppler interferometry (PDV) sensors, the rear free surface displacement of the target is measured with respect to time to evaluate the velocity changes associated with stress wave propagation in the sample.

Two distinct sample sets were used. The first set was used to compare samples fabricated using identical process parameters to examine the influence of impact direction relative to build orientation. The second set possessed specific void sizes and distributions, engineered into the sample via the design file, to examine the influence of porosity.

The structure of the thesis is outlined below. In Chapter 2, background information related to additive manufacturing technologies, fracture mechanics, material wave properties, dynamic (spall) tensile fracture, plate impact test, and stainless steel material characteristics can be found in Chapter 2. The experiment methodology including data sets analyzed and instruments used is in Chapter 3. Detailed results on the build-impact orientation and the randomly distributed engineered porosity studies are located in Chapters 4 and 5, respectively. Modeling of the experiment using commercial finite element tools is done in Chapter 6. Details of a follow up single-void study are located in Chapter 7. Development of a follow up engineering design based on the earlier findings is in Chapter 8. Summary of the findings and conclusions are found in Chapter 9. The suggestions for future work are found in Chapter 10.

Chapter Two

Background

The purpose of this research is to examine the behavior of AM 316L SS when exposed to high velocity impact, the associated shock wave propagation, and the resistance to fracture under these conditions. The material response as a function of build orientation will be examined, along with the influence of internal engineered porosity. The research will address how the unique attributes and capabilities of AM can be used to control shock wave propagation and influence the material's associated resistance to impact damage. Two distinct hypotheses have been developed related to this question.

Hypothesis 1: Impact orientation with respect to build direction will influence the wave properties, the spall strength, and the associated damage evolution in AM 316L SS.

Hypothesis 2: Purposefully placed internal voids will influence the wave properties, the spall strength, and the associated damage evolution in AM 316L SS samples with powder filled void spaces that are engineered using the input design file.

This chapter will provide relevant scientific information to support the formation of these hypotheses.

Historical Background

Additive Manufacturing Technology

Additive manufacturing (AM) is a process of joining materials to make objects from 3D model data, usually layer upon layer, as opposed to traditional subtractive manufacturing methodologies [9]. Once thought of as a novelty used for rapid prototyping, AM has emerged into a rapidly growing technology for end-user products across a wide range of industries [10]. Figure 2 provides an overview of metal AM technology categories.

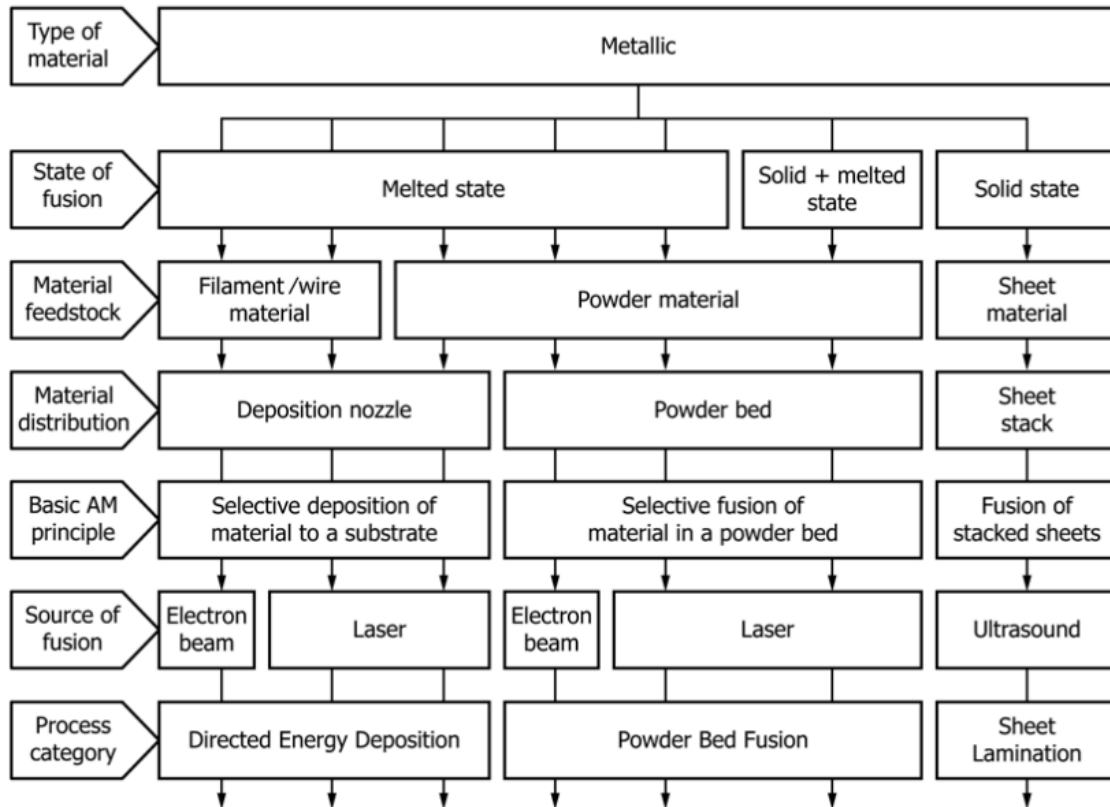


Figure 2: Overview of AM processing principles for metallic materials. [10]

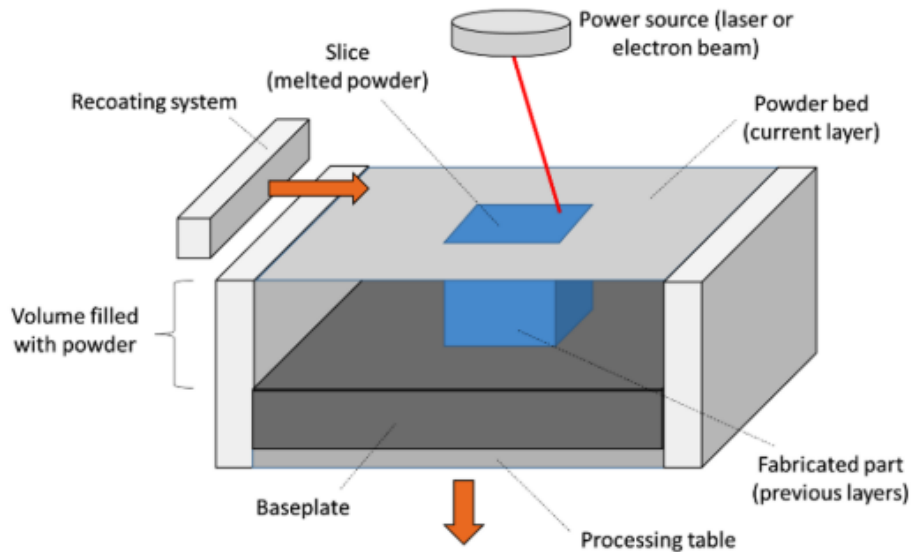


Figure 3: Schematic of LPBF process [23]

Powder bed fusion (PBF) is an AM process in which thermal energy selectively melts and fuses regions of a powder bed [9, 10]. The energy source can either be a laser or an electron beam (EB). With sequential spreading of powder, melting, and solidification of pre-designated regions within these thin layers of metal powders, layer by layer a 3D component is fabricated on top of a metal substrate. In laser powder bed fusion (LPBF), the laser melts the corresponding “slice” from the design file for a given powder layer with a pre-determined scan strategy. The user controls a set of process parameters that define how each “slice” is fabricated. Those commonly used in LPBF are laser power, laser scan speed, hatch spacing, powder layer thickness, and scan strategy.

The combination of small powder particles (0.010-0.100 mm), thin layer thickness (0.020 to 0.050 mm), and a focused laser beam (0 to 1000 W at a spot size of 0.100 to 0.150 mm) allows LPBF machines to create parts with complex geometries, including overhangs, contours, designed voids, etc. and intricate features less than 100 μm [11, 12]. The ability to incorporate internal channels, void space, lattices, and other custom structures within the build provides an almost limitless design space. The development of topology optimization tools [13, 14] has helped evolve the “design for AM” concept in which the product form is driven by its function and requirements while reducing the amount of material. Each individual layer within the completed LPBF AM part experiences its own thermal evolution. The powder is melted to a liquid state that is fused with the previous layer as a part of the solid. The overall thermal cycle involves a rapid heating above melting temperature due to the absorption of energy from the laser and its transformation into liquid, a rapid solidification of the molten material after the heat source has moved on, and numerous re-heating and re-cooling processes when the subsequent layers are welded and the volume element is still exposed to heat through conduction [20]. This thermal cycling has a direct impact on the properties of the finished component. It has been demonstrated that differences in these thermal cycles can result in varied material microstructure, even within the same part [15].

From a larger perspective, the overall AM process flow includes complex relationships between numerous process inputs, process signatures, and product characteristics [16]. The process inputs include a combination of user-defined build parameters (part design, laser power, laser speed, etc.), material feed dependent properties (particle size, chemistry, etc.), and others that are a product of the operating environment (oxygen content, temperature, etc.). The complex combinations of interacting factors (e.g. heat transfer, fluid flow, melting, evaporation, condensation, solidification, solid-state phase transformation, plastic deformation) lead to a variety of microstructures which are sensitive to laser tracking and powder layer spreading, which in turn modify the global and local performance and mechanical properties of the finished part [17]. As a result, the reliability of these products is a function of all these interactions [18-22]. As AM progresses to more mainstream and critical applications, it is important to predict or describe the performance of AM products with non-destructive evaluations (NDE) and connect the data sets to form robust design-process-part relationships.

Although NDE methods are needed for qualification of AM components at the part scale, they too must be validated against mechanical property data in order to provide a sufficient level of confidence and applicability. Tests controlled by standardized methods published by ASTM, ASME, etc. can help relate standard acceptance criteria to the very non-standard AM process. While industry struggles to find ways to qualify AM processes and the parts generated, mechanical testing to accepted standards provides some level of confidence. Both the destructive and non-destructive components of product evaluation must work together to build confidence and process knowledge. At the same time, it is important to understand the fundamental science behind these test results and the AM process, as the material properties of a part are sensitive to the specific geometry (and may differ from the generic test piece geometry).

Every manufacturing process has the potential for defects, which must be understood, addressed, and mitigated. All AM processes, including LPBF, must

also satisfy the geometry-process-structure-property correlations. Grasso [23] categorizes the main defect modes observed in LPBF as (1) Porosity, (2) Balling, (3) Geometric defects, (4) Surface defects, (5) Residual stress, and (6) Microstructure inhomogeneity. All are caused by the events that take place throughout the build process. This study looks at the impact of porosity and microstructure on the product performance. However, rather than focus on these characteristics as negative defects that should be minimized, the study examines how to leverage the differences to a possible design or performance advantage.

Fracture Mechanics

Although this research focuses on dynamic fracture, the basic principles of fracture mechanics are still relevant to form a foundational basis for the current research.

Basics of (Static) Fracture Mechanics

At the atomic level, during the equilibrium (no strain) state, the spacing and the cohesive force between atoms is at a baseline condition. there is no external force applied and the potential energy of attraction is at a maximum. As external tension force is applied, the separation distance between atoms increases. Initially, the repulsive and attractive forces between atoms balance the tensile load. As the strain continues to increase a point is reached where the repulsive force is negligible and the attractive force begins to decrease with continued separation of atoms. This maximum on the curve (Figure 4.Bottom) represents the theoretical cohesive strength of the material. Continued strain causes the cohesive bond energy between the atoms to decrease until the applied force overcomes the cohesive force of the atoms and the bond is broken. [24, 102]

From a macroscopic perspective, there are two main approaches that attempt to model and describes fracture behavior: the Energy Balance Approach and the Stress Concentration Approach.

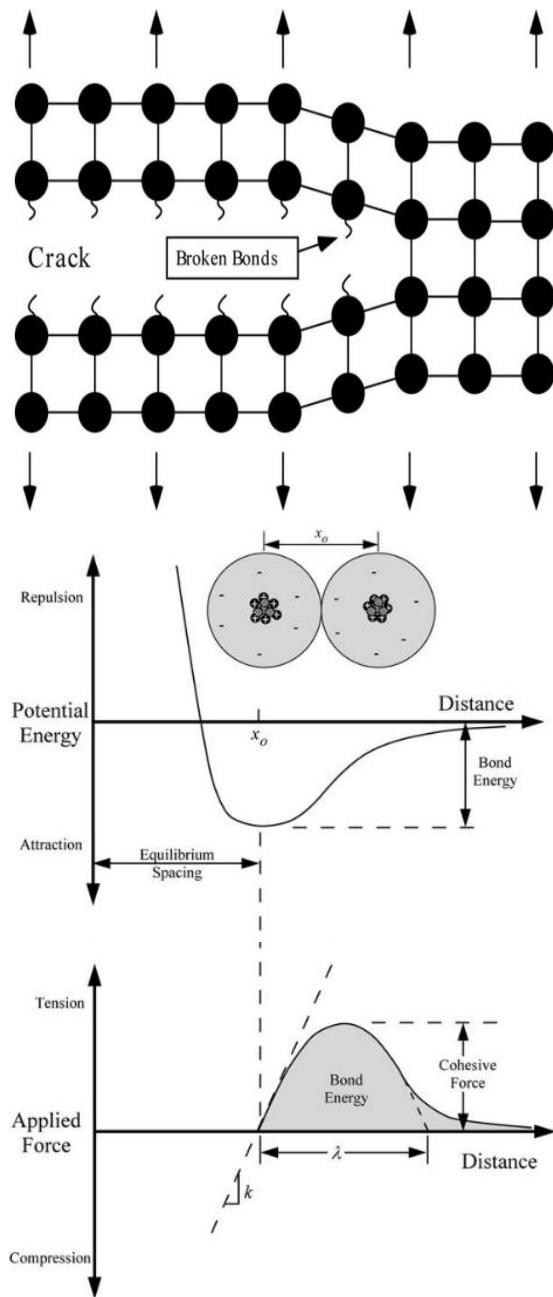


Figure 4: Microscopic fracture example (Top). Potential energy as a function of atomic separation (Middle). Force as a function of atomic separation (Bottom). [24]

The energy balance approach was primarily developed by Griffith [24]. As the name implies, it focuses on the balance between the competing energies within a solid. The potential energy is a function of the applied stress, the material volume, and the material properties (primarily Young's modulus). The surface energy is defined as the energy required to create new surfaces within the material (through breaking of bonds). In the equilibrium state, the surface energy is greater than the potential energy meaning that no new surfaces are being formed. As tension force is applied, these energies change. If the potential energy changes at a faster rate than the surface energy eventually a critical value will be achieved, beyond which crack growth occurs. The fracture stress required to initiate this failure is a function of the material properties (Young's modulus, E , and specific surface energy, γ) and the crack geometry.

Griffith's energy criterion states that fracture occurs when the energy available for crack growth is sufficient to overcome the strength of the material. That energy is a function of the crack size, material properties, and applied stress. Griffith also developed the concept of an energy release rate, a measure of the energy available for an increment of crack extension, for which a critical value exists that represents the energy required to form new surfaces. For a given scenario, fracture occurs when the energy release rate reaches this critical value. Relating back to the energy balance principles, the energy release rate and the critical energy release rate correspond to the change in potential and surface energies, respectively.

While the Energy Balance approach takes an outside-in methodology to focus on the changes of the available and required energy to evaluate the material behavior, the Stress Concentration approach looks at specific configurations and loading modes to determine the stress experienced at discrete locations within the solid, more of an inside-out method.

The stress concentration factor, k , is defined as the ratio of the stress experienced at a specific location to the global applied stress [24]. If that specific stress equals a critical value, then failure occurs. The stress intensity factor, K , is

another way of reporting this behavior for locations within the material. The stress intensity factor has a π factor that better matches the polar coordinate system typically used to indicate location relative to a void or defect, where the stress concentration at a location is a function of the relative distance and angular displacement.

At the tip of a crack, the stress intensity factor is a maximum value (see Figure 5), corresponding to a maximum stress experienced in the material. As the distance and relative location from the crack tip increases, the resulting stress returns to the bulk applied stress value.

The stress intensity at a location also depends on the loading mode. Mode I is crack opening (tension), Mode II is in-plane shear, and Mode III is out-of-plane shear. Different functions are used to describe the stress intensity under different loading modes. As previously mentioned, Mode I is the focus of this study.

If we examine the Mode I relations for failure stress in both the Energy approach and the Stress Concentration approach, we find many similarities. At failure, the stress concentration can be directly linked to the material modulus of elasticity and the energy release rate. This indicates a similarity between the approaches and shows that the resulting stress at a specific location is independent of the approach used.

The stress experienced at a void, or defect, location is dependent on several characteristics. The void size, shape, orientation, and relative location all effect the stress intensity.

Size is the first and most obvious characteristic to examine. For any void, the location of maximum stress is located at the tip normal to the applied stress. The stress experienced (and the Mode I stress concentration) is a function of the void width. For a simple, through crack normal to the applied stress, the stress concentration is a function of pore size (a).

$$K_I = \sigma_{\infty} \sqrt{\pi a}$$

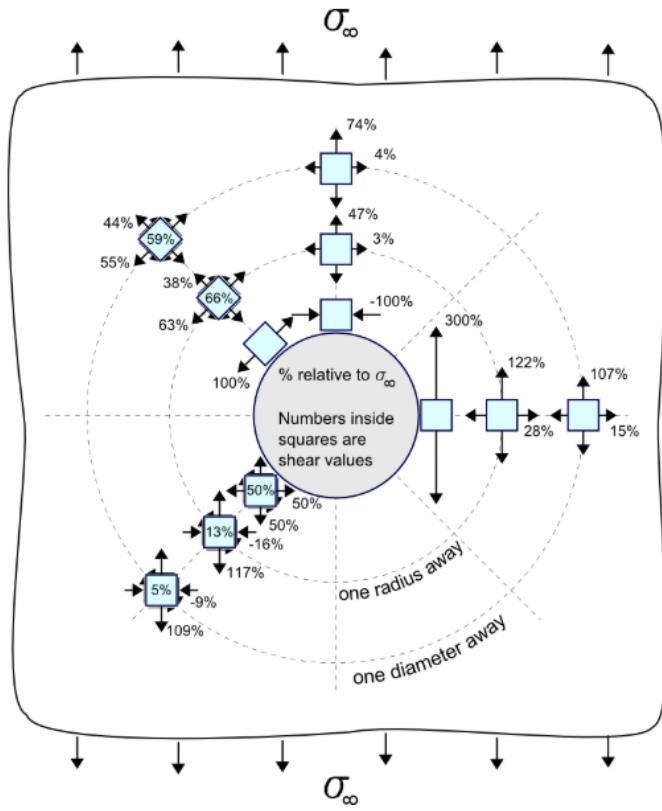


Figure 5: Influence of location relative to defect on stress intensity [24]

In a more complete form that takes into account the void shape, not just width, the stress experienced at the crack tip is a function of the global applied stress, the crack width, and the voids aspect ratio (ρ).

$$\sigma_A = 2\sigma_\infty \sqrt{\frac{a}{\rho}} \quad \rho = \frac{b^2}{a}$$

Along with size, the stress experienced is also a function of the void's aspect ratio (i.e. radius of curvature). In curved voids, the aspect ratio is given as the ratio of the void's height and width. At sharp edges, the radius of curvature approaches zero and the stress approaches infinity. There is, of course, a limit but the sharp-edged location can be used as a maximum for comparisons.

Orientation must be examined because voids are typically not perfectly normal to the applied stress. Also, when a void is rotated relative to the load it experiences both Mode I (tension) and Mode II (shear) stress even if the load is uniaxial. However, each of the resulting stress concentrations are functions containing sine and cosine terms. Since sine and cosine terms are always less than 1, the max stress condition will always occur with a void located at (or very near) the normal relative to the applied load.

The general form for a through crack with stress concentration in the same as an applied force (K_I), is:

$$K_I = \sigma_\infty \cos^2(\beta) \sqrt{\pi a}$$

The factor for a similar condition with the pore oriented normal to the load ($\beta = 0$) is: $K_I = \sigma_\infty \sqrt{\pi a}$

Combining these relations yields the following, which is a function of the angle relative to applied stress.

$$K_\beta = K_I \cos^2(\beta)$$

Configuration of the void(s) is slightly more complex of than the other characteristics discussed. The specific examples used for the earlier relations considered an *infinite plate* (one where the void width is sufficiently less than the distance to the nearest neighboring void or edge that is considered independent of any interactions). Actual conditions are not infinite, so it is necessary to

determine when the assumption is valid and how to approach the case where it is not valid (when interactions must be accounted for). One consideration is the width of the void relative to the sample width. Relations have been developed to estimate the stress concentration relative to the independent case. The relative orientation of the interacting voids is also important (see Figure 7). Collinear voids (spaced normal to the applied load) experience increased stress concentrations, even at the far edge. Consecutive voids, on the other hand, demonstrate decreased stress concentrations that approach the single void stress intensity value as the spacing reduces to zero. The energy flow visualization (Figure 6-c, d) helps explain these phenomena.

Since the spacing factor has 2 components, horizontal spacing and vertical spacing, each component has a different impact on the stress concentration (as seen in Figure 7).

The components can be split into separate factors, such that: $K_S = K_{Sx}K_{Sy}$

$$K_{Sx} = \sigma_{\infty} \sqrt{\pi a} f_x \left(\frac{S}{2a} \right), \quad K_{Sy} = \sigma_{\infty} \sqrt{\pi a} f_y \left(\frac{S}{2a} \right)$$

Again, recall that for the single isolated case: $K_I = \sigma_{\infty} \sqrt{\pi a}$. So,

$$K_{Sx} = K_I f_x \left(\frac{S}{2a} \right), \quad K_{Sy} = K_I f_y \left(\frac{S}{2a} \right)$$

The combination of these factors concludes that, for a given stress, the local stress concentrations caused by individual voids are functions of measurable characteristics – dimensions, angle of orientation, and nearest neighbor spacing. Linear elastic stress analysis of sharp cracks predicts infinite stresses at the crack tip. In real materials, however, stresses at the crack tip are finite because the crack-tip radius must be finite. Plastic material deformation leads to further relaxation of crack-tip stresses and nonlinearity in the material response to stress. This plastic zone limits that stress experienced at a given point to the yield strength, which is less than the max stress obtained from the elastic estimation (See Figure 8). As a result, material plasticity changes the sharp crack geometry to a more blunted crack because of the deformation in the plastic zone.

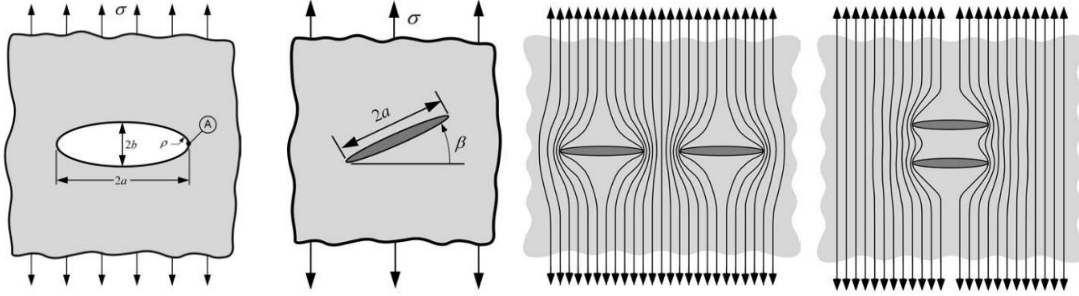


Figure 6: Diagrams of stress concentration conditions. (a) Void diameter and shape. (b) Void orientation relative to stress. (c) Void collinear spacing. (d) Void consecutive spacing. [24]

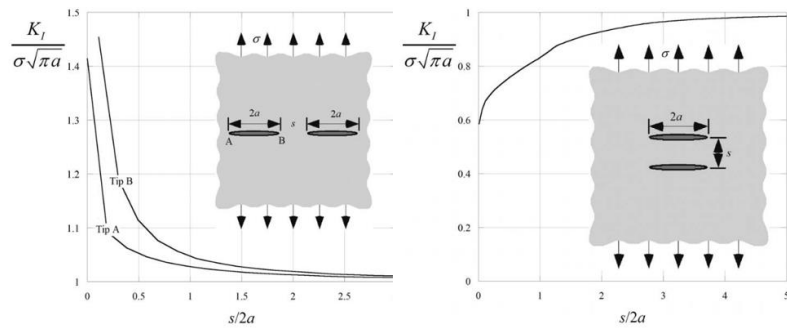


Figure 7: Stress concentration as function of void spacing. Collinear (L) and Consecutive (R). [24]

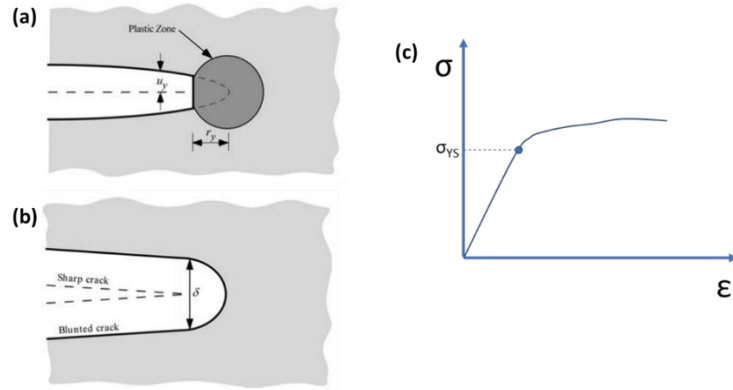


Figure 8: Schematics of plastic zone blunting at crack tip. (a) Estimation of the crack-tip opening displacement in the plastic zone. (b) An initially sharp crack blunts with plastic deformation at the crack tip. (c) Idealized stress-strain diagram indicating yield point where material behavior transitions from elastic to plastic.

The difference in this displacement is a function of the stress concentration (K) of the crack geometry and location, the yield strength (YS) of the material, and the elastic modulus (E) of the material.

In a typical stress-strain diagram obtained from quasi-static mechanical tensile or compression test, this change from linear (elastic) to non-linear (plastic) behavior is observed by a change in the curve that is defined as the material yield strength (or yield point). During this plastic yielding, the stress experienced by the sample is somewhat relaxed although the strain continues to increase.

Dynamic Fracture Fundamentals

Dynamic fracture mechanics examines the specific case in which high loading rates result in a different material response than observed in traditional static or quasi-static scenarios. Three specific complicating factors are present in dynamic fracture: (1) inertia forces, (2) reflected stress waves, and (3) rate-dependent material behavior. [24] Figure 9 provides a schematic.

Inertia forces

Inertia, in its simplest form, is a property that urges a solid body to stay at rest (existing state) rather than change its velocity when exposed to an external force. This principle is important in the case of dynamic fracture mechanics because at high loading rates a portion of the applied energy is converted to kinetic energy (of motion) in addition to deformation energy that stresses the material. This differs from quasi-static cases where the applied energy exclusively deforms the sample.

To better bound the condition where inertia forces are involved, it can be helpful to establish a transition time where the material response is dominated by inertia effects early on and dominated by deformation energy after, to the extent that the scenario effectively becomes quasi-static at sufficiently long time interval. Models have been developed to estimate this transition time [24].

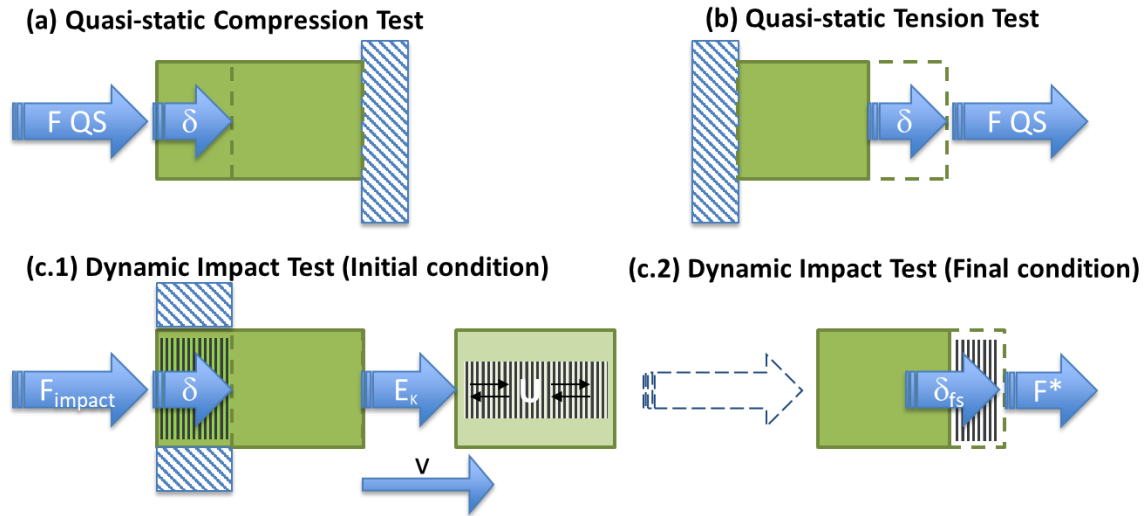


Figure 9: Schematics comparing quasi-static and dynamic testing. (a) Quasi-static compression test setup and deformation. (b) Quasi-static tension test setup and deformation. (c.1) Initial condition of dynamic impact test. Initial material compression driven by wave propagation. Impact causes change in sample velocity. (c.2) Final condition of dynamic impact test. Tensile force driven by wave reflection at rear free surface.

Reflected Stress Waves

The propagation of waves is fundamental to the dynamics of solids. Any solid structure will respond to a transient disturbance through the propagation of stress waves [24]. The initial stress waves generated by the applied force propagate as compression waves. Once reflected from the far surface, they are reflected as rarefaction waves. Rarefaction waves are simply the opposite of compression waves within the material. At high strain rates (greater than 10^4 s^{-1}), the stress wave velocity through the material is very fast, on the order of microseconds. Depending on the location within the material at any given time step, the stress state may be in either tension or compression due to the directions and intensities of the specific interacting stress waves. Wave interactions can also produce transverse waves (normal to the direction of interest) which drives the analysis away from the simple uniaxial approach. Unlike more readily observable processes, development of scientific laws governing the behavior of cracks subjected to these types of stress waves is still in its infancy [25]. Many existing relations are valid only at short times, initial conditions, or infinite bodies and neglect the effects of reflected waves. For cases with finite samples where stress waves reflect back to the crack tip, the dynamic stress intensity is too complex to determine analytically and must be extrapolated either experimentally or numerically. Due to the complexity, more global and continuum approaches are often preferred when examining the bulk material properties of samples tested under high strain rates.

Rate-dependent material behavior

If the effects of inertia and reflected stress waves can be eliminated, one is left with the rate-dependent material response [24]. One of the most extensively used models for predicting the material behavior and failure in metals under non-standard conditions is the Johnson-Cook material model. The model quantifies the equivalent stress at any given set of conditions by applying three

components: (a) strain hardening effect, (b) strain rate strengthening effect, and (c) temperature effect.

$$\sigma = (A + B\varepsilon^n) (1 + C \ln \dot{\varepsilon}^*) (1 - T^{*m})$$

$$\dot{\varepsilon}^* = \frac{\dot{\varepsilon}}{\dot{\varepsilon}_{ref*}} \quad T^* = \frac{T - T_{ref}}{T_m - T_{ref*}}$$

The strain hardening effect is controlled by the yield stress of the material at standard conditions (A), a strain hardening variable (B), the equivalent plastic strain of the material (ε), and a strain hardening factor (n).

The strain rate strengthening effect is controlled by a strengthening factor of strain rate (C), and a dimensionless strain rate ($\dot{\varepsilon}^*$) which is calculated as a ratio of the applied strain rate ($\dot{\varepsilon}$) and a reference strain rate ($\dot{\varepsilon}_{ref}$).

The temperature effect takes into account a homologous temperature (T^*) and a thermal softening coefficient (m). The homologous temperature is a function of the deformation temperature (T), the material melting temperature (T_m), and a reference deformation temperature (T_{ref}).

As indicated by the Johnson-Cook model, application of HSRs tends to elevate the flow stress of the material, but this effect depends on the specific failure mechanism. In stress-controlled material, HSRs tend to decrease the cleavage resistance, whereas strain-controlled materials often see an increase in toughness because more energy is required to reach a given strain value. Ductile failure, as seen in most stainless steels, is primarily strain controlled [24].

Material Properties and Microstructure of 316L Stainless Steel

316L stainless steel (SS316L) is used in a variety of applications due to its mechanical properties, such as high tensile strength at a significant plastic strain (40% elongation in tension) [26]. Stainless steels are a subset of steels that contain increased chromium (Cr) content for improved corrosion resistance [27, 28]. 316L stainless steel (AISI316L) has a defined composition as listed in Table 1. The “L” designation indicates that SS316L is a low-carbon steel, with a maximum C content of 0.03% by weight. Low-carbon steels are attractive in

welding applications because of the resistance to grain boundary carbide precipitation [26] and composition that prevents solidification cracking [29, 30, 31]. 316L is an austenitic stainless-steel alloy with a primary face centered cubic (FCC) crystalline structure [27]. As such, SS316L typically experiences standard ductile fracture evolution of (1) void nucleation, (2) void growth, and eventual (3) coalescence of voids, when sufficient tensile stress is applied [28]. Ductile fracture sites are typically characterized by growth of the plastic zone around the individual voids and interaction of those, whereas brittle fracture typically tends to fail as crack growth along the length with sharp tips [25].

It is documented in welding literature [29, 32] that SS316L undergoes a δ -BCC to γ -FCC phase transformation during cooling,. The Fe-Cr-C pseudo-binary diagram developed by Lippold [30] at 17% Cr (Figure 10) indicates this for the low carbon content in SS316L (<0.03%). In both welding and AM processing, this leads to a strengthening effect that is also often associated with decreased ductility [29, 32, 33, 34]. The strengthening effect is related to a refined microstructure that forms during welding and AM, combined with ferrite/austenite interface boundaries. The observed reduction of ductility is often related to defect formation during AM processing [29, 35], and/or higher impurity contents of the AM build.

The solidification behavior related to phase composition of a Fe-Cr-Ni system (which includes SS316L) is heavily influenced by the Ni and Cr content (Figure 11) [36]. It has been further documented that the ratio of chromium-to-nickel-equivalent (Cr_{eq}/Ni_{eq}) affects the formation of delta ferrite during solidification of stainless steels [36-39]. There are four distinct modes normally considered based on this ratio. These four modes are Fully Austenitic (A), Austenitic Ferritic (AF), Ferritic Austenitic (FA), and Ferritic (F). The formation reaction and microstructure associated with each mode is governed by the Cr_{eq}/Ni_{eq} ratio, which was further quantified in works by Saluja (38).

Table 1: Chemical Composition of AISI316L

	Element (Weight %)							
	C	O	Si	Mo	Cr	Mn	Ni	Fe
AISI 316L	< 0.03%	n/a	< 1%	2-2.5%	16.5-18.5%	< 2%	10-12.5%	Bal. (> 63%)

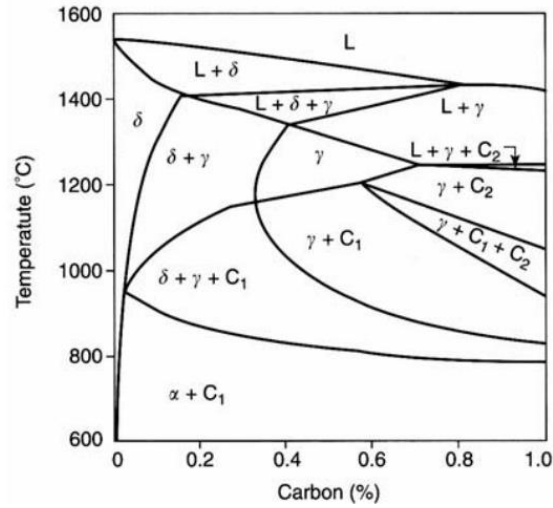


Figure 10: Fe-Cr-C pseudo-binary diagram at 17% Cr [30]

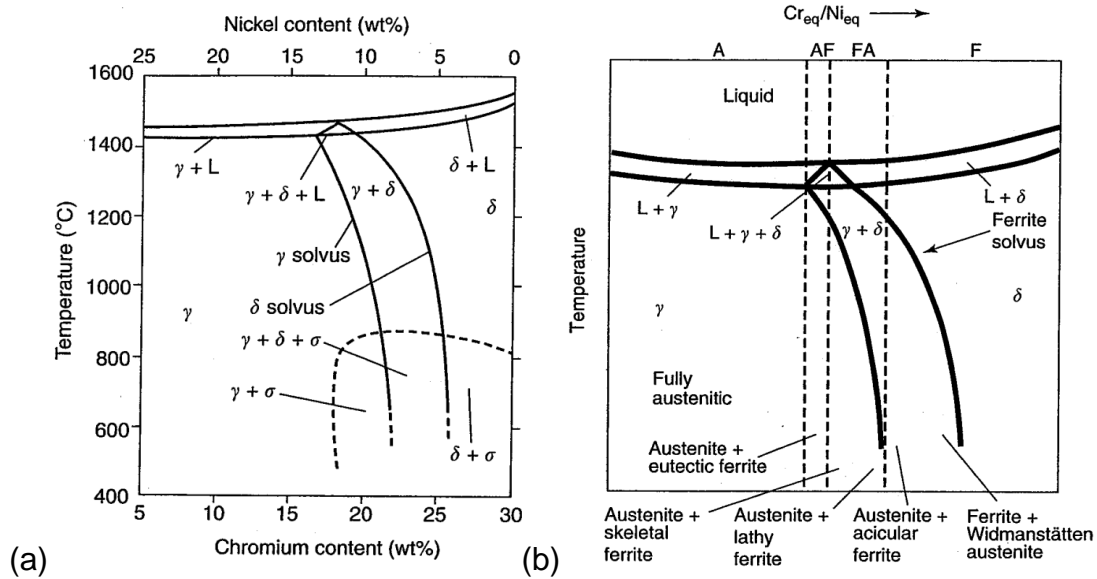


Figure 11: Pseudobinary Fe-Cr-Ni ternary diagrams (a) Pseudobinary section of the Fe-Cr-Ni ternary diagram at 70% Fe. (b) Modified pseudobinary section showing solidification modes. [30]

The ferrite content in stainless steels can be determined using a variety of methods, including image analysis, magnetic measurements, and X-ray diffraction (XRD) analysis [37]. Putz et al [37] evaluated these methods and concluded that image analysis to be the most accurate method for measuring the ferrite content in duplex stainless-steel welds. Although considered as a well-known reliable method for phase structure measurement, XRD was found to not be a reliable measurement method due to the grain morphology of the welds, which contained primarily large ferrite grains of a preferred orientation rather than the several small grains with random orientation [37]. Regardless of the measurement method used, the authors observed a decrease in ferrite content as the number of weld layers increased, possibly due to the formation of secondary austenite from reheating. Accordingly, the final weld bead (that was not reheated by further welds) again showed a higher ferrite content.

The work by Godfrey et al [55] looked closely at the solidification process of individual melt pools associated with LPBF AM. The results of that study revealed the melt pool boundaries to be associated with the fcc- γ -austenitic mode of solidification while the regions within the melt pool region, although austenitic at room temperature, originally solidified as bcc- δ -ferrite. Using interface response function (IRF) and heat transfer models, the authors determined that the melt pool boundaries possessed a high thermal gradient (G) and low solid-liquid interface velocity (V), which leads to γ solidification at the boundary, and that the velocity increases toward the inner region of the melt pool the solidification transitions to δ . This leads to the conclusion that there is a massive solid-state transformation of δ to γ that occurs after solidification.

Table 2: Solidification modes, Reactions, and Final Microstructure Cr/Ni ratio and solidification mode association [38]

Solidification Mode	Equivalent Ratio	Reaction	Microstructure
A – Fully Austenitic	$\text{Cr/Ni} < 1.25$	$L \rightarrow L + A \rightarrow A$	Fully Austenitic
AF – Austenitic Ferritic	$1.25 < \text{Cr/Ni} < 1.48$	$L \rightarrow L + A \rightarrow L + A + (A + F) \rightarrow A + F$	Ferrite at cell and dendrite boundaries
FA – Ferritic Austenitic	$1.48 < \text{Cr/Ni} < 1.95$	$L \rightarrow L + F \rightarrow L + F + (F + A) \rightarrow F + A$	Skeletal and/or lathy ferrite resulting from ferrite to austenite transformation
F – Ferritic	$1.95 < \text{Cr/Ni}$	$L \rightarrow L + F \rightarrow F \rightarrow F + A$	Acicular ferrite or ferrite matrix with grain boundary austenite and Windmaslatten side plates

Relevant Theory and Fundamentals

Material Wave Properties and Modulus

Impact, or similar mechanical disturbance, at the surface of a solid material produces a propagating wave response within that material [40]. Waves propagate as a pulse that causes movement of the individual particles relative to one another. This phenomenon has been modeled as a semi-infinite mass-spring system where each mass represents the individual material particles and the springs correspond to the interconnecting bonds [40]. Depending on the characteristics of the disturbance and the material properties of the sample, this wave may be either elastic or plastic. In the conceptual sense, the term “particle” refers to a small unit of matter. A particle can be nano-scale (subatomic electrons and protons), micro-scale (atoms and molecules), or macro-scale (powder particles). In context of wave theory, a particle is synonymous with atoms or molecules and is used to differentiate the movement of the small units of mass within a sample from the wave that is traveling through the material (i.e. particle velocity vs. shock wave velocity).

Elastic waves change the stress and potential state, but the material then relaxes to the original state once the stress is removed. Acoustic waves are an example of an elastic wave. Plastic waves, including shock waves, cause deformation of the material. Waves propagating within a continuum are primarily longitudinal (where the particle velocity is parallel to the direction of wave propagation) or transverse (where the particle velocity is perpendicular to the direction of wave propagation). Transverse waves are also referred to as shear waves. Several other types of waves also exist but are primarily bound to certain special conditions [4]. These special waves include surface (Rayleigh) waves, interfacial waves, love waves, and bending waves.

Elastic wave properties of a material are measurable using ultrasound techniques [41] as preliminary characterization prior to the shock loading experiment (such as plate impact). Later on in the process, these elastic wave properties are coupled with the data from the plate-impact experiment to

calculate dynamic strength properties of the material sample. Using a pulser/receiver, appropriate ultrasonic probes, and an oscilloscope for data collection the wave properties are determined.

Longitudinal waves produce particle motion that is parallel to the direction of wave propagation. Shear waves, on the other hand, produce particle motion that is perpendicular to the direction of wave propagation. A third component, the bulk wave speed, is simply the total net resulting wave speed when the longitudinal and shear components are combined. The elastic modulus (also referred to as Young's modulus) is a measure of the materials resistance to strain from applied tensile stress. The shear modulus measures the resistance to shear strain from applied shear stress. The bulk modulus is a volumetric term that relates the materials ability to resist volume change when stress is applied from all directions.

The longitudinal (C_L) and shear (C_S) sound wave velocities are directly measured; the other properties are calculated using relations of those measured properties (shown below). The other properties are bulk sound speed (C_B), elastic modulus (E), shear modulus (G), and bulk modulus (B).

$$C_b = \sqrt{C_L^2 - \frac{4}{3}C_S^2} \quad \text{Poisson's Ratio } (N) = \frac{E}{G} - 1$$

$$C_b = \sqrt{\frac{B}{\rho_0}} \rightarrow B = \rho_0 C_b^2 \quad C_S = \sqrt{\frac{G}{\rho_0}} \rightarrow G = \rho_0 C_S^2 \quad C_L = \sqrt{\frac{E}{\rho_0}} \rightarrow E = \rho_0 C_L^2$$

In these measurements, a pulse is applied that travels to the free surface, is reflected at the free surface, and returns. The equipment used to collect these measurements includes a few components. A pulser/receiver in the pulse echo configuration is attached to an ultrasonic probe. The ultrasonic probe is designed to send and receive either a longitudinal or shear wave, and the wave speed is measured accordingly. Different transducers are used to generate longitudinal (compression/rarefaction) and transverse (shear) wave signals. The data is recorded using an oscilloscope.

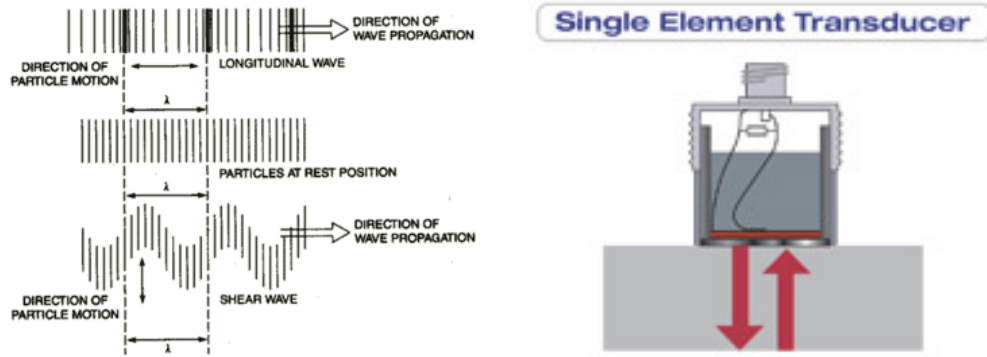


Figure 12: Schematic of Longitudinal and Shear wave propagation (L). Example of ultrasonic transducer (R) [42]

Gas gun Plate impact tests are capable of achieving strain rates in excess of 10^4 , up to 10^6 s^{-1} in some cases, and causing large stresses (in the GPa range) within the impacted target that result in a material response much different than the more common quasi-static tensile or compression testing methods [4]. A shock wave is defined as a discontinuity in pressure, temperature (internal energy), and density [4]. For solids, the shock front produces a combination of deviatoric and hydrostatic stresses that must be differentiated between. Deviatoric stresses control the distortion of the body resulting from unequal principle stresses (shape changes), while hydrostatic stresses result from the average of the three normal stress components to control the bulk compression of the body (volume change). If the hydrostatic stress exceeds the deviatoric stress sufficiently such that the deviatoric stress component is negligible, then the flow stress treatment normally reserved for fluids can be applied. The properties for shock waves are based on this hydrodynamic treatment.

The calculation of shock wave parameters is based on the Rankine-Hugoniot conservation equations of mass, momentum, and energy. A fundamental requirement for consideration as a shock wave is that the velocity of the pulse, U , increases with increasing pressure, P [4]. For examination of the conservation equations, the shock front itself is used as the reference frame. The state ahead of the front are considered initial or ambient values for pressure (P_0), density (ρ_0), and temperature (T_0), while the properties behind the shock front are referred to as the shock state properties (P , ρ , T). From a velocity perspective, the particles in front of the shock wave are stationary ($U_0 = 0$), the velocity of the shock is U_s and the resulting velocity of the particles behind the shock is referred to as the particle velocity (U_p). The particle velocity is the product of displacement of the particles from the pressure applied by the moving shock front.

Of particular importance is the $\rho_0 U_s$ term in the conservation of momentum equation. This term is commonly referred to as the “shock impedance” and plays an important role in shock wave reflection and transmission across different materials.

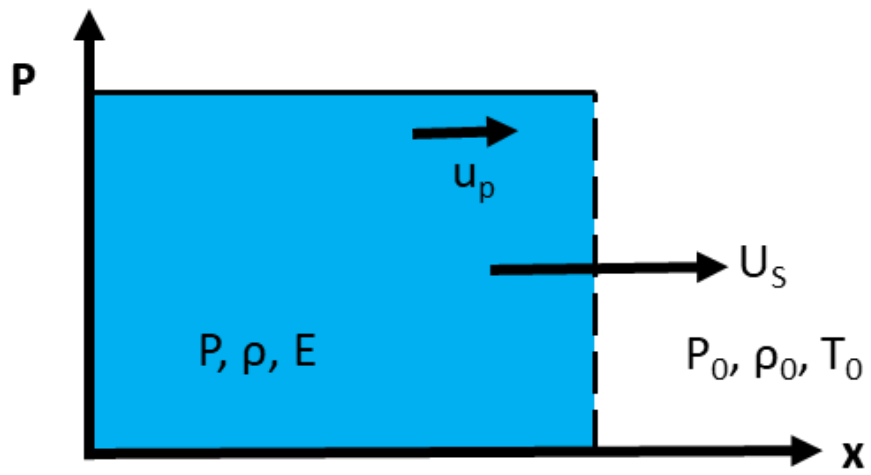


Figure 13: Schematic of shock front.

Based on these inputs the conservation equation become:

$$\text{Conservation of Mass:} \quad U_S \rho_o = (U_S - U_P) \rho \quad (1)$$

$$\text{Conservation of Momentum:} \quad P - P_o = \rho_o U_S U_P \quad (2)$$

$$\text{Conservation of Energy:} \quad E - E_o = \frac{1}{2}(P + P_o)(V_o - V) \quad (3)$$

The conservation equations alone cannot be used to solve for all the unknowns. A fourth equation is needed, typically either a constitutive equation or an equation of state (EOS). For the case of shock wave propagation, the shock-hugoniot EOS is used. An empirical relationship between U_s and U_p is used to establish an EOS for the particular material of interest. It uses the elastic sound wave speed of the material and an empirical constant to relate the shock wave velocity to the particle velocity. The full EOS is given as the multi-term polynomial equation: $U_S = C_o + S_1 U_P + S_2 U_P^2 + \dots$, where the S terms are empirically determined constants and C_o is the sound velocity of the material at zero pressure. For most metals, S_2 and beyond is equal to zero, reducing the EOS to a linear relationship between particle velocity and shock velocity (EQN 4). The other relations can then be obtained using that information.

$$\text{Shock-Hugoniot EOS:} \quad U_S = C_o + S_1 u_P \quad (4)$$

A common term used to describe a materials response to a propagating shock wave is “shock impedance”. The shock impedance is rooted from the relationship between the pressure generated by the shock wave, P , and the particle velocity behind the shock front, u_p . This relationship can be used to generate the P - u_p plot known as the shock-Hugoniot. The Hugoniot is a locus of all possible shock states for a particular material under the defined conditions [4].

In the purest sense, the resulting pressure, P , of the Hugoniot is a second-order relationship with respect to the particle velocity, u_p , if we define the shock velocity, U_s , in EQN 2 with the EOS in EQN 4. To simplify, a linear approximation

can be made for situations with defined start and end states. The line connecting the particular shock's end states on the Hugoniot is known as the Rayleigh line. Referring back to EQN 2, the slope of this Rayleigh line is equal to $\rho_0 U_s$ and is referred to as the material's shock impedance.

Information related to a specific experiment can be obtained from the Rayleigh line and Hugoniot plot using a graphical analysis method known as impedance matching. The slope of the Rayleigh line is obtained using the sample material density (measured a priori) and the shock velocity (obtained from experiment data). This line represents the target sample. A second line is derived as a reflection of this Rayleigh line, having negative slope and intersecting the vertical axis at the experimental impact velocity. This line represents the flyer plate (of like material). Initially (just before impact) the flyer is traveling at maximum velocity and there is zero pressure, as the samples are not in contact with each other. At impact the stress in the flyer and target must be equal to satisfy the conservation of momentum. This leads to a simultaneous increase in the target velocity and decrease in the flyer velocity. This peak stress condition corresponds to generated particle velocity on the P-v plot (Figure 14).

The same graphical impedance matching technique is also used to examine the effect of the shock wave transmission between different materials (possessing differing shock impedance). This concept will be discussed in detail later in this section. First, a special case will be reviewed which applies to the resulting reflection of a square shock wave (as is created by plate impact experiments) as it reaches a free surface. Wave reflection at the free surface is an important tenet of the plate impact experiment. The free surface represents a special case where the second medium has a shock impedance equal to zero, therefore providing full reflection of the wave and zero transmission.

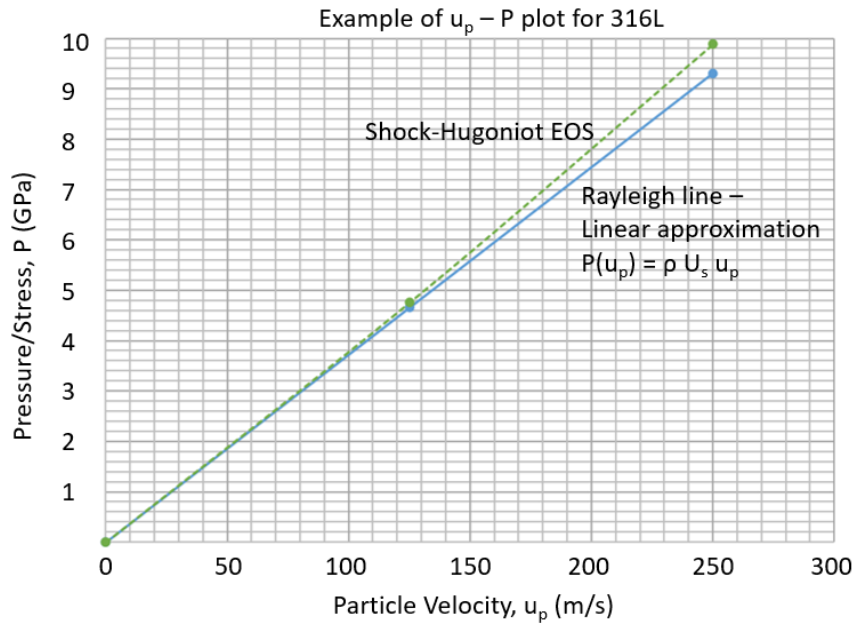


Figure 14: Example u_p vs P plot for 316L. Compares Shock-Hugoniot EOS and Rayleigh Line Approximation

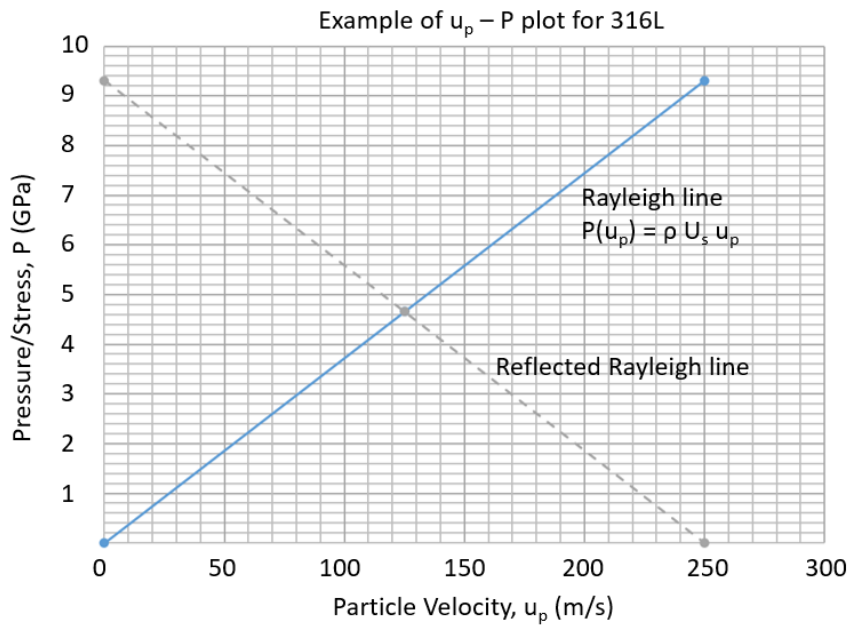


Figure 15: Example u_p vs P plot for 316L, showing "impedance matching" technique for reflection at free surface.

Figure 16 [4] demonstrates the behavior of pressure and particle velocity at the free surface of the target sample. In this depiction it is readily observable that the pressure wave is fully reflected by the free surface and tensile stress is generated within the target.

When a shock wave propagates from one material to another, changes in pressure, wave velocity, and density occur. Similar to the impact example, continuity at the boundary dictates that the particle velocity and pressure will be the same in both materials [4]. Since the shock impedance term is the product of material density and shock wave velocity (per EQN 2), it is greater for materials with high density and high sonic velocity (which is a major factor in resulting shock velocity). The shock impedance corresponds to the slope in the P-v plot used for impedance matching. As a result of the changing impedance, the full pressure of the shock wave is not transmitted, as a portion is reflected either as a compressive or rarefaction pulse. The impedance matching technique used for analyzing this phenomena utilizes a “reflected” plot (not to be confused with the reflected wave pulse) of the same slope as the starting material (Material A) and two plots representing the shock impedance of the two materials of interest (A and B). The graphical concept of impedance matching basically tracks the reflected plot (AR) from the intersection with A to the intersection with B. The latter represents the pressure and particle velocity state of the transmitted wave.

The case of a shock wave propagation from a material of higher impedance (A) to a material of lower impedance (B) is shown in Figure 17-R. The compressive pressure (stress) decreases as the wave is transmitted to material B due to the reduced resistance in that material. The remaining portion is reflected back into material A as a rarefaction wave. This reflection is like the free surface case (zero impedance) except that a portion of the wave is transmitted.

The case of a shock wave propagation from a material of lower impedance (A) to a material of higher impedance (B) is shown in Figure 17-L. Conversely, the compressive pressure (stress) increases as the wave is transmitted to material B due to the increased resistance in that material. The remaining portion is again

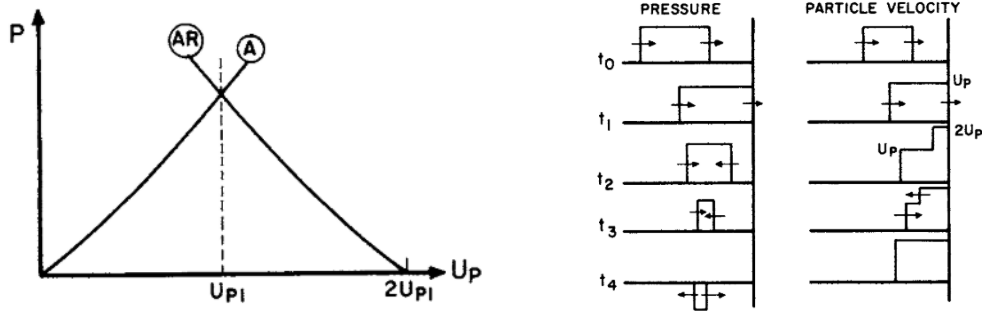


Figure 16: Reflection of shock wave at a free surface (Left). Pressure-distance and Particle velocity-distance profiles at free surface interface (Right). [4]

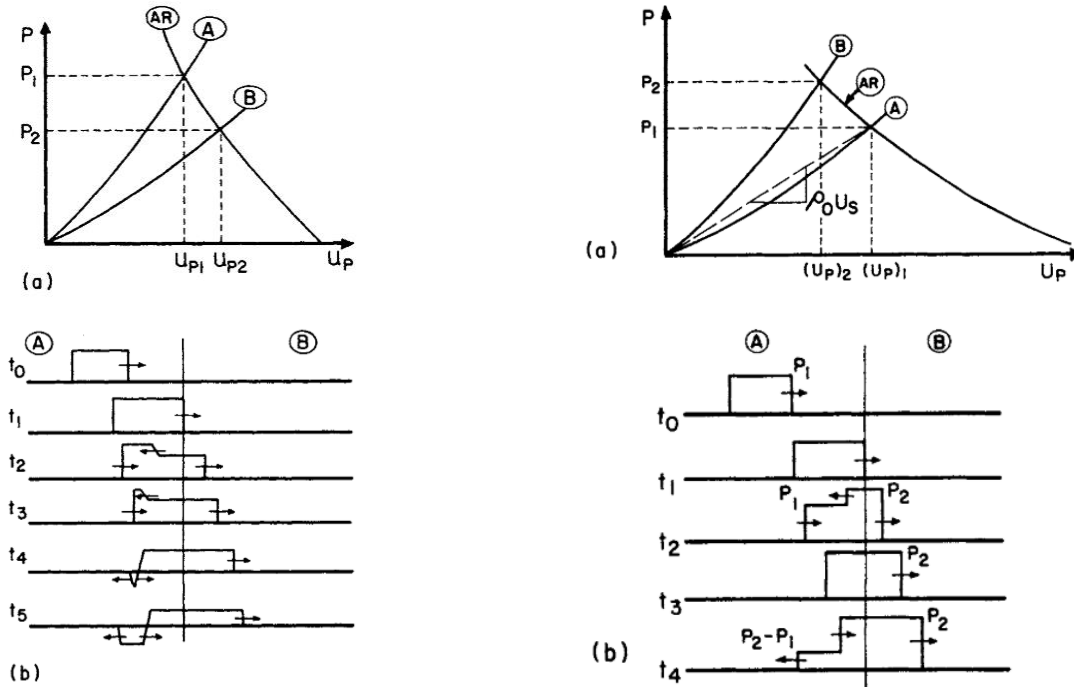


Figure 17: Transmission of shock wave from one material to another. (Top Left) Pressure-Particle velocity plot of high to low shock impedance transmission. (Bottom Left) Stress profile of high to low impedance transmission. (Top Right) Pressure-Particle velocity plot of low to high impedance transmission. (Bottom Right) Stress profile of low to high impedance transmission. [4]

reflected into material A. However, to maintain equilibrium, this reflected wave is compressive in nature with a magnitude equal to the pressure difference in the A-AR and B-AR intersections on the plot.

As referenced earlier, when a compressive stress wave propagates from one material to another, a portion of that wave is reflected. The specific details of that reflection depend on the shock impedance of each material involved, but wave reflection must be considered regardless of those specifics. The portion of the wave stress reflected (and transmitted) can be determined based on the impedance properties of the materials involved using impedance matching techniques [4].

The phenomena of wave reflection and transmission discussed earlier focuses on the ideal case in which the material interface boundary is completely perpendicular (normal) to the direction of wave propagation. However, if the interface boundary occurs at an angle (as seen in Figure 18) then some form of refraction takes place as well. The figure displays a longitudinal wave that intersects the interface between material A and material B at an angle θ_1 .

The result is four-fold. (1) A longitudinal wave is transmitted into material B, but at a different angle, θ_2 . (2) A second longitudinal wave is reflected back into material A, at θ_3 . (3) A transverse wave, created by the angled interface, is transmitted into material B. And (4) a final transverse wave is reflected in similar fashion to the reflected longitudinal wave. The magnitude and angle associated with each resulting wave can be found using the variation of Snell's law.

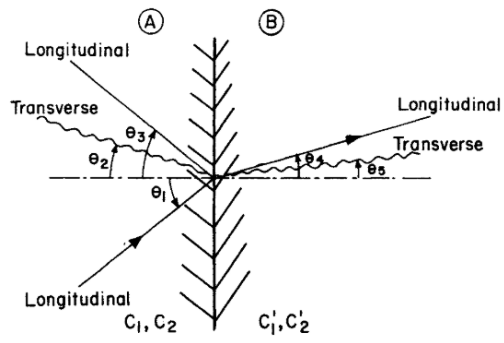


Figure 18: Longitudinal elastic wave intersecting material A-B boundary, generating refracted and reflected waves. [4]

Spall Fundamentals and the Plate Impact Experiment

Plate-Impact Experiment Details

Gas gun plate impact experiments generate shock waves by impacting a thin target with a flyer projectile. A schematic of the sample configuration is shown in Figure 19. The projectile consists of a sabot that drives a flyer plate of similar material. The target sample holder is fixed using an epoxy so that both the flyer and target can pass through for soft-recovery of samples. Both the flyer and the target sample holder are machined and lapped to achieve very parallel conditions at each face. Each sample is designed with a taper to allow it to break away from the holder following impact.

The basic operation involves impacting a thin target plate with a high velocity flyer plate at velocities ranging from 200-1000 m/s. The resulting failure process is related to nucleation, growth, and coalescence of microvoids and microcracks. The projectile (with impacting flyer plate) is launched by a breech of high pressure compressed gas (usually a light gas such as helium or hydrogen). The projectile accelerates as it travels down the barrel section. The initial driving pressure force is calculated in advance to deliver the projectile at a desired impact velocity when it reaches the target plate. A large chamber is located at the end of the barrel. In addition to collecting the specimens for post-mortem characterization, the chamber also allows a free space for the waves to propagate freely through the sample without touching other surfaces that could constrain the movement and interfere with results. The time-scale of the experiment is on the order of microseconds.

The sample target geometry is a thin plate. This geometry influences one-dimensional wave propagation, which results in a uniaxial strain state. Using photon Doppler interferometry (PDV) sensors, the rear free surface displacement of the target is measured with respect to time to evaluate the velocity changes associated with stress wave propagation in the sample. The experiment is typically designed with the flyer plate one-half the thickness of the target to generate spall fracture near the mid-plane of the sample. Sample recovery is

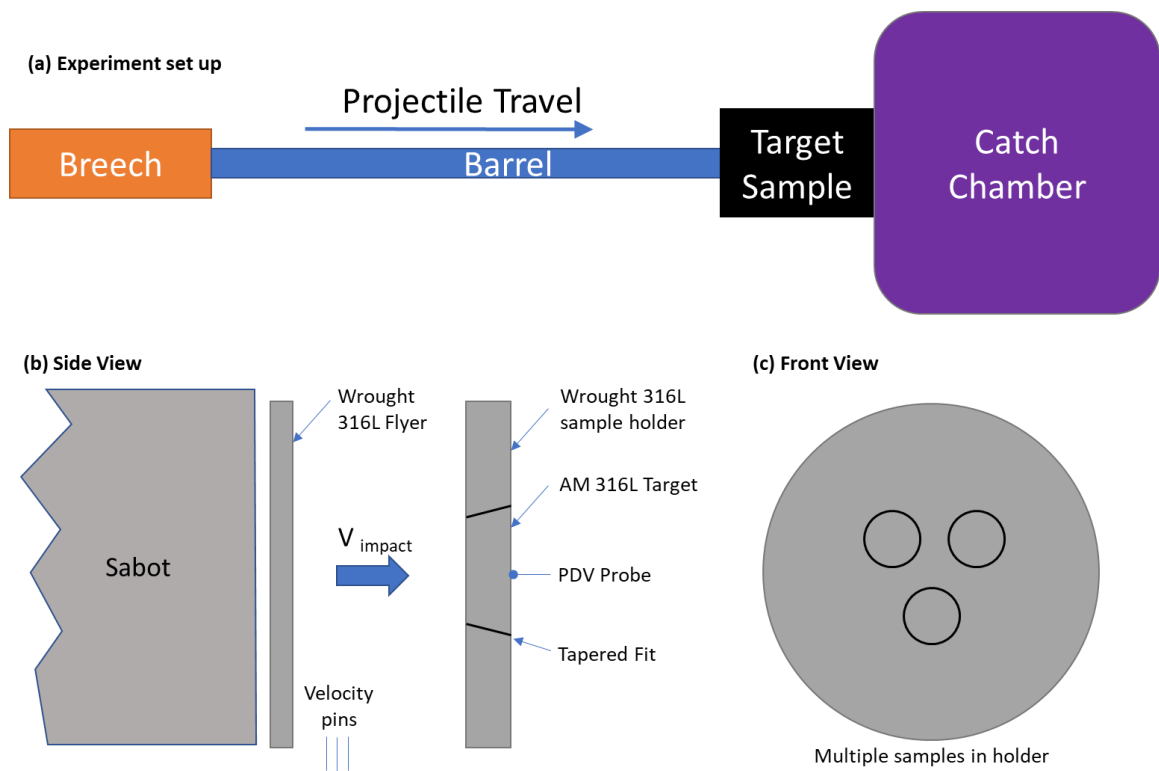


Figure 19: Experiment details (a) Diagram of Light Gas Gun setup for High-velocity plate impact experiments. (b) Side view schematic of flyer-target sample configuration, (c) Front view of target sample holder

performed using a bed of soft rags (or similar) located in a catch tank beyond the sample chamber. Recovered samples are inspected for any damage away from the impact face to ensure that no secondary impact events occurred during the experiment.

During these experiments, the internal material behavior (stresses, etc.) resulting from the wave propagation and interactions is not directly observable. Instead, the free surface velocity is measured using laser interferometry and plotted as a function of time and used, in conjunction with measured material properties, to determine the internal activity within the material during the experiment.

Figure 20 provides simplified diagrams of the events that take place during a typical gas gun plate impact experiment [3]. Figure 20(a) shows the wave propagation by relative location vs time. Figure 20(b) shows the free surface velocity profile over time. Initially, at t_0 , the target is at rest and the corresponding free surface velocity is zero. The impact generates a compressive pulse consisting of an elastic precursor wave and a plastic (shock) wave. The elastic precursor wave, traveling at the longitudinal sound speed (~ 5700 m/s for SS316L), reaches the rear free surface of the target at t_1 . This corresponds to a sharp increase in the measured free surface velocity. At a certain point, the measured velocity transitions to a more gradual increase. This indicates that the Hugoniot elastic limit (HEL) has been reached. The HEL is the point at which a solid, loaded in compression can no longer support elastic distortion and begins to plastically deform the structure [3]. It is analogous to the dynamic compressive yield stress, and is calculated using the velocity at the HEL, the corresponding initial density, and longitudinal wave speed, given by EQN (5).

- $$\sigma_{HEL} = \frac{1}{2} \rho_0 C_L u_{HEL} \quad (5)$$

The slower moving shock wave arrives at the rear free surface at t_2 , resulting in a more rapid velocity change. This shock pulse drives the target to the peak free surface velocity. After t_2 , a rarefaction wave begins progressing back into the sample, relaxing the compressed material in an effort to restore the material to its

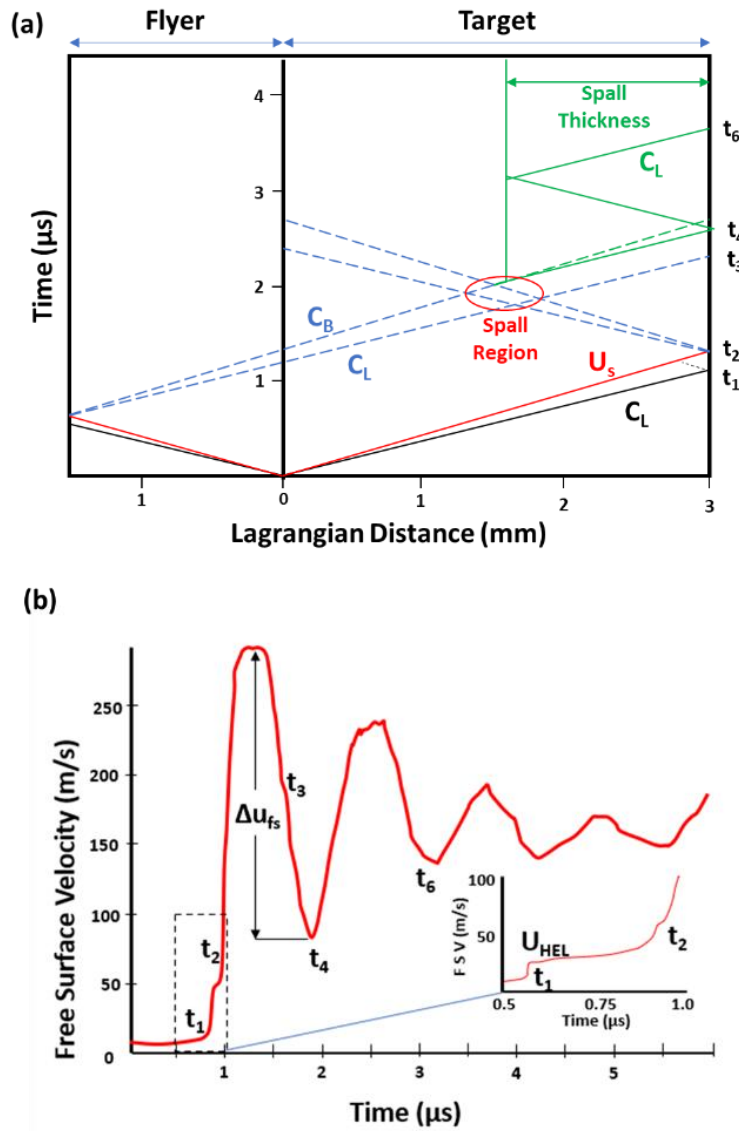


Figure 20: Representative example (a) x-t diagram and (b) free surface velocity profile, for plate impact experiment

original equilibrium condition. At the same time, a similar condition of compression followed by rarefaction is taking place in the opposite direction. The interaction of these two conflicting rarefaction waves causes an extreme tension in the material. If this tensile stress is sufficient to overcome the strength of the material, then “spall” fracture occurs. Leading up to the spall event, as the material is stressed the internal tension reduces the free surface velocity detected at the rear free surface. The exact time that the spall occurs is difficult to pinpoint from plot data alone. Since the spall occurs in the internal structure of the sample, the time of occurrence is not directly detectable by the free surface velocity measurement. This also effects determination (or verification) of the spall plane location. The detectable free surface event that indicates spall has occurred is the rapid increase, referred to as “pullback”, at t_4 . The “pullback” is caused by the resulting compressive pulse generated by energy released as the sample material fractures during the spall event. The continued cyclic “humps” that are seen beyond t_4 , also referred to as “ringing”, are the result of the wave pulse continuing to travel back and forth in the spalled scab of material.

Figure 20(a) depicts the location of the waves traveling through the material with respect to time. From this plot we can see that there are several points where major wave events occur and are directly observable at the rear (sample) free surface. Stated otherwise, these plot locations indicate where a compressive pulse reaches the free surface, resulting in rapid acceleration (increased velocity).

The first compressive pulse at t_2 corresponds to the shock wave arrival at the rear free surface, which results in a very steep acceleration to the peak velocity state. The rarefaction wave that eventually causes the spall tensile stress travels back into the sample. The head of the rarefaction wave travels at the longitudinal wave speed (C_L) and the tail travels at the bulk wave speed (C_B) [43, 44]. The “spall region” is defined by the interaction of the two reflected rarefaction waves with the final release pulse being produced at the arrival of the tail to the spall plane. This release has a “recoil” effect that generates a compressive pulse that

reaches the rear free surface at t_4 , resulting in the “pullback” acceleration that is indicative of spall. This compressive pulse travels at the longitudinal wave speed [43, 44]. If spall does not occur, the free surface velocity continues to decrease (no pullback) to near zero as the rarefaction pulse travels the full length of the sample [45].

The shape of the “pullback” signature also provides insight into the spall behavior of the material. Based on the work done by Utkin [54] in acoustic analysis, a rate of growth of the volume of voids that is approximately equal to the expansion rate in the unloading wave ($dV_u/dt \cong dV/dt$ in Figure 21) is associated with constant free surface velocity (corresponding to the Green line in Figure 21).

As Kanel demonstrated [44] theoretically perfect, instantaneous spall fracture would occur from a series of void formation localized precisely along the spall plane (indicated by the Red line in Figure 21). This “instantaneous spall” would be characterized by a fully vertical pullback slope. In reality, this rate cannot be infinite (as indicated by the Black line in Figure 21) and the computed spall strength represent the competing increase of tensile stress at the spall plane and the material relaxation due to the void initiation and growth. However, the pullback slope (u_2) can still be a strong indicator of the spall fracture mechanisms involved. Greater pullback slope indicates a closer resemblance to ideal spall condition, with a large number of ductile voids simultaneously form along the plane of maximum stress. A reduced slope, or more gradual change in the plot (as shown in the Yellow line in Figure 21), indicates a slow or “viscous” fracture. This case may be evidenced by the extended growth of a smaller number of voids which lead to larger isolated voids post-mortem or may result in just a small decrease of deceleration of the surface motion without fracture. In either case, the rate may vary during the fracture process indicating a change in fracture mechanisms.

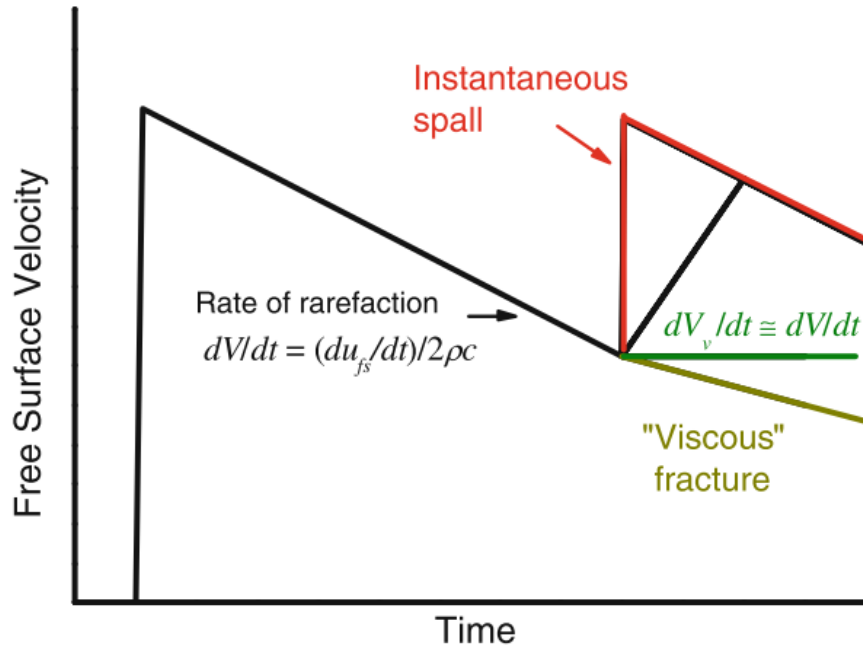


Figure 21: Influence of the fracture rate on the shape of spall pulse in the free surface velocity history. It follows from acoustic analysis that the rate of growth of the volume of voids dV_v/dt which is approximately equal to the expansion rate dV/dt in the unloading wave is associated with constant free surface velocity [44]

The spall strength (or strength of the material sample to resist dynamic tensile failure) is calculated using a combination of the velocimetry data and the material characteristics measured a priori. The material density (ρ_0) and bulk wave speed (C_B) are measured prior to experiment. The change in free surface velocity (ΔU_{fs}) is the reduction from the peak velocity to the “pullback” at the first minimum [4] collected from the velocimetry plot.

$$\sigma_{spall} = \frac{1}{2} \rho_0 C_B \Delta u_{fs} \quad (6)$$

Alternate methods are also presented in literature using a correction factor [46] that aims to account for the interacting wave conditions within the material. However, in the same work, Kanel notes “the fact that the spall strength can be determined by different methods with the use of same measuring technique shows that the analysis is not sufficiently advanced and calls for more careful study of wave interaction under spalling conditions in an elastoplastic body” [46]. While there exist many relations for determining the specific value of “spall strength”, each has a unique set of assumptions and requirements for use. A simple form (without additional correction factors) can be used to examine differences within a common sample set.

A concept introduced by Cochran and Banner [47] found that the ratio between the peak free surface velocity during initial compression and the next velocity peak after spall provided good correlation with void densities (damage) at the spall plane [4]. The authors referred to this ratio as a “damage parameter”. The concept will also be explored in this study as a qualitative measure and attempt will be made to correlate quantitative data, as well.

Principles of Laser Interferometry

Laser interferometry is a measurement technique that is based on the interference of fringes that appear when different laser beams interact [4]. Developed in the 1960s, laser interferometry advantages the fact that a laser is a monochromatic light beam. As such, if two beams have slightly different

wavelengths, interference patterns will occur. Similar occurs if two beams having the same wavelength are offset. Figure 22 demonstrates an example of this concept. When the free surface (reflecting) moves to the right, the reflected beam is displaced. This reflected beam is given by the dotted line. The reflected beam is later juxtaposed to a reference beam that remains unchanged.

Over time the technology and its applications have progressed from the Michelson interferometer [48] to the Velocity Interferometer System for Any Reflector (VISAR) technology developed at Sandia National Lab in the 1970s [49, 50] to the multiplex Photon Doppler Velocimetry (PDV) methods used today. It is important to remember that although these techniques may be referred to as a “velocity” measurement, the equipment is actually measuring displacement and integrating with respect to time to obtain those values. The signal wavelength is proportional to the distance between the target and the detector, with all measurements being tracked in time. This method also leverages the power of FFT (fast Fourier transform) in processing the signal to obtain exceptional resolution. In short, FFT is a mathematical tool that uses an algorithm to transform a function of time into a function of frequency (or vice versa). In this case, the FFT converts the series of frequency data collected by the detector into velocity data. Figure 23 shows an example of the relationship between the object velocity and signal frequency detected. As the object velocity increases, so does the signal frequency (i.e. wavelength decreases). This plot also corresponds loosely to the free surface velocity experienced in the light gas gun experiments discussed earlier.

The currently preferred velocimetry technology is PDV (over its predecessors) because of the simplicity and improved data collection rate capacity. Likewise, PDV technology continues to progress by attaining improved resolution and increased processing capacity allowing for arrays of multiple sensors across a given sample. One example of this is the multiplex PDV (MPDV) arrangement, with configurations of up to 20 discrete probes currently available for use.

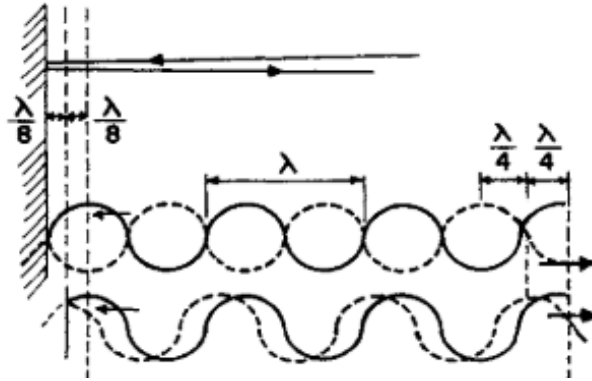


Figure 22: Example of interference created by surface movement [4]

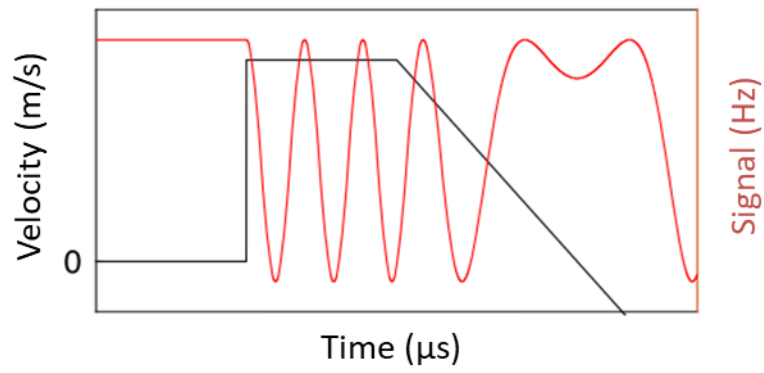


Figure 23: Relationship between free surface velocity and signal vs time [51]

Relevant Literature on Research Topic

Static and Quasi-static Studies on AM

A large majority of the mechanical property testing for AM samples has been dedicated to static loading conditions [52, 53]. Density, yield and tensile strength, compression, and bending stresses are examples of the typical data that is collected [11-12, 56-57]. Even fatigue properties are normally evaluated using cyclic static loads [58-60]. These static properties are often cited because they represent commonly accepted attributes, typically with defined acceptance criteria, that are used by most design engineers for material selection. Because of this demand, most testing labs can readily provide the tests to demonstrate these properties. These tests are useful in providing information that can be used for quantitative comparison with test samples prepared by other fabrication methods but do not fully address the material's response to many real-world forces, as many are dynamic rather than static.

The anisotropic behavior of AM processed components is well documented in literature. Research by Neindorf [61] looked at the anisotropic microstructure that results from LPBF processing, specifically the trend of elongated columnar grain growth in the build direction. Other research by both Gu [62] and Suryawanshi [63] examined the anisotropic mechanical properties, noting the differences in strength and ductility based on sample orientation. A range of other materials have been examined in the quasi-static regime [64-66]. Research has also been reported for split-Hopkinson pressure bar (SHPB) experiments using a variety of materials [67-70]. However, much less work has focused on the highest strain rate (plate impact) regime.

In a study conducted by Hensley, et al [71] sets of engineered porosity bars with varying size and degree of randomly distributed engineered voids were subjected to quasi-static tensile testing. The findings demonstrated the general trend that increased void size and content correlate to slight decrease in yield and tensile strength and a major decrease in ductility (Figure 24). The authors also observed that the application of hot isostatic press (HIP) to the samples reduced the

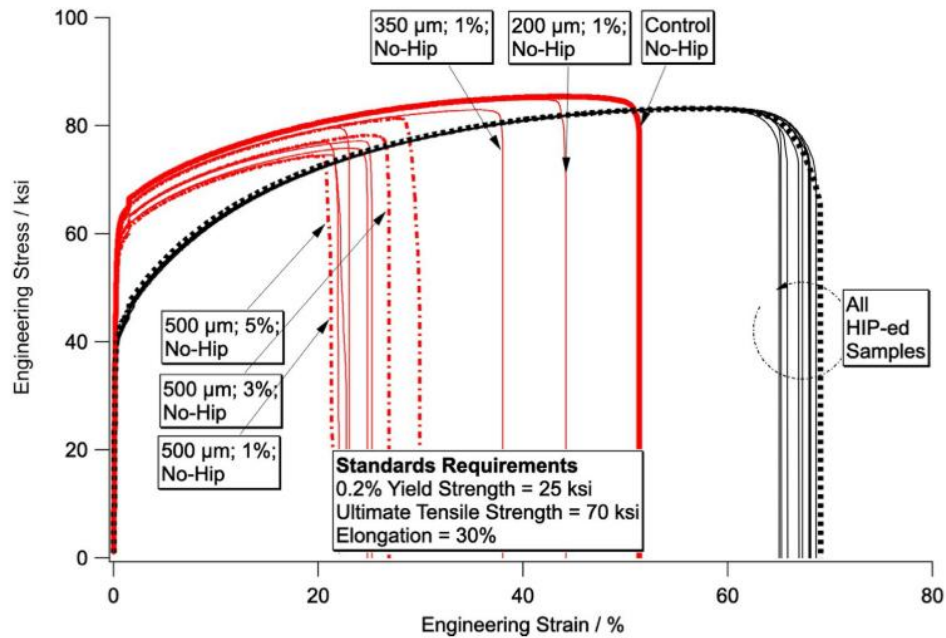


Figure 24: Comparison of stress-strain diagrams comparing quasi-static tensile behavior of samples with varied size and content of voids. Samples are compared with and without post-processing HIP treatment [71]. The general trend demonstrates a slight decrease in strength and a major decrease in ductility with increasing void size and content. The application of HIP to reduce porosity improves the performance.

porosity, which improved the performance and reduced the spread of results across the sample space.

In quasi-static and even up to bar impact test (10^3), it has been observed that the presence of internal voids corresponds to reduced strength. Furthermore, these initial voids typically serve as preferential failure sites [71,72]. Work by Fadida et al [72] examined split Hopkinson bar (SHB) tests performed on Ti-6Al-4V samples with engineered porosity built using LPBF. The researchers found that increasing the pore size reduced both the strength and ductility of the sample and introduction of multiple pores further degraded the properties.

Dynamic Studies Related to Steels and Other FCC Metals

Li et al [6] examined mild carbon steel under high strain-rate loading with gas gun impact test to assess the spall damage resulting from different loading variables. The effect of peak stress, strain rate, and pulse duration on spall strength and damage was the main focus of the study. The peak stress influence was examined by changing the flyer velocity, keeping all other variables constant. The pulse duration was examined by varying the flyer plate thickness. The strain rate was examined by maintaining the flyer velocity and the flyer-target thickness ratio at 1:2, while varying the thickness of both the flyer and target.

The authors concluded that the spall strength was heavily influenced by the peak stress and the strain rate, but only a weak dependence on pulse duration. Spall strength was observed to increase with increasing peak stress, though the effect is weakened at higher peak stresses. The authors attributed this to compression induced “pre-damage” or thermal softening at high stresses. The resulting damage was observed to increase with increasing peak stress and increasing pulse duration. The geometry of the damage locations gave insight to differences in damage evolution. The damage at the higher strain rate and peak stress conditions produced more plastic deformation and ductile spall, as evidenced by the nucleation and growth of many small voids with mostly rounded edges. The lower peak stress and strain rate tests fracture through more brittle spall in the

way of growing cleavage cracks, caused by the application of a lower stress across a longer time period. In both cases, the damage was observed to nucleate primarily at grain boundaries and triple junctions.

This texture dependent spall behavior is similarly observed in other FCC materials. Thomas et al [73] examined the influence of crystal orientation in both single-crystal and polycrystalline copper. That work demonstrated that crystal orientation had strong influence on the measured wave speeds and corresponding spall strength of single-crystal samples (Figure 25). The polycrystalline sample exhibited properties within the average range of the 3 orientations, suggesting the result of a combination between the single-crystal cases. The authors also point out that although the elastic waves between the different orientations are very similar, the spall signature is quite different.

Whelchel [43] observed similar behavior with respect to orientation on the spall behavior of rolled aluminum plate. Those studies again showed different spall behavior and damage characteristics based on orientation, but also demonstrated that the differences trend toward a common result as the impact velocity (and corresponding stress) increases.

In a study of magnetic pulse welding (MPW) of aluminum alloy (AA6061-T6) conducted by Zhang et al [75] significant strain and spalling was observed away from the welded region. The authors concluded this to be the result of localized deformation due to alternating compression and tension deformation waves. However, the cause for spalling at the exact location was not definitively answered. From the spall experiment principles outlined in other literature [6, 43] it seems that the thickness of the flyer relative to the target in the MPW experiment causes the spalling to occur near the far free surface (away from the weld).

Ogorodnikov et al [75] examined ST20 and 09G2S steels by impacting samples in the parallel and perpendicular orientation relative to the rolling direction. The authors found that the dynamic yield strength was consistent with respect to orientation while there were obvious differences observed in the spall strength.

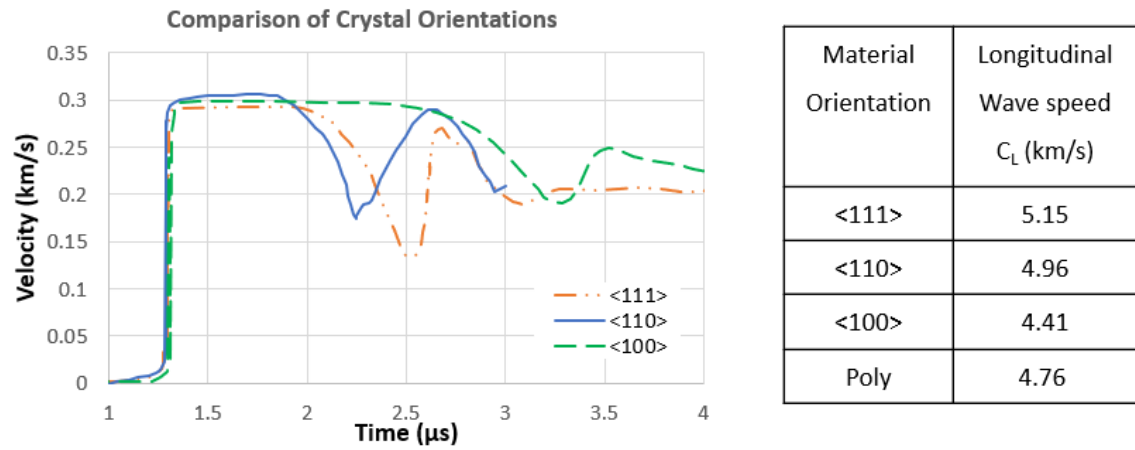


Figure 25: Velocity-time plot comparing different crystallographic orientations of single-crystal copper [73].

Across a total of 10 experiments each, the ST20 steel dynamic yield strength was in the range of 0.7 – 0.9 GPa for transverse impact and 0.7 – 1.0 GPa for parallel impact, while the spall strength was 1.3 – 1.6 GPa for transverse impact and 1.6 – 1.8 GPa for parallel impact. The 09G2S steel dynamic yield strength was 0.8 – 1.1 GPa for transverse impact and 0.9 – 1.2 GPa for parallel impact. The spall strength for 09G2S steel was 0.7 – 1.4 GPa for the parallel impact and 0.9 – 1.2 GPa for transverse impact. However, there were some specific differences that were not discussed by the authors. While the calculated spall strength values are similar for 09G2S steel in both directions, many of the velocity profiles of the 09G2S parallel experiments do not exhibit the definitive pullback that is typical of spall.

Dynamic Studies Related to AM

Characterization of AM samples has demonstrated that the grain orientation varies significantly with build direction and corresponding results for quasi-static material properties have been reported [6, 11, 74, 76]. Considering the implications between modulus and wave properties, it is reasonable to consider similar relationships for dynamic response.

Literature has shown that the spall behavior for austenitic stainless-steel materials fabricated using AM differs from that of traditionally fabricated wrought material [6, 62, 77]. These differences are observed in both the measured spall strength and observed damage evolution of the samples.

Work by Gray et al [5] compared spall behavior of wrought samples, AM as-built samples, and AM samples subjected to a post-build recrystallization heat treatment (1060°C for 1 hour under vacuum following by cooling to room temperature in 2.5 minutes by rapid argon gas quenching). The heat-treated samples developed a fully recrystallized AM microstructure whereby evidence of deposit interfaces, layer boundaries, and directional solidification normally associated with AM was replaced with a microstructure that more closely resembled the equiaxed microstructure of the wrought samples (although coarser

and more varied). Spallation experiments were performed with the plate impact parallel to the build direction. The AM samples presented reduced spall damage and increased spall strength compared to the wrought. The study showed damage characteristics of the recrystallized AM samples more similar to the wrought samples than the as-built AM samples, which experienced damage evolution across a wide range of locations rather than just along the spall plane of maximum tension (Figure 26). The damage locations appeared to preferentially occur at the build layer boundaries, leading the authors to a “weak link” hypothesis that suggests that unconsolidated powder at some but not all of these solidification boundaries was the driving factor.

Work by Jones et al [78] looked at Ti-6Al-4V samples built with LPBF, comparing the spall strength and damage both to wrought and investigating the effects of sample orientation. The initial quasi-static characterization results showed that the elastic modulus and yield strength were almost identical for samples in both orientations, while the ductility was greater for the through thickness (TT) compared to the vertical (V) sample. Two sets of gas-gun plate impact experiments were performed, using impact velocities of 310 m/s and 415 m/s. In both cases, the TT sample behaved similar to the wrought control sample while the V sample exhibited reduced spall strength (roughly 60% of wrought) as well as increased damage. The hypothesis proposed by the authors is that the difference is primarily due to the different orientation between the tensile stress direction and the AM build layer interfaces. As the voids grow, the stress state moves away from simple 1D tension and allowed shear stress to act across the weaker build layer interfaces.

In a study focused on the spall fracture of AM tantalum, Jones et al [79] examined tantalum samples that were fabricated via LPBF compared to wrought and investigated the effects of sample orientation and porosity on the spall behavior. In all cases examined, the AM samples demonstrated a higher HEL (dynamic yield strength) and lower spall strength compared to the wrought samples. The authors attributed this to the interstitial oxygen impurities formed

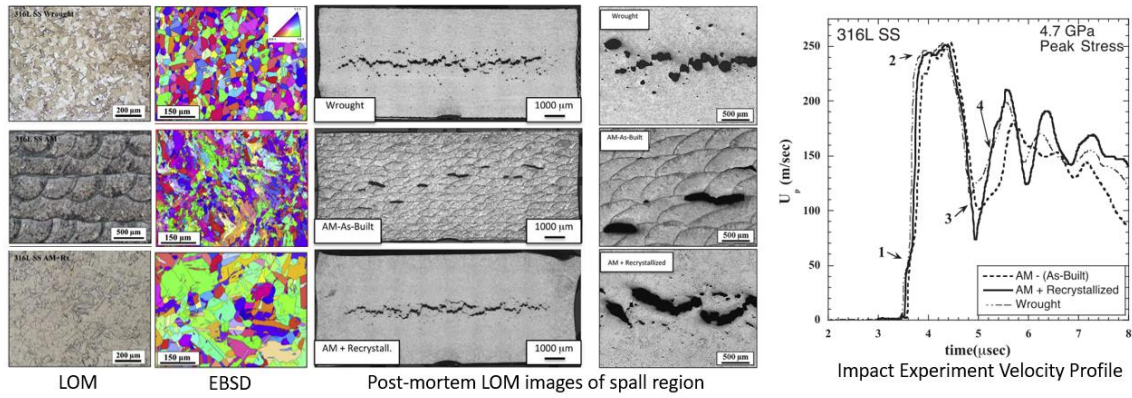


Figure 26: Information on AM-Wrought-AM Rx study. (Left) Pre-test images, LOM and EBSD, (Mid) Post-shot LOM images, (Right) Velocity-time plot [5]

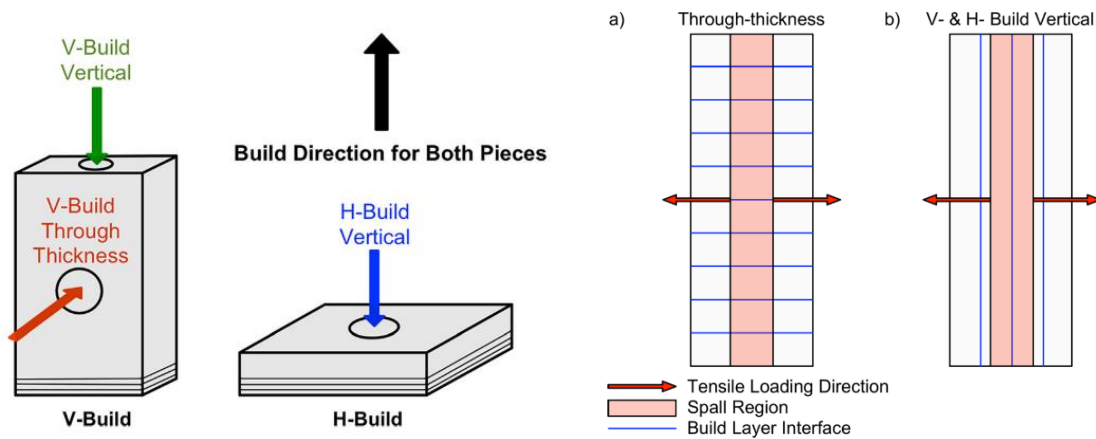


Figure 27: Images from [78] Ti-6Al-4V study. Sample build direction and orientation (Left). Orientation between tensile loading direction and build layers (Right).

during the AM build process. Similar effects have been observed in quasi-static testing of tantalum with varying oxygen content, where the yield strength increased but the ductility decreased with increasing oxygen content. A similar correlation between HEL and spall strength was observed within the AM sample group, as well. The general trend was that the samples with greater HEL exhibited reduced spall strength. Similar to Gray's work [5] with 316L SS, the spall damage in the AM samples was dispersed across a wider region than in the wrought and appeared to favor grain boundaries as nucleation sites. Unlike in the previous study of Ti-6Al-4V [78], no significant difference was observed related to loading direction. Worth noting in this study is that the porous sample impacted parallel to the build direction demonstrated increased spall strength over the solid sample. This was rationalized by the authors that the pre-existing voids allowed the sample to compress and reduce the dislocation pile up caused by the impurities attributed to the spall strength reduction in the AM samples. Also noted was that the damage in the porous sample appeared to form as growth of the existing voids whereas the solid sample showed cracks initiating exclusively at the grain boundaries. These existing voids were small cracks resulting from hot-tearing during the process with dimensions on the order of 100 μm in length along the X-Y plane and thickness of 10-50 μm .

Other work focused on ballistic impact performance [80] was performed by researchers at Oak Ridge National Laboratory (ORNL). That research coupled analytical studies, computer modeling, and physical fabrication and testing of complex titanium-ceramic composite structures. The fabrication method utilized electron beam fusion to create custom plates that later infused an internal layer of ceramic via hot pressing to create a composite structure. The goal of this study was to maximize the ballistic penetration resistance of material samples for armor applications. The composite structures improved the performance by greater than 30% compared to the standard titanium plates.

A couple of closely related characteristics that contribute to the anisotropic behavior of AM materials are the layer-by-layer build process and the observed

presence of elongated, columnar grains [11]. Each of these could be expected to manifest anisotropic properties in comparison to a more equiaxed case. A study using CTH dynamic simulation software by Specht [81, 82] on a layered Ni-Al composite demonstrated variations in the strain and temperature at the layer interfaces based on layer orientation relative to impact. The authors attributed much of this variation to the differing wave speeds of the two layered materials. The magnitude of wave speed difference between the Ni and Al is similar to that of the different orientations of single-crystal copper materials examined by Thomas [73], suggesting that a similar orientation dependence may be applicable to the interface strains at either layer or crystallographic grain boundaries.

Conclusion

Literature has shown that AM materials exhibit very directionally dependent texture. It has also been demonstrated in similar anisotropic materials that crystal orientation influences both the material wave properties and the dynamic spall response. Previous works focused on properties of AM materials under quasi-static conditions also indicate that engineered porosity will influence the dynamic fracture behavior as well.

The collection of these background materials contributes to the hypothesis that the spall behavior of AM stainless steel will be controlled, to some degree, by the relative orientation of the applied impact stress and by the purposeful distribution of void sections and features within the samples.

Chapter Three

Methodology

Introduction

The overall goal of this research is to investigate the influence of some of the unique microstructure characteristics and design capabilities associated with additive manufacturing (AM) techniques on the spall behavior of 316L stainless steel. These specific features of AM examined in this research are (1) directional anisotropy relative to build direction and (2) the ability to purposefully place powder-filled void sections inside of otherwise solid parts. The studies performed involved coupling characterization of the as-built samples using a variety of techniques, shock wave propagation of samples using high velocity plate impact experiments, and post-mortem characterization of the samples to evaluate the influence of orientation and internal voids on the behavior of AM samples exposed to high strain rate conditions.

It is well documented that AM produced components possess anisotropic strength properties under static and quasi-static loading conditions. However, little work has been performed to evaluate this behavior in the high strain rate regime. Characterization of the as-built samples serves to establish baseline information on the microstructure, porosity, and chemistry. This both verifies that the fabricated samples are consistent with typical LPBF characteristics and provides a data set for comparison with the post-mortem soft recovered samples. The high velocity plate impact test is a typical mechanical test used to evaluate the shock wave propagation in materials [2]. The data collected from this experiment is discussed in detail in later sections. To support analysis of the impact experiment, nondestructive ultrasound testing is included in the pre-test characterization to determine the material wave speed and modulus properties. The post-mortem analysis refers to characterization of the samples that are soft recovered following the impact test. Those results are compared with the pre-test data to observe changes and trends resulting from the experiment, as well as

correlated with the impact experiment data to build cause and effect relationships between the observed events in the test and the resulting sample damage.

The concept of using purposefully placed engineered porosity to simulate actual conditions has been explored by others in AM research [71]. However, like the orientation study, earlier work has focused on the static or quasi-static regime. For this sample set, the pre-test characterization serves to validate the nominal size and distribution of these engineered voids in addition to providing the set of baseline information. X-ray computed tomography (XCT) analysis is used to a greater extent on the engineered void scope to examine the details of the as fabricated and soft recovered samples relative to purposefully placed internal features across the full sample.

Sample Fabrication

The samples were fabricated using commercially available LPBF equipment and materials.

The samples for all studies except for the Engineering Design Study (Chapter 8) were built with an SLM Solutions, SLM280 machine. The machine utilizes twin 400W lasers. The relatively small samples were located in the build space to allow a single laser to fabricate each part, so that laser interface boundaries were not a concern. The samples were built using a layer thickness of 0.030 mm. The operating parameters used for the fabrication of samples were as follows: laser power of 190W, laser speed of 750 m/s, and 0.12 mm hatch spacing. The scan pattern used incorporates a simple border-line fill strategy with successive fill layers rotated by increments of 67 degrees. An inert argon environment with oxygen content less than 200ppm was maintained throughout the build.

Due to equipment availability, the samples for the Engineering Design Study (Chapter 8) were fabricated using a Farsoon FS273M machine. The machine capabilities and performance specifications are equivalent to the SLM280 machine. The same build parameters and scan strategy were used, also.

The 316L SS powder used to fabricate the samples was gas atomized powder provided by SLM Solutions. The chemical composition of the powder is shown in Table 3 as measured by EDS (energy-dispersive X-ray spectroscopy) using a JEOL JIB-4501 dual beam SEM with EDS detector. The powder feed used had a mean particle size of 21 μm with a D10-D50-D90 particle size distribution of 14-19-31 μm as measured using a Malvern Morphologi G3 optical.

Samples for Build-Impact Orientation Study

Two distinct sample types were fabricated for this study. The naming convention for each sample type corresponds to the impact direction relative to the build (Z) direction. Schematics of the “parallel” and “perpendicular” samples are shown.

The parallel sample was fabricated as a solid right cylinder oriented vertically such that the impact direction corresponded to the build (Z) direction, with 15mm diameter and 30mm length. All samples were post-machined to a cylindrical disc specimen of approximate dimensions 15mm diameter x 3mm thickness for impact testing. Samples were obtained from the middle of the printed specimens to reduce edge effects. The samples were lapped flat and parallel to within 1 milliradian to ensure a 1D shock wave could be generated through the sample.

Due to machine-process limitations, the perpendicular sample was fabricated as a horizontally orientated solid rectangular prism, with dimensions 15mm x 15mm x 50mm. Samples were post-machined identical to the parallel sample.

Samples for Engineered Porosity Study

The samples were fabricated as 12 mm diameter x 60 mm length bars. These bars were fabricated vertically with the major axis in the Z-direction. To achieve the desired porosity profiles, small cubic voids of desired size were designed in the Abaqus FEM CAD package and dispersed within the Magics STL file. The discs used for spall impact testing were taken from sections near the vertical center of the bars. The discs were lapped flat and parallel to within 1 milliradian to ensure a 1D shock wave could be generated through the sample.

Table 3: Chemical composition (weight %) of powder feedstock and build sample. AISI 316L composition shown for reference.

	Element (Weight %)							
	C	O	Si	Mo	Cr	Mn	Ni	Fe
Powder	0%	0.71%	0.14%	1.47%	18.77%	1.79%	11%	66.11%
Build	0%	0.56%	0.32%	1.44%	19.52%	1.44%	10.9%	65.82%
AISI 316L	< 0.03%	n/a	< 1%	2-2.5%	16.5-18.5%	< 2%	10-12.5%	Bal. (> 63%)

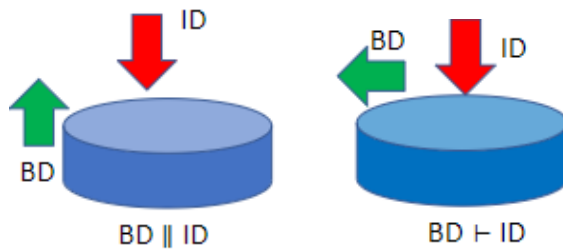


Figure 28: Schematic of build-impact orientations

The designated void fractions represent a total void fraction of the sample volume with voids that are randomly distributed across each cross section. Since the voids were randomly distributed, the spacing of the voids (in all directions) was not intended to be uniform. The focus of this study is more on the general size and overall void fraction. Due to the nature of the LPBF process, the voids are likely not to be exactly cubic as in the design file. In general, the cyclic melting nature and the variations of powder particle size and shape make features below 100 μm very inconsistent. Also, since the voids are created by locations where the laser does not melt, they are filled with un-melted powder. These voids are not, therefore, representative of the keyhole mode or lack-of-fusion pores typically associated as defects with LPBF processing [71]. On the other hand, they represent a potential unique design space should the features demonstrate influence over the spall behavior of the material.

Samples for Single Void Study

As an extension to the randomly distributed void study, samples were fabricated with a single void of desired size. The void sizes used in this study correspond to the size set used in the Random Porosity study (0.200 mm, 0.350 mm, and 0.500 mm). The samples used for this study were fabricated as 15 mm diameter x 3.5 mm thickness discs, then lapped flat and parallel to within 1 milliradian to ensure a 1D shock wave could be generated through the sample. These discs were fabricated vertically with the impact face in the Z-direction. The single voids were located at the center of each sample, both radially and vertically. The small cylindrical voids of desired size were designed in the Solidworks CAD package.

Samples for Engineering Design Study

Based on the findings of the initial orientation, random, and single void studies, a focused study was conducted to further utilize purposeful engineering design to control the propagation of the shock wave (and associated pressure front) through the material. The utilization of internal features, a capability unique to

AM, to reduce the pressure stress and increase the stress wave arrival time at the rear free surface was the primary goal of this study. Discs containing solid upper and lower sections with a hexagonal honeycomb section at the midplane were fabricated. The honeycomb section was constrained to a 6 mm x 6 mm section at the radial center of the disc to allow for baseline data to be collected by probes in the solid area. Three different sample sets were fabricated with different orientations of the same the honeycomb pattern to examine whether the unique pattern or the bulk void volume has a more significant effect on the spall behavior.

Sample Characterization

The samples were characterized both before and after the gas gun impact experiments. The pre-test characterization consisted of bulk density measurements, ultrasound wave speed measurements, moduli calculations and microstructure characterization. Non-destructive evaluations were performed on each tested sample, and analysis requiring cross-section was done on representative section from the same printed sample specimen. The post-test characterization was performed on soft-recovered samples collected after the experiment and consisted primarily of cross-section analysis.

Bulk density of the samples was measured using both gas pycnometer and Archimedes method. Results from each method were compared for agreement.

Light optical microscopy (LOM), scanning electron microscopy (SEM), and electron backscatter diffraction (EBSD) were utilized to characterize each sample both prior to and following the plate impact experiment. Sample preparation consisted of cleaning and polishing the surfaces of interest using progressively finer grit papers and diamond slurries and finished with colloidal silica. For examination of melt pool structure, the samples were electro-etched with oxalic acid.

LOM images were acquired at various magnifications using a Zeiss Axio Imager. For the pre-shot samples, baseline porosity content and melt pool structure was

collected. Voids created as spall damage from the shot experiments were analyzed on the post-shot samples. The spall plane location and damage distribution relative to the rear free surface of the sample was examined. Analysis of defects and voids was performed using ImageJ software.

SEM and EBSD images were collected using either a JOEL JSM-7600F Field Emission SEM multi-detector system or a Tescan Mira Field Emission SEM outfitted with an EDAX Velocity EBSD detector. Baseline porosity and grain structure were collected on the pre-shot samples. For the post-shot samples, SEM was used to examine the damage locations in greater detail. The defect morphology (size, shape, orientation) was of particular importance on both the pre- and post-shot samples. EBSD was used to look at the grain structure in areas of observed spall damage and undamaged areas. EDAX TEAM software was used for data collection, and EDAX OIM software was used for post-processing analysis. The grain size, shape, and orientation characteristics were compared between the pre- and post-shot samples. Spall damage location and characteristics relative to grain structure was also assessed.

X-ray computed tomography (XCT) data was collected on the samples both before and after impact test. The XCT data was collected at the ZEISS Quality Excellence Center located at the Oak Ridge National Lab Manufacturing Development Facility (ORNL-MDF). The purpose of XCT data differs depending on the test scope. For the random engineered porosity cylinders, XCT was used to verify that the as-built cylinders did, in fact, contain voids of the general size and distribution as prescribed by design. Post-test XCT of the random engineered set examined the spall damage relative to the engineered voids at locations across the sample beyond that observable at the simple cross-section. For the single void study, XCT images were collected both before and after the impact test to examine the influence of the void on spall damage.

Ultrasonic Testing

Sound speed measurements were made using an Olympus 5072PR pulser/receiver in the pulse echo configuration attached to both Ultratran VSP-200 and SRD50-5 ultrasonic probes for longitudinal and shear wave velocity measurements, respectively. The data was recorded using a Tektronix DPO 5104 1GHz oscilloscope. The longitudinal and shear sound wave velocities are directly measured; the other properties are calculated from those measured properties using the relations shown in Chapter 2.

Plate Impact Testing

Gas gun tests are capable of achieving strain rates in excess of 10^4 s^{-1} , up to 10^6 s^{-1} in some cases. In addition to providing increased strain rates, the sample geometry used in gas gun tests also provides information under an applied uniaxial strain that produces triaxial stress conditions (plane strain) [4], giving increased insight to the bulk material properties. The plate impact experiments performed for this study were performed using the 80mm diameter x 7.6m length single-stage light-gas gun at the Georgia Institute of Technology. A schematic of the sample configuration is shown in Figure 19 in Chapter 2. The projectile consisted of a stainless-steel sabot with a 70mm 316L SS flyer plate. The target sample holder was 80mm diameter and fixed using an epoxy so that both the flyer and target could pass through for soft-recovery of samples. The experiment was designed with the flyer plate one-half the thickness of the target to generate spall fracture near the mid-plane of the samples. Both the flyer and the target sample holder were machined from wrought 316L SS and lapped parallel to less than 1 mrad of tilt. Each sample was designed with an LT2 locational transition fit to allow them to break away from the holder following impact. Soft-recovery of samples was performed using a bed of soft rags located in a catch tank beyond the sample chamber. Recovered samples were inspected for any damage away from the impact face to ensure that no secondary impact events occurred during the experiment.

The basic operation of a gas gun test involves impacting a thin target plate with a high velocity flyer plate (ranging from 200-1000 m/s). The resulting failure process is related to nucleation, growth, and coalescence of microvoids and microcracks. Using photon Doppler interferometry (PDV) sensors, the rear free surface displacement of the target is measured with respect to time to evaluate the velocity changes associated with stress wave propagation in the sample. Full details of the theoretical basis for the experiment are discussed in Chapter 2.

The spall strength (or strength of the material sample to resist dynamic tensile failure) is calculated using a combination of the material density (ρ_0) and bulk wave speed (C_B) measured prior to experiment and the change in rear free surface velocity (ΔU_{fs}) from the peak velocity to the “pullback” at the first minimum [26] collected from the velocimetry plot. Due to the complexities observed in the AM microstructure and the material response to the impact experiments, the basic form of the spall strength calculation (EQN 6) is used in this research.

Post Impact Recovery

As mentioned earlier, the target samples from each experiment were “soft-recovered” using a bed of soft rags located in the catch tank beyond the sample chamber. Recovered samples were inspected for any damage away from the impact face to ensure that no secondary impact events occurred during the experiment.

A non-instrumented secondary sample was used for the post-mortem characterization. From experiment design, this sample experiences identical shock loading conditions as the PDV-measured sample. Removal of the probes used to collect velocimetry data presents the potential for specimen damage. Examining the secondary sample ensures that any damage observed is the result of the impact experiment. The soft-recovered samples were cross-sectioned and used for the post-mortem characterization described earlier in this chapter.

Presentation of Results

The following chapters will discuss the dynamic response of additively manufactured 316L stainless steel with several different sets of characteristics unique to LPBF fabrication. The presentation of this information is organized as follows:

- **Chapter 4:** The influence of build-impact orientation on the elastic wave properties, dynamic strength properties, and damage evolution will be discussed. This data will be compared to wrought samples and each other. The focus of this chapter is on directional anisotropy of the AM samples. The results of this chapter will be used as a baseline for following chapters that utilize engineered void spaces within the samples.
- **Chapter 5:** The influence of randomly distributed porosity on the spall characteristics will be discussed. Both the local and global behavior of the samples with respect to the as-built voids is examined. This chapter aims to discuss whether the presence of internal void features results in a stronger or weaker sample when exposed to high velocity impact loading.
- **Chapter 6:** The initial compression stage of the spall experiment is modeled using a finite element analysis computer software package. These numerical experiments both increase the understanding of results observed in earlier studies and are applied as a design tool for informing the future experiments.
- **Chapter 7:** The influence of strategically placed voids at known locations on the spall behavior will be discussed. The experimental results in this chapter are coupled with computer simulation models to gain increased insight to the effect of internal voids on shock wave propagation and spall response in the samples.

- **Chapter 8:** The design strategy and influence of strategically engineered internal features will be examined in this chapter. The primary goals of the designs presented in this chapter are to (1) delay the arrival of the generate shock wave at the RFS and (2) to minimize the pressure observed at the RFS.

Chapter Four

Build-Impact Orientation Study

Portions of this Chapter correspond to a published journal article:

K. Lamb, K. Koube, J. Kacher, T. Sloop, N. Thadhani, and S.S. Babu. Anisotropic spall failure of additively manufactured 316L stainless steel. *Additive Manufacturing*, Volume 66. (2023). <https://doi.org/10.1016/j.addma.2023.103464>.

This study involves sample characterization, plate impact spallation testing, and post-mortem analysis of 316L stainless-steel (SS) samples fabricated using LPBF. Samples built in different orientations with respect to impact plane (parallel and perpendicular) are compared, along with comparison to wrought 316L SS plate samples. The samples were characterized both before and after the gas gun impact experiments. The data sets collected for analysis include light optical microscope (LOM), scanning electron microscope (SEM), electron diffraction spectroscopy (EDS), electron back scatter diffraction (EBSD), x-ray diffraction (XRD), and x-ray computed tomography (XCT). It is hypothesized that these testing results will demonstrate anisotropic behavior relative to build-impact orientation.

Experiment

Sample Fabrication

The 316L stainless-steel (SS316L) samples were fabricated as outlined in Chapter 3. The parallel sample (15mm diameter and 30 mm length) was fabricated as a solid right cylinder oriented vertically such that the impact direction corresponded to the build (Z) direction. Due to machine-process limitations, the perpendicular sample was fabricated as a horizontally orientated solid rectangular prism (15 x 15 x 50 mm). All samples were post-machined to a cylindrical disc specimen of approximate dimensions 15mm diameter x 3mm thickness for impact testing. Samples were obtained from the middle of the printed specimens to reduce edge effects. The samples were lapped flat and

parallel to within 1 milliradian to ensure a 1D shock wave could be generated through the sample. The samples were fitted into a wrought SS316L sample holder for the impact test. Full details on experiment set up are in later sections.

Material Feedstock:

The 316L SS powder used to fabricate the samples was gas atomized powder provided by SLM Solutions. The chemical composition and particle size distribution of the powder is consistent with that listed in Chapter 3.

Physical Property Characterization:

The samples were characterized both before and after the gas gun impact experiments. The as-built characterization consisted of bulk density measurements, ultrasound wave speed measurements, moduli calculations and microstructure characterization. Non-destructive evaluations were performed on each tested sample, and analysis requiring cross-section was done on representative section from the same printed sample specimen. The post-test characterization was performed on soft-recovered samples collected after the experiment and consisted primarily of cross-section analysis.

The AM fabricated material characterization consisted of physical measurements of the bulk density and ultrasound wave speed and evaluation of the microstructure. The bulk density of the sample discs was measured using both gas pycnometer and the Archimedes method. Results from each method were compared for agreement. Ultrasound wave speed measurements were calculated as described in Chapter 3 – Methodology. The measured density and wave speeds, as well as the moduli for each sample, are listed in Table 4. Data from the wrought sample is shown for reference.

Bulk density (measured using both gas pycnometer and Archimedes method) indicated that the AM fabricated samples had density within 1% the standard expected value for 316L stainless steel (8.00 g/cc) and were thus considered

“fully dense”. There are observable differences in elastic properties between the different orientations. The longitudinal wave speed (C_L) is greater in the IP sample than the TT sample, whereas the shear wave speed (C_s) is lower for the IP than TT. This indicates a directional dependence of wave propagation through the AM material. The calculated modulus values (elastic, bulk, and shear) demonstrate a corresponding significant difference as a function of build orientation. The density values for each sample orientation differ slightly but are within $\pm 1\%$ of the AISI standard value for 316L SS of 8.00 g/cm^3 ; a density variation of this magnitude is not considered to have significant impact.

Light optical microscopy (LOM), scanning electron microscopy (SEM), electron backscatter diffraction (EBSD), x-ray diffraction (XRD), and x-ray computed tomography (XCT) were utilized to characterize each sample both prior to and following the plate impact experiment. Sample preparation consisted of cleaning and polishing the surfaces of interest using progressively finer grit papers and diamond slurries and finishing with colloidal silica. For examination of melt pool structure, the samples were electro-etched with oxalic acid. LOM images were acquired at various magnifications. For the as-fabricated samples, baseline porosity content and melt pool structure was collected. Voids created as spall damage from the soft-recovered impact experiments were analyzed to identify the spall plane location and damage distribution relative to the rear free surface of the sample. Analysis of voids was performed using ImageJ software.

Baseline porosity and grain structure were collected from the as-fabricated samples. For the post-shot samples, damage locations were examined in greater detail. The defect morphology (size, shape, orientation) was of particular importance on both the pre- and post-shot samples. The grain structure in areas of observed spall damage and undamaged areas was characterized and compared. Spall damage location and characteristics relative to grain structure were assessed in image analysis.

Table 4: Measured wave and moduli properties for orientation impact samples

Property	IP Sample	TT Sample	Wrought Sample
CL (mm/ μ s)	5.738 \pm .008	5.450 \pm .046	5.670
CS (mm/ μ s)	2.795 \pm .072	3.146 \pm .033	3.088
CB (mm/ μ s)	4.744 \pm .047	4.062 \pm .028	4.408
G (GPa)	62.2 \pm 3.2	80.2 \pm 2.2	76.27
B (GPa)	179.1 \pm 3.5	133.6 \pm 2.7	155.42
E (GPa)	167.2 \pm 7.4	200.4 \pm 5.2	196.64
v (Poisson's ratio)	0.34 \pm .01	0.25 \pm .001	0.29
ρ (g/cm ³)	7.96 \pm 0.000	8.09 \pm 0.03	7.96 \pm 0.07

Characterization results from as-fabricated representative samples of each orientation are shown in Figure 29. In the un-etched conditions, the micrographs reveal the presence of fine pores that are very close to the microscopic resolution ($< 1\mu\text{m}$) in the AM fabricated materials. It is noteworthy that these small fractions of pores did not impact the overall density measured by the Archimedes method. In the etched LOM images, the melt pools in successive laser scan tracks (Figure 29.b) and successive layers (Figure 29.e) are evident. In the XZ plane, there is also evidence of varied grain growth across multiple layers oriented in the build direction, as well as lightly etching grains (Figure 29.e). The corresponding SEM images (Figure 29.d) of these samples reveal small pores aligned along some of the melt pool boundaries. EBSD of the XZ plane (Figure 27.f) show large columnar grains accompanied by a significant number of smaller grains closer to the melt pool boundaries (marked by yellow arrows). The EBSD images of the XY plane (Figure 29.c) shows similar grain refinement at the melt pool track boundaries (marked by yellow arrows). This microstructure differs greatly from the as-built microstructure of the wrought control sample (Figure 29.h), which possesses a uniform equiaxed grain structure.

X-ray computed tomography (XCT) analysis was performed on the soft recovered samples after impact testing. The purpose of the XCT analysis was to evaluate the spallation void formation across the full three-dimensional (3D) volume of the sample, rather than only the 2D view of the cross-sectioned location in the sample. The XCT data was collected using a ZEISS Xradia 620 Versa at the ZEISS Quality Excellence Center located at the Oak Ridge National Lab Manufacturing Development Facility (ORNL-MDF). The integrated 3D image file was converted to a Volume Graphics software format. The files were qualitatively evaluated using a MyVGL Volume Graphics viewer. Quantitative evaluations were performed using 2D images of individual slices analyzed with FIJI/ImageJ image analysis software.

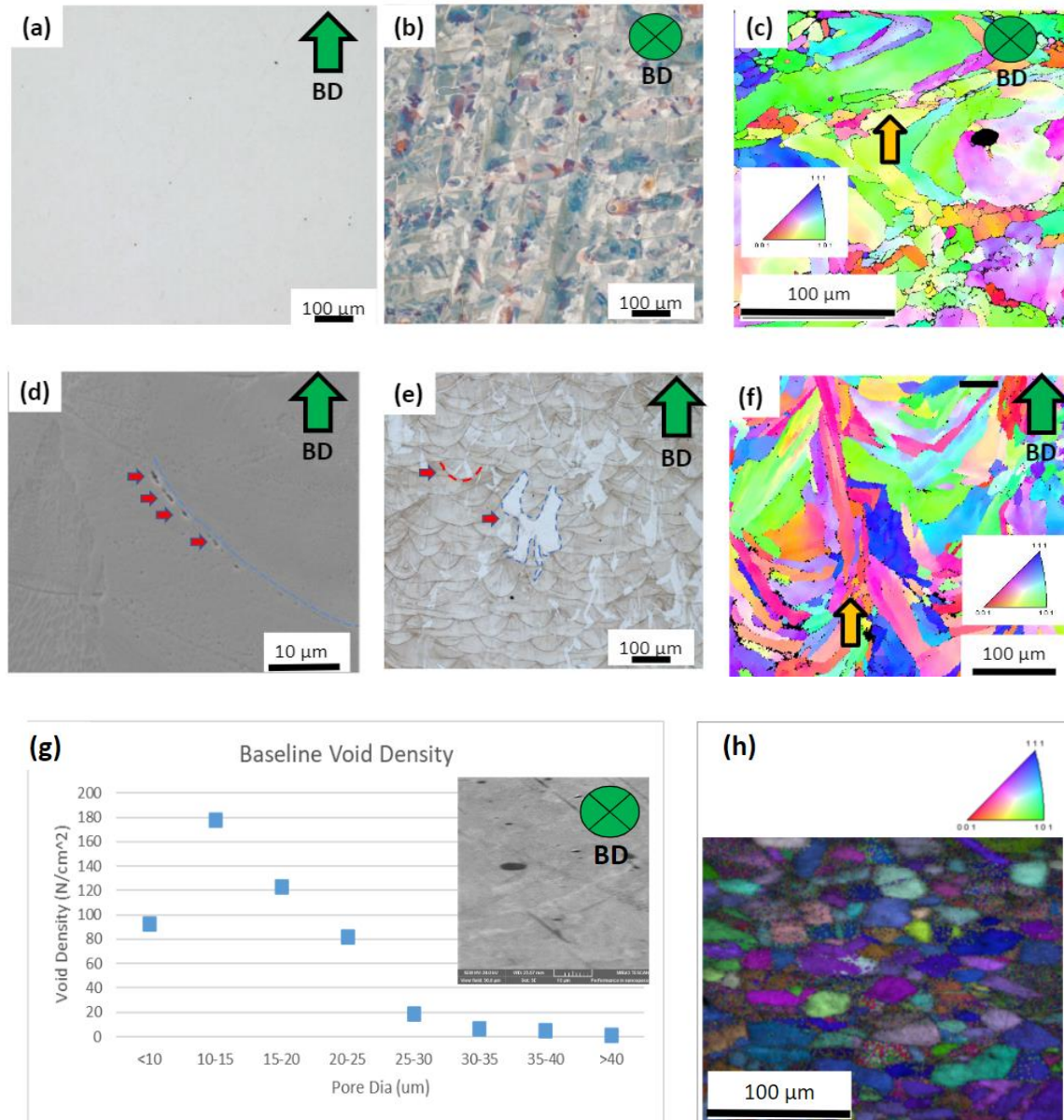


Figure 29: Pre-shot characterization of as-built samples. (a) Optical image showing very small porosity resulting from build which is often lower to the pixel resolution of the image. (b) Optical micrograph of the XY plane showing etched to highlight the melt pool tracks. (c) EBSD results of the XY plane in the form of inverse pole figure (IPF) for FCC crystal show smaller grains at the boundaries of adjacent melt pool tracks as indicated. (d) SEM image showing high concentration of voids along melt pool boundaries. (e) Optical micrograph of the XZ plane showing as-built melt pool layers and varied grain shapes and lightly etching grains. (f) EBSD results of the XZ plane in the form (IPF) for FCC crystal show columnar grains and small grains near the melt pool boundary typically referred as “fish-scale” boundaries. (g) Measure of pore size distribution from many images. (h) EBSD results of the Wrought sample in the form of IPF shows the more consistent equiaxed crystal structure compared to the AM samples.

X-ray diffraction (XRD) analysis was performed on the full set of samples (IP, TT, AM control pre-shot, and Wrought). The results provided indication of a full FCC structure with negligible amount of BCC. Full details are located in the Appendix.

The as-built characterization demonstrates several aspects of the as-fabricated AM samples that are important to note.

- A polycrystalline columnar grain structure is observed with the primary axis of the grains oriented parallel to the build direction.
- A distribution of small pores was evident throughout. Typical for LPBF fabricated samples.
- Differences in the modulus properties was observed based on build orientation.

Plate Impact Testing

Gas gun plate-impact experiments were performed as described in Chapter 3. The experiments were performed at a velocity of approximately 250 m/s with impact direction (ID) parallel (or in-plane, IP) to build direction (BD), denoted by $BD||ID$, as well as, the ID perpendicular (or through-thickness, TT) to the BD, denoted by $BD\perp ID$. Each experiment consisted of three samples mounted in the target holder. These included two AM samples with one instrumented with PDV for velocimetry and the other non-instrumented for soft-recovery. The third included a wrought control sample also backed by PDV for comparison. For each build-impact orientation (TT and IP), the soft-recovered sample was cross-sectioned and prepared for microstructural examination as described above.

Results

PDV Velocity Profiles and Measured Properties

Figure 30 shows the free surface velocity profiles captured using PDV interferometry for each of the samples impacted at a velocity of 250 m/s. The peak free surface velocities were measured to be roughly 240 m/s for each

orientation of samples tested. This corresponds to a calculated peak stress of approximately 4.5 GPa.

The HEL is marked as “1” in Figure 30.a. The calculated HEL stress (σ_{HEL}) values shown in Table 5 are greater in the TT sample than the IP sample, which is consistent with the trend in variation of elastic modulus values shown in Table 4, and the effects of anisotropy observed in AM materials under quasi-static conditions reported in literature [2, 63, 83].

Following the HEL, the velocity rises to the peak velocity and maintains the peak state over a time delay (pulse duration marked ‘2’ in Figure 30.a) between the shock front and the reflected rarefaction wave from the flyer back surface. The deceleration from the peak velocity is followed by a recompression as the reflected wave interactions result in spall failure if the tension generated exceeds the dynamic tensile strength of the material (marked ‘3’ in Figure 30.a).

The spall strength (or dynamic tensile strength) value is calculated using the material density (ρ_0) and bulk wave speed (C_B) measured prior to experiment and the change in rear free surface velocity (ΔU_{fs}) from the peak velocity to the “pullback” at the first minimum [4] obtained from the velocimetry profiles, as given by EQN (6).

The difference in pull-back magnitude (depth from the peak velocity) suggests different spall strength values based on orientation as the TT sample exhibits greater spall strength than the IP AM and wrought samples (Table 5). Both AM samples demonstrated increased spall strength over the wrought sample, matching the results of previous studies [2, 5, 61, 83].

The bi-linear slope (often referred to as “shoulder”) observed before and after the pull-back on the IP sample is common in spall experiments. The decompression rate, the slope prior to pull-back (u_1), is directly related to the strain rate experienced by the material to drive the spall fracture. The change in this slope indicates the level of deformation prior to spall. A steeper u_1 slope is often associated with a narrower spall region due to strain localization while a less steep slope corresponds to increased stress accommodation and broader spall

Table 5: Experiment results for each sample. Velocimetry Data and Calculated Properties.

Property	IP	TT	Wrought
Velocity/Strength Characteristics (from experiment)			
U_s (mm/μs)	4.938	4.243	4.589
u_{HEL} (m/s)	64	74	36
σ_{HEL} (GPa)	1.46	1.61	0.81
u_p (m/s)	126	118	118
Δu_{fs} (m/s)	168	193	149
σ_{spall} (GPa)	3.17	3.17	2.61

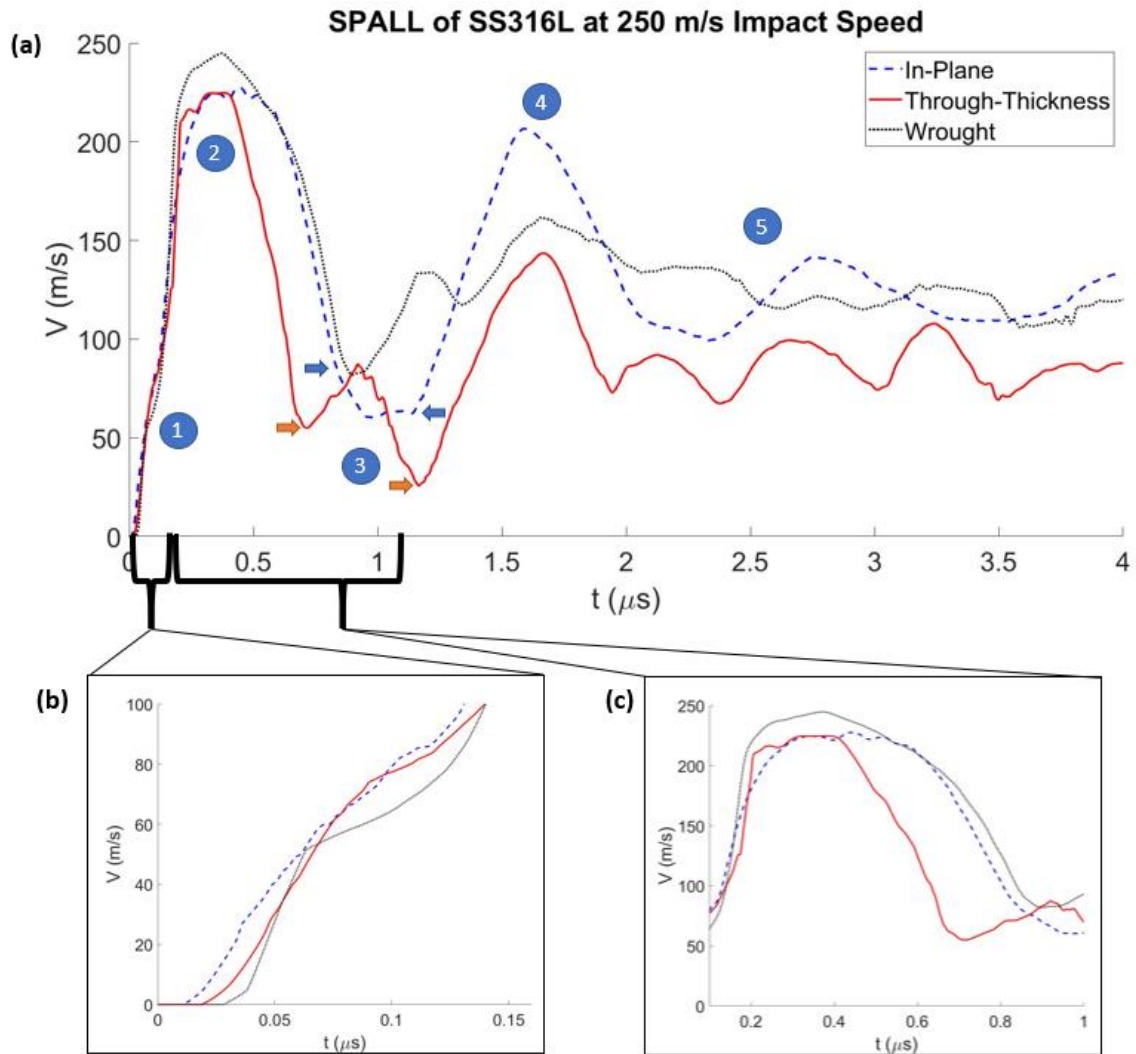


Figure 30: Velocimetry (v-t) data results plot. Results of shot test showing free surface velocity vs. time. (a) Plot of full data set. The blue arrows indicate the “shoulder” observed in the IP sample. The orange arrows indicate the “double hump” observed in the TT. (b) Plot showing closer inspection of initial rise times and the HEL, (c) Plot showing closer inspection of pulse duration at peak velocity.

region. The recompression rate, the slope following pull-back (u_2), gives insight into the damage mechanisms involved. The “shoulder” in this region of the plot can indicate a period of independent void nucleation and growth across many simultaneous sites followed by transition to a period of coalescence of those voids and/or more rapid growth, such as propagating cracks. In some cases, these characteristics can be used as part of a “correction factor” for calculation of spall strength [46], but that is not pursued in this study due to the complex velocity response observed.

The “double-hump” observed in the TT sample is less common. One possibility is that each of the pull-back minima coincides with a separate region of increased spall damage. The time-distance-velocity relationships of the waves traveling within the sample material mean that the first minimum (with respect to time) on the plot coincides to a location closer to the rear free surface, while the second minimum corresponds to a location farther away from the rear free surface. The first minimum has a greater decompression rate and a lesser recompression rate, compared to the second minimum. This suggests that the first minimum corresponds to a spall region with less observable damage closer to the rear free surface, while the second region (located farther from the rear free surface) has a greater degree of damage.

A concept introduced by Cochran and Banner [47] found that the ratio between the peak free surface velocity during initial compression (V_a) and the next velocity peak (marked ‘4’ in Figure 30.a) after spall (V_c) provides a good correlation with void densities (damage) at the spall plane [4, 25]. The authors referred to this ratio as a “damage parameter”. The concept was explored in the present work as a qualitative measure and it was found that the IP sample demonstrates a higher “damage parameter” than the TT sample (Table 6), which is also supported by the results of post-mortem microstructural analysis presented in the next section.

Table 6: Experiment-induced damage results for each sample. Velocimetry Data Calculations and Image Analysis results

Property	IP	TT	Wrought
From Velocimetry Data			
Va (m/s)	225	225	244
Vc (m/s)	210	158	169
Damage Parameter (Vc/Va)	0.94	0.71	0.66
From image analysis			
Void Count (in spall region*)	137	40	92
Width of Spall region* (mm)	0.55	0.30	0.62
Peak Void Fraction**	1.45%	1.19%	1.17%
<p>* Spall region is considered the region surrounding the spall plane of maximum damage with greater than 0.2% void fraction</p> <p>** The peak void fraction occurs at the spall plane of maximum damage.</p>			

The continued oscillations that are seen beyond t_4 , also referred to as “ringing” (marked ‘5’ in Figure 30.a), are the result of the wave pulse continuing to travel back and forth in the spalled material. The observed “double-hump” characteristic continues throughout the subsequent “ringing” stage of the TT sample. This suggests that the “double-hump” is not only present during the spall event but is likely also observable in the post-mortem sample.

As the post-spall “ringing” signal continues to reverberate between the rear free surface and the spall region, the time period required for the (now elastic) wave to travel is evidenced by the time period between successive peaks. Here, there is a demonstrated difference in this time period between the IP and TT samples, with the TT sample having a shorter period than the IP sample. The ultrasound measurements performed on as-fabricated AM samples indicated that longitudinal wave speed was greater in the IP samples than in the TT sample, suggesting that the IP samples have a shorter “ringing” period. However, the opposite is observed, indicating that the spall damage for IP and TT occurs on different planes along the sample thickness and not necessarily along the expected mid-plane based on the flyer-target thickness ratio. The post-mortem analysis (Figure 31) indicates that the spall plane in the TT sample is nearer to the rear free surface than is observed in the IP sample.

In summary, the impact test results indicate that (a) AM samples experience reduced spall damage and higher σ_{HEL} and σ_{spall} compared to wrought material; (b) measured wave velocity profiles are different based on build-impact orientation; (c) spall strength calculated from pull-back signals is different based on build-impact orientation, and (d) location of spall fracture is different based on build-impact orientation

Post-mortem microstructure characterization of impacted samples

The signatures captured in the PDV profiles provide limited understanding of the spall failure mechanisms. It is therefore important, particularly in a heterogeneous and anisotropic material, to couple the interferometry data with

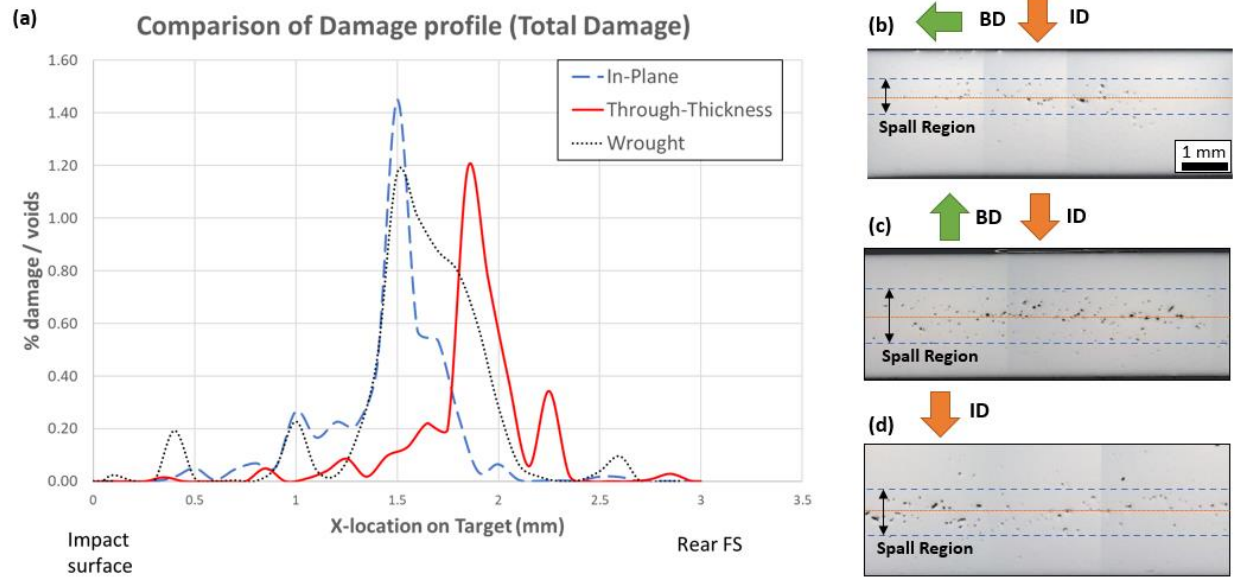


Figure 31: Spall damage results from shot test.(a) Spall damage distribution. (c-e) Optical micrograph showing spall damage of (c) TT sample, (d) IP sample, and (e) Wrought sample.

post-mortem microstructural analysis. For each build-impact orientation (TT and IP), the soft-recovered sample was cross-sectioned, polished, and mounted for examination as described earlier.

Optical microscope images (Figure 31) of the cross-sections of soft-recovered impacted samples indicate that the TT sample experienced less spall damage than the IP sample. ImageJ software was used to quantify the number and area fraction of the spall voids in each sample as a function of location relative to the rear free surface. As shown in Table 6, the IP sample contained a greater number of voids and greater overall void fraction than the TT sample. This qualitatively supports the “damage parameter” estimation obtained from the velocimetry plots based on the decompression rate (u_1) and recompression (u_2) slope data in the spall pullback region. Figure 31.a shows the damage profile of each sample as void fraction measured against location (relative to the rear free surface).

The damage profile (Figure 31.a) for the TT sample shows a primary damage peak along with a second, smaller peak closer to the rear free surface, while the IP sample demonstrates a single spall plane near the center of the sample.

The primary spall planes for the TT and IP samples occur at different locations (relative to rear free surface), with the IP sample being closer to the mid-plane (as intended by experiment design), as shown in Figure 31. The IP sample, having a similar longitudinal wave speed to wrought, also has a similar spall plane location as the wrought sample. Although the exact reasoning for differing spall plane is uncertain at this time, it is believed that the orientation of the melt pools and grain boundaries relative to impact greatly influences the wave propagation characteristics, resulting in a shift in the spall plane location.

The etched LOM images (Figure 32) reveal that the specific damage site locations preferentially occur at or near the melt pool boundaries. This is observed for both the IP and TT samples.

The EBSD data (Figure 33) also suggests that many of the fracture locations occur at or near melt pool boundaries, as evidenced by regions of high-angle

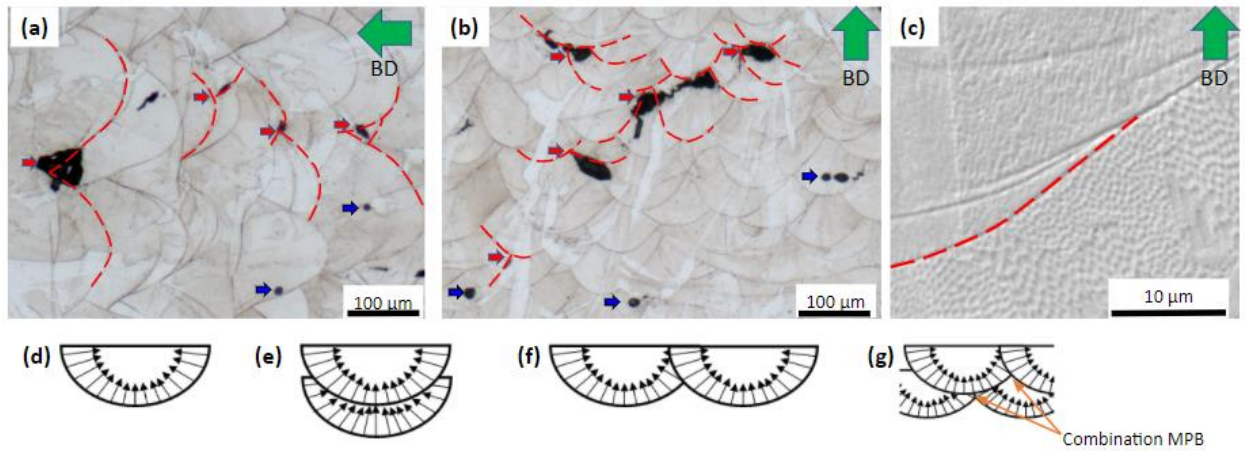


Figure 32: Details of MPB characteristics. (a) Optical image highlighting damage sites related to MPB and smaller ductile fracture sites for TT sample, (b) Same for IP sample, (c) SEM image showing grain structure difference above and below melt pool, (d) Example of single melt pool, (e) Example of Layer-Layer MPB, (f) Example of Track-Track MPB, and (g) Example of Combination MPB.

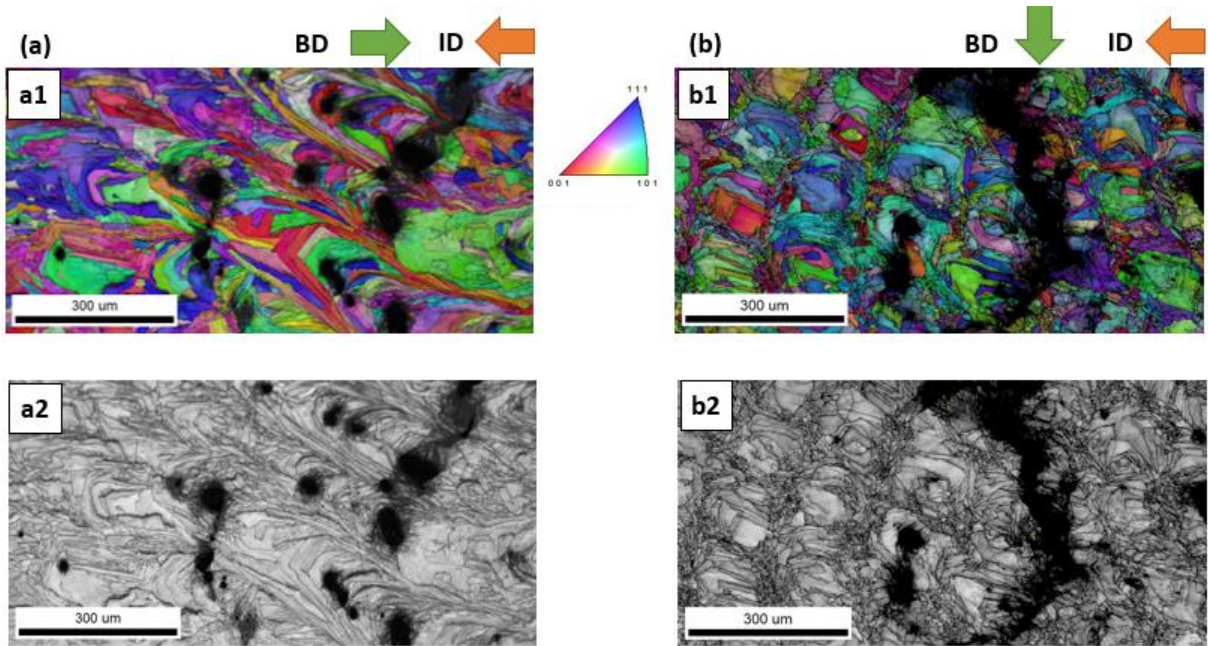


Figure 33: Post-shot characterization of samples. (a) IP, (b) TT. (a1 and b1) Inverse pole figure (IPF) maps showing examples of spall fracture relative to grain structure. (a2 and b2) IQ map showing dark areas of strained material near spall fracture locations.

grain boundaries and grain refinement near the fracture locations. These characteristics are typically observed at melt pool boundaries in AM fabricated parts [84]. The spall damage planes on both samples demonstrate voids and highly strained material. Severe plastic strains and presence of voids lead to poor diffraction pattern quality, which is presented as dark regions on the image quality map [74].

The XCT data (Figure 34) shows that spall damage is focused on an inner radius that is approximately 75% of the total sample width. The edges, in all radial directions, experience virtually no spall, possibly due to radial wave interactions.

The image analysis of the post-shot samples revealed a damage distribution profile similar to that observed in the 2D sample cross section that was evaluated using optical microscope images. Figure 34 displays a comparison of the damage observed for the individual 2D cross section layers compared to the total damage observed across each layer of the 3D volume. The peak indicating maximum spall damage occurs at the same vertical layer location for both data sets, and the general trend for damage profile as a function of layer location is consistent as well. The “double-peak” observed in the damage profile of the perpendicular sample is even captured.

These results indicate that using the optical microscope analysis of the sample cross section to assess spall damage provides a reasonably qualitative approximation of the damage experienced across the full sample volume for a sample with a relatively consistent microstructure. However, the results also present the potential for individual layers to possess differing spall damage than the specific cross section being examined.

In summary, the impact test results indicate that:

- The wave velocity profile is different based on build-impact orientation
- The spall strength is different based on build-impact orientation
- Location of spall fracture is different based on build-impact orientation
- Regardless of orientation, the primary fracture sites correspond to layer and melt pool boundaries.

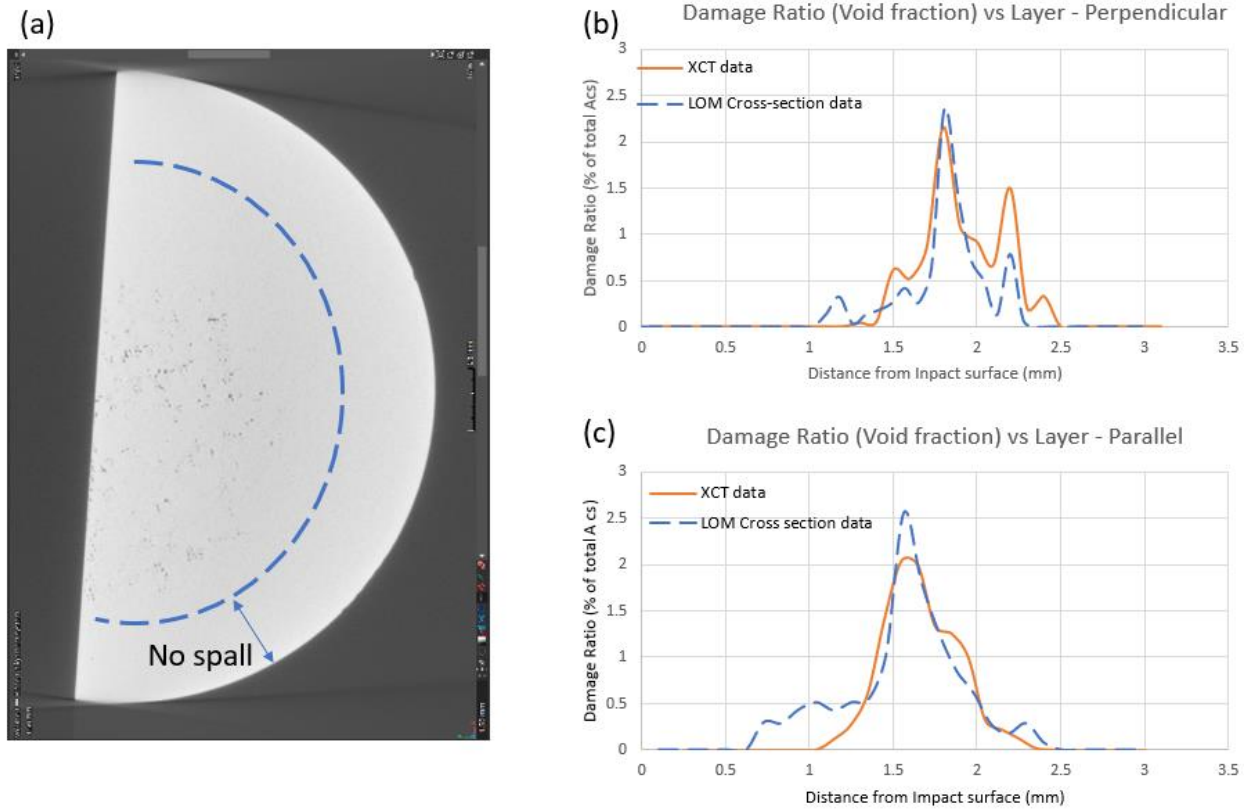


Figure 34: Post-shot sample X-ray computed tomography (XCT). (a) Example XCT slice of parallel sample at spall plane, (b) Spall damage distribution plot for perpendicular sample comparing XCT data with LOM data at cross-section, (c) Spall damage distribution plot for parallel sample comparing XCT data with LOM data at cross-section.

Discussion

The differences observed in the physical and mechanical properties measured between the samples of different build-impact orientations can be attributed to two main microstructural factors. These include (a) bulk microstructural anisotropy effects on directionally dependent elastic, plastic, and dynamic (spall) fracture properties and (b) local microstructure effects due to presence of melt pool boundaries and layer interfaces, phase distributions, and build process induced defects on spallation.

Bulk microstructural anisotropy effects on measured properties

Variations in modulus were observed between the orientations of as-fabricated samples examined in this study. This is consistent with variations in elastic modulus based on build orientation of LPBF fabricated SS316L obtained in previous studies using both quasi-static tensile and resonance methods [85-87]. These observations illustrate that crystallographic texture through grain orientation, pore morphology, and residual stress are contributing factors to the observed modulus anisotropy.

The spall strength (σ_{spall}) is a function of the material density (ρ), bulk wave speed (C_b), and the change in free surface velocity (Δu_f) obtained from the peak velocity to the first minimum (as observed in the impact experiment). The density and wave speed are both bulk properties measured on the as-fabricated materials. The wave speed can vary greatly (due to orientation, processing conditions, or other factors) compared to the density for samples of the same bulk composition [4, 6, 30, 46]. The other major factor in spall strength comes from the experiment. The change in free surface velocity results from the deceleration that occurs during generation of the spall surface until a compressive pulse (characteristically caused by the spall event) reaches the free surface causing a steep acceleration.

In this study, a directional dependence was observed for the measured elastic wave velocities (and modulus) (Table 4) as well as the pullback velocity (Table

5). The IP impacted sample demonstrated a higher bulk wave speed than the TT sample; however, the IP sample had a lower pullback velocity. The resulting spall strength calculation shows the TT sample as having a higher spall strength than the IP sample, indicating that (as a whole) the TT sample is more resistant to tensile and shear deformation (i.e. stiffer under those loading conditions).

Differences in elastic wave propagation as a function of build orientation also affect the location of the spall plane. The longitudinal wave speed (C_L), a measure of the particle movement parallel to the direction of wave propagation is higher for the IP sample, while shear wave speed (C_S) is lower for the IP sample than the TT sample. This indicates the significant influence of microstructural anisotropy on wave propagation.

Figure 35 illustrates the calculated Lagrangian distance (x) versus time (t) diagrams based on the shock velocity calculated using the empirical constants for 316L [5] and the measured elastic wave speeds and particle velocity estimated from the wave profiles captured using PDV interferometry. It can be seen that the x - t diagrams predict a difference in the spall plane location for the two cases of the IP and TT samples, because microstructural anisotropy influences wave speeds which in turn affect the location where the reflected release waves interact and generate tension resulting in spall failure.

In continuum mechanics and fluid flow analysis, Lagrangian specification of a flow field plots the position of an individual parcel (in this case the head of the wave front) with respect to time which gives a pathline of the parcel. Eulerian specification, on the other hand, focuses on a specific location in space through which the fluid flows in and out over time.

In Figure 35, the arrival of the shock pulse at the rear free surface at t_2 and of the post-spall recoil pulse at t_4 are both directly indicated based on the velocimetry data. Between these two discrete moments the spall event occurs.

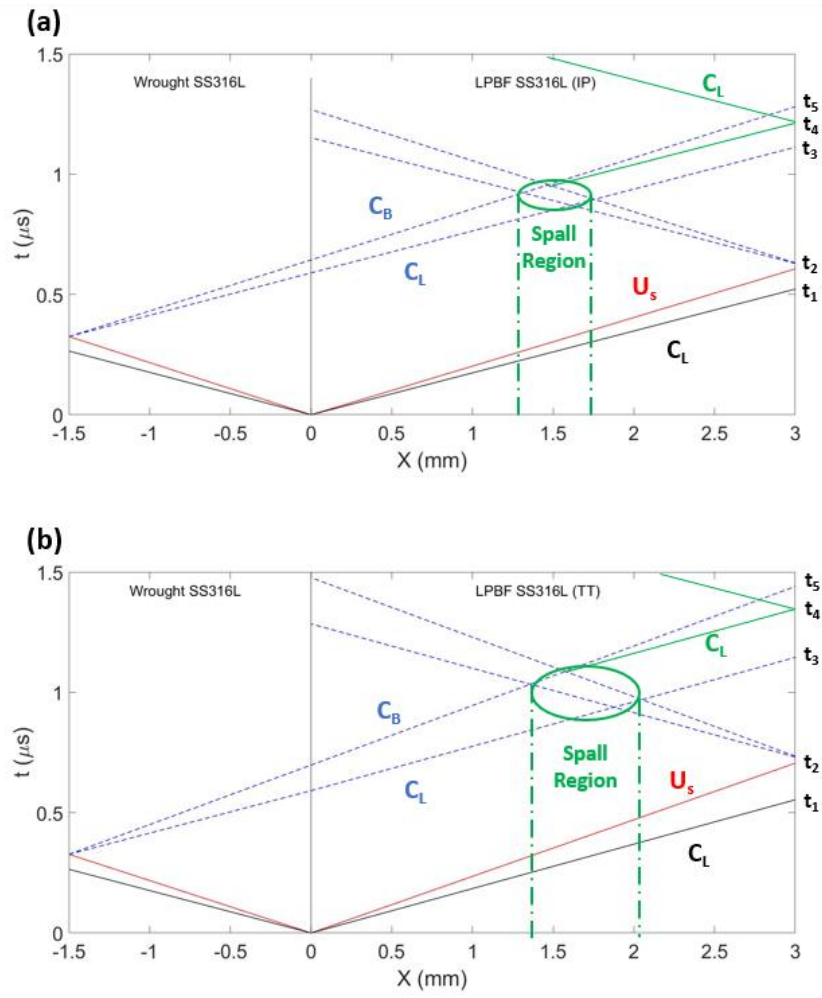


Figure 35: Lagrangian x-t plots of (a) IP sample and (b) TT sample.

The distance from the rear free surface to the spall plane can be established using the measured wave speeds and the unknown time segments t_{2-s} (time between t_2 and spall) and t_{s-4} (time between spall and t_4).

- $X_{spall} = X_{2-s} = C_b \Delta t_{2-s}$ (7)

- $X_{spall} = X_{s-4} = C_L \Delta t_{s-4}$ (8)

Since this distance must indicate the same location regardless of path, a relation between the time steps can be established using the known sound wave properties. Also, the individual time steps combine to account for the known time recorded in the experiment between the free surface arrival times t_2 and t_4 .

- $\frac{C_b}{C_L} = \frac{\Delta t_{s-4}}{\Delta t_{2-s}}$ (9)

- $\Delta t_{2-4} = t_4 - t_2 = \Delta t_{2-s} + \Delta t_{s-4}$ (10)

This set of equations can then be solved for the intermediate time interval.

- $\Delta t_{2-s} = \frac{\Delta t_{2-4}}{1 + \frac{C_b}{C_L}}$ (11)

A simplified approach is then possible based on the time intervals available directly from the velocimetry data. As mentioned, the arrival of the shock pulse is observed at t_2 . This pulse travels the full length of the sample and incorporates both the elastic and plastic flow components. Since the wave propagation is considered one-dimensional, the rarefaction wave that travels from the rear free surface to the spall plane is exposed to the same conditions but across a different time interval and distance. Using the relation of the distance traveled by the shock wave (X_{target}) and the relative time intervals for shock wave arrival (t_2 from velocimetry) and spall occurrence (Equation 11), the general location of the spall plane can be determined to within a reasonable estimation.

- $X_{spall} = \frac{\Delta t_{2-s}}{t_2} X_{target}$ (12)

Using this relation with the values for Δt_{2-s} calculated previously for TT and IP samples (0.37 μs and 0.50 μs , respectively), the spall plane distance from the rear free surface is estimated to be at 1.2 mm (for TT) and 1.5 mm (for IP).

These approximations are in agreement with the locations for primary spall damage plane observed in the post-mortem optical images (Figure 31).

Local microstructure effects

As stated earlier, the etched LOM images (Figure 32) reveal that the specific damage site locations preferentially occur at or near the melt pool boundaries. This is not uncommon in AM fabricated materials, as the differences in properties across adjacent locations lead to stress concentrations at these boundaries [4, 24, 25]. Referring to the basic principles of fracture mechanics in metals, stress concentrations are greatest at cracks or voids oriented normal to the direction of stress [4]. The geometry of the melt pools dictates that a greater portion of these boundaries are oriented normal to impact (stress) in the IP samples than in the TT samples, resulting in a greater amount of fracture damage. Although small, the observed voids at these melt pool boundaries (Figure 29.d) in the as-built AM samples indicate starting points for damage growth. This is similar to the failure observed in quasi-static studies [63, 83, 87], where small voids and defects at the melt pool boundaries serve as failure initiation sites. Due to the time scales involved, quasi-static tensile fracture behavior is also influenced by the tortuous path of connecting melt pool boundaries [63], a phenomenon that is not observed in this work but could be realized if the shock impact loading is sufficient to approach full spall fracture.

LPBF fabricated stainless steel samples develop a “coarse grain zone” and nonequilibrium elemental segregation below the melt pool boundaries [62, 88]. Similar to the heat affected zone (HAZ) in conventional welds, this area below the melt pool boundaries is a preferential failure location due to the differences in microstructure and properties compared to the neighboring material. SEM images of the as-built samples (Figure 33.c) demonstrate a similar difference in solidification morphology above and below the melt pool boundary. Other research has also shown elemental segregation on the nanometer scale near

these boundaries, though similar analysis was not conducted as part of this study.

The melt pool developed by the applied laser is elliptically shaped and solidifies from the outer edges in toward the center (Figure 32.d). Although an individual melt pool is very symmetrical, the compilation of the tracks and layers results in a very directionally dependent structure. The edges of each melt pool are remelted by subsequent layers, while the lower base of each is not, leading to the typical AM “fish scale” pattern. This leads to three basic categories of melt pool boundaries: Layer-Layer (L-L), Track-Track (T-T), and combination boundaries. As the individual melt pools solidify from the outer edge toward the center, each of these boundary types presents a different interaction between melt pools. The solidification direction of a pure L-L boundary (Figure 32.e) is generally in a consistent orientation. T-T boundaries are usually much smaller than L-L boundaries due to the laser scan patterns used and are mostly remelted by subsequent layers. Combination boundaries (Figure 32.g), on the other hand, can exhibit very sharp intersection angles and a high degree of misorientation; the observation of grain refinement and high angle grain boundaries at melt pool boundaries (Figure 33) supports this. As such, these locations are more vulnerable to be crack initiation sites [83] and are observed to be preferential spall damage locations (Figure 32.a, b). The fracture characteristics are also different at these intersections than the fractures that occur elsewhere. The fractures occurring at melt pool boundary intersections are sharper, elongated cracks that appear to initiate as microcracks and grow along the interface. In contrast, the fractures occurring not at melt pool boundaries are more circular in shape indicating a pure ductile fracture.

The orientation of these combination melt pool boundaries with respect to the impact direction is also of significance. When a flaw or void is present in a solid material, the corresponding stress concentration is highly influenced by the void's geometry and orientation, with a sharp crack oriented normal to the loading direction having the greatest stress concentration [24]. This stress concentration

reduces as the void shape is more rounded or rotation of its primary axis relative to the direction of loading reduces. In context of the present study, the voids that occur at these combination melt pool boundaries have an orientation that makes the stress concentration greater when impacted from the direction in-plane to build direction than along the through-thickness direction (Figure 32.a, b).

The primary build defect inherent to AM fabricated materials is porosity. This type of build defect can reduce the overall strength and present areas that are more susceptible to failure [24]. The observed pores are small (less than 30 μm diameter) and appear to align along melt pool boundaries. These locations are observed as preferential spall initiation sites. The LPBF process results in orientation of these interfaces that is anisotropic in nature. The local stress state experienced in a sample is controlled, in part, by the loading direction relative to the build direction, as the stress concentration near a void is controlled by the geometry of the void relative to the direction of loading [24]. In this case, the characteristics of the melt pool interfaces present a scenario where voids aligned along the MPB will possess an angle closer to normal when loaded from the IP direction (Figure 36.b) than when loaded in the TT direction (Figure 36.c). This presents a greater stress concentration under the same applied load, leading to increased damage in the IP sample.

As is the case with most LBPf fabrication, the specific morphology of the individual build defect pores varies. Circular, symmetrical pores are also present that behave similarly when loaded from either the in-plane or through-thickness direction.

Summary and Conclusions:

The spall response for 316L stainless steel AM samples fabricated in different orientations (in-plane and through-thickness relative to build direction) is examined through execution of light gas gun plate impact experiment, combining time-resolved interferometry (PDV) measurements and microstructure characterization of the soft-recovered impacted materials.

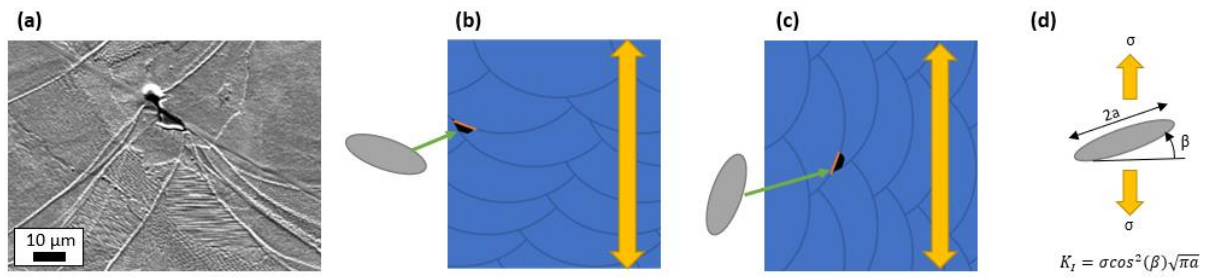


Figure 36: Porosity build defect example. (a) SEM image of void located at MPB, (b) Schematic of void at MPB subjected to IP loading, (c) Schematic of void at MPB subjected to TT loading, (d) Diagram of stress concentration relationship for void at angle relative to loading direction, indicating that the stress concentration increases as the angle relative to normal decreases.

Specifically, the study presented reveals:

- The AM SS316L exhibits orientation dependent behavior, with the spall strength affected by the relative orientation between build direction and impact direction. This is influenced greatly by the bulk microstructural anisotropy and the effects of local AM process inherent defects including melt pool tracks and layers associated with LPBF microstructure.
- The individual spall damage locations for each sample correspond heavily with melt pool layer boundaries but not necessarily with grain boundaries.
- The spall plane location (distance from rear free surface) differs based on impact direction relative to build orientation. This phenomenon is observed in the post-mortem samples and supported by the velocimetry data.
- A complex spall behavior is observed in the through-thickness (TT) sample, which is evidenced in both the “double-hump” demonstrated in velocimetry data and the IP damage planes seen in the post-mortem characterization.

Chapter Five

Randomly Distributed Engineered Porosity Study

Portions of this Chapter correspond to a published journal article:

K. D. Koube, T. Sloop, K. Lamb, J. Kacher, S. S. Babu, and N. N. Thadhani. An assessment of spall failure modes in laser powder bed fusion fabricated stainless steel 316L with low-volume intentional porosity. *Journal of Applied Physics*, Volume 133. (2023). <https://doi.org/10.1063/5.0143744>.

This study involves sample characterization, plate impact spallation testing, and post-mortem analysis of AM 316L stainless-steel (SS) samples with varying degrees of “engineered porosity”. The “engineered porosity” was achieved by placing void spaces in the electronic CAD files that would not be melted by the laser scan during build fabrication. These voids were cube-shaped and were randomly distributed across the bulk of each sample. The samples were characterized both before and after the gas gun impact experiments. The data sets collected for analysis include light optical microscope (LOM), scanning electron microscope (SEM), electron diffraction spectroscopy (EDS), electron back scatter diffraction (EBSD), and x-ray computed tomography (XCT). It is hypothesized that these results will show strong correlation between bulk porosity content and spall behavior, with samples of greater porosity content and void size possessing reduced spall strength and increased resulting spall damage.

Experiment

Sample Fabrication

The samples were fabricated using the process outlined in Chapter 3. Each sample was fabricated as a solid right cylinder oriented vertically so that the target sample disc(s) could be cut appropriately. The “engineered porosity” was achieved by placing void spaces in the electronic CAD files that would not be melted by the laser scan during build fabrication. Figure 37 shows an example of this in the .STL format. These void spaces do not constitute true “porosity” as

each contains unmelted powder rather than completely empty “void” space. The fact that the voids contain powder is an important distinction, as the wave propagation behavior can differ greatly between a void filled with powder compared to one filled with only gas.

The voids were cube-shaped with nominal dimensions of 200, 350, and 500 μm . Due to some of the process limitations associated with LPBF, the cube void dimensions are not extraordinarily precise. At the vertical edges, there is a tendency for powder particles that are intended to be unmelted by the design to fuse with the melted regions. Likewise, the top boundary of the void attempts to be built on top of loose powder. Considering the general shape of the melt pools and the reality that each pass penetrates beyond the current layer, the characteristic geometry for the upper cube surface will likely not be a sharp straight line.

The voids were randomly distributed across the bulk of each sample to create relative void volumes of 1%, 3%, and 5% porosity. To accomplish this, the FEM CAD package within ABAQUS was used to randomly remove small cubes of material from a solid cylinder based on a bulk percentage of the total volume. This configuration was then transferred to the .STL model files for each cylinder. Since the positions were randomly distributed within the bulk volume and not constrained with any minimum spacing in either the horizontal or vertical direction, there is the possibility that some voids may be very close to nearby voids. To avoid pore-edge interaction effects, the porosity distribution is focused on the inner ~9mm diameter of each sample.

For simplicity, a naming convention that incorporates the nominal void size and the distribution content into a simple, unique identifier is used for each of the samples. Table 7 identifies the name for each sample within the test matrix.

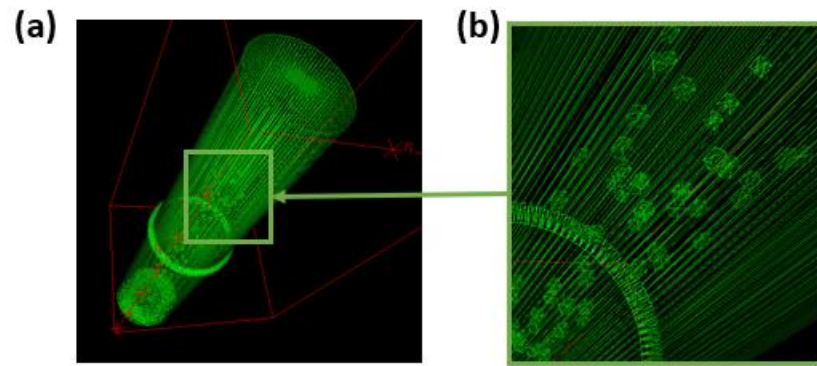


Figure 37: Details of sample fabrication. (a) STL file showing engineered voids on 0.500 mm at 5% sample, (b) Enlarged image of STL file to highlight the voids placed in the file.

Table 7: Engineered porosity distribution matrix and sample ID labels

		Bulk Volume Porosity		
		1%	3%	5%
Pore Size	200 μm	2-1	2-3	2-5
	350 μm	35-1	35-3	35-5
	500 μm	5-1	5-3	5-5

Material Feedstock:

The 316L SS powder used to fabricate the samples was gas atomized powder provided by SLM Solutions. The chemical composition and particle size distribution of the powder is consistent with that listed in Chapter 3.

Physical Property Characterization:

The samples were characterized both before and after the gas gun impact experiments. Sample preparation and characterization analysis was performed as described in Chapter 3. The as-built characterization consisted of bulk density measurements, ultrasound wave speed measurements, moduli calculations, XCT analysis, and microstructure characterization. To ensure consistency with earlier experiments, baseline porosity and grain structure were also collected from the as-fabricated samples. Non-destructive evaluations were performed on each tested sample, and analysis requiring cross-section was done on representative section from the same printed sample specimen. The post-test characterization was performed on soft-recovered samples collected after the experiment and consisted primarily of cross-section and XCT analysis.

Bulk density (measured using both gas pycnometer and Archimedes method) indicated a general trend of decreasing density correlating to increased porosity content (Table 8 and Figure 38). This trend was observed for the individual populations (200, 350, and 500 μm) as well as the sets for each content class (1%, 3%, 5%) when compared collectively. The lone outlier was sample 2-3. Since the porosity content of each sample is based on the percentage of bulk volume from a cylinder, the potential exists for the void content of each individual disc section machined for testing and analysis to deviate slightly from the nominal prescribed value.

Table 8: Density measurements for each sample

		Bulk Volume Porosity		
		1%	3%	5%
Pore Size	200 μm	$7.93 \pm 0.00 \text{ g/cm}^3$	$7.86 \pm 0.10 \text{ g/cm}^3$	$7.91 \pm 0.03 \text{ g/cm}^3$
	350 μm	$7.94 \pm 0.01 \text{ g/cm}^3$	$7.92 \pm 0.02 \text{ g/cm}^3$	$7.91 \pm 0.04 \text{ g/cm}^3$
	500 μm	$7.93 \pm 0.04 \text{ g/cm}^3$	$7.93 \pm 0.02 \text{ g/cm}^3$	$7.90 \pm 0.03 \text{ g/cm}^3$

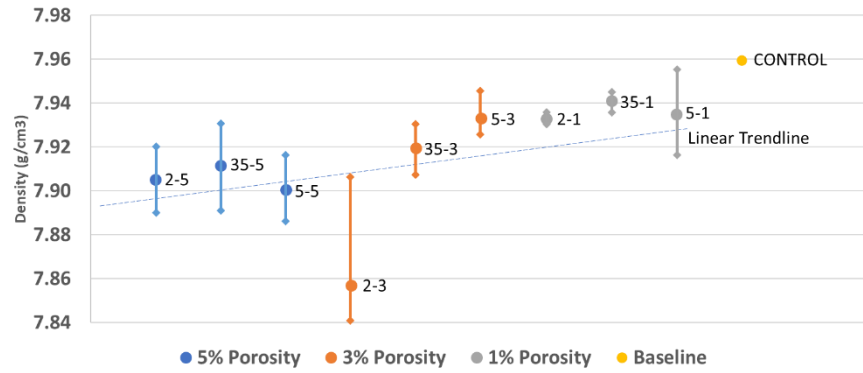


Figure 38: Density Measurements for each sample.

The measured wave speeds and moduli for each sample are listed in Table 9 and displayed visually in Figure 39. There are observable differences in properties across the sample population, along with some consistent trends. In particular, there are some interesting trends demonstrated for both the longitudinal wave speed (C_L) and the shear wave speed (C_S).

For the 5% void content set, the C_L increases with increasing void size. For the 3% set, although the C_L increases some with increasing void size, the values are fairly consistent across the 3 void sizes. For the 1% set, the C_L decreases with increasing void size. For both the 200 μm and 350 μm void size sets, the C_L decreased with increasing porosity content. For the 500 μm void size set, on the other hand, the C_L was observed to increase with the increasing porosity. Overall, 7 of the 9 measured C_L values, were greater than the baseline control sample. Only the 2-5 and 5-1 samples were slightly ($<0.3\%$) lower than the control sample.

In the shear wave speeds (C_S) among the sets, some variation was seen, but no distinct trends relating to either void size or content were observed. All of the C_S values for the engineered porosity samples were greater than the baseline control sample. Combined with the observations in the longitudinal wave speeds, this suggests that the wave travel speed through unconsolidated powder is greater than through solid, fused material of the same chemical composition.

The calculated bulk wave speeds (C_B) follow trends that are somewhat of a combination of the longitudinal and shear wave observations. This is not surprising, as the bulk wave speed is calculated as a function of the two measured wave speeds. Within the discrete void content sets (1%, 3%, 5%) variation is observed, but no definitive increasing or decreasing trends are observed, similar to the shear wave results. Conversely, the trend observed within the void size sets mimics the longitudinal wave speed results. For both the 200 μm and 350 μm void size sets, the C_B decreased with increasing porosity content, while the C_B increased with increasing porosity for the 500 μm void size set. Overall, the bulk wave speed values for the engineered porosity samples did

Table 9: Pre-test sample characterization data

Property	Control	200-1%	200-3%	200-5%	350-1%	350-3%	350-5%	500-1%	500-3%	500-5%
CL mm/ μ s	5.78 \pm .005	5.85	5.78	5.73	5.85	5.79	5.81	5.72	5.80	5.87
CS mm/ μ s	2.79 \pm .050	2.93	2.84	2.89	2.85	2.89	3.03	2.91	2.88	2.92
CB mm/ μ s	4.74 \pm .033	4.78	4.76	4.66	4.83	4.73	4.64	4.63	4.75	4.80
G GPa	62.19 \pm 9.10	67.89	63.31	66.14	64.55	65.94	72.46	67.32	65.96	67.38
B GPa	179.1 \pm 22.9	181.1	178.1	171.6	185.5	177.3	170.7	169.9	178.8	181.7
E GPa	167.2 \pm 17.17	181.1	169.8	175.8	173.5	176.0	190.4	178.4	176.2	179.9
Poisson's ratio	0.34 \pm .05	0.33	0.34	0.33	0.34	0.33	0.31	0.33	0.34	0.33
ρ g/cm ³	7.96 \pm .00	7.93	7.86	7.91	7.94	7.92	7.91	7.93	7.93	7.90

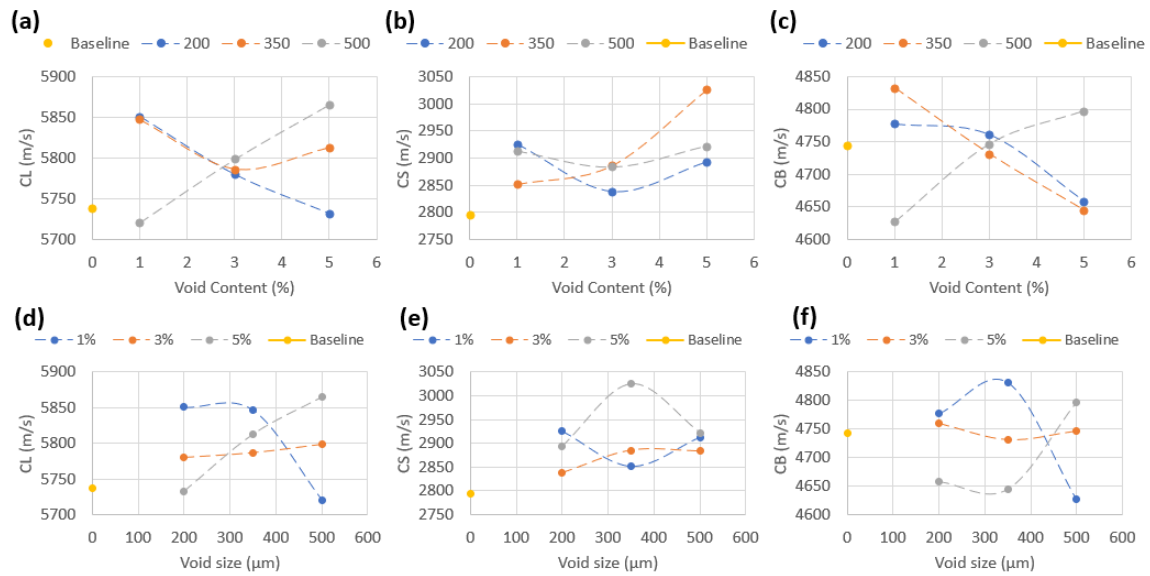


Figure 39: Elastic wave speeds for engineered void samples. (a-c) Data points grouped by void size. (a) Longitudinal wave speed, (b) Shear wave speed, (c) Bulk wave speed. (d-f) Data points grouped by distribution percentage. (d) Longitudinal wave speed, (e) Shear wave speed, (f) Bulk wave speed.

not exhibit a consistent trend when compared to the baseline control sample (some slightly greater and some slightly lower) with an average within 0.3% of the baseline value.

No major trends were observed within the individual void size or content sets for any of the calculated modulus values (elastic, shear, or bulk). The overall modulus values showed the following overall general trends compared to the baseline. All of the engineered porosity samples demonstrated greater elastic modulus (E) than the baseline, a greater shear modulus but to a lesser extent than elastic, and bulk modulus values very near to the control sample. The results are found in Table 9.

XCT data was collected on the sample cylinders prior to sectioning into discs for impact testing. The purpose of this analysis was to examine the void distribution as a function of location, examine the nominal size of the voids, and to assess potential variation within the sample. The random distribution of voids across the bulk of the printed cylinders presents the potential for a high level of variation across layers. Evidence of this was observed by measuring the void fraction for individual layers as a function of Z-height (Figure 40.d). Sample 2-5 is shown as an example, but similar trends were observed in all samples. In three images (Figure 40.a, b, c) spaced 0.025 mm, roughly corresponding to the layer thickness used (0.030mm), the measured void fraction varies considerably. It was observed that the engineered voids roughly matched the nominally intended dimensions. However, the unmelted sections were not precise cubes as depicted in the CAD files, due to the process limitations of LPBF.

Characterization using LOM, SEM, EBSD, and EDS was performed on non-impact tested representative specimens of each sample set. The LOM images revealed several things about the engineered voids. First, the engineered voids were not precise cubes as constructed in the design files. The shapes were somewhat deformed due to the fusing of unmelted powder to nearby melt tracks, a phenomenon typical of LPBF processing. This is observed in all of the samples (Figure 41). The nominal size of the voids matched the intended dimensions

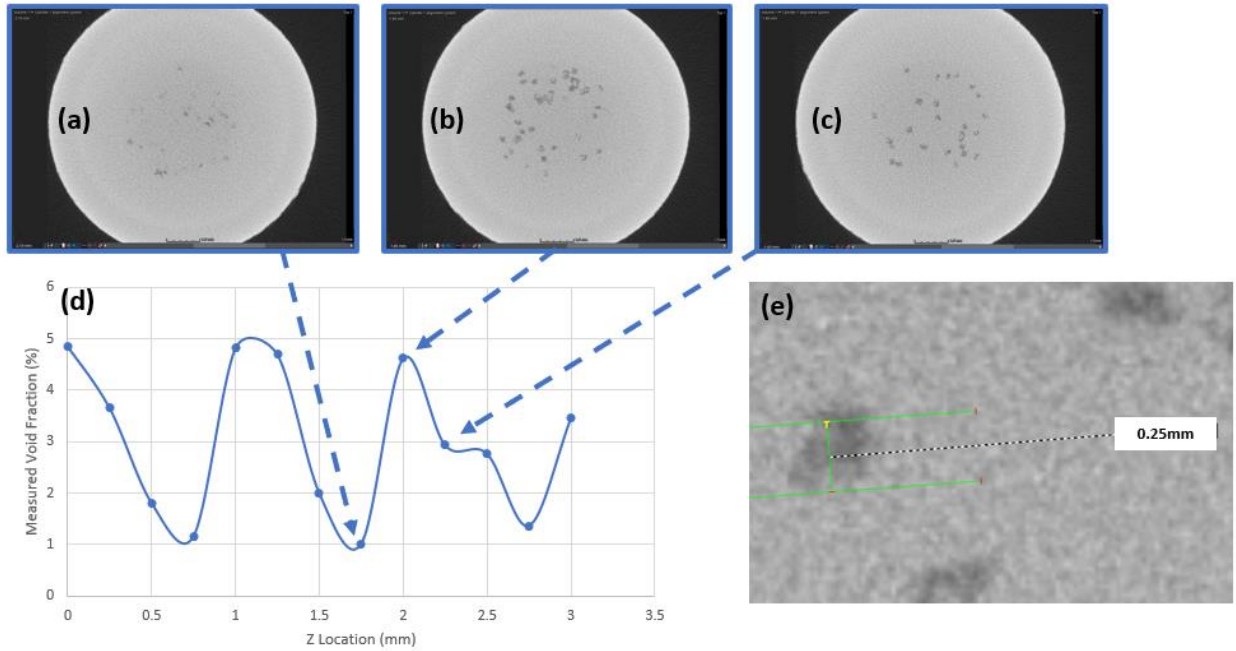


Figure 40: XCT analysis of 200-5% sample. (a-c) Slice images of XY plane at three consecutive Z-layer locations, (a) $Z = 1.75\text{mm}$, (b) $Z = 2.00\text{mm}$, (c) $Z = 2.25\text{mm}$, (d) Plot of void fraction measured via XCT vs. Z location, (e) XCT image demonstrating measurement of engineered void within build sample.

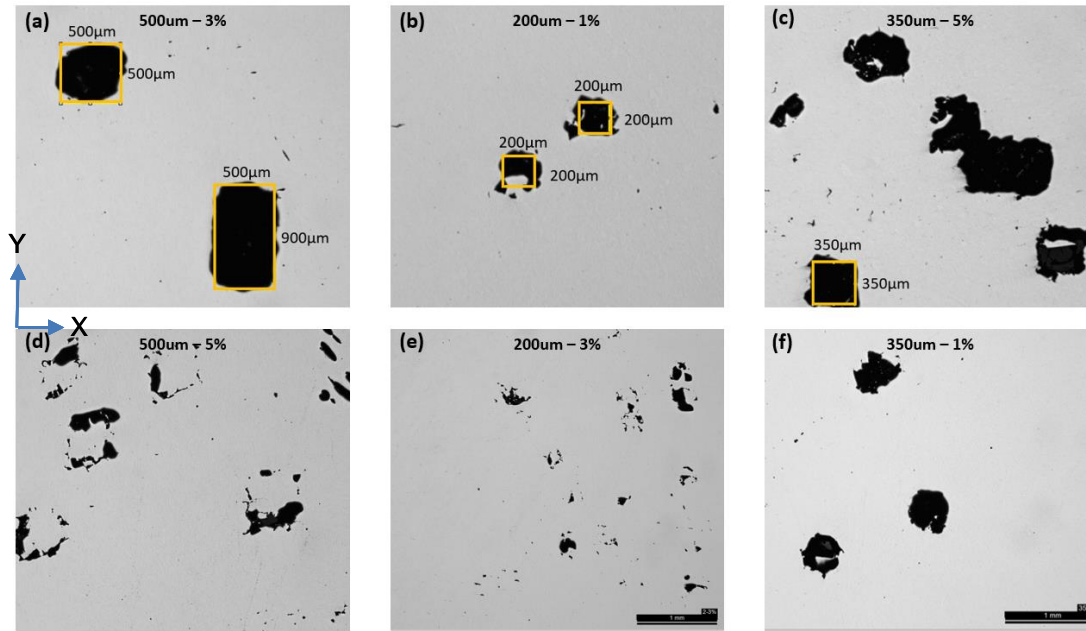


Figure 41: As-built LOM images of engineered void samples. Note that the images indicate random distribution, irregular void shapes, and void volumes that reasonably meet the design goals. (a) 500-3%, (b) 200-1%, (c) 350-5%, (d) 500-5%, (e) 200-3%, (f) 350-1%.

(200, 350, 500 μm) to a reasonable degree. However, in some cases it was evident that small spacing distance between voids resulted in formation of a single, larger void (Figure 41.a, c). The distribution of the voids was also truly random, as intended.

There were clusters of voids and large areas with no voids observed within the same sample. The general trend of increasing void content (1%, 3%, 5%) was satisfied, based on the observed number and size of the measured voids. The specific distribution of void space also appeared to vary among layers. For example, while most of the images displayed fully formed voids of the anticipated size, some layer images such as Figure 41.d (of the 5-5% sample) shows many irregular void regions and relatively few of the fully formed cubic engineered voids. These irregular shapes are likely locations near the top or bottom layers of the engineered void where powder outside the intended laser scan was fused with the melted region.

The SEM images (Figure 42) corroborated the observation of non-cubic void shape and verified that the voids are, in fact, filled with powder. This is an important distinction, as wave propagation will react differently to a space filled with powder compared to a true void in the sample. The fused regions of powder at the edge of the voids also result in a variation of the solidified microstructure compared to the more well-defined melt pool boundaries seen elsewhere in the sample (Figure 42). EBSD data reveals reduced grain size along the border of the voids (Figure 42.e). This is typical among all the samples.

The pre-test characterization demonstrates several aspects of the as-built AM samples that are important to note.

- The nominal size and relative content of the voids corresponds with the design intended in the build file.
- The location and spacing of the voids is random in nature.

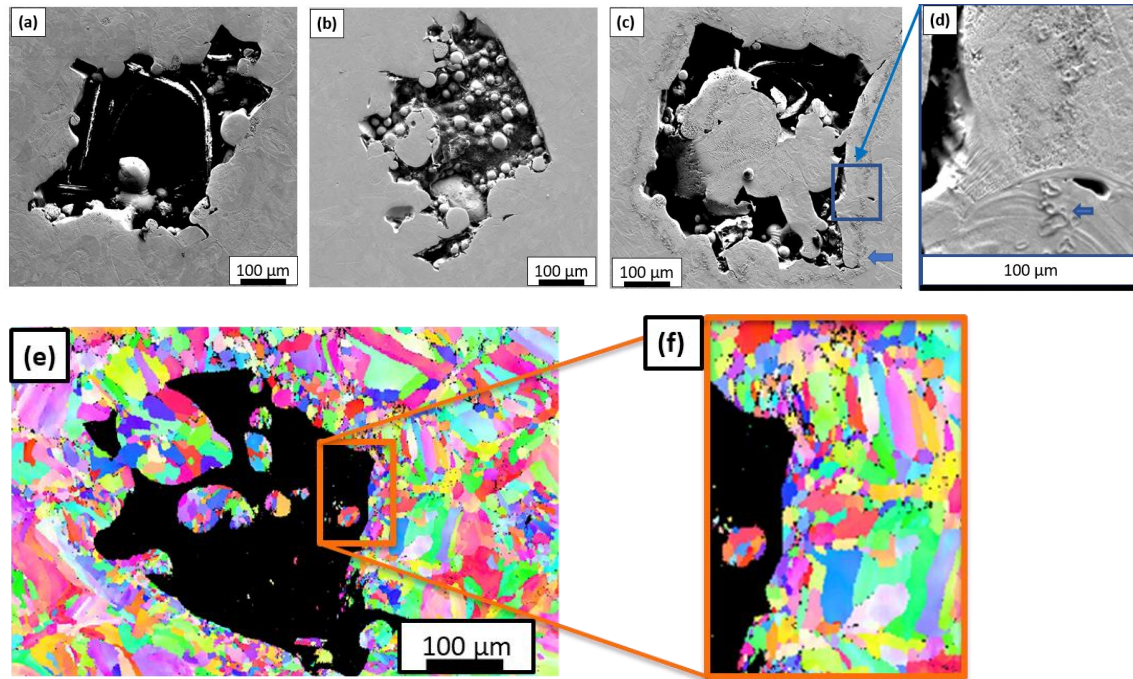


Figure 42: SEM and EBSD images of as-fabricated engineered voids. (a) 0.500 mm at 3%, (b) 0.350 mm at 5%, (c) 0.500 mm at 3%, (d) Zoomed image of (c) to highlight material at edge of void that fused with neighboring powder. (e) EBSD image of void in 0.500mm at 3%. (f) Zoomed image of (e) to highlight the grain refinement along the edge of the void.

Plate Impact Testing

For this study, all flyer plate impact experiments were performed with impact direction (ID) parallel to build direction. An impact velocity of approximately 250 m/s was used. Each test shot consisted of three sample targets mounted in the sample holder: (1) the PDV instrumented sample that collected velocimetry data, (2) the non-instrumented soft-recovered sample, and (3) a wrought control sample to verify experiment consistency. For each test sample, the soft-recovered sample was cross-sectioned, polished, and mounted for examination as described in earlier sections of this paper.

Results

Impact Test

The peak velocities resulting from the plate impact experiments were approximately 250 m/s for each orientation tested. In a standard impact test with solid material, this corresponds to a peak stress of approximately 4.4 GPa. Figures 43 and 44 show the free surface velocity data collected for each of the samples. Table 10 shows the data in tabular form, with “Slope1” represents the rise to peak velocity by initial compression and “ t_{full} ” representing the estimated time a peak velocity. Several inferences can be made from these results.

Overall, a gradual rise in the FSV was observed. This is not typical for this type of plate impact experiment. The normal progression in spall experiments (as shown in the baseline sample) is typically a very steep, almost instantaneous rise to peak velocity, followed by a plateau at the peak velocity indicating a fully developed shock front. The gradual rise suggests that the shock wave progression to the RFS is being slowed by something in the sample, which also reduces the time duration observed at the peak velocity. The 350-3 sample is the only one in this data set that exhibits the prototypical spall response. It shows the common initial acceleration due to the shock wave arrival. The steep pullback slope is more indicative of true spall [44] than the other samples and indicates the greatest rate of simultaneous void nucleation.

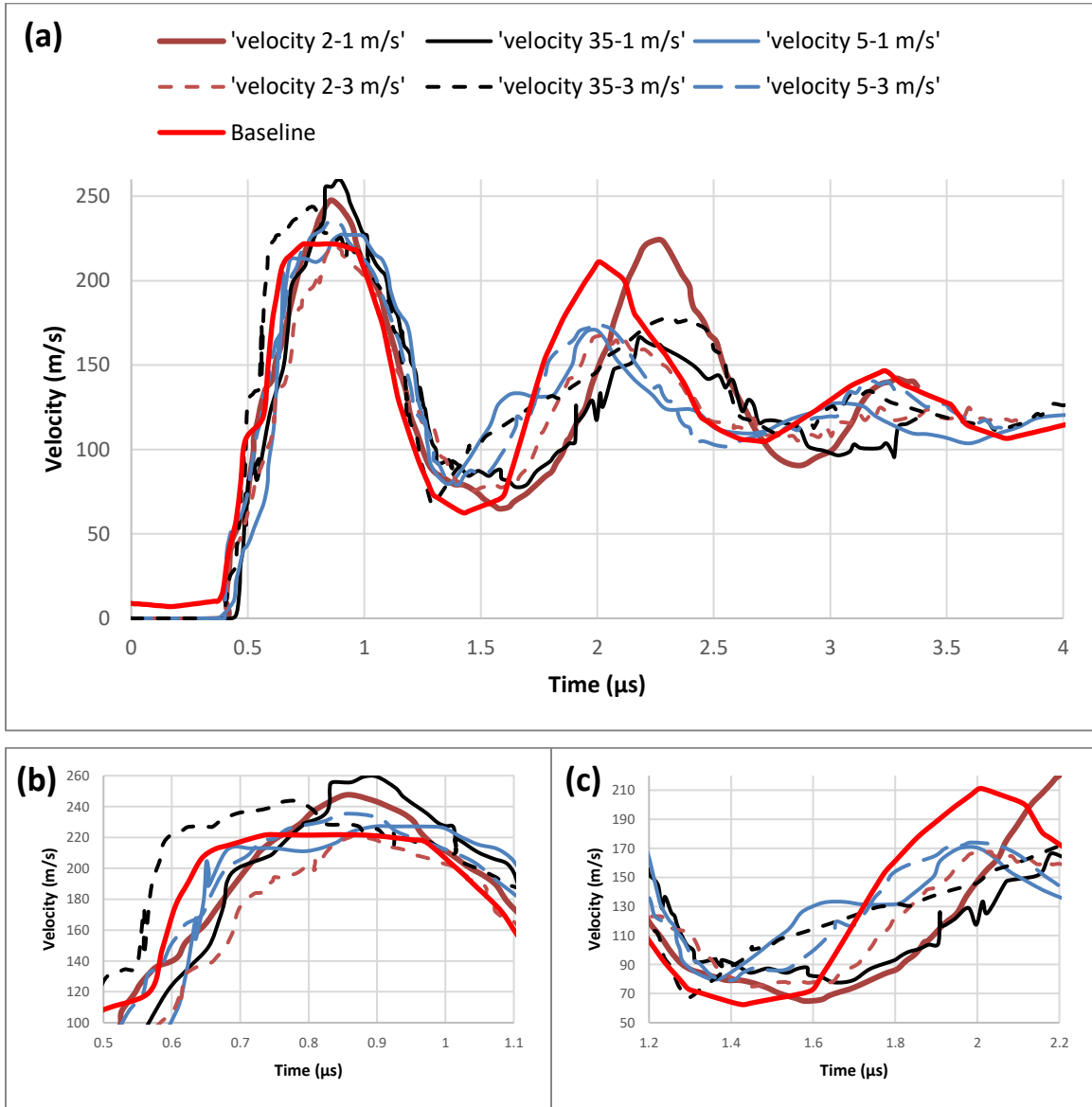


Figure 43 - Velocimetry plots for Engineered void impact experiments for 1% and 3% porosity. (a) Full experiment data set. (b) Closer view of initial velocity rise region of plot. (c) Closer view of pullback region of plot.

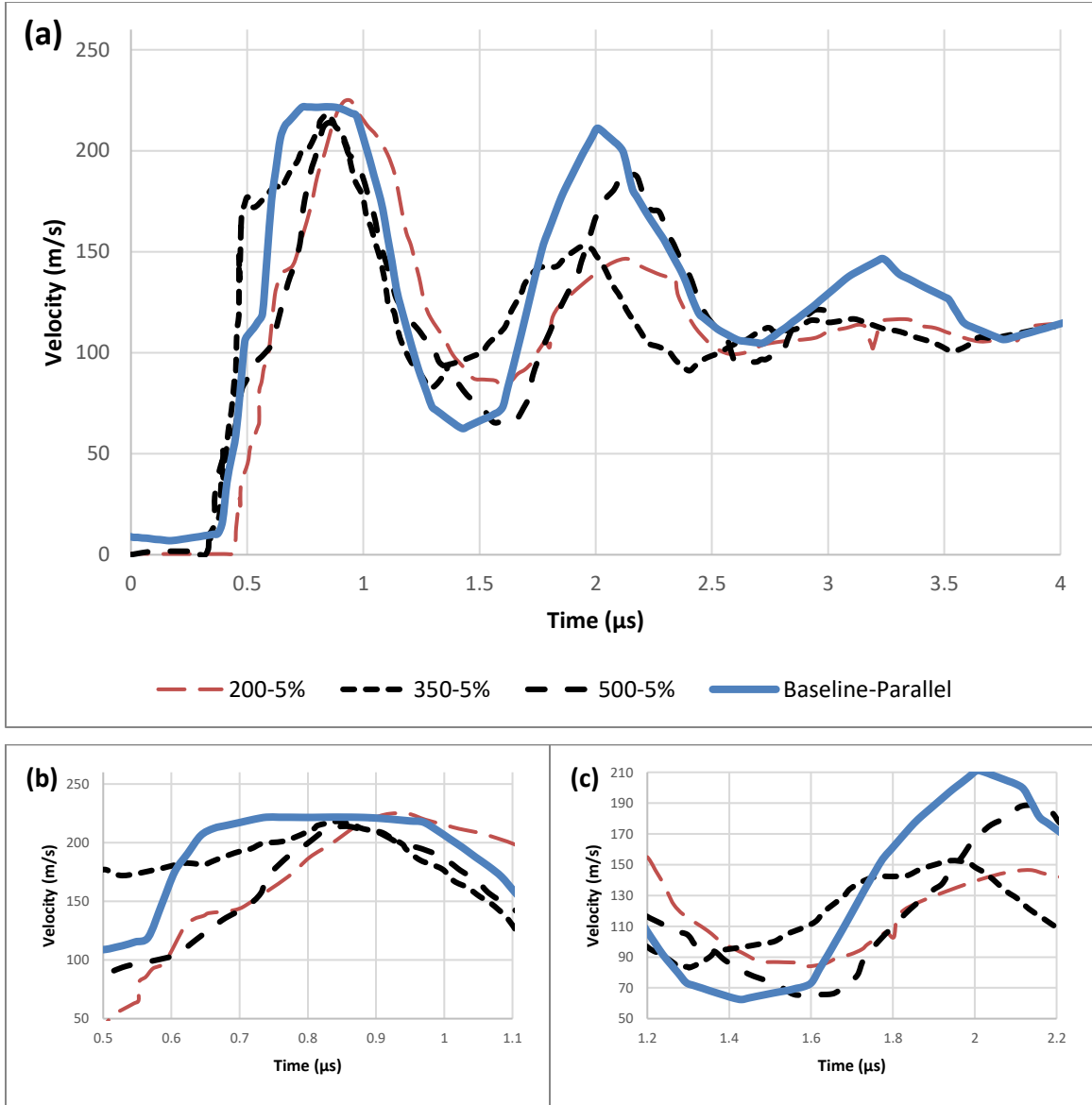


Figure 44 - Velocimetry plots for Engineered void impact experiments for 5% porosity. (a) Full experiment data set. (b) Closer view of initial velocity rise region of plot. (c) Closer view of pullback region of plot.

Table 10: Slope and timing information from velocimetry plots.

	CON	2-1	35-1	5-1	2-3	35-3	5-3	2-5	35-5	5-5
Slope1	624	528	628	453	475	680	521	463	424	420
t_{full}	0.192	0.09	0.02	0.14	0.01	0.15	0.08	0.028	0.009	0.021
σ_{spall}	2.77	3.45	3.48	2.70	2.75	3.30	2.94	2.59	2.48	2.81

In 1% and 3% samples (Figure 43), 200-1 is expected to demonstrate the greatest amount of spall damage according to the “damage parameter” principles described in Chapter 2. Sample 200-1 also has the common 2-stage pullback slope that indicates accelerated void growth, possibly from stress concentrations caused by the presence of existing voids. The 500-1 sample experiences a lower peak velocity (coinciding with lower peak stress). Increased damping is also observed on the 500-1 sample, as evidenced by the reduced slope to the peak velocity and the extended period seen during the post-spall ringing peaks.

All 5% porosity samples (Figure 44) exhibit the apparent damping behavior due to voids. Gradual slope to peak velocity is seen in the initial compression rather than the steep jump that is typical of spall experiments, along with absence of a velocity plateau at the peak velocity state (Figure 44.b). Also, there is a reduction in pre- and post-spall rates of velocity change (Figure 44.c), indicating a more viscous failure mechanism rather than spall.

In comparing each of the void size sets (200, 350, and 500 μm), a general trend is observed of decreasing slope of the rise to peak velocity that corresponds to increasing void content (1%, 3%, 5%). The exceptions are 350-1 and 350-3, which demonstrate a slope similar to the baseline sample. It is likely that the instrumented sample for those sets did not possess voids in the vicinity of the PVD probe and, therefore, the measured velocity data was not affected. Since the voids were randomly distributed, the location of voids in the soft-recovered sample is not necessarily representative of the instrumented sample.

The pulse duration (t_{full}) is a representation of the time elapsed between the shock front reaching the rear free surface and the reflected rarefaction wave reaching the spall plane (Table 10). The shock front arriving at the rear free surface generates an acceleration to the peak velocity. The more gradual slope demonstrated in most of these samples indicates that the internal voids reduce the rate of acceleration (Table 10). The velocity profile of the typical spall experiment has a plateau at the peak velocity that is often referred to as a fully developed shock front. Along with the gradual acceleration, these samples tested

do not exhibit this plateau, indicating that the full shock wave front is not being fully transferred to the RFS but rather partially reflected or absorbed.

The values for both measured HEL velocity and calculated HEL stress are shown in Table 11 for all samples. Although there is variation across the sample set, there does not appear to be any direct correlation between the HEL properties and void size or distribution.

The spall strength (or strength of the material sample to resist dynamic tensile failure) is calculated using a combination of the material properties and data collected from the velocimetry plot. Similar to the elastic wave, modulus, and HEL properties mentioned earlier, there is variation but no definitive trends observed for the spall strength.

The “damage parameter” concept is explored in this study as a qualitative measure only. In this experiment, the results suggest that the samples with smaller 0.200 mm voids appear to exhibit greater damage evolution than the samples with larger voids (Table 11). The post-mortem image analysis supports this assertion. There is also an observed inverse trend indicating a decrease in observed damage with increased void content for the 0.200 mm set. A conflicting trend is observed in the 0.500 mm set, but this may be due to the reduced initial peak (V_a) in the 5% sample.

In summary, the impact test results indicate that:

- There is a gradual rise in velocity profile of most test samples, rather than the steep acceleration that is typical of spall experiments. There is also an absence of the “plateau” region that is typically seen at the peak velocity in spall experiments, indicating that the shock front is not fully developed. This suggests that the presence of these engineered voids has a damping effect on the propagating shock wave front.
- Although there is variation observed for the elastic wave speeds, moduli, HEL, and spall strength, there is no definitive correlation between these results and void size or distribution.

Table 11: Experiment results for each sample. Velocimetry Data, Calculated Properties, and Image Analysis results

Property	Control	200-1%	200-3%	200-5%	350-1%	350-3%	350-5%	500-1%	500-3%	500-5%
Velocity/Strength Characteristics (from experiment)										
U_s (mm/μs)	4.647									
u_{HEL} (m/s)	66.52	73.47	40.46	45.23	74.03	97.73	88.27	42.79	49.26	63.21
σ_{HEL} (GPa)	1.45	1.70	0.92	1.02	1.72	2.24	2.03	0.97	1.13	1.47
u_p (m/s)	112.35	123.6	110.7	112.3	129.7	121.76	109.1	113.6	117.7	107.0
Δu_{fs} (m/s)	170.00	182.3	146.8	140.6	181.6	176.38	135.0	147.3	155.4	148.3
σ_{spall} (GPa)	2.77	3.45	2.75	2.59	3.48	3.30	2.48	2.70	2.93	2.81
Damage Characteristics										
From Velocimetry Data										
V_a (m/s)	225	247	221	225	259	244	218	227	235	214
V_c (m/s)	210	224	168	146	167	179	153	170	174	189
V_c/V_a	0.94	0.91	0.76	0.65	0.64	0.73	0.70	0.75	0.74	0.88

Post-mortem Characterization

The signatures captured in the PDV profiles provide limited understanding of the spall failure mechanisms. It is therefore important, particularly in samples such as these with random heterogeneity and velocity profiles that differ from those typically seen in plate impact experiments, to couple the interferometry data with post-mortem microstructural analysis. For each unique void profile (size and distribution), the soft-recovered sample was cross-sectioned, polished, and mounted for examination as described earlier in Chapter 3.

Post-mortem optical microscope images (Figure 45) of the samples indicate some unique spall results relative to the locations of engineered voids. The areas near the engineered voids experience little, if any, spall damage. Conversely, in areas away from the engineered voids, typical spall damage is observed. This appears to be more prevalent in the samples with larger voids. Although a more typical spall plane appears to be present in the samples with smaller 200 μ m voids, it is shifted toward the RFS for the sample with higher void content (200-5%). This suggests that whatever effect contributes to the no-spall condition in the 350 and 500 μ m samples is also present to a lesser extent in the 200 μ m set. Since the voids are randomly distributed across the volume of each test piece, XCT was used to examine the resulting damage across the full sample volume. The 3D renderings were qualitatively reviewed for observable trends and compared to previous samples. The coordinates and size of each void were also compiled as a quantitative metric to examine the damage characteristics of each sample with respect to the presence of engineered void locations.

The damage observed across the full sample volume was consistent with that seen in the cross-section images. The small 200 μ m-5% samples exhibited a spall plane shifted toward the RFS, with evidence of spall damage spread across a wider than usual band. The samples with larger engineered voids (350 and 500 μ m) demonstrated no spall damage near those voids, as witnessed in the cross-section analysis. However, the XCT analysis did reveal small areas of spall damage occurring away from the large engineered voids (Figure 46.c).

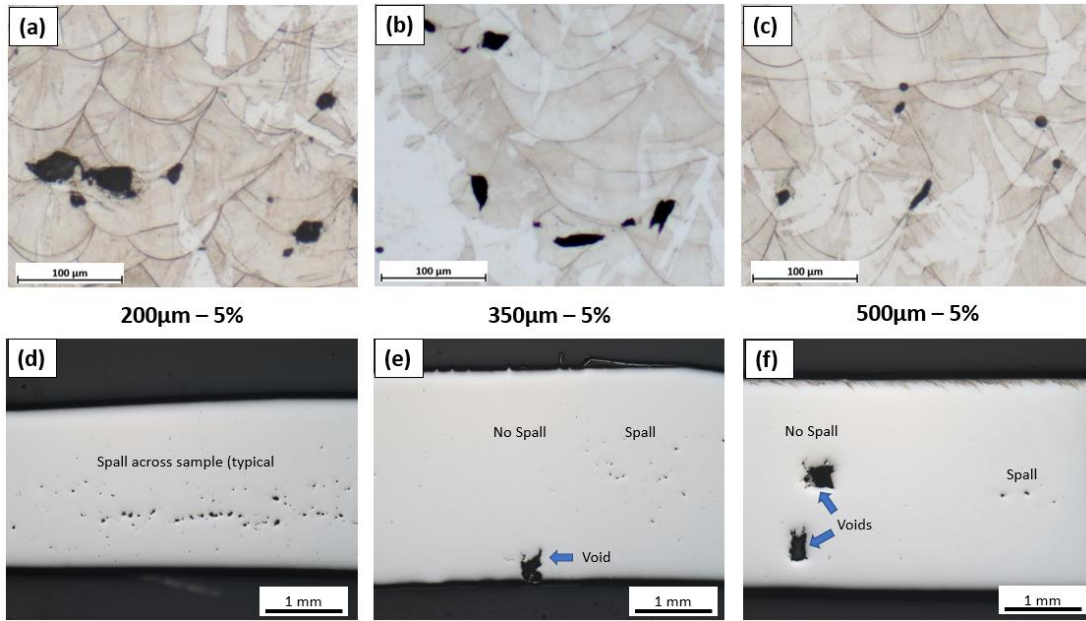


Figure 45: Post-shot characterization of samples (a-c) Etched LOM images showing spall formation along melt pool boundaries: (a) 0.200 mm x 5%, (b) 0.350 mm x 5%, (c) 0.500 mm x 5%, (d-f) LOM images showing spall formation relative to engineered void locations: (d) 0.200 mm x 5%, (e) 0.350 mm x 5%, (f) 0.500 mm x 5%

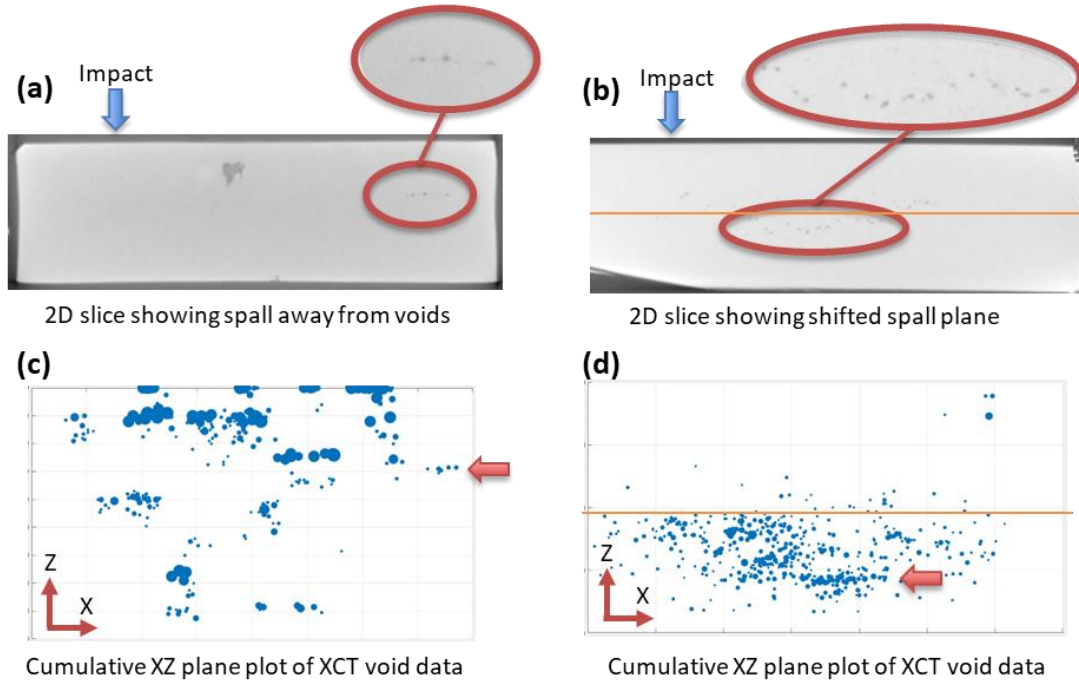


Figure 46: XCT images and data from Engineered void samples post-mortem.(a-b) Individual 2D slices of XCT. Impact direction indicated by blue arrow. (a) 500-5%, (b) 200-5%. (c-d) Cumulative data of XZ damage locations compiled across the Y-direction. (c) 500-5%, spall damage located away from engineered voids is highlighted, (d) 200-5%, shifted spall plane is highlighted. Orange line indicates sample centerline corresponding to expected spall plane location.

SEM and EBSD data of the damage locations revealed indications of void collapse at some of the engineered void locations. Areas located near the impact surface appeared to experience more complete collapse than voids located closer to the rear free surface (Figure 47). The void collapse is caused by the compressive force of the initial plastic-shock front that results from impact.

The observed void collapse is not as prevalent in the samples with smaller voids (200 and 350 μm), due to the smaller initial dimensions of those voids leading to a more fully collapsed state that is less visible. Under greater magnification (as in Figure 48) a similar result is seen in those samples. These regions of damage are distinguishable from the traditional spall voids by geometry. While spall damage forms either small circular voids or cracks aligned at melt pool boundaries, the collapsed voids present a squared edge with dimension matching the designed width. Regions of damage that extend at sharp angles from the edges of the collapsed voids (as seen in Figure 48.a, .c, and .e) are believed to correspond to areas of extreme shear from edge effects and jetting that resulted during the action of void collapse.

Discussion

Several unique observations are presented. The characterization and experiment results are influenced by the presence of engineered voids, although the specific void size and distribution percentage do not present definitive correlations to the resulting performance. As such, (a) the influence of the bulk void distributions, (b) specifics of the spall fracture locations, (c) wave reflection and transmission, and (d) limitations of the LPBF build process are discussed in more detail.

Bulk Void Distributions

The engineered voids present in the samples used for this study were randomly distributed with respect to the bulk volume. Porosity distributions of 1%, 3%, and 5% were distributed across the bulk of the sample as voids in the design file, which resulted in powder filled cavities at various locations within each sample.

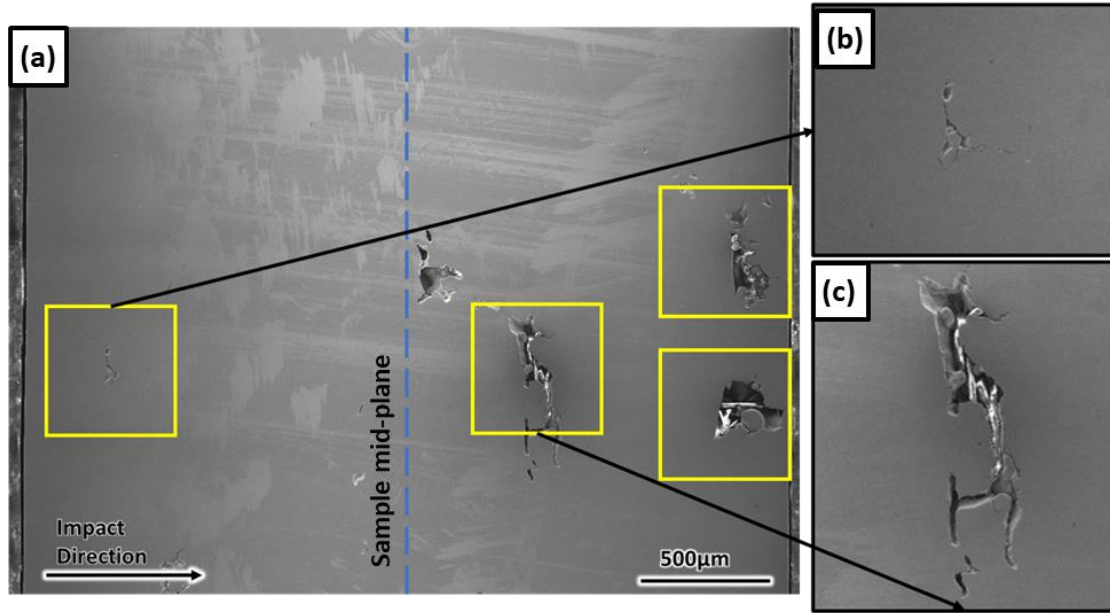


Figure 47: SEM image of 500-1% sample showing void collapse. Yellow boxes are 500 μm square to indicate relative reduction in size. (a) Full sample length showing voids relative to sample mid-plane. (b) Area of suspected void collapse near the impact surface. (c) Area of suspected void collapse near the rear surface.

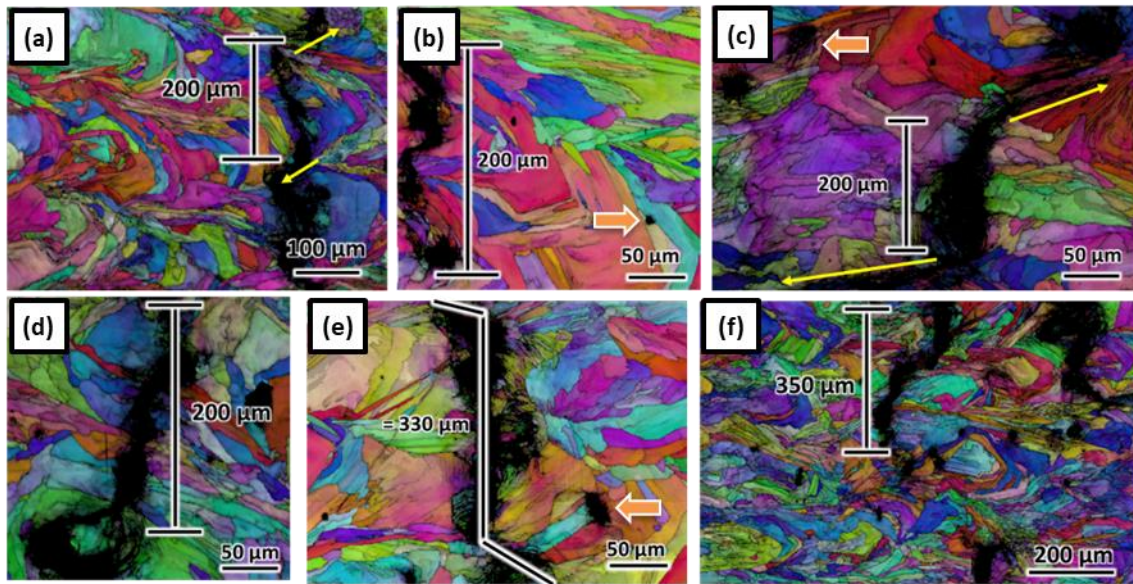


Figure 48: Post-mortem IPF images of engineered void samples,, indicating void collapse. (a) and (b) Examples in 200-5% sample, (c) Example in 200-3% sample, (d) Example in 200-1%.sample, (e) and (f) Examples in 350-5% sample. Dimension bars show the expected width of the square void. Yellow arrows note potential jetting locations. Orange arrows indicate locations of traditional spherical spall damage.

As is the case in a truly random distribution, the locations and spacing between voids vary throughout each sample. There is the potential for merging of voids within close proximity into a single, larger void as well as large spaces without voids. Both instances are observed in the samples.

These bulk void distributions do not accurately represent local behavior, as each individual void produces localized variation in the measured properties and material response to the impact test. This is evidenced in the lack of distinct trends in the ultrasonic wave speed measurements, as well as the velocimetry data from the experiment. Figure 49 demonstrates an example of the different potential void distributions for three individual slices of the same bulk distribution. Using this same rationale, evaluation across different samples (such as 500 μ m at 1%, 3%, and 5%) does not provide true direct comparison.

The velocimetry data collected during the spall impact testing is also affected by this argument. The experiment design is intended to produce a 1-D shock wave transmitted from the impact surface to the rear free surface. However, literature [77] has shown that the shock wave arrival time, and thus its velocity, can vary with sensing location at the rear free surface. In much the same way, location of the PDV sensor relative to engineered voids can have a great impact on the measured time-velocity profile. This makes it unrealistic to accurately connect specific data trends in the velocimetry data from the instrumented sample to the post-mortem characterization of the soft-recovered sample. As such, only general trends with respect to the baseline fully dense sample are significant.

Spall Fracture Locations

In quasi-static and even up to bar impact test (10^3), it has been observed that the presence of internal voids corresponds to reduced strength. Furthermore, these initial voids typically serve as preferential failure sites [72]. Work by Fadida et al [72] examined split Hopkinson bar (SHB) tests performed on Ti-6Al-4V samples with engineered porosity built using LPBF. The researchers found that increasing the pore size reduced both the strength and ductility of the sample and

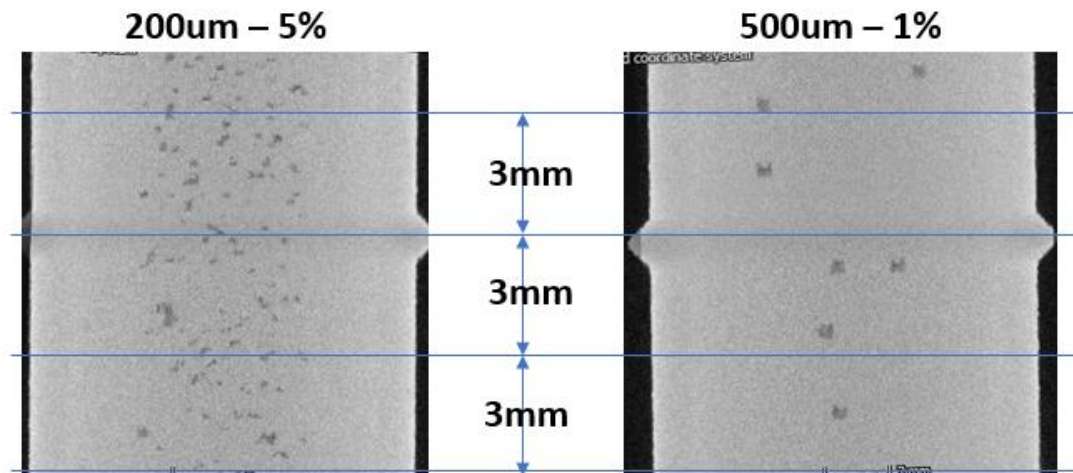


Figure 49: XCT images of as-built Engineered void samples.

introduction of multiple pores further degraded the properties. In the current study, the random nature of the samples somewhat negates the direct comparison of the raw number values for spall strength as a useful metric.

The calculation of spall strength depends heavily on the measured bulk density and bulk wave speed of the material sample. The wave propagation through the material is very path-dependent, influenced heavily by the void distribution. The bulk density values are somewhat misleading because each sample has essentially identical density for the solid regions with varied volumes of powder, rather than a uniform distribution of lower density across the sample. Therefore, it is more useful to focus on the specific damage locations rather than the calculated strength values for this experiment.

In the current study spall fracture sites do not appear to correspond with the engineered void locations. Quite the contrary was observed. The spall fracture locations for each sample were observed to occur at locations away from the engineered voids. The areas near the void locations, conversely, did not demonstrate spall failure. The damage observed can be categorized as either traditional spall or void collapse.

Void collapse is caused by the compressive force of the shock wave applied to the as-fabricated voids during the initial propagation through the sample and can be partial or full, depending on the location and the as-fabricated void size. For the smaller 200 μm voids, the result is full void collapse and a shifted spall plane due to the slowing of the wave at the void. For the 350 μm voids, full collapse is also evident in many locations and although the presence of voids seems to reduce the spall near observable voids, the overall damage characteristics are very mixed. For the 500 μm voids, partial collapse is seen as the dimensions are reduced from the as-built condition. The large voids sufficiently slow the shock wave such that spall damage is not observed near the voids but is apparent in locations away from the void.

The traditional spall locations are observed away from the engineered void locations, particularly for the large voids. In much the same manner observed in

fully dense samples, demonstrated spall fracture preferentially occurred at the melt pool boundaries. This is not an uncommon observation in AM materials, as the differences in properties across adjacent locations lead to stress concentrations at these boundaries [25, 47]. Furthermore, the contributing factors discussed in the previous chapter (build process induced porosity at the melt pool boundaries, grain structure differences at the boundaries, and melt pool solidification interfaces) are also applicable to this set of LPBF samples.

Wave Reflection Transmission – Speed and Stress Reduction

An important contributing factor to the observation of delayed shock wave arrival at the RFS and reduced spall damage is the behavior of the wave pulse at the solid-powder interface regions of the engineered voids. The principles of shock wave reflection, transmission, and shock impedance dictate this behavior. When a shock wave propagates from one material to another, changes in pressure, wave velocity, and density occur. Continuity at the boundary dictates that the particle velocity and pressure will be the same in both materials [4]. Since the shock impedance term is the product of material density and shock wave velocity (per EQN 2), it is greater for materials with high density and high sonic velocity (which is a major factor in resulting shock velocity). Specific to this study, a powder-filled void has a lower density and lower shock impedance than the solid material.

The general response as a shock wave propagates from a material of higher impedance (Material 1) to a material of lower impedance (Material 2) is discussed in Chapter 2. The compressive pressure (stress) decreases as the wave is transmitted to Material 2 due to the reduced resistance in that material. The remaining portion is reflected back into Material 1 as a rarefaction wave. This reflection is like the free surface case (zero impedance) except that a portion of the wave is transmitted.

The case of a shock wave propagation from a material of lower impedance (Material 2) to a material of higher impedance (Material 3) is likewise discussed

in Chapter 2. Conversely, the compressive pressure (stress) increases as the wave is transmitted to Material 3 due to the increased resistance in that material. The remaining portion is again reflected into Material 2. However, to maintain equilibrium, this reflected wave is compressive in nature with a magnitude equal to the pressure difference.

In the scenario presented here, the beginning and end states are that of solid material (Material 1 and Material 3) while the intermediate state (Material 2) is that of powder. Due to irreversibility in the process, this transition from high-to-low-to-high impedance results in a net loss of both particle velocity and stress (as shown in Figure 50). This loss serves to both slow the progression of shock wave as it and to reduce the pressure stress that is applied by the wave front.

Plotting this out conceptually using simplified 1-D Lagrangian x-t diagrams (Figure 51) for baseline case, two 200 μm voids, and a single 500 μm void provides a visual comparison of how this concept slows the wave progression and shifts the spall plane location. Since the wave speed in powder is not directly measurable, a shock impedance based on the relative powder density (approximately $\frac{1}{2}$ the solid metal density) is used to demonstrate the concept.

The baseline diagram (Figure 51.a) refers back to the theoretical case for shot planning that results in spall plane at the mid-plane of the target. The diagram with two 200 μm voids (Figure 51.b) shows that each void slows the shock wave such that the interaction between the rarefaction waves takes place closer to the rear free surface, resulting in a shift of the spall plane. The diagram with a single 500 μm void (Figure 51.c) further slows the shock wave sufficiently that the rarefaction wave from the flyer surface reaches the rear free surface at roughly the same time as the compressive shock wave, resulting in the no spall condition.

Also worthy of note is the timing information that can be inferred from the Lagrangian plots. The plateau at peak velocity in the velocity-time plot corresponds to the time period between the arrival of the shock wave at the rear free surface (t_2) and the spall event. This time interval is reduced by the voids as

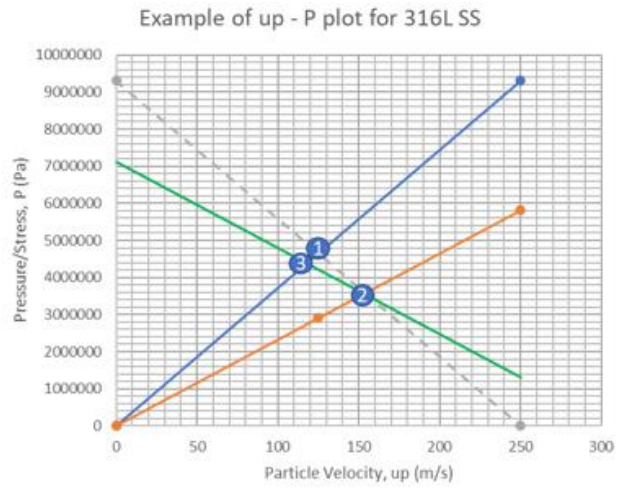


Figure 50: Schematics of shock wave transmission between materials with different shock impedance.

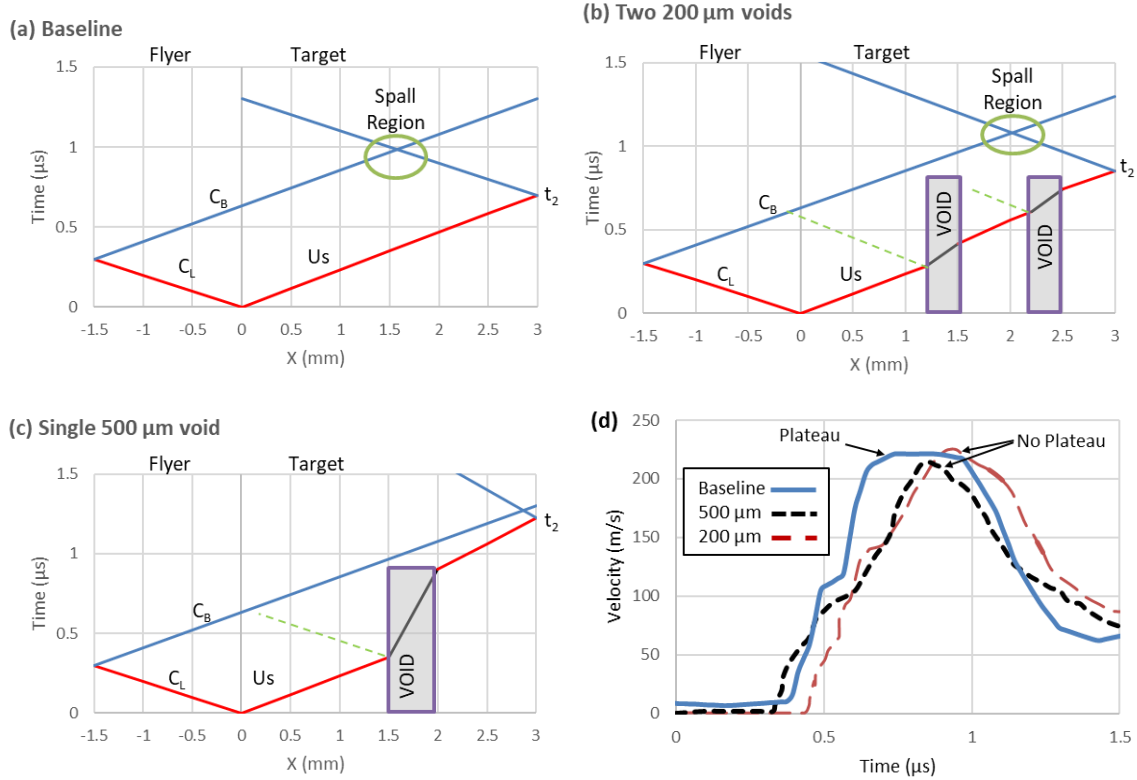


Figure 51: Conceptual Lagrangian X-t diagrams showing influence of void on the wave propagation in sample. (a) Baseline, (b) Multiple 200 μm voids, (c) Single 500 μm void, (d) Velocity-Time plot from experiment showing absence of plateau at peak velocity for samples with voids.

shown in Figures 51.b and 51.c, which leads to a reduction (or absence) of the typical plateau at peak velocity. The experimental data for the samples with voids (as seen in Figure 51.d) supports this hypothesis.

Irregular Shape of Voids

As noted in the characterization results, the voids present in these samples are not uniform cubes but rather the sides have uneven surfaces due to process limitations of LPBF fabrication. While wave transmission across a material interface results in reflection, when a wave meets an angled interface a certain degree of refraction also occurs. Further discussion on the specifics of this phenomenon is found in Chapter 2.

The influence of this refraction on the resulting free surface velocity measurement is threefold. **(1) Increased travel distance.** The redirected portion of the wave (and its stress component) is delayed in reaching the rear free surface due to the increased travel distance. **(2) Introduction of a shear wave.** The resulting refracted wave has both a longitudinal and shear wave component. As such, the problem is no longer one-dimensional and the uniaxial stress assumption may no longer be valid. **(3) Wave interaction.** If voids are collocated within a certain distance then interaction between the waves, particularly the shear component, may occur. This greatly complicates the situation, as these interactions are not observable at the rear free surface – the only means of collecting experiment data.

Full realization of the degree of influence each of these factors has on the material behavior is not attainable from this experiment due to the random nature of the void distribution. However, there appears to be a limit to the “wake zone” around a void that changes the spall behavior.

Conclusions

The spall response for SS316L AM samples fabricated with varying size and quantities of randomly distributed purposeful “engineered porosity” is examined

through execution of light gas gun plate impact experiment and microstructure characterization. The AM technology used to fabricate the samples is LPBF. In summary, it was observed that the spall response of AM material is heavily influenced by the presence of internal powder-filled voids.

Although is variation observed for the elastic wave speeds, moduli, HEL, and spall strength, there is no definitive correlation between results and void size or content.

There is a gradual rise in velocity profile of most of the engineered porosity test sample set, rather than the steep acceleration that is typical of spall experiments. There is also an absence of the “plateau” region that is typically seen at the peak velocity in spall experiments, indicating that the shock front is not fully developed. This suggests that the presence of these engineered voids has a damping effect on the propagating shock wave front.

However, the random distribution of voids within the samples makes it impossible to identify any trends across the sample sets, as bulk porosity distribution may mask local behaviors. The PDV probes used to measure velocity in plate impact experiments collect 1D data for a specific location, and calculation of the “spall strength” and “HEL strength” of a material sample assumes some degree of homogeneity across the sample. The post-mortem analysis, however, demonstrates that areas with internal voids behave much differently than areas farther away. Additional studies are needed to isolate the influence of individual voids.

Chapter Six

Numerical Modeling

Introduction

This section involves using finite element analysis (FEA) as a tool to inform the future plate impact experiments for SS316L samples fabricated using LPBF. The goals of this study were twofold: (1) Demonstrate the behavior observed in the earlier experiments to increase understanding of the internal stress wave propagation, and (2) Inform the design of experiments for future research.

It is hypothesized that simple FEA models can be used to effectively demonstrate the compressive wave behavior that occurs during the first phase of the plate impact experiment for qualitative comparison studies between different void distributions and internal features.

Abaqus Model Setup

A two-dimensional solid model was developed to simulate the compressive pulse generated by the plate impact experiment using the explicit solver in ABAQUS finite element analysis (FEA) software. The model consists of a stationary target impacted by a moving flyer. The intent of this model is to serve as a design tool that can be used to better understand the propagation of the compressive pressure wave that is transmitted through the target as the result of impact (Figure 52). This model is not intended to estimate spall behavior, spall strength, or spall damage evolution.

The pressure is related to the particle velocity (which is a function of impact velocity) through the conservation of momentum equation (see Chapter 2). The dimensions of both the flyer and target are based on the impact experiment samples. The diameter of each is 15mm. The thickness of the target and flyer are 3mm and 1.5mm, respectively. The coordinate system orientation for the model is that the flyer travel path is downward in the vertical (Y) direction, and the position across the impact surface is along the horizontal (X) direction.

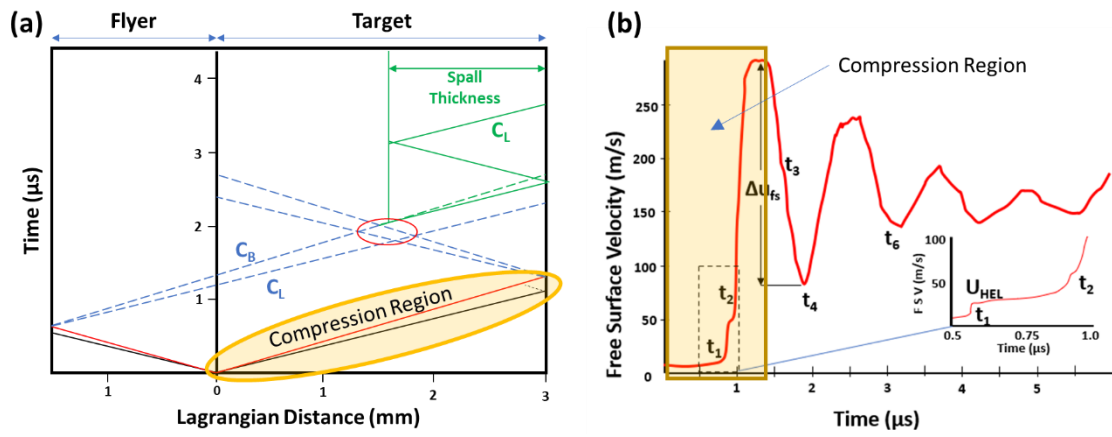


Figure 52: Plots highlighting the initial compressive section that is being simulated. (a) Lagrangian x-t plot. (b) Velocimetry v-t plot.

The material properties of SS316L were applied to each part in the model. The density, elastic modulus, and Poisson's ratio were assigned the values measured in the baseline parallel sample (Chapter 4). The coefficient of thermal expansion and Johnson-Cook damage parameters were obtained from published data [33]. Although the Johnson-Cook model is used in the simulations, the plastic deformation of the structure is not analyzed as part of the results. Only the elastic response is modeled, which provides a simplified approach for qualitative comparison of the pressure wave progression based on the design geometry. While the stresses experienced exceed the plastic yield strength for SS316L, the time scales preclude the observance of onset of plastic deformation. This is a somewhat conservative approach, as plastic deformation of the structure serves as another form of energy damping and consumption within the overall system. Initially, the target is stationary and the flyer has a velocity of 250 m/s normal to the target. The contact between the mating flyer and target surfaces is modeled as "hard" contact normal to the surface and a kinematic contact with finite sliding, to produce a 1D impact force. A mesh size of 0.1mm with CPS4R elements was used to accommodate potential mesh distortion, particularly when evaluating more complex internal geometries.

This material model and simulation setup is consistent for all sub-studies in this modeling and design section of the research.

Simulation outputs that were examined for the study include:

- Contour plots demonstrating progression of the pressure wave with respect to time. These were visually compared as a qualitative measure.
- The velocity values at each time step were plotted with respect to time for the RFS elements.
- The arrival time of pressure wave at Rear Free Surface (RFS) corresponds to the time of peak velocity at the RFS element in the location of interest. Arrival time at elements across the RFS were measured to examine the width of influence caused by the specific geometries.

- The maximum velocity experienced at the RFS element(s) was used as a qualitative number for comparison between samples.
- Scalar values of arrival time and max velocity as function of X-location were also plotted and examined.

Simulation results

Baseline – Reconstruction of Solid sample experiments to validate model

First, a baseline model was constructed with a solid target (Figure 53.a). The purpose of this model was to validate the model setup by comparing the simulation results with those of the earlier baseline impact experiments. The comparator for this was the “parallel” sample used in the earlier Build-Impact Orientation Study (Chapter 4).

This simulation resulted in a pressure wave that progressed uniformly (1D) through the target and arrived at the rear free surface (RFS) approximately 0.6 μ s after impact. The peak pressure generated across the sample was 4.3 GPa and the peak RFS velocity was 225 m/s. Figure 53.b demonstrates these results. The results match well with the experiment data obtained for the baseline (parallel) samples in the Build-Impact Orientation Study (Chapter 4).

Single void – How to model powder filled voids

Before simulations with engineered voids can be used to guide the design stage, a determination is required on how the voids themselves will be modeled. The term “engineered void” in this research is somewhat of a misnomer. These “voids” are not typical void spaces but rather areas of unmelted powder within the solid build.

Three possibilities are considered for methods to represent these “void” areas.

- **Empty void approach.** This is the simplest method. The “void” is represented as a true void in the model, an area with no material.

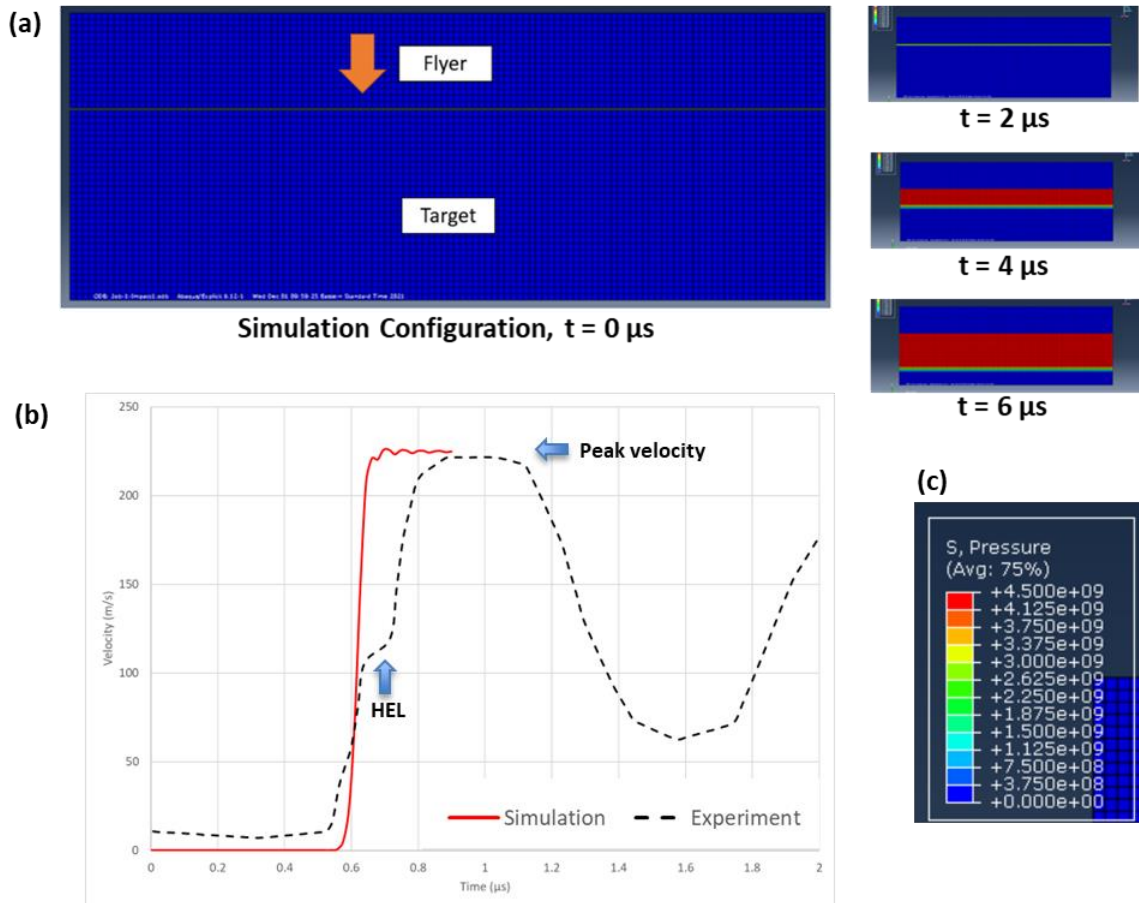


Figure 53: Baseline model details and results.(a) Simulation setup with Flyer impacting stationary target and contour plot showing progression of pressure wave. (b) Simulation result: Velocity-Time plot measured at rear-free surface. (c) Legend associated with contour plot.

- **Bulk continuum approach.** This method models the “void” region as a solid with different material properties assigned to represent the density of loose powder. For this case, surface interactions are essential to ensure that the pressure is properly transferred between the regions. The powder density properties are based on properties found in literature [89].
- **Individual powder particles approach.** This method is the most realistic, yet the most cumbersome to set up and execute. Individual powder particles of relevant size were sketched and distributed within the void space. This initial particle distribution used in the experiments had a range of 0.020-0.050 mm diameter with an average diameter of 0.037 mm. This distribution was achieved using a repeating array that was made up of 45% particles at 0.050 mm, 35% particles at 0.030 mm, and 20% particles at 0.020 mm. Although slightly larger than the typical powder used for experiments, this powder particle model is intended to represent the general size used in the process. If the results of this initial study indicate that further investigation is warranted, then the powder particle size and distribution will be revised to more closely represent the actual conditions. The individual powder particles were manually placed into the void space to maximize the volume of powder for this simulation. Each particle was modeled as having surface interaction properties with each of the neighboring particles. The material properties and mesh assigned to the solid metal were also applied to each powder particle.

The pressure stress contour plots (Figure 54), velocity-time profile (Figure 55), and tabular data sets (Table 12) were collected from each simulation case similar to the baseline case. The results were compared with both the solid baseline simulation, the baseline experiment results (Chapter 4), and the randomly distributed engineered porosity experiment results (Chapter 5). The void space used for this comparison was a 0.500 mm square located at the center of the target in both directions (horizontal and vertical).

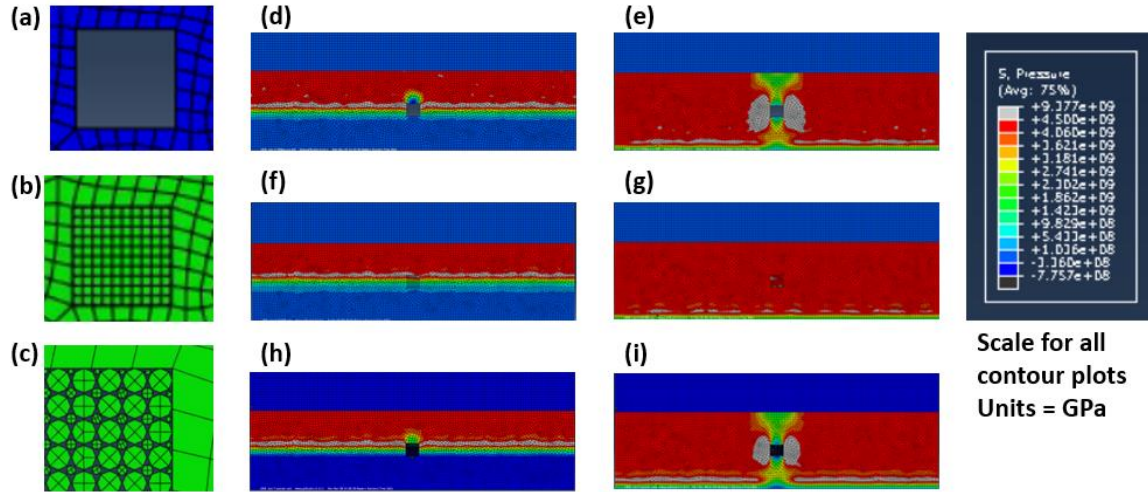


Figure 54: Void model details and contour plot results. (a) Partial mesh view of Empty Void approach, showing void area. (b) Partial mesh view of Bulk Continuum approach, showing void area. (c) Partial mesh view of Individual Powder Particle approach. This image is zoomed in to display the individual powder particles. (d-i) Abaqus contour plots of pressure wave distribution in samples. (d) Empty void approach at 0.3 μs , (e) Empty void approach at 0.6 μs , (f) Bulk continuum approach at 0.3 μs , (g) Bulk continuum approach at 0.6 μs , (h) Individual powder approach at 0.3 μs , (i) Individual powder approach at 0.6 μs .

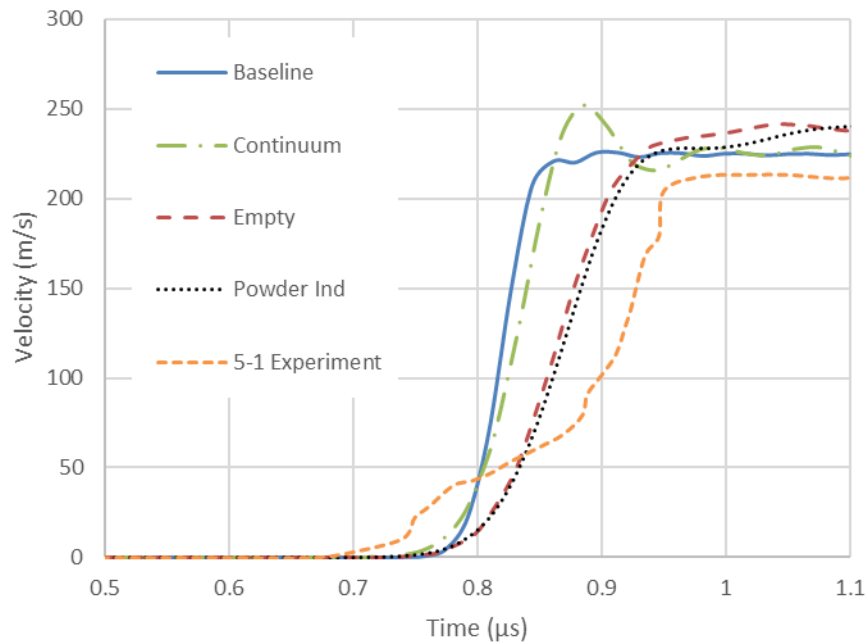


Figure 55: Velocity-time plot of Void model results. Data measured at RFS. The Empty Void and Individual Powder approaches provide very similar results.

Table 12: Comparison of velocity rise to peak for void models and 500-1% experiment

	Baseline	Continuum	Empty	Powder Ind	5-1 Exp.
Slope to peak $\Delta v / \Delta t$ [m/s / s]	2873	2704	1594	1586	1672

The contour plots (Figure 54) demonstrate a very similar progression of the pressure front profile for the empty and individual powder particle models. The continuum model, on the other hand, results in a profile very similar to the baseline case shown earlier.

There is not experiment data for direct comparison of these simulation results. The single void study discussed in Chapter 7 was performed at a greater impact velocity, which effects both the rate of velocity rise and the peak velocity achieved. The best experimental case for comparison is the 500 μm – 1% sample in the random engineered porosity study performed at a similar impact velocity. Although the voids are randomly distributed, the 1% void content sample presents the best likelihood of a single 500 μm void to be present in the measurement path.

The velocity-time plots (Figure 55) provide similar results to the contour plot, with the Empty and Individual Powder cases presenting similar results while the Continuum approach more closely resembles the baseline case.

Since the simulation only models the initial compression phase of the experiment and does not predict the HEL, the slope from the mid-point (50%) of the rise time to the peak is used for comparison with the experiment data (Table 12). These results again demonstrate that the Continuum model closely matches the Baseline case and similarity between the Empty and Individual Powder cases. The Individual powder case also provides reasonable agreement (within 5%) of the value obtained in the experiment data.

A summary of the results from this simulation study indicates that:

- It was observed that the bulk continuum method for modeling powder filled voids results in data very similar to the baseline solid material results and does not match the observations from the Randomly Distributed Engineered Porosity Study (Chapter 5).
- The individual powder particles interact and serve to further dissipate the energy of the pressure pulse. The net result of the powder particle simulation is very similar to the Empty void scenario, although more

conservative. In the case of small voids, this seems to serve as a reasonable approximation for qualitative comparisons.

- The empty void scenario provides a more conservative version of the powder filled reality, as the individual powder particles model exhibited slightly reduced max stress and slightly more delayed pulse arrival time than the empty void case.

The results of this section of the simulation study indicate that using empty void space to represent the powder filled “engineered voids” within the target build provides a reasonable (and somewhat conservative) approximation of the actual powder-filled void behavior. The empty void modeling approach also greatly reduces the model set up and simulation processing time, allowing for a greater number of supporting comparative studies. As such, future simulations in this research will model the “engineered void” spaces within the part as empty space.

Single void simulations

This study examined the effect of placing a single engineered void located at the horizontal center of the target. Two void sizes were examined, 0.200 mm and 0.500 mm square. These sizes coincide with the void sizes explored in the Randomly Distributed Engineered Porosity Study (Chapter 5). The experimental results from that study are used as a comparator for the simulation results. Of particular importance is the effect on the pressure front arrival at the RFS and the peak pressure observed. The results of the Randomly Distributed Engineered Porosity Study (Chapter 5) suggest that large voids slow the arrival of the compressive wave and reduce the applied stress by reflecting or diverting portions of the compressive wave, leading to a nonuniform wave front.

The vertical location of the 0.500 mm void was also varied to study the effect of distance between void and RFS. A total of three vertical locations were used: (1) The vertical center location (centered at 1.50 mm from RFS), (2) An UP position (centered at 2.25 mm from RFS), and (3) A DOWN position (centered at 0.75 mm from RFS).

The contour plots of results (Figure 56) indicate that the presence of a void reflects a portion of the pressure pulse in a manner similar to the reflection at the free surface. The void also tends to reroute the flow stress in a manner analogous to a stone rerouting water flow in a river. This creates a “wake” behind the void that leads to an area of reduced stress. The size of the void matters, as the larger void creates a larger wake. This large wake reduces the pressure stress and velocity, delaying the pulse arrival at the RFS in the area in-line with the void. This supports the Randomly Distributed Engineered Porosity (Chapter 5) experiment data that revealed a slowed arrival time and reduced spall damage for the samples containing larger 0.500 mm voids. The phenomenon was not observed on the samples with smaller, 0.200 mm voids.

The vertical location of the void (i.e. distance from void to RFS) also has an influence on the stress wave propagation (Figure 57). The UP sample experienced a less delayed arrival at the RFS than either the CENTER or DOWN samples. Conversely, the DOWN sample experienced the lowest peak pressure and the most delayed arrival. There appears to be a diminishing effect as the pressure wave progresses away from void and travels to the RFS. The void located very near the RFS somewhat shields the surface in the “wake” zone, while the void located far away has sufficient time to return toward the baseline case. Returning to the earlier river example, this is much like the presence of the stone being unnoticeable once the flow is sufficiently downstream.

In summary, these results indicate that:

- The presence of void reflects a portion of the pressure pulse.
- The size of the void matters as a larger void creates a larger “wake” that both reduces the max stress observed and delays the pulse arrival at the RFS (in the void path).
- The distance of the void from RFS matters as increased distance allows the pulse to escape the wake zone and trend back to the baseline solid condition.

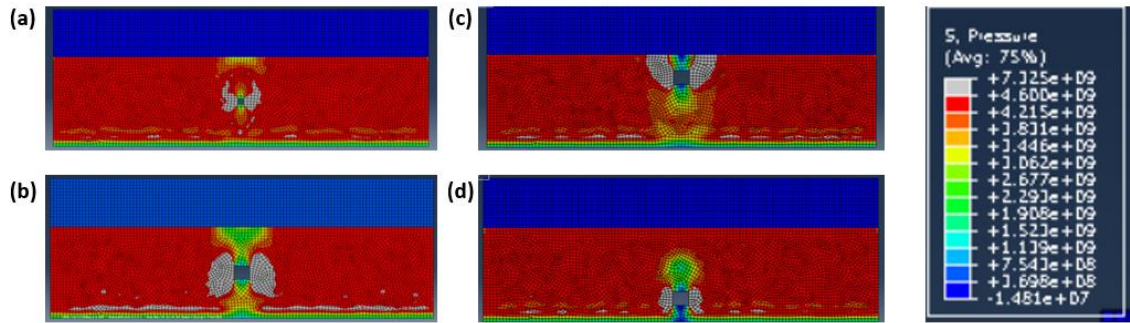


Figure 56: Pressure-time contour plots of Single-void simulations. (a) 200 μm void located at center, (b) 500 μm void located at center, (c) 500 μm void shifted "UP" toward impact surface, (d) 500 μm void shifted "DOWN" toward RFS

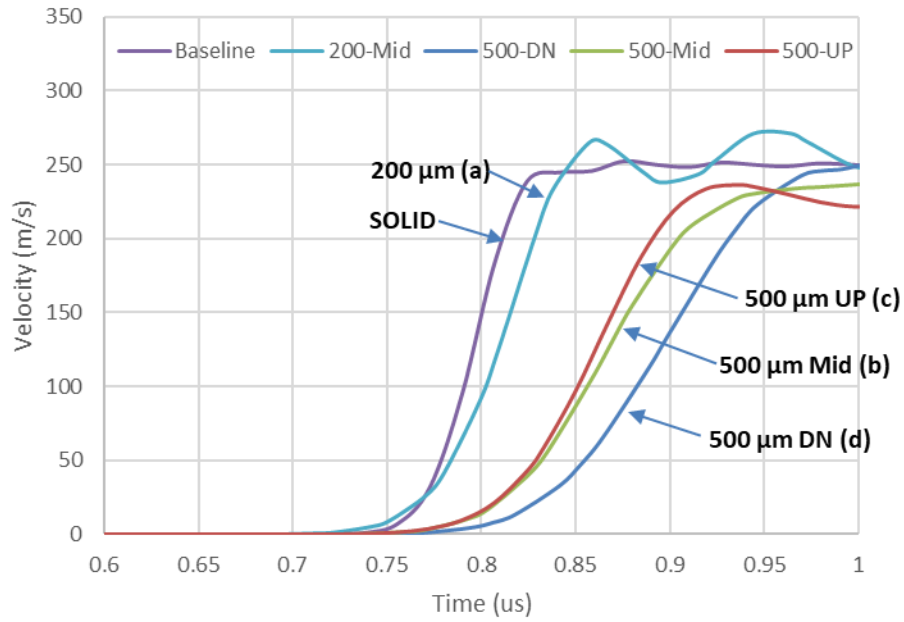


Figure 57: Velocity-time profile comparison of Void size & location. Measurement location is at center of sample, directly in-line with void.

To both minimize the compressive pressure and maximize the arrival delay observed at the RFS, two key factors are: (1) Increase the void size, and (2) Reduce the distance to RFS.

Arrays of multiple voids

Since single voids were demonstrated to influence the wave propagation within a sample, then there should be some critical distance where the behavior transitions between performing as isolated voids and interacting with the wake of adjacent voids. This hypothesis is similar to the basics of simple static fracture mechanics [24]. To analyze this hypothesis, arrays of voids (both vertical and horizontal) were placed within the sample structure using the same plate impact Abaqus model described earlier in this Chapter. Based on earlier simulation results, 0.500 mm square voids were used.

The horizontal arrays of voids (Figure 58) were arranged within the same vertical plane. The vertical location of the voids is at the mid-plane of the sample. The spacing of the voids was varied to examine the range of the wake interaction between collinear voids. Spacing distances of 0.500 mm (1 void length, 1L) and 1.000 mm (2 void lengths, 2L) were used.

It was observed that the effect of the more closely spaced voids (1L) had sufficient overlap to create a single, unified “wake zone” that slowed the pressure wave across a wide area (Figure 59). However, the array with more spacing (2L) demonstrated areas between the voids that reverted back to the baseline condition.

The vertical arrays of voids were arranged in two different configurations: One set as a column of 2 voids, and the other set with the 2 voids staggered in horizontal position. In addition to comparison with each other, the vertical array simulations were compared with the previous “500 μ m Mid” simulation to isolate the contribution of the single void located near the RFS, and the “500 μ m Down” simulation as a reference point.

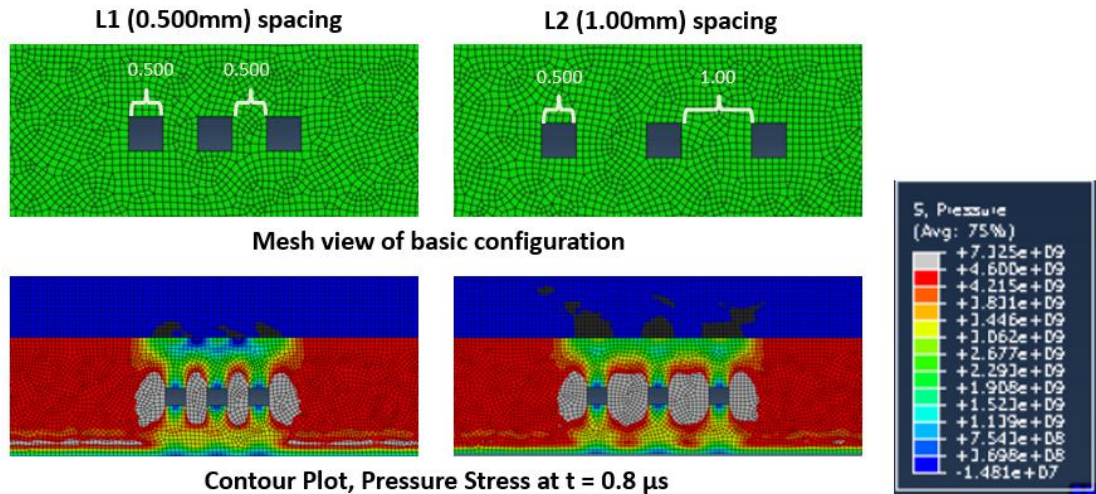


Figure 58: Horizontal array void simulation details and results

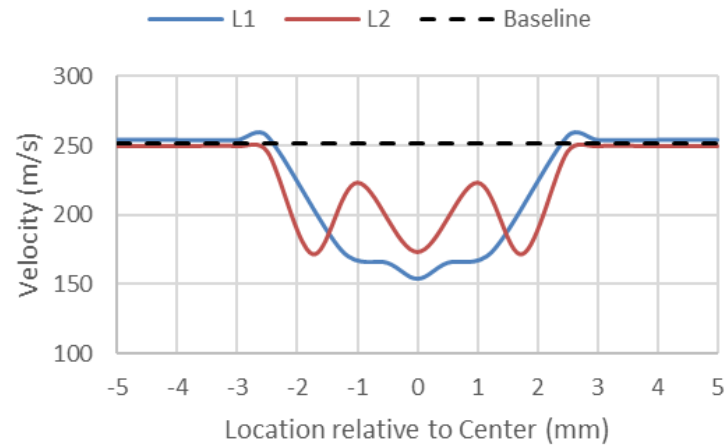


Figure 59: Plot of FS location vs. Velocity (at $t = 0.8 \mu s$, for Horizontal Array of Voids)

The results of the vertical arrays (Figure 60 and 61) indicate that a void located near the RFS creates a delay in the arrival of the pressure wave at the RFS when compared to a void farther away from the RFS, supporting the earlier results, but that a series array of voids in the flow path provides minimal additional benefit to slowing the arrival time of the wave. However, the series array of voids does contribute to further reduce the magnitude of the pressure wave that arrives at the RFS. Furthermore, the staggered series provides a more significant reduction than the stacked series. This is perhaps due to the increase in shear direction from the staggered series having horizontal spacing in addition to vertical spacing. This is an interesting finding in light of the “engineered porosity” results in Chapter 5, as the random arrangement of voids most often results in arrays that are staggered.

In summary, these results indicate that:

- An array of collinear voids can create a “unified front” of reduced pressure if the lateral spacing is sufficiently small.
- An array of voids in series has some reducing effect on the pressure front arrival at the RFS. However, the distance of the void with respect to the RFS has a more significant influence on arrival time.
- Similarly, an array of voids in series does provide some reduction in magnitude of the pressure wave that reaches the RFS.

To both minimize the compressive pressure and maximize the arrival delay observed at the RFS, in addition to the earlier recommendations (1) Minimize the lateral spacing of the voids.

Conclusions

The propagation of the pressure stress wave generated by the plate impact experiment is modeled and analyzed using FE simulations. Of particular concern in this study is the validation of the previous baseline studies and to increase the depth of understanding of the results demonstrated in the engineered porosity study. Specifically, the results of these simulations demonstrate the following:

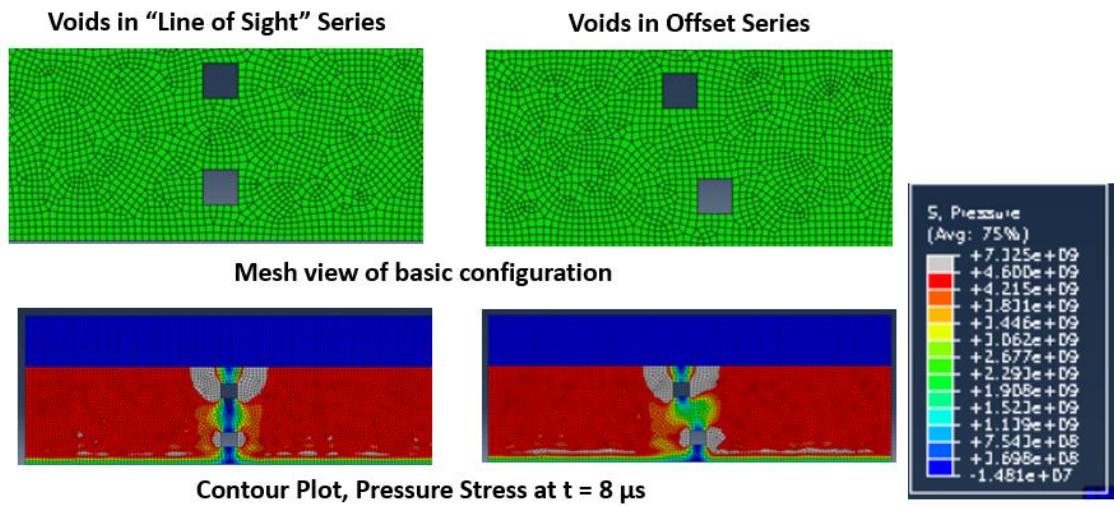


Figure 60: Vertical array simulation details and contour plots of results.

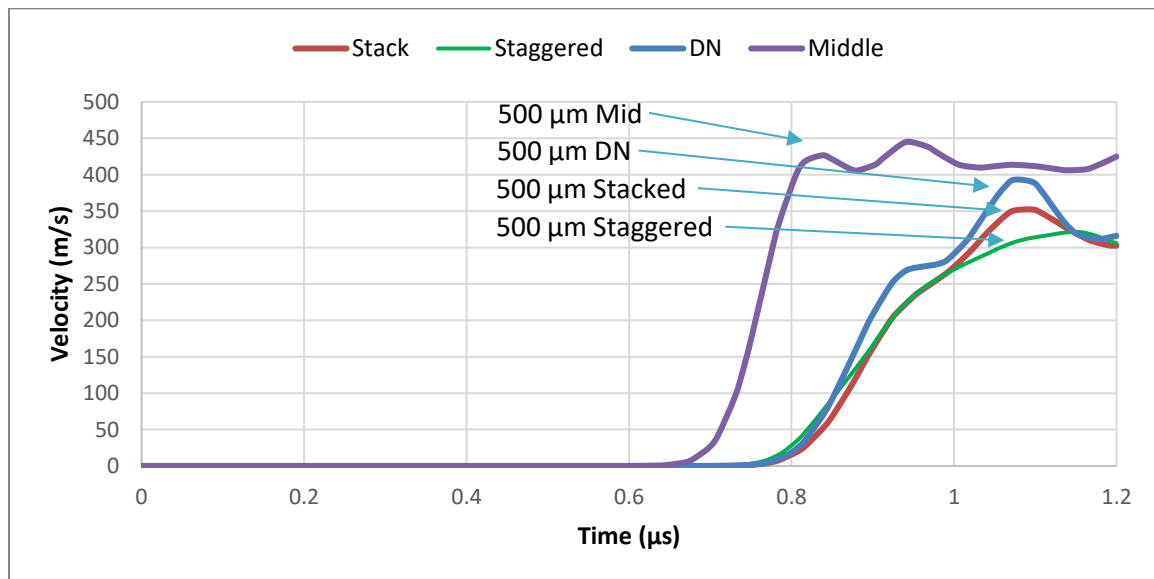


Figure 61: Array simulation velocity-time result plot.

- The proposed simulation successfully demonstrated the results of the baseline experiment (shown in Chapter 4).
- Engineered voids can be simulated to evaluate the influence on the wave propagation behavior. Modeling these powder-filled voids as true void spaces rather than a continuum with different properties is shown to be a reasonable approximation of the powder-filled behavior while utilizing a much less computationally intensive approach. This approach also provides good agreement with the experimental results in Chapter 5.
- The presence of a void reflects a portion of the pressure pulse and creates a “wake” that both reduces the max stress observed and delays the pulse arrival at the RFS in-line with the void. The magnitude of this “wake” is highly dependent on the size of the void responsible.
- As the distance from the void in the direction of wave propagation increases, the influence of the “wake” diminishes and the resulting behavior trends back to the baseline solid condition.
- An array of collinear voids can create a “unified front” of reduced pressure if the lateral spacing is sufficiently small.
- An array of voids in series has some reducing effect on the pressure front arrival at the RFS. However, the distance of the void with respect to the RFS has a more significant influence.
- Incorporating plastic yielding into the model would likely provide a more comprehensive perspective on the wave response. This deformation would provide additional damping. Increasing time scale of the simulations and evaluating the local strain behavior would provide this insight.

Chapter Seven

Single Engineered Void Study

Introduction

This study involves sample characterization, plate impact spallation testing, and post-mortem analysis of AM SS316L samples with single “engineered voids” of varying size. Each “engineered void” was achieved by placing a void space in the electronic CAD files that would not be melted by the laser scan during build fabrication. Each void was a right cylinder disc located at the center of the sample both radially and vertically (see Figure 62).

The samples were characterized both before and after the gas gun impact experiments. The primary data set collected for analysis in this study was x-ray computed tomography (XCT). FE simulations were also performed to help inform the hypothesis. It is hypothesized that these results will show strong correlation between void size and spall behavior, with samples of greater size possessing reduced spall damage in the area of the void and reduction of the shock wave front as evidenced by delayed arrival of the wave at the RFS. This hypothesis is based on the results of the earlier random engineered porosity study and the numerical simulations.

Modeling and Numerical Simulation

A model was developed to simulate the plate impact experiment using ABAQUS finite element analysis (FEA) software. Details of the general model setup are found in Chapter 6. To support the study in this Chapter, the baseline model was modified to include the single engineered void. The interactions, properties, dimensions, and boundary conditions from the baseline simulation were used for this case, as was the focus on elastic behavior only.

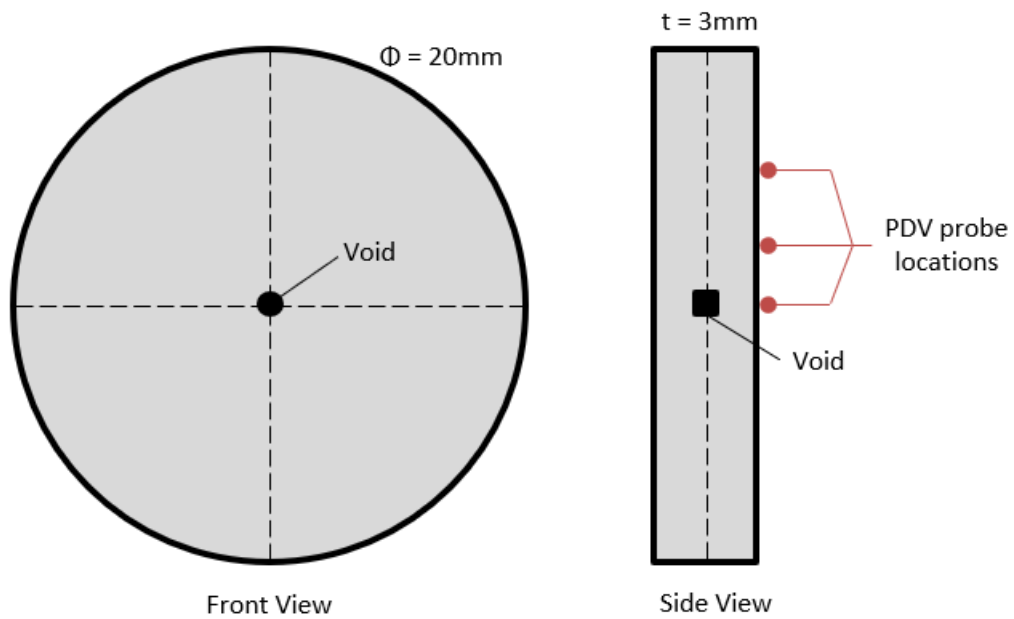


Figure 62: Test sample configuration for Single Pore study

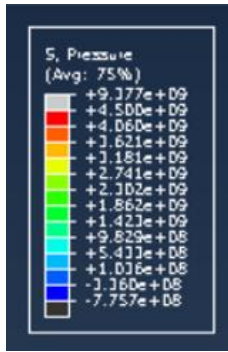
Of primary interest for this study was the variation of pressure front magnitude and wave arrival time across the rear free surface (RFS) relative to the void location. As such, scalar values of both the maximum RFS velocity achieved and the arrival time at the RFS were collected and plotted as a function of location.

The ABAQUS simulation presents variation in both the pressure front that arrives at the RFS and the arrival time, but only in the area directly in-line with the void. Both the pressure magnitude and the wave speed revert quickly back to the baseline condition as the data is collected away from the void location.

Examining the contour plots for the 200- and 500- μm cases compared to the baseline model provides qualitative results that visually demonstrate the behavior (Figure 63). Both void sizes disrupt the continuous wave front. However, in the smaller (200 μm) void case, the wave front comes back together and closely approaches the baseline condition as the wave front reaches the rear free surface. The effect appears similar to that of a liquid flowing around an obstacle, in which a turbulent “wake” is generated but will eventually revert to the steady state condition, given sufficient time and distance.

Looking at the 500 μm void case (Figure 64), the slope to peak velocity is reduced for the points in-line with the void (Points A, B, C). However, moving only 0.25 mm from the edge of the void (Point D), the slope increases back to the baseline slope observed very far from the void (Point F). The peak velocity attained is not reduced by the void, although the peak is delayed as shown in Table 13.

Plotting both the arrival time and peak velocity as a function of free surface location for the 200 μm case provides similar results. When compared to the 500 μm case, the smaller void has even less influence on the peak condition and the affected area is smaller due to the smaller void size.



Scale for all
contour plots
Units = GPa

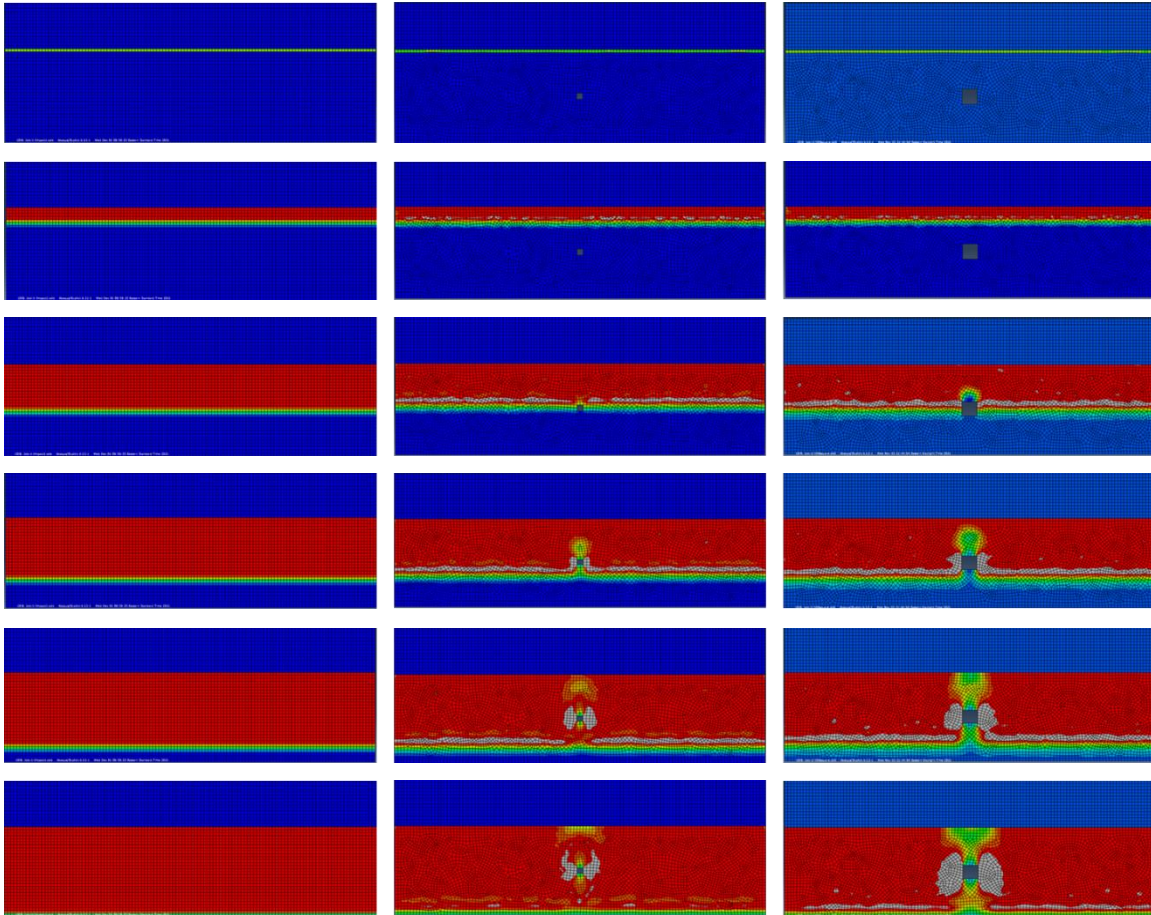


Figure 63: Contour plots of pressure magnitude for Baseline, 200 μm , and 500 μm void simulations. The 200 μm void presents minimal disruption to the pressure front while the 500 μm provides reflection and reduces the pressure stress magnitude in area directly in-line behind it.

Table 13: Peak Velocity (v_{peak}) and Arrival time (t_{arrival}) from simulation at locations in Figure 64

	A	B	C	D	E	F
v_{peak} (m/s)	400.6	389.3	396.5	405.5	397.0	412.1
t_{arrival} (μs)	0.946	0.935	0.881	0.774	0.774	0.774

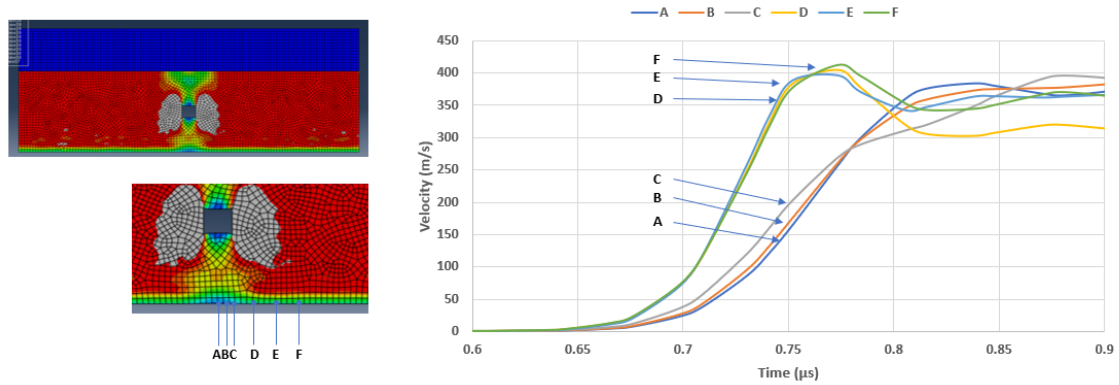


Figure 64: Simulation results for 500 μm single pore experiment.

Experiment

Sample Fabrication

The samples were fabricated using an SLM Solutions, SLM280 machine. The machine specifications and baseline parameters, as described in Chapter 3, are applicable. Each sample was fabricated as a solid cylindrical disc oriented vertically with dimensions of 20 mm diameter by 3.5 mm height. These samples were printed in the final dimensions with minimal excess to better locate the void locations during the impact experiment. Build parameters and processing conditions identical to the earlier samples (Chapter 3 and 4) were used.

The engineered voids were strategically placed in the electronic CAD files that would not be melted by the laser scan during build fabrication. As with the randomly distributed engineered porosity study (Chapter 5), these void spaces do not constitute true “porosity” as each contains unmelted powder rather than completely empty “void” space. The voids were designed as right-cylinders with nominal diameters of 200, 350, and 500 μm and were strategically located at the center of each sample both vertically and horizontally. The height of each void corresponds to its diameter. All samples were post-machined for plate impact testing to the standard test sample requirements outlined in Chapter 3.

Material Feedstock:

The 316L SS powder used to fabricate the samples was gas atomized powder provided by SLM Solutions. The chemical composition and particle size distribution of the powder is consistent with that listed in Chapter 3.

Physical Property Characterization:

As-built samples were characterized before the gas gun impact experiments. Post-mortem characterization was planned for soft-recovered samples after the experiment, however, excessive damage to the samples during experiment prevented it. The pre-test characterization consisted of bulk density and ultrasound wave speed measurements, moduli calculations, and XCT imaging.

Non-destructive evaluations were performed on each tested sample. No analysis requiring cross-section was completed for this study. The results of the pre-test characterization were compared with each other and against a fully dense control sample (of the same build orientation) as a baseline (Figure 65).

The bulk density of the samples shows a trend of decreasing density corresponding to the increase in void size. This matches the intuitive conclusion and the data trends demonstrated in earlier Chapters that the density of the powder filled volumes is less than the solid metal volume.

The measured wave speeds for the single void samples are all slightly (could be considered insignificantly) faster than the baseline case but show little variation between the samples of different void size. A void within the solid sample reflects a portion the wave, causing it to return to the sensing location ahead of the majority of the remaining pulse. This reduces the time step for the return signal slightly, increasing the calculated wave speed. The sensing probe has an active diameter of ~12 mm and the void sizes are 0.200-0.500 mm, making the void area less than 1% of the total probe sensing area. Further comparing the elastic wave speeds of these single void samples with the values obtained for the random samples (Chapter 5), it can be seen that the measured wave speeds are similarly within a fairly consistent range that is slightly greater than the baseline.

The XCT image data was used to validate the location and size of the internal void in each sample, as prescribed by design. Two-dimensional (2D) images of individual slices were collected and analyzed using FIJI/ImageJ software. Post-test XCT was intended to examine the spall damage relative to the engineered voids at locations across the sample beyond that observable at the simple cross-section, but as mentioned previously the samples were not able to be analyzed.

The approximate location of both radial and longitudinal center was verified (Figure 66). The nominal size of the voids was verified to match the intended size prescribed in the build file. Worth noting is that each void demonstrates a “sag” on upper edge of void due to process limitations. This “sag” is more pronounced in the larger void case (500 μm).

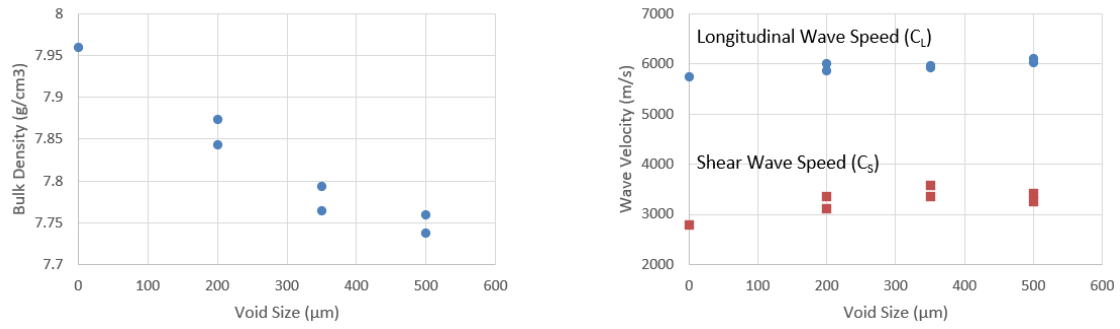


Figure 65: As-built properties of single void samples. (L) Plot of bulk sample density as function of void size. (R) Plot of elastic wave speeds as function of void size.

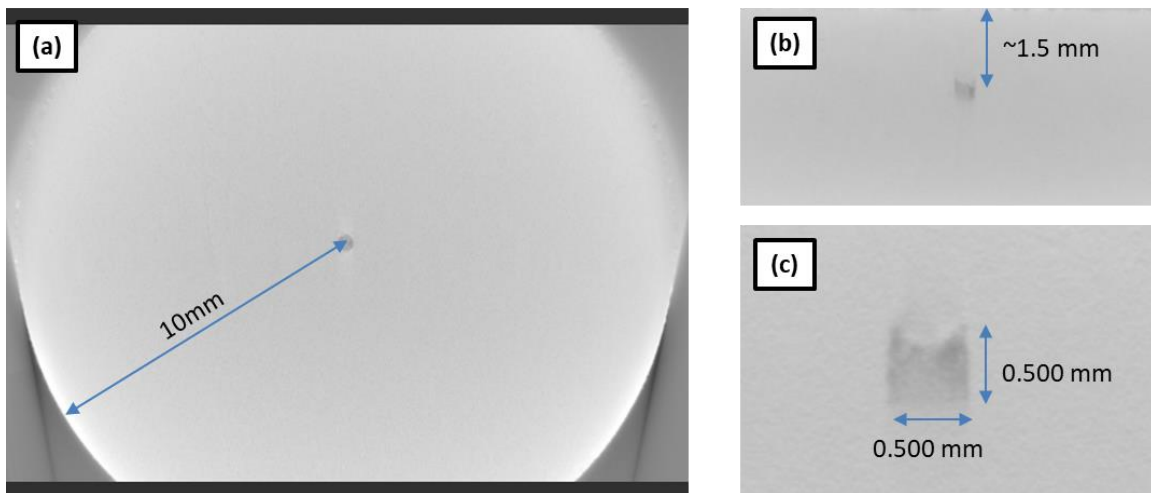


Figure 66: XCT images of 0.500 mm Single Void sample. (a) X-Y plane slice showing center location of void. (b) X-Z plane slice showing vertical position of void. (c) X-Z plane slice showing approximate void dimensions.

Table 14: Wave speeds for Single pore study

Sample	Density (g/cm ³)	C_L (m/s)	C_S (m/s)	C_B (m/s)
200 um single	7.84	6003.7	3357.6	4584.0
350 um single	7.79	5921.7	3580.9	4239.0
500 um single	7.76	6099.5	3259.5	4799.8
AM control	7.82	5814.9	3025.5	4648.5
Wrought	7.92	5775.0	3136.4	4498.3

Due to some of the process limitations associated with LPBF, the void dimensions are not exactly precise. At the vertical edges, there is a tendency for powder particles that are intended to be unmelted by the design to fuse with the melted regions. The top boundary of the void attempts to be built on top of loose powder, resulting in the “sag” observed in Figure 66.c. Considering the general shape of the melt pools and the reality that each pass penetrates beyond the current layer, the characteristic geometry for the upper surface of the voids will likely not be a sharp straight line. This is like the void discussion in Chapter 5.

Plate Impact Testing

The plate impact experiments for this study were performed using the 80mm diameter x 7.6m length single-stage light-gas gun at the Georgia Institute of Technology. Details are described in Chapter 3.

For this study, all flyer plate impact experiments were performed with impact direction (ID) parallel to build direction. Following a recommendation from the gas gun impact test subject-matter-experts at Georgia Institute of Technology, an increased impact velocity of 400 m/s was used (rather than 250 m/s). Increasing the impact velocity helps provide a stronger response signal for collecting the velocity data at multiple discrete locations on the sample. For these tests, a relatively newer technique for PDV data collection known as multiplexing was used. Multiplex PDV arrangements allow for collection of up to 20 discrete probe signals simultaneously. Using this technique, all three of the single void samples and the baseline control sample could be examined in a single shot.

For each test sample, PDV probes were placed at three separate locations to evaluate the velocity profile relative to distance from the engineered void. A schematic showing the placement of these probes and voids is shown in Figure 67.

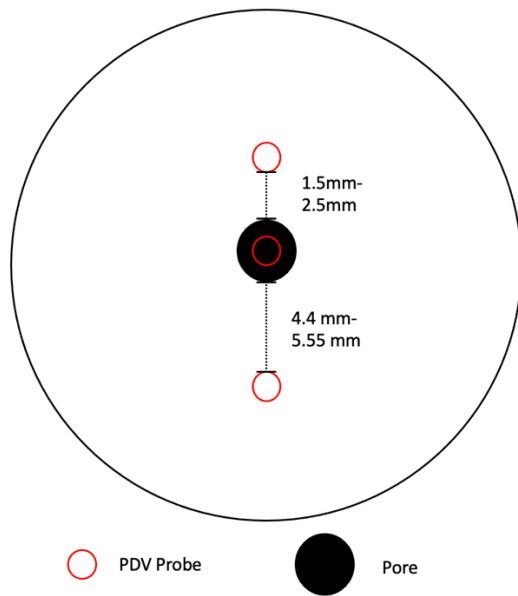


Figure 67: Schematic of PDV and Void Layout

Results

Plate Impact Experiment

Consistent with literature and earlier studies in this research, the AM SS316L control sample had higher HEL and spall strength than wrought (Table 15). Little difference was observed in comparing the single void samples to the control sample. All exhibited very similar rise time, HEL properties, pulse duration, pullback velocity, and spall strength (Figure 68). Very little variation was observed with respect to the probes at different locations within each sample (Table 15 and Figure 68).

The 350 μm Far probe returned a weak signal that was not able to be used for comparison with the others. The 350 μm Center probe and 500 μm Center probe exhibited much distortion in the signal data. The 350 μm Center probe and the AM Control 3 probe each had too much distortion in the signal data over the initial rise to peak velocity to accurately identify an HEL velocity and, thus, the corresponding HEL strength. However, those probes did provide the pullback velocity (Δu_{fs}) data needed to calculate a spall strength value. The 500 μm Center probe signal was distorted across the full range to obtain either HEL or spall strength.

The experimental results provide reasonable agreement with the simulation results (Figure 69). The 200 μm single void case (Figure 69.a) presents similar rise to peak velocity and plateau behavior between the experiment and simulation data. This holds for both the center location (probe placed at void) and the “Near” location, approximately 1.5 mm from center. For clarity, additional data points were not displayed. The “Far” probe closely matches with the “Near” data, and the simulation data reverts to the baseline case beyond the 1.5 mm location.

Table 15: Experiment data for Single Pore Study

Sample	HEL (m/s)	Δu_{fs} (m/s)	σ_{HEL} (GPa)	σ_{spall} (GPa)
Wrought	36	123	0.823	2.192
AM Control 1	76	159	1.729	2.891
AM Control 2	63	165	1.433	3.000
AM Control 3	n/a	156	n/a	2.837
200 μ m Center	76	151	1.789	2.718
200 μ m Near	81	154	1.907	2.759
200 μ m Far	55	150	1.295	2.696
350 μ m Center	n/a	157	n/a	2.593
350 μ m Near	56	146	1.281	2.411
350 μ m Far	n/a	n/a	n/a	n/a
500 μ m Center	n/a	n/a	n/a	n/a
500 μ m Near	51	169	1.207	2.247
500 μ m Far	54	147	1.278	2.737

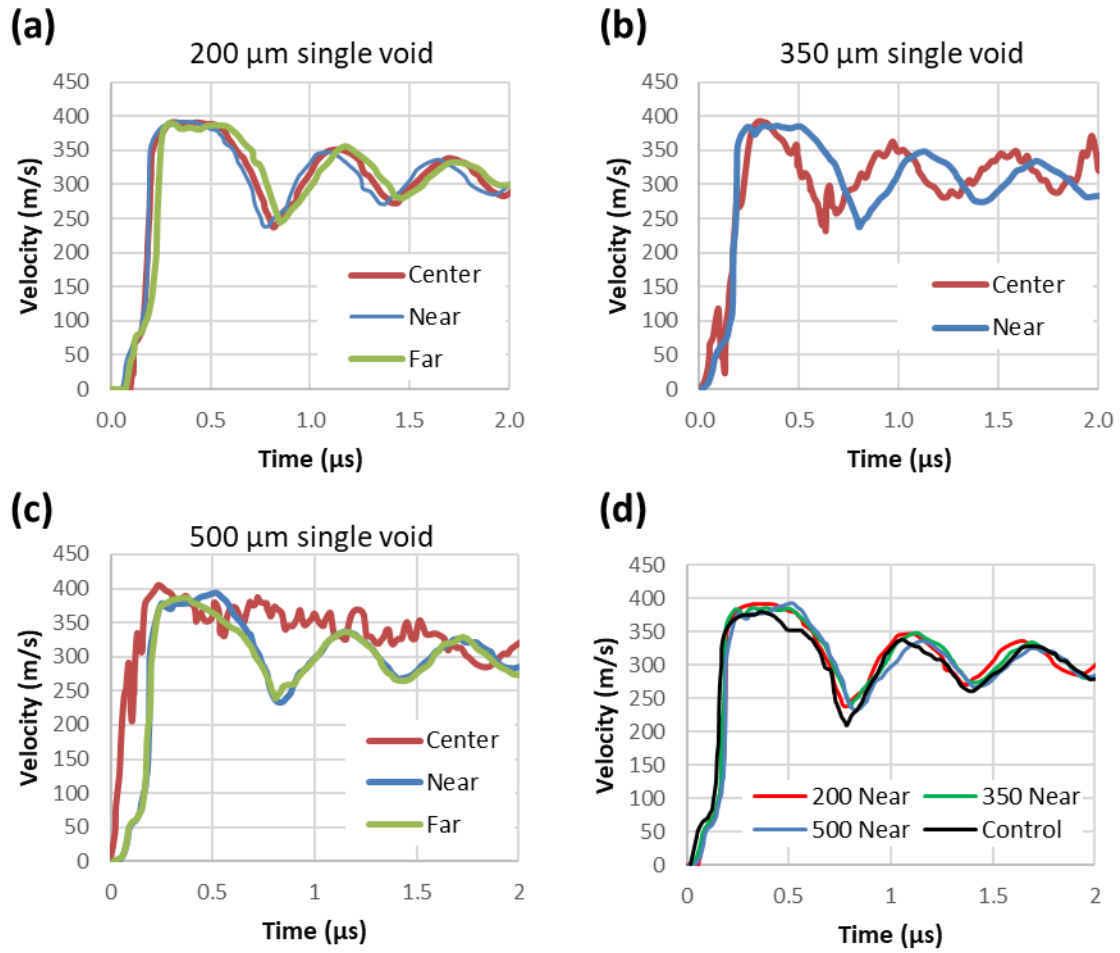


Figure 68: Velocity profiles for single void plate-impact experiment. (a) 200 μ m single void, (b) 350 μ m single void, (c) 500 μ m single void, and (d) Comparison of "near" probe on each to Control.

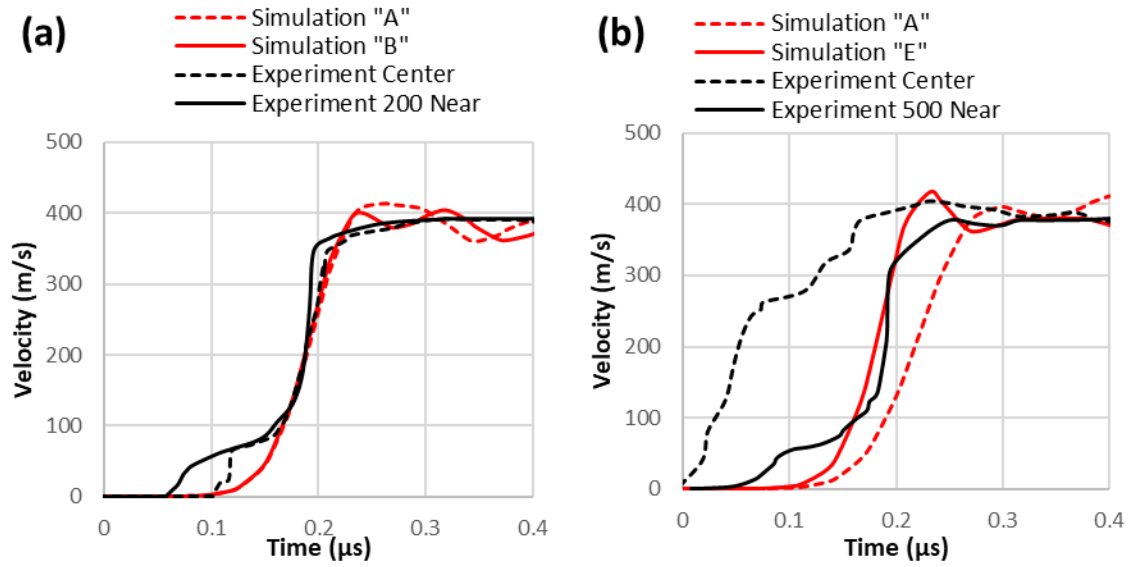


Figure 69: Comparison of Simulation and Experiment results. (a) Velocity-Time plot of 200 μm single void case. (b) Velocity-time plot of 500 μm single void case.

The 500 μm case similarly presents agreeable results for the “Near” probe (Figure 69.b). However, the center probe results differ greatly. The simulation presents a velocity rise that is both delayed and at a reduced rate of rise compared to the “Near” probe, as would be expected based on the results from the earlier Random Porosity results. The “Center” probe from the experiment was heavily distorted and did not provide reliable data to determine the HEL or spall strength, so the results from that probe is not a reliable comparison.

Post-mortem Characterization

All three of the single void samples, along with the soft-recovered samples, tested at 400 m/s impact velocity experienced full spall fracture (i.e. the resulting sample was fractured into two pieces). As such, the samples were not in condition to cross-section and perform post-mortem analysis.

The extra metal that appears outside the sample edge (Figure 70) is from the sample holder plate. Secondary impact of inside the catch chamber caused the sample to re-compress and pinch a section of the sample holder. The sample was very difficult to fully remove from the holder.

Discussion

Differences in Numerical Model results vs. Experiment

The simulations indicated a reduction in both the speed and magnitude of the shock front but only in the region directly beyond the void line-of-sight. The simulation results for the 200 μm void presented an insignificant change compared to the baseline, while the 500 μm void case provided a more observable reduction in both the speed and magnitude of the compressive pressure wave front. However, this influence dissipated quickly in the regions outside the void’s direct line-of-sight.



Figure 70: Post-mortem image of 200 μm single void sample. Complete spall fracture.

The experimental results presented no significant difference in the velocity profile of the single void samples when compared to the baseline, especially at the locations outside the void line-of-sight. While the center probe for the 200 μm sample showed an insignificant change from the baseline condition, the center probe for the 350 and 500 μm samples returned a weak, distorted signal.

Based on the simulations in this study and analogous observations of fluid flow around obstacles, the larger voids may be a contributor to the resulting signal.

The ability to examine very discrete locations using small mesh sizes is helpful in using a numerical simulation to better understand the problem, but sometimes the available mesh resolution produces results that cannot be verified through experiment due to the physical constraints of the sensing and test equipment. In this study a mesh size of 0.100 mm was used, but the maximum resolution of the PDV probes used to measure the free surface velocity is 0.200-0.300 mm. In future studies, the mesh size should be verified to meet the potential resolution of the measuring instruments if the data sets are to be compared.

Results from single void compared to many voids

In comparing the results of this study with the earlier (Chapter 5) study involving distributions of random porosity, there is a much different behavior observed. This bears the question, “Why are these differences observed?”. The simplest answer to that question stems from the hydrodynamic treatment of the shock front that forms the basis for shock theory [4]. Examining the shock behavior in this manner requires a few assumptions that lead to the solid material behaving as a fluid in motion.

When a fluid in motion meets an obstacle, the fluid is routed around that obstacle. If a single obstacle is presented, then the fluid experiences a temporary disruption that results in mostly laminar flow that is overcome in short order. If the obstacle is large enough, then the disruption may lead to a more turbulent flow condition near the obstacle but eventually revert back to the steady flow at a sufficient distance downstream. An arrangement of multiple obstacles, however,

will present a much more complex situation. The disruption caused by many obstacles causes complex reflection, refraction, and interactions between competing flow streams, leading to very turbulent behavior.

Under the hydrodynamic treatment of shock fronts, a similar behavior can be expected from the shock wave propagation through a solid material. As demonstrated by these studies, a single void has little influence on the wave progression, while a distribution of many voids leads to an overall slowing of the wave front through the material.

Conclusions

The spall response for SS316L AM samples fabricated with single engineered voids strategically located is examined through execution of numerical simulation and light gas gun plate impact experiment. The AM technology used to fabricate the samples is LPBF. In summary, it was observed in both simulation and experimental results that the presence of a single, internal powder-filled void has minimal influence on the spall response of AM material.

Numerical simulations suggest that there is a “wake zone” surrounding a void that influences the shock wave propagation. However, this zone is relatively small – constrained to the area directly in line-of-sight with the void. Both the elastic wave properties and the shock wave propagation behavior quickly revert back to the baseline case for locations elsewhere in the sample. Plastic yielding was not included in that analysis, but would serve as another form of energy damping and consumption within the overall system.

This study demonstrates that a single powder-filled void (up to 500 μm) within a large volume (comparative to “semi-infinite” assumption) has relatively little impact on the overall shock wave propagation. This result is demonstrated in both the elastic and shock wave behavior.

Chapter Eight

Engineering Design study

Introduction

This study involves finite element analysis (FEA), engineering design, sample fabrication and characterization, plate impact spallation testing, and post-mortem analysis of SS316L samples fabricated using LPBF. This focused study was based on the findings of the initial orientation, random void distribution, and single void studies to further utilize purposeful engineering design to reduce the propagation of the shock wave (by slowing the wave velocity and reducing the magnitude of the associated pressure front) through the material. The utilization of internal features, a capability unique to AM, is the primary goal of the study.

FEA was utilized to develop optimized designs. A sequential approach was used to apply the basic principles of shock impact testing to develop designs that maximize the time required for the shock front to reach the rear free surface (RFS) of the sample, minimize the pressure front applied, and take greater advantage of the capabilities and limitations of the LPBF process.

The samples were characterized both before and after the gas gun impact experiments. The data sets collected for analysis include elastic wave speed evaluations, LOM and XCT.

It is hypothesized that the results will demonstrate:

- That internal void features can be used to disrupt the shock wave propagation which will both reduce the pressure front applied to the RFS and extend the arrival time.
- The geometric orientation, not just the volume fraction of void space, will have an influence on the level of disruption for the shock wave propagation in the samples.

Modeling and Simulation

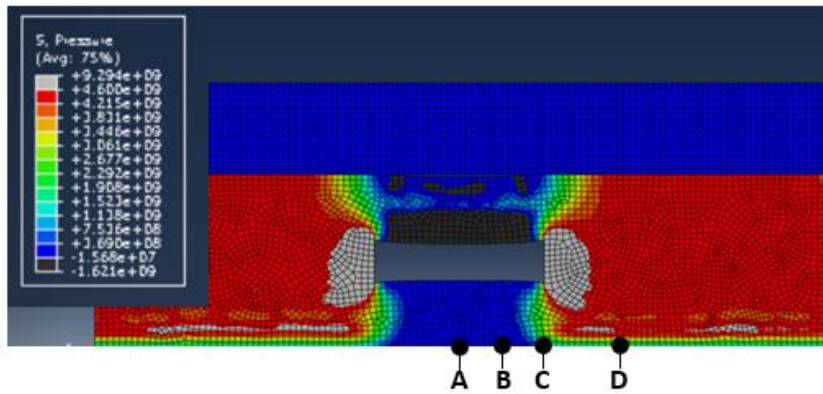
The ABAQUS model presented in Chapter 6 was used to evaluate the resulting pressure wave behavior in samples with several iteratively constructed designs. For each case, the baseline model was used with the specific engineered features designed into the target. The resulting velocity magnitude and arrival at the rear free surface was assessed for each case.

Single Large Void

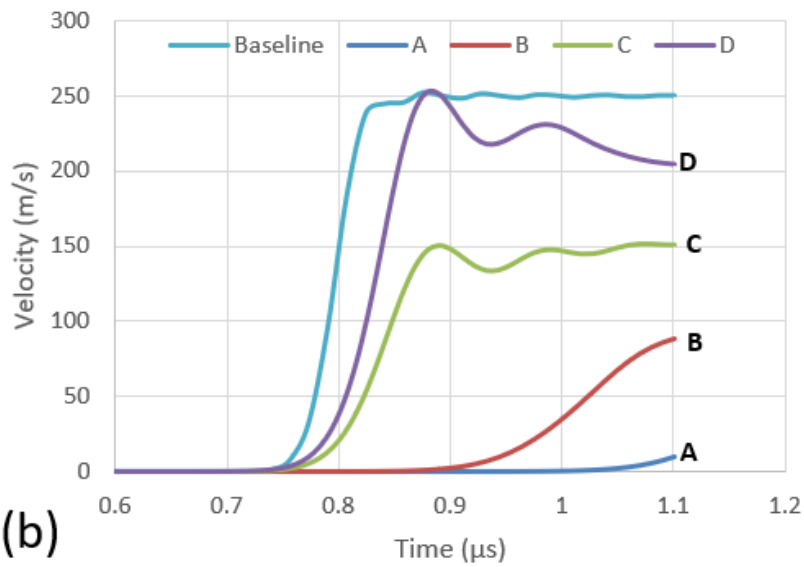
A free surface provides the case for maximum reflection of the wave front. A simple way to model this within a structure is to place a very large void space within the sample. To demonstrate this phenomenon, a single large void was placed inside the target for the baseline simulation model (Chapter 6). The void had a width of 3 mm and height of 1 mm within the 15 mm wide by 3 mm thick sample (as shown in Figure 71).

The region behind the void was observed to experience extreme reduction in pressure and a major slowing of the pulse, resulting from almost full reflection of the wave front by the large void. No rise to a peak stress was observed in the area directly shielded by the large void. As the location moves away from the center of the void, the velocity-time profile begins to revert back to the baseline case result.

This demonstrates that a large internal free surface will reflect the shock pulse. However, this actual geometry could be unfavorable for practical use as it would (1) have a greatly reduced static loading strength and (2) present limitations in building on most current LPBF systems due to the large overhang area. Still, the major take-away from this simulation is that a large void space can be used to reflect the wave pulse similar to the behavior at a free surface.



(a)



(b)

Figure 71: Results of Single Large Void simulation. (a) Contour plot of Pressure at time = 0.9μ s. (b) Velocity-time plot of different locations across free surface.

Internal Lattice (X patterns)

A feature that has been explored greatly in LPBF is the use of lattice structures to reduce part weight while still providing the general shape. Examining lattice options using the simplified 2-D ABAQUS model, the geometry reduces to a simple “X” pattern (Figure 72 and 73). In this study, several lattice designs with varying strut size and void space content were evaluated. To maintain relevance to the earlier studies, void sizes of 0.500 and 0.200 mm were used. Each void was considered as a square rotated at 45°. The strut sizes used were 0.500, 0.250, and 0.100 mm. Each unique lattice design was inserted at the center of the target sample with dimensions of 1 mm (H) x 3 mm (W).

It was observed in the simulations that reducing the strut size results in decreasing the pressure stress and velocity, thus delaying the arrival at the rear free surface. It was also observed that reducing the void size results in a more uniform region of reduced pressure and speed at the rear free surface with less variation. Since the overall void region dimensions are maintained constant, reduced void size correlates to an increased number of voids. This creates an increased number of barriers within the flow path, which increases the number of reflection/refraction opportunities. This is consistent with the earlier studies (Chapter 5 and 7) that suggested a slowing of the wave front associated with increased quantity of voids.

Hexagonal Honeycomb (Final Design)

Based on literature, findings of earlier studies, and simulation results, a set of designs was developed to examine a unique structure that takes advantage of the LPBF capabilities. The use of hexagonal honeycomb structure in engineering applications is well documented in existing literature [90] for its lightweight construction and energy absorption capacity. Under out-of-plane compression, additively manufactured hexagonal honeycomb structures have demonstrated similar yielding and failure characteristics to that of solid cylinders [91] [92].

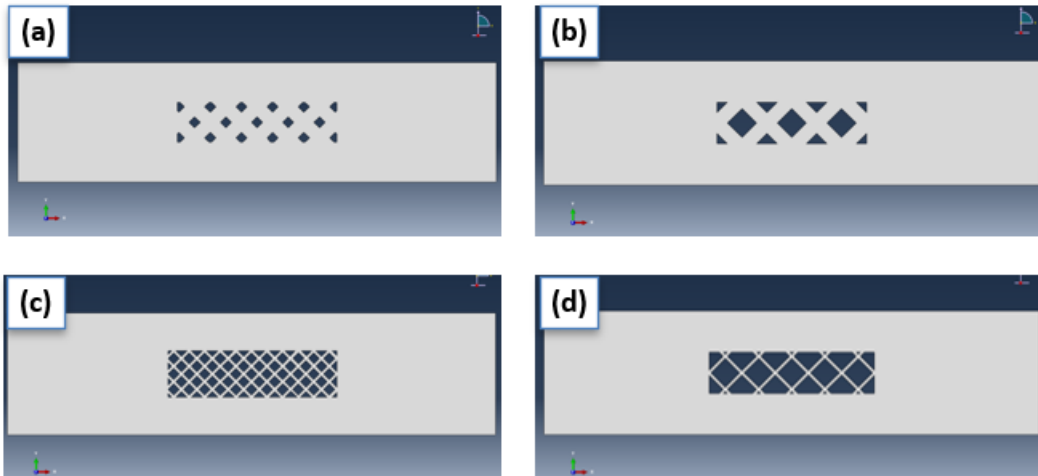


Figure 72: ABAQUS models of 2-D "X pattern" that represents lattice. All configurations are "Void Size" x "Member Size". (a) 0.200 mm x 0.500 mm, (b) 0.500 mm x 0.500 mm, (c) 0.200 mm x 0.100 mm, (d) 0.500 mm x 0.100 mm.

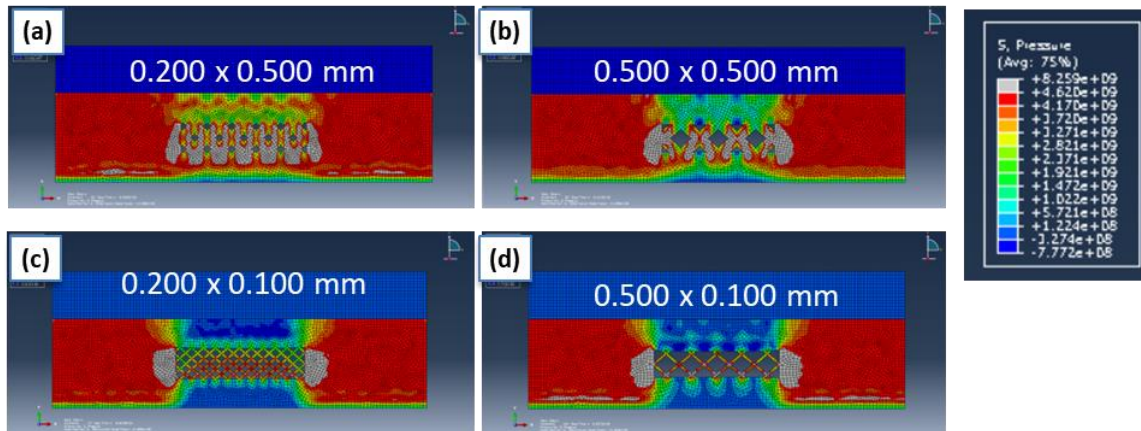


Figure 73: ABAQUS simulation results of 2-D "X pattern" that represents lattice.

Anisotropic mechanical properties have also been observed for hexagonal honeycombs under quasi-static in-plane loading, including initial yield strength [93] and crushing deformation modes [94]. However, under dynamic loading, while the unit cell level deformation and stress response differ [90], the macro-scale crushing deformation is similar for both X- and Y- load directions [95].

This set of engineered designs uses a hexagonal honeycomb as the base structure. Three sets of samples were examined with the hexagonal honeycomb structure oriented in different configurations.

A hexagonal honeycomb structure maximizes void space in comparison to a simple “X” shaped lattice structure (from a 2-D perspective). Because of the intersecting angles, it is readily expanded into a repeated two-dimensional array and is easily modeled in 2-D space. Hexagonal honeycomb structures translate well to physical fabrication using AM, as there are no significant overhangs or steep angles. Also, the natural configuration of a hexagon allows for distinct differences based on orientation (angle face vs. flat face vs. normal to structure).

For this study, a base hexagonal honeycomb structure was examined. The base geometry was a regular hexagon (meaning six sides of equal length) inscribed in a 0.500 mm diameter circle with member thickness of 0.100 mm. Three different orientations were compared (as shown in Figure 74): Horizontal Side, Horizontal Top, and Vertical. This terminology refers to the honeycomb orientation relative to impact. All samples are intended to be fabricated with the impact face (top) of the disc as the XY plane and built in the Z-up orientation. The Horizontal Side honeycomb structure is oriented with the honeycomb facing the horizontal (XZ or YZ) direction and the hexagon “side” facing the impact direction. The Horizontal Top structure is similarly orientated in the horizontal plane, but the hexagon “top” (or angled face) is facing the impact direction. The Vertical honeycomb is oriented with the honeycomb structure vertically facing the impact (XY) plane.

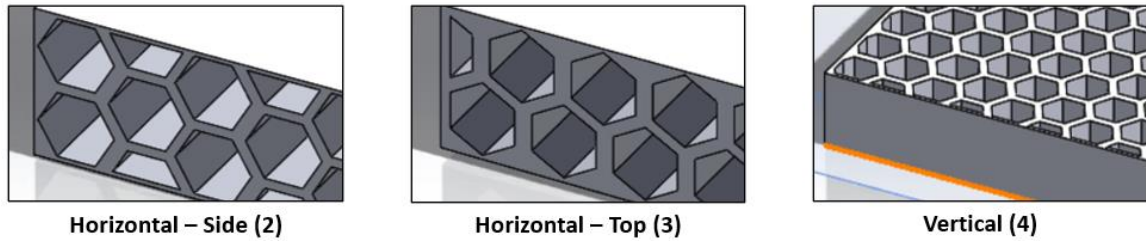


Figure 74: CAD renderings of hexagonal honeycomb arrangements examined in this study.

Like the previous designs in this section, each of the honeycomb structures were inserted at the center of the target sample occupying a volume with nominal dimensions of 1 mm (H) x 3 mm (W). Image analysis of the 2-D cross section for each estimates the void fraction of each sample section to be as follows: Horizontal-Side, 66%; Horizontal-Top, 59%; and Vertical, 82%. It is important to also note that the void fraction in the Vertical sample is somewhat less accurate as the actual 3D volume will include the member material at various cross-sections.

All three cases are expected to present increased delay of the pressure front, based on the reflection resulting from increased void space. The difference in how the different samples will behave is controlled by the geometry with respect to loading direction. Hexagonal honeycombs (and all polygon structures) go through several stages of failure: elastic yielding, followed by a transition to plastic deformation (which may be primarily at the hinge points or buckling of the vertical members), then unit cell collapse takes place until densification begins to take place, at which point the behavior approaches that of solid material. Due to the time-scales involved, the analysis for this loading condition will focus only on the elastic-plastic yielding. Relations exist for the stress required for transition from elastic to plastic behavior for each stress direction.

$$(\sigma_{pl}^*)_1 = \frac{2}{3} \sigma_{YS} \left(\frac{t}{l} \right)^2 \quad (13)$$

$$(\sigma_{pl}^*)_2 = \frac{1}{2\cos\theta} \sigma_{YS} \left(\frac{t}{l} \right)^2 \quad (14)$$

$$(\sigma_{pl}^*)_3 = 5.6 \sigma_{YS} \left(\frac{t}{l} \right)^{\frac{5}{3}} \quad (15)$$

Since the material yield strength, member thickness, and member length are constant for all orientations, the equations have been normalized for simplified comparison.

$$(\sigma_{pl}^*)_1 = 0.667 \sigma_{YS} \left(\frac{t}{l} \right)^2 \quad (16)$$

$$(\sigma_{pl}^*)_2 = 0.577 \sigma_{YS} \left(\frac{t}{l} \right)^2 \quad (17)$$

$$(\sigma_{pl}^*)_3 = 16.36 \sigma_{YS} \left(\frac{t}{l}\right)^2 \quad (18)$$

These resulting relationships indicate that the Horizontal-Side (σ_2 -direction) will transition to plastic yielding first, followed by Horizontal-Top (σ_1 -direction) and then Vertical (σ_3 -direction). As a “less stiff” structure, the Horizontal-Top sample should also provide the greatest damping of the wave progression. As shown in Figure 75, the Horizontal-Side geometry has no vertical members, so it will deform completely via “plastic hinge”. The Vertical geometry has no angle or normal members, so it will deform completely via plastic buckling. The Horizontal-Top geometry has both vertical and angled members, so it should exhibit a combination of plastic hinge and buckling. This supports the results in Equations (16-18).

Based on the relative elastic-plastic relationships shown here and the Chapter 4 results that show similar directional behavior for both quasi-static and dynamic (plate-impact) loading, it can be expected that the vertical honeycomb will have the least influence on the pressure front as more of the energy will be directly transferred and the Horizontal-Side honeycomb will provide the most damping.

The simulation results (Figure 76) indicate that all three arrangements delay the wave front arrival at the rear free surface and reduce the maximum free surface velocity observed. As seen in earlier simulations, the affected area is restricted to that in line-of-sight with the honeycomb structure. The Vertical and Horizontal-Top cases present similar behavior, while the Horizontal-Side case exhibits an even more delayed arrival time and a further reduction in the peak velocity.

These results agree with the analytical conclusion that the Horizontal-Side configuration will allow increased flex at the member connections that will serve as hinge points to transfer more of the energy to the shear direction. The vertical members of the Vertical and Horizontal-Top configurations directly allow energy flow as the structure is more rigid in the simulated stress case for those configurations.

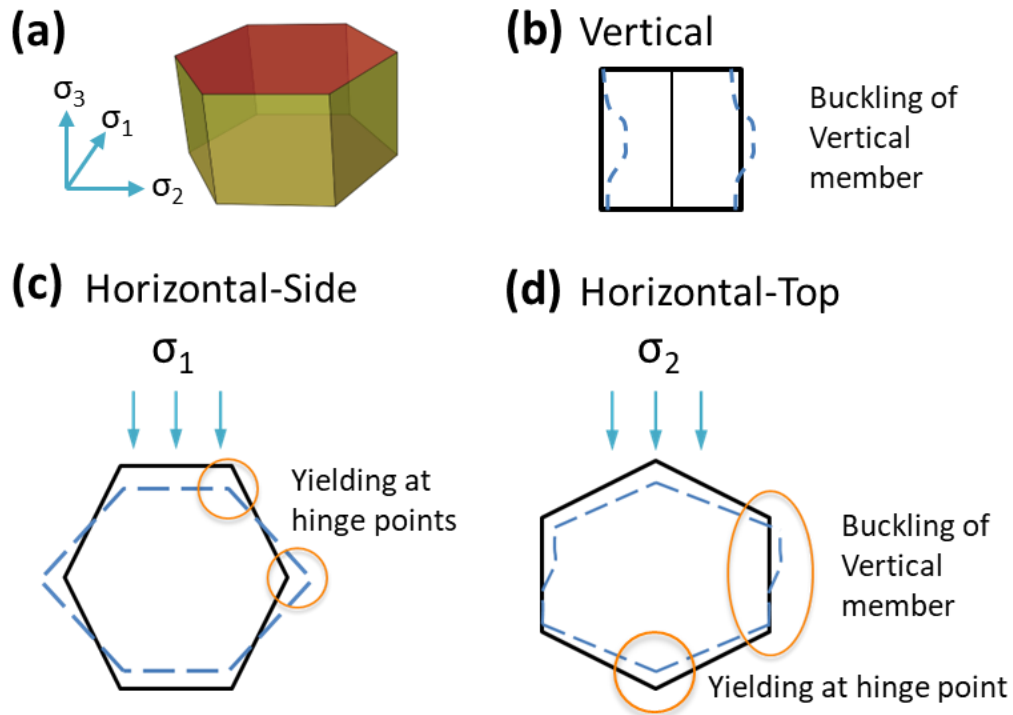


Figure 75: Deformation mechanisms in hexagonal honeycomb structures. (a) Isometric view showing relative orientation of applied stress. (b) Vertical configuration showing buckling of vertical member. (c) Horizontal-Side configuration showing yielding at the hinge points. (d) Horizontal-Top configuration showing combination of buckling and hinge.

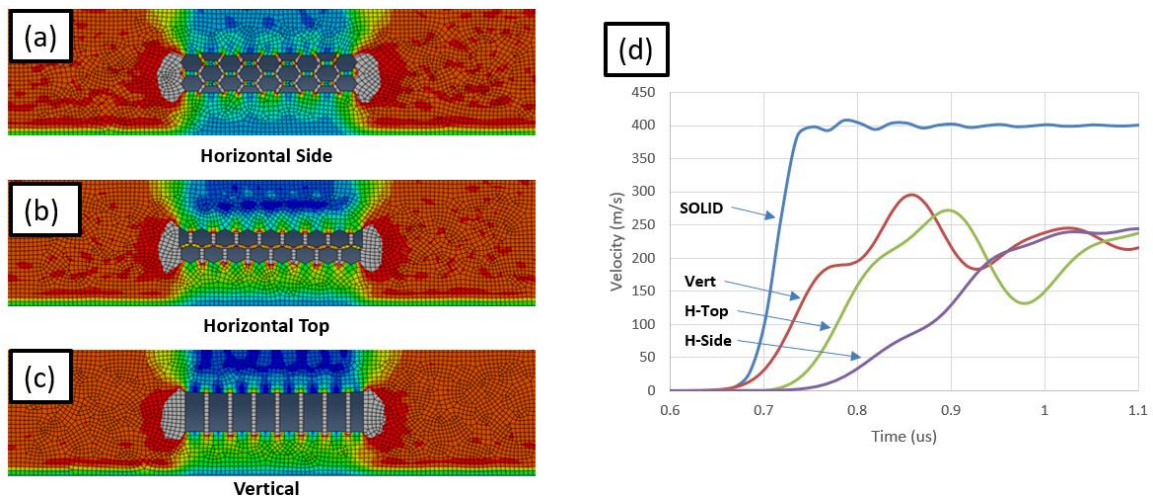


Figure 76: Simulation results of 2-D hexagonal honeycomb designs.

Experiment

The experiment for this study focused on the hexagonal honeycomb section insert into the target sample. The three orientations examined in the simulation planning (Horizontal-Side, Horizontal-Top, and Vertical) were fabricated. However, based on results observed in the as-built characterization, only one of the samples was used in the plate impact experiment.

Sample Fabrication

The samples were fabricated using the Farsoon FS273M LPBF machine located at the University of Tennessee. The machine utilizes twin 400W lasers. Each sample was fabricated as a solid cylindrical disc oriented vertically with dimensions of 15 mm diameter by 3.5 mm height. The relatively small samples were located in the build space to allow a single laser to fabricate each part, so that laser interface boundaries were not a concern. Similar build parameters and scan strategy to those outlined in Chapter 3 were used.

The engineered hexagonal honeycomb structure for each sample was designed as an insert and strategically placed in the electronic CAD files that the internal hexagonal void spaces would not be melted by the laser scan during build fabrication. As with the randomly distributed porosity study (Chapter 5), these void spaces do not constitute true “porosity” as each contains unmelted powder rather than completely empty “void” space.

Material Feedstock:

The 316L SS powder used to fabricate the samples was gas atomized powder. The chemical composition and particle size distribution of the powder is consistent with that listed in Chapter 4.

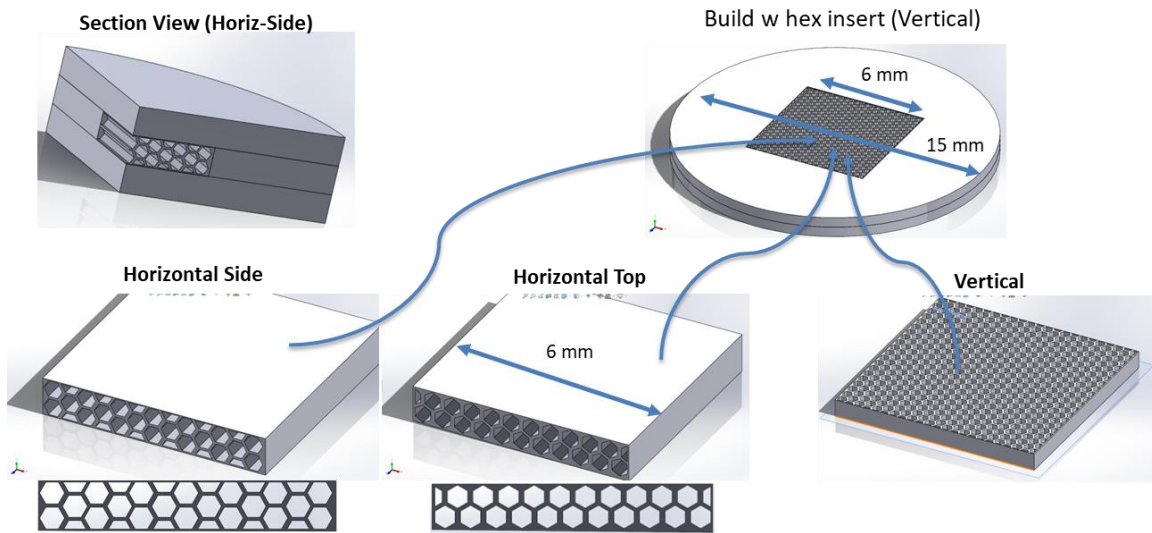


Figure 77: CAD renderings of target samples with hexagonal honeycomb designs.

Physical Property Characterization:

The as-built samples were characterized before the gas gun impact experiments. Post-mortem characterization was performed on soft-recovered samples collected after the experiment. The pre-test characterization consisted of bulk density measurements, ultrasound wave speed measurements, moduli calculations, LOM image analysis, and XCT imaging. The results of the pre-test characterization were compared with each other and against a fully dense control sample (of the same build orientation) as a baseline. LOM images were acquired at various magnifications using a Zeiss Axio Imager. Of particular interest in the as-built samples was the general geometry of the internal void region.

The XCT data was collected at Georgia Institute of Technology. XCT was used to verify the internal geometry as prescribed by design. Two-dimensional (2D) images of individual slices were also collected and analyzed using FIJI/ImageJ software. Post-test XCT was used to examine the resulting damage relative to the engineered features prior to cross-section analysis.

Plate Impact Testing

The plate impact experiment for this study was performed using the 80mm diameter x 7.6m length single-stage light-gas gun at the Georgia Institute of Technology. Details on the test configuration and setup are described in earlier Chapters. For velocity data collection, three PDV probes were placed in similar arrangement to the single-void samples described in Chapter 7.

Complex internal features (such as honeycombs) can significantly refract portions of the shock wave front. This introduces a complicating shear wave element and drives the experiment away from the one-dimensional case. The uniaxial stress state is one of the key assumptions required for the dynamic strength calculations (σ_{spall} and σ_{HEL}) and the information that is obtained from the velocity-time plot. Changing the stress state to a multi-dimensional case invalidates much of the material property information that can be derived from the velocimetry data collected in the plate-impact experiment. The arrival of the wave

front and the resulting stress is still applicable as those are directly associated with the free surface velocity sensed by the PDV probe. For these reasons, the plate impact experiment is typically not used to evaluate samples with these types of internal geometries. The amount of tedious sample preparation required to ensure the mating impact surfaces are flat and parallel along with the PDV probe materials and signal processing is a costly endeavor to undertake for the amount of valid information obtained. Ballistic impact tests are often used to more efficiently collect information on energy absorption by complex structures including layered and composite materials [99]. A similar approach may be applied when evaluating the damping capacity associated with complex internal geometries created by AM methods.

Results

Pre-Test Characterization

No presence of a defined structure was observed in the cross-section LOM images collected for any of the hex honeycomb samples (See Figure 78). Each of the three variations presents as a single, large powder-filled void with dimensions matching the overall insert size. Although the planned honeycomb orientation does appear to influence the specific geometry of the large powder-filled void, none of the internal members are distinguishable. The only resemblance of successful fabrication of the internal design occurs at the void edge, where a slight outline of the outer edges of the border honeycomb is observable (Figure 79). This is particularly true in the horizontal honeycomb samples (Side and Edge).

The data obtained from XCT (Figure 80) provided similar results to the cross-section images. A single, large void space is observed at the insert section of the sample. However, small ridges spaced at approximately 500 μm were observed along the void perimeter. Since none of the honeycomb structures were successfully built, the samples will be referred to as engineered samples for the remainder of this Chapter.

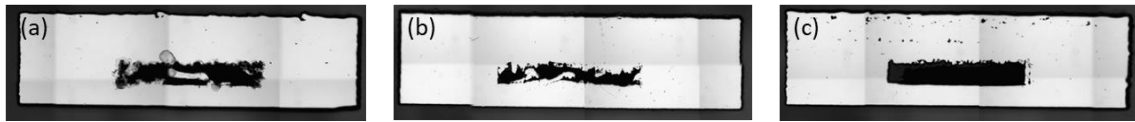


Figure 78: LOM images of as-built engineered samples. Notice that the individual struts were not successfully built in any of the samples. (a) Side hex orientation, (b) Edge hex orientation, (c) Vertical hex orientation.

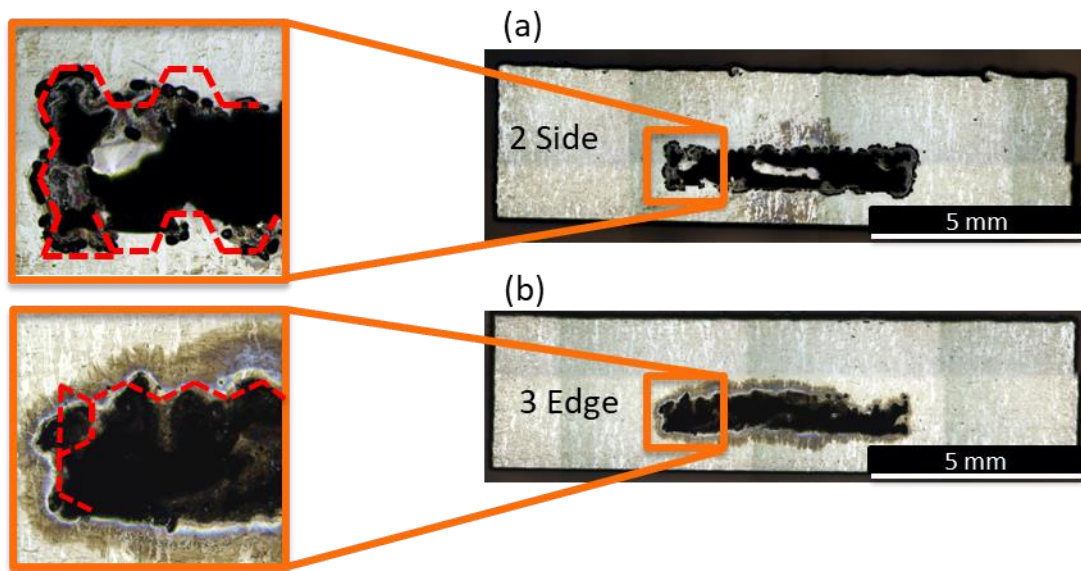


Figure 79: Etched LOM images of as-built engineered samples. (a) Side hex orientation, (b) Edge hex orientation. The hex honeycomb cells at the boundary of the insert appear to have attempted to build but did not fully form, as indicated by the outline on the zoomed images.

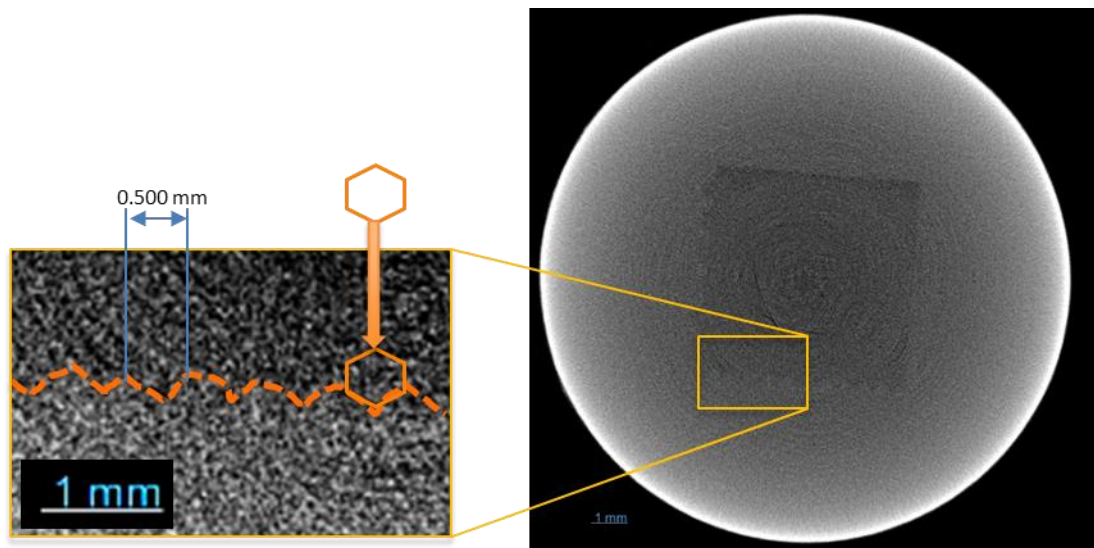


Figure 80: XCT image of as-built Vertical hex honeycomb sample. Insert indicates that the void edge has artifact of the hex cells along that boundary.

The bulk density of the engineered sample is noticeably less than the baseline and small void samples (Table 16). This is expected due to the increased volume of powder-filled void space in this sample. The value collected for measured longitudinal wave speed of the engineered sample is much greater than that of the control sample. This can be mainly attributed to the reflection provided by the large void acting as a free surface.

The extreme difference observed in the measured longitudinal wave speed results for the control and engineered samples is influenced more by the internal geometry of the sample than by the physical material properties. Longitudinal wave speed measurements are obtained by using the measured thickness of a sample along with the time interval between initiation of a pulse and the echo return to the sensor. However, in the engineered sample this echo returns from the internal void rather than the opposite free surface. Considering that the void surface is located at approximately 1/3 of the total sample thickness, the longitudinal wave speed calculated using the full sample thickness is roughly three times greater than the actual speed of the solid material. One-third of the longitudinal wave speed presented in Table 16 for the engineered sample is 5957 m/s. This value is much more in line with the other wave speed values.

The measured shear wave does not deviate as much from the control sample (only about 10%). This is due to differences in the sensing probes used and the transmission geometry of the waves. The VSP-200 transducer probe used to measure the longitudinal wave speed has an active diameter of 4.5 mm, while the SRD50-5 transducer probe used to measure the shear wave speed has an active diameter of 12.5 mm. Considering that the void insert is 6 mm x 6 mm, the longitudinal measurement returns signal from the void area only, and the shear wave measurement captures the solid area outside the void as well. The operating frequency of the SRD50-5 shear wave probe is 5MHz, which corresponds to a wavelength of 0.664 mm. Given the void dimensions and location, this allows the potential path for the shear wave pulse to be slightly influence, but not fully reflected by, the void region (Figure 81).

Table 16: As-built properties of Engineered Sample.

Sample ID	Density (g/cm ³)	Longitudinal Wave Speed (m/s)	Shear Wave Speed (m/s)
AM Control	7.82	5,814	3,025
Engineered	7.53	17,871	3,332

Plate Impact Experiment

Although the distinct hex honeycomb structure did not effectively build due to process limitations, a large powder-filled void section was still present at the internal of the sample. As such, it was decided to proceed with plate impact testing of the engineered samples and couple the findings with the large void simulations reported earlier in this Chapter.

PDV probes were placed at three locations on the sample rear free surface. One probe was placed at the center (indicated as Red in Figure 82), and the other two probes were placed approximately 1.5 mm (Blue in Figure 82) and 3 mm (Black in Figure 82) from the center. The engineered sample showed distinct velocity profiles at all three locations (Figure 82.b). Due to physical limitations with probes, it is likely one of the probes was not fully on the void section, most likely the probe labelled as Black. The peak velocity and the velocity rate of change for each probed location in the engineered sample are both reduced when compared to the baseline control sample. The experiment data was also compared with simulation results (Figure 83).

The velocity profile recorded for two of the probe locations (Blue and Black in Figure 83) correlate very closely to the corresponding locations in the simulation. The Blue probe corresponds to the location “B” as it is located approximately half the distance between the center and the void edge. The Black probe corresponds to the location “C” as it is located at the edge of the void. The Red probe corresponds to the location “A” at the center of the void. However, the velocity profiles for the experiment and simulation at the center do not match as closely as the other two probe locations.

Post-mortem Characterization

The primary (and only) characterization method for the post-mortem samples was XCT analysis. This method allowed for examination of the full internal volume of the samples.

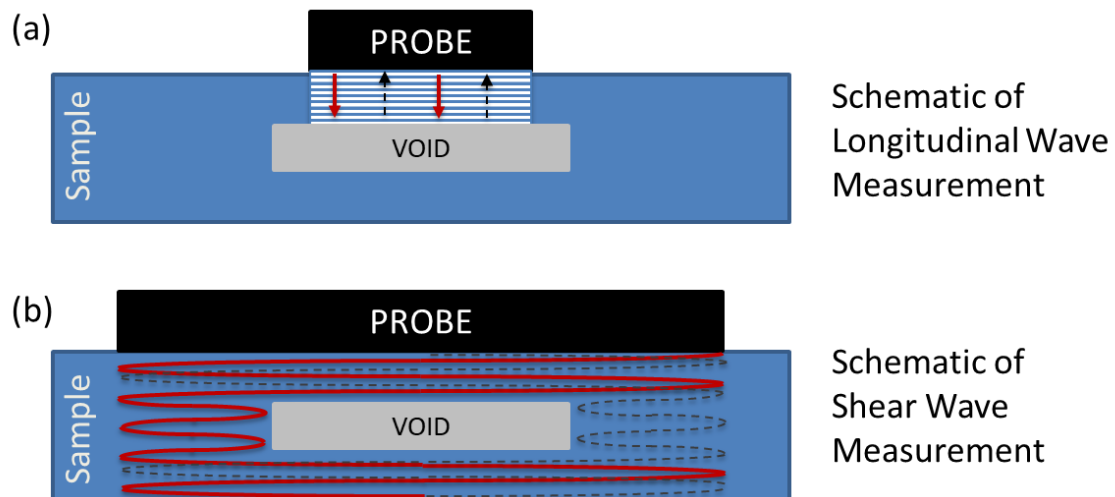


Figure 81: Schematics of Wave Measurement Probes.

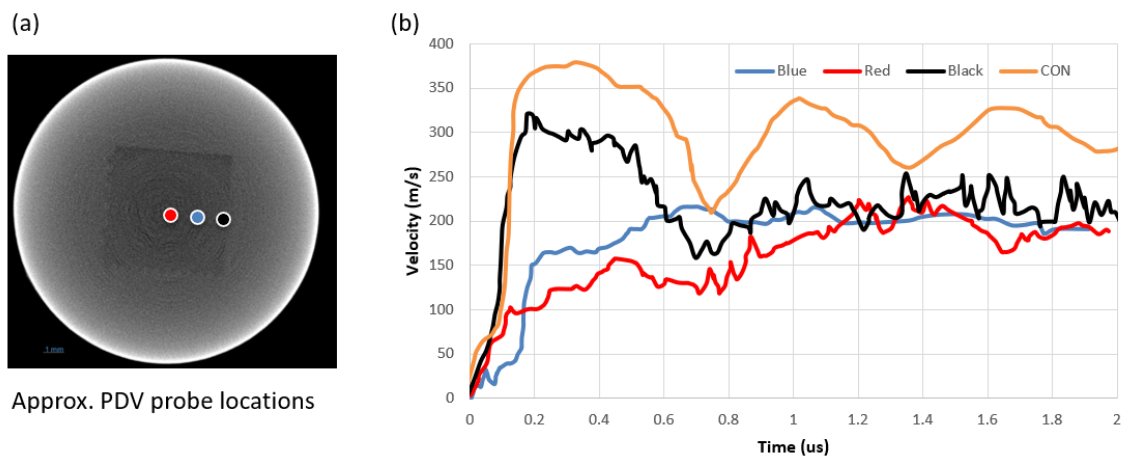


Figure 82: Velocity plot of engineered sample. (a) XCT image indicating approximate location of probes. (b) Velocity-time plot from plate-impact experiment. Each probe location is shown along with CONTROL sample data for comparison.

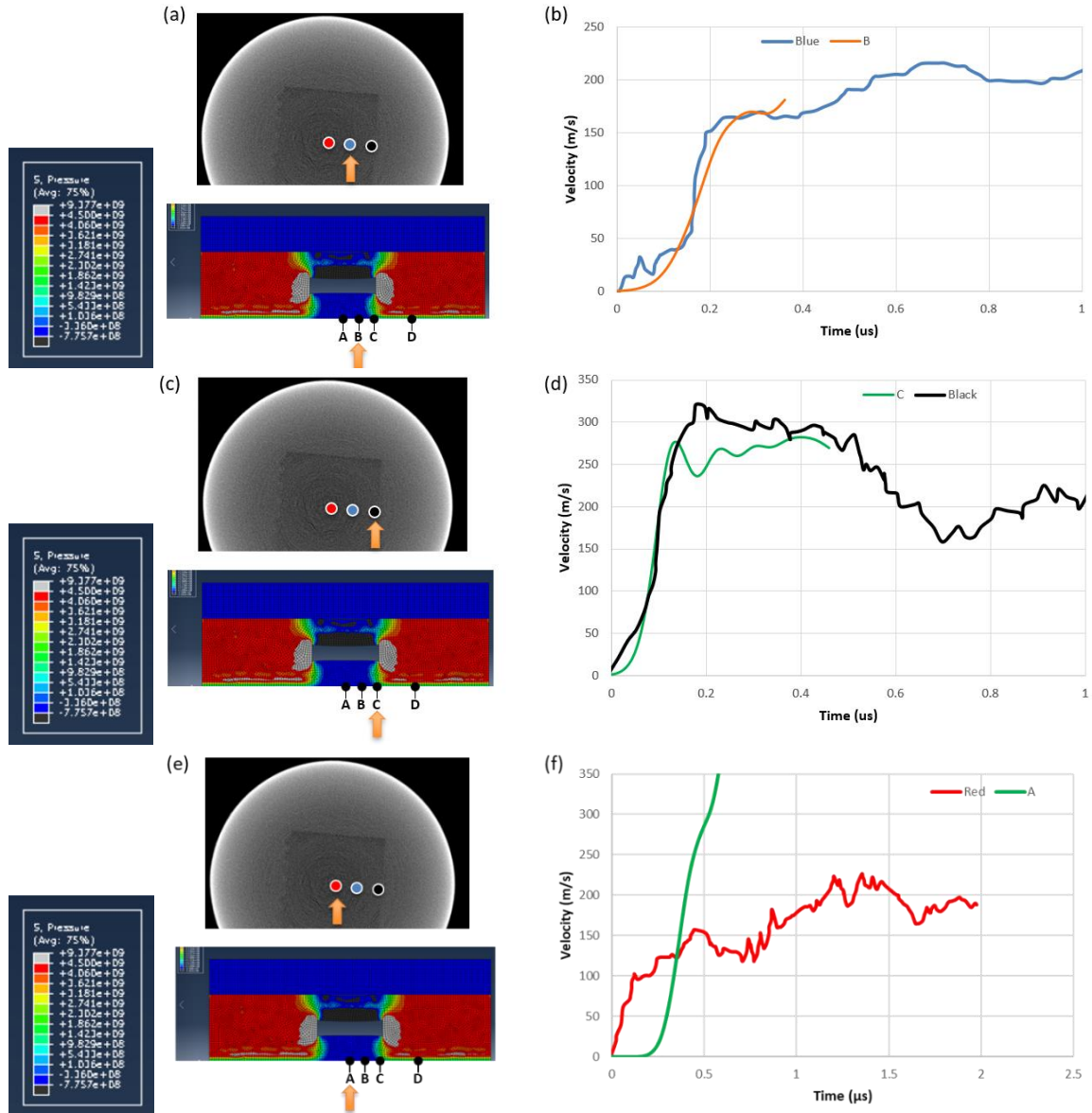


Figure 83: Engineered sample velocity data comparison with simulation. (a) Blue probe location and the corresponding model location. (b) Velocity-time plot of the Blue probe location and the corresponding model location. (c) Black probe location and the corresponding model location. (d) Velocity-time plot of the Black probe location and the corresponding model location. (e) Red probe location and the corresponding model location. (f) Velocity-time plot of the Red probe location and the corresponding model location.

After impact, the central void is no longer visible (Figure 84). The post-impact sample appears to have a solid section where the large void space was in the original as-built sample. Additionally, voids form along the edges of the sample in the spall region, similar to 500 μm at 5% random porosity sample (Chapter 5).

Discussion

Shock wave reflection and compression of powder void area

When the compressive shock wave reaches a free surface, it is reflected as a rarefaction wave. Similarly, when a shock wave reaches an interface with a lower shock impedance (typically less dense material) a portion of the wave is reflected while the remainder of the wave is transferred to the second media. The proportion of the wave reflected is a function of the relative difference between the shock impedance of the two materials, of which density is a major component [37]. For the specific scenario demonstrated in this experiment, there are a few different aspects to explore:

1. The transition from high-to-low-to-high shock impedance between two material medium states.
2. The momentum transfer within the powder-filled volume
3. The compressive sintering of the powder particles within the volume.

Shock wave behavior at material interface

When a shock wave propagates from one material to another, changes in pressure, wave velocity, and density occur. Continuity at the boundary dictates that the particle velocity and pressure will be the same in both materials [37]. Specific to this study, a powder-filled void has a lower density and lower shock impedance than the solid material. By examining the powder volume as a continuum, this leads to reflection of a portion of the pressure front and transmission of a wave front at reduced pressure. This phenomenon is discussed in depth in Chapter 4.

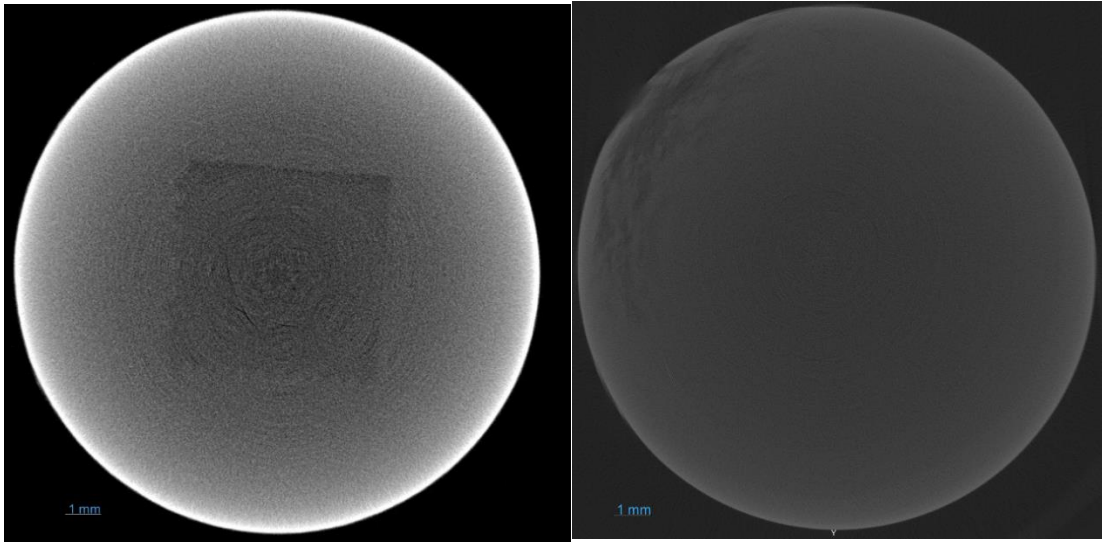


Figure 84: XCT image comparison of as-built and post-impact engineered sample.

Momentum transfer within powder-filled volume

Plate impact experiments with solid materials result in a state of uniaxial strain and one-dimensional stress (shock) wave propagation. However, a powder bed of individual particles changes the mode to a multi-dimensional state of motion and stress. The interfaces between powder particles are not parallel and planar in the way that the plate surfaces are for the experiment set up. The way that the powder in the volume settles and packs results in each powder particle contacting several other powder particles at varying angles and orientations. The size of the particles also varies.

Through conservation of momentum principles, the applied impulse is distributed across many powder particles. The angle of interaction between particles also produces motion and particle deformation normal to the direction of impact. Both of these factors have a damping effect, reducing the particle velocity and the magnitude of the pressure front.

Dynamic powder compaction/consolidation

In damping applications using solid or composite materials, the main mechanism of damping is local plastic deformation within the greater material matrix structure [69]. Similarly, the application of using high pressure shock waves to consolidate powders is an experimental technique that has been explored but has not been transitioned to a feasible production process because of some issues with process control and product uniformity [96, 97]. Although varying specific techniques, all forms of shock consolidation utilize a solid plate to deliver the rapid shock front to the powder volume. The process may be impact or explosive driven. The sample configuration, experiment setup, and the resulting post-mortem observations for this experiment all present great similarity to the dynamic consolidation process.

To successfully consolidate the powder a certain amount of energy is consumed by the process [100]. Relating the dynamic consolidation process to this experiment, as energy is consumed during the powder deformation and bonding

process, the magnitude of the pressure front is reduced. This reduction is realized in the velocity achieved at the rear free surface of the target.

Agreement between experiment and simulation results

In general, good agreement was observed between the experimental and simulation results. Locations B and C on the simulation (Figure 83) match very closely with the experimental results for locations BLUE and BLACK, respectively. However, the location at the center of the void (A on Simulation and RED in Experiment) were not as comparable. The experiment results for the RED probe are as should be expected, slow acceleration and reduced peak velocity.

The A location in the simulation, on the other hand, demonstrates a farther extended delay and a very rapid increase to a much higher than expected velocity. It is hypothesized that this is caused by deflection that occurs at the center point of the 2D model. Analogous to a beam loading scenario, the center of the 2D simulation model is a location of maximum deflection when loaded equally at both ends. This delays the observed velocity magnitude increase. The relaxation caused by wave reflection from the rear free surface results in a direction change for this deflection at Point A. The rate of change in this deflection (displacement) term is very high, resulting in a rapid rise to a very high velocity. In the experiment, the powder within the void prevents (or at least mitigates) this deflection, resulting in the damped response.

Energy Balance

The many aspects of the data and results observed in this study lead to a need for assessment of the input and output energy forms to better understand the process going forward. To accomplish this, an energy balance of the system is needed. Based on the first law of thermodynamics, the change in energy of a system is equal to the sum of the changes to the individual energy components.

The input energy is applied to the system by the flyer plate impact on the target. This energy is transferred or consumed, to different extents, by several individual component energies. A portion is transferred to kinetic energy as the target as the impact results in displacing the target sample from the sample holder. Energy is required to form the new surfaces that are created by spall fracture, as well as the plastic deformation that occurs prior to fracture. Previous literature research has established that adiabatic heating occurs as part of the spall fracture event. Energy is also lost as wave attenuation due to the interactions that occur at the material interfaces (grain and melt pool boundaries, voids, etc.).

The specific contributions and mechanisms of each energy need to be further evaluated. This follow on work will help to define each component and better inform future efforts on both geometry design and modeling/simulation.

Conclusions

The spall response for SS316L AM samples fabricated with engineered internal, powder-filled void space examined through execution of light gas gun plate impact experiment and microstructure characterization. The AM technology used to fabricate the samples is LPBF. In summary, it was observed that the internal powder-filled void region has a significant influence on the shock wave propagation behavior of the material. As with the earlier studies in this research, the focus on the analytical and numerical modeling was centered on the elastic response and plastic yielding was not examined in depth. For more complex internal geometries (such as honeycomb and lattice) plastic yielding begins to have a more significant role as the deformation of the local structures serves as another form of energy damping and consumption within the overall system. Specifically, the study presented reveals:

- The powder-filled void section provides an energy damping region that slows and weakens the shock front.
- The pressure stress provided by the shock front is sufficient to consolidate the powder-filled internal void region.

Chapter Nine

Summary and Conclusions

Introduction

This research investigated the effects of build orientation and powder-filled voids on the dynamic tensile fracture (spall) and damage resistance to dynamic shock loading of additively manufactured SS316L. The overall objective of this research was to examine the influence of the unique microstructure characteristics and design space capabilities associated with LPBF fabrication on the spall response of SS316L for future applications involving the control and/or mitigation of shock wave propagation. The spall experiments were performed using high velocity plate impact testing in a single-stage light-gas gun.

Summary of Results

Build-Impact Orientation Study

Specifically, the study presented reveals:

- The AM SS316L exhibits orientation dependent behavior, with the spall strength affected by the relative orientation between build direction and impact direction. This is influenced greatly by the bulk microstructural anisotropy and the effects of local AM process inherent defects including melt pool tracks and layers associated with LPBF microstructure.
- The individual spall damage locations for each sample correspond heavily with melt pool layer boundaries but not necessarily with grain boundaries.
- The spall plane location (distance from rear free surface) differs based on impact direction relative to build orientation. This phenomenon is observed in the post-mortem samples and supported by the velocimetry data.
- A complex spall behavior is observed in the through-thickness (TT) sample, which is evidenced in both the “double-hump” demonstrated in velocimetry data and the IP damage planes seen in the post-mortem characterization.

Randomly Distributed Engineered Porosity Study

Although there is variation observed for the elastic wave speeds, moduli, HEL, and spall strength, there is no definitive correlation between these results and void size or distribution.

There is a gradual rise in velocity profile of most of the engineered porosity test sample set, rather than the steep acceleration that is typical of spall experiments. There is also an absence of the “plateau” region that is typically seen at the peak velocity in spall experiments, indicating that the shock front is not fully developed. This suggests that the presence of these engineered voids has a damping effect on the propagating shock wave front.

However, the random distribution of voids within the samples makes it impossible to identify any trends across the sample sets. Additional studies will be needed to isolate the influence of individual voids.

Single Engineered Void Study

Numerical simulations suggest that there is a “wake zone” surrounding a void that influences the shock wave propagation. However, this zone is relatively small – constrained to the area directly in line-of-sight with the void. Both the elastic wave properties and the shock wave propagation behavior quickly revert back to the baseline case for locations elsewhere in the sample.

This study demonstrates that a single powder-filled void (up to 500 μm) within a large volume (comparative to “semi-infinite” assumption) has relatively little impact on the overall shock wave propagation. This result is demonstrated in both the elastic and shock wave behavior.

Engineering Design

Although the original hexagonal honeycomb design was not successfully fabricated due to manufacturing limitations, the single large void produced a beneficial case study in applying an engineered feature to influence the shock wave propagation behavior and damage resistance. The powder-filled void provided a damping mechanism that both slowed the progression of the wave front, slowing its travel to the rear free surface, and reduced the stress magnitude transmitted by the wave upon arrival. The experimental results were in good general agreement with the simulation study for the like geometry.

Additionally, the energy absorbed by the powder-filled void space was sufficient to compact the powder into a solid (as determined by XCT analysis). This result is analogous to high velocity compaction (HVC) used in powder metallurgy.

Conclusions

The compilation of this work reveals several conclusions that can be drawn related to the use of AM SS316L in shock loading and impact applications.

Relative orientation between the build direction and the shock loading has an influence on the wave propagation, dynamic strength properties, and fracture behavior. This is driven by the directional differences in modulus controlled by solidification characteristics of the melt pools and orientation of melt pool boundaries. Similar to quasi-static conditions, the intersections at melt pool boundaries are likely damage initiation sites for AM SS316L under high strain rate (shock) loading conditions, with orientation of these intersections with respect to loading playing a key role.

Powder-filled voids slow the shock wave progression through material. Depending on the size and distribution of internal voids, this can lead to (a) Delay in the shock wave front arrival at the rear free surface of the sample, (b) Reduced pressure stress applied by the shock wave at the rear free surface of the sample, (c) Reduced spall damage, and (d) shift or absence of the primary spall plane. This is the result of the reflection and diffraction of portions of the wave front by

the voids, as well as energy absorption (damping) by the loose powder within the voids. Plastic yielding at voids also provides additional energy damping but was not explored in depth as part of this research.

Simple numerical simulations can be used to evaluate new designs that are intended to slow the shock wave propagation by demonstrating the compression loading phase of the impact. The simulations used in this research focus on the elastic response only; incorporating plastic yielding into the model would likely provide a more comprehensive perspective on the wave response.

Overall, this research provides evidence that AM (LPBF) has the capability to utilize unique internal engineered features to dampen, and otherwise control, the speed and magnitude of shock wave propagation through a material and reduce damage associated with high velocity impact.

Chapter Ten

RECOMMENDATIONS AND FUTURE WORKuture work building on this research should focus in three primary areas: (1) Increasing depth focused on the anisotropic properties of AM structures under a wider range of impact velocities (and strain rates), (2) Pursuing depth of understanding for the powder-filled and void space areas from a physics and thermodynamic perspective, and (3) Expanded research into engineering design for shock wave control and energy damping.

The directional anisotropy exhibited in the build-impact orientation study should be further explored. Variations of operating parameters to control melt pool structures and the response at elevated impact velocities should both be examined. Other works in literature [5, 43] have demonstrated that variations in the spall behavior based on crystallographic orientation or small defects disappear as the impact velocity (and the corresponding applied stress) is sufficiently large. It is expected that the samples discussed here would follow that same trend.

More research should also be performed to examine the shock damping capability of internal features that can be engineered into metal components using AM fabrication techniques. Specifically, future samples should be carefully planned for proper fabrication using LPBF. This could include using a variety of build parameters to improve the structure build and looking to architecture and nature for examples of structures. Engagement of LPBF operators and designers is key for this. In addition to LPBF, other AM techniques should be considered.

The use of specialized shock physics codes, such as CTH or iSALE, should be utilized to efficiently evaluate new designs. The inclusion of plasticity characteristics and thermodynamic heating models into these modeling efforts is needed to provide a more complete perspective of the processes that are taking

place. A detailed, physics-based energy balance evaluation is needed to support this understanding, as well.

Additionally, ballistic-type tests should be utilized in the future to provide a more efficient method of evaluating future designs. Ballistic impact tests require much less rigor in sample preparation and provide adequate data on sample damage and energy damping capacity for comparison among different designs. Also, much of the information that is provided by plate impact tests (such as spall strength) is invalidated by complex structures that introduce shear wave component and move the stress state away from the uniaxial case.

Overall, an organized approach that involves leveraging advantages of partners at other institutions, laboratories, agencies, and industry partners will be pursued to accomplish continued research in the areas mentioned. A summarized roadmap of this future work is listed below.

Focus Areas:

1. Anisotropic properties under a wider range of impact velocities
2. Physics and thermodynamic analysis of powder-filled void spaces
3. Engineering design for shock wave control and energy damping

Components of each study:

- Collaborations will be utilized to leverage expertise in areas of numerical simulation, plate impact testing, and the crossover topics such as energy damping and high velocity compaction of powder.
- Engineering design and supporting analysis. This includes developing both analytical and numerical solutions. Also, available specialized shock physics codes will be utilized to provide depth.
- Ballistic (steel ball projectile) impact testing. This will be used primarily as a rapid-response test for qualitative comparison of designs.
- Plate impact testing. Once conceptual designs have been optimized, test methods presented in this research will provide useful velocity information. Strategic placement of PDV probes at multiple locations will provide increased data from each test.

- As-built and post-mortem characterization. As presented in this research, with an increased emphasis on XCT data before and after testing.

List of References

- [1] A. A. Yuichi, M. Kakizaki, & T. Hideshima (1949). An Investigation of Mechanical Properties of Materials at very High Rates of Loading Related content Anisotropy in Mechanical Relaxations in Uniaxially Oriented Polymers Yasuaki Kawamura and Yasaku Wada - Molecular Motions and Related Mechanical Relax. *Proc. Phys. Soc. B*, 62.
- [2] R. L. Sierakowski, "Strain rate behavior of metals and composites," 1997. [Online]. Available: <http://www.gruppofrattura.it/ocs/index.php/cigf/igf13/paper/view/206>.
- [3] C. Williams, & B. Love. (2010). Dynamic Failure of Materials : A Review, (August).
- [4] M. A. Meyers. *Dynamic Behaviour of materials*, 1994.
- [5] G. T. Gray et al., "Structure/property (constitutive and spallation response) of additively manufactured 316L stainless steel," *Acta Mater.*, vol. 138, pp. 140–149, 2017.
- [6] C. Li, B. Li, J. Y. Huang, H. H. Ma, M. H. Zhu, J. Zhu, and S. N. Luo. Spall damage of a mild carbon steel: Effects of peak stress, strain rate and pulse duration. *Materials Science and Engineering A*, 660, 139–147, 2016.
- [7] G. W. Swan, G. E. Duvall, & C. K. Thornhill. (1973). On steady wave profiles in solids. *Journal of the Mechanics and Physics of Solids*, 21(4), 215–227.
- [8] S. A. Thomas, M. C. Hawkins, M. K. Matthes, G. T. Gray, and R. S. Hixson. Dynamic strength properties and alpha-phase shock Hugoniot of iron and steel. *Journal of Applied Physics*, 123(17). 2018.
- [9] ASTM F2792. (2017). Standard Terminology for Additive Manufacturing – General Principles.
- [10] ISO/ASTM 52900:2015(E). (2015). Standard Terminology for Additive Manufacturing – General Principles – Terminology. ASTM International, i, 1–9.
- [11] G. Jacob, C. U. Brown, M. A. Donmez, S. S. Watson, & J. Slotwinski. (2017). Effects of powder recycling on stainless steel powder and built material properties in metal powder bed fusion processes. *National Institute of Standards and Technology*.

- [12] J. S. Keist, & T. A. Palmer. (2016). Role of geometry on properties of additively manufactured Ti-6Al-4V structures fabricated using laser based directed energy deposition. *Materials and Design*, 106, 482–494.
- [13] L. Krog, A. Tucker, & G. Rollema. (2011). Application of Topology, Sizing and Shape Optimization Methods to Optimal Design of Aircraft Components.
- [14] S. Yoder, S. Morgan, C. Kinzy, E. Barnes, M. Kirka, V. Paquit, and S. S. Babu. (2018). Characterization of topology optimized Ti-6Al-4V components using electron beam powder bed fusion. *Additive Manufacturing*, 19, 184–196.
- [15] J. Raplee, A. Plotkowski, M. M. Kirka, R. Dinwiddie, A. Okello, R. R. Dehoff, & S. S. Babu. (2017). Thermographic Microstructure Monitoring in Electron Beam Additive Manufacturing. *Scientific Reports*, 7(October 2016), 1–16.
- [16] M. Mani, B. Lane, A. Donmez, S. Feng, S. Moylan, & R. Fesperman. (2015). Measurement Science Needs for Real-time Control of Additive Manufacturing Powder Bed Fusion Processes.
- [17] S. Kramer, J. L. Jordan, H. Jin, J. Carroll, & A. M. Beese. (2018). Mechanics of Additive and Advanced Manufacturing, Volume 8: *Proceedings of the 2018 Annual Conference on Experimental and Applied Mechanics*. 5-16. Springer International Publishing.
- [18] A. G. Demir, C. De Giorgi, & B. Previtali. (2017). Design and implementation of a multi-sensor coaxial monitoring system with correction strategies for selective laser melting of a maraging steel. *Journal of Manufacturing Science and Engineering*, 140(April), 1–14.
- [19] Y. Liu, Y. Yang, & D. Wang. (2016). A study on the residual stress during selective laser melting (SLM) of metallic powder. *International Journal of Advanced Manufacturing Technology*, 1–10.
- [20] D. Herzog, V. Seyda, E. Wycisk, & C. Emmelmann, C. (2016). Additive manufacturing of metals. *Acta Materialia*, 117, 371–392.
- [21] A. Migliori, T. Darling, J. Baiardo, and F. Freibert. (2009) Resonant ultrasound spectroscopy (RUS). *Experimental Methods in the Physical Sciences*, Volume 39, Pages 189-220. Los Alamos National Laboratory Los Alamos, New Mexico, USA.

- [22] C. Tuck. (2015). SLM of aluminum and titanium alloys - Some lessons learned. EPSRC Centre for Innovative Manufacturing in Additive Manufacturing.
- [23] M. Grasso, & B. M. Colosimo. (2017). Process defects and in situ monitoring methods in metal powder bed fusion: A review. *Measurement Science and Technology*.
- [24] T. L. Anderson. (2005). *Fracture Mechanics – Fundamentals and Applications*. Third Edition. CRC Press, Boca Raton, FL. 2005.
- [25] M. A. Meyers, and C. Taylor Aimone. Dynamic fracture (spalling) of metals. *Progress in Materials Science*, 28(1), 1–96. 1983
- [26] M. A. Bevan, A. A. Ameri, D. East, D. C. Austin, A. D. Brown, P. J. Hazell, & J. P. Escobedo-Diaz. (2017). Mechanical Properties and Behavior of Additive Manufactured Stainless Steel 316L. *Minerals, Metals and Materials Series*, Part F7(November 2019), 577–583
- [27] W. E. Frazier (2014) Metal additive manufacturing: a review. *Journal of Material Eng Performance* 23(6): 1917–1928
- [28] H.K.D.H. Bhadeshia, S.R. Honeycombe, 12 - stainless steel, in: H.K.D.H. Bhadeshia, S.R. Honeycombe (Eds.), *Steels*, third ed., Butterworth-Heinemann, Oxford, 2006, pp. 259–286.
- [29] T. DebRoy, H. L. Wei, J. S. Zuback, T. Mukherjee, J. W. Elmer, J. O. Milewski, ... W. Zhang. (2018). Additive manufacturing of metallic components – Process, structure and properties. *Progress in Materials Science*, 92, 112–224.
- [30] J. C. Lippold. and D. A. Kotecki., *Welding Metallurgy and Weldability of Stainless Steels*. Wiley-Interscience, 2005.
- [31] S. Kou. "Welding metallurgy." New Jersey, USA 431.446 (2003): 223-225.
- [32] J. W. Elmer, G. F. Ellsworth, and J. N. Florando. Microstructure and Mechanical Properties of 21-6-9 Stainless Steel Electron Beam Welds. *Metall Mater Trans A* 48, 1771–1787 (2017).
- [33] A. Yadollahi, N. Shamsaei, S. M. Thompson, & D. W. Seely, Effects of process time interval and heat treatment on the mechanical and microstructural properties of direct laser deposited 316L stainless steel. *Materials Science and Engineering: A*, Volume 644 (2015).

- [34] Z. Wang, T. A. Palmer, & A. M. Beese. Effect of processing parameters on microstructure and tensile properties of austenitic stainless steel 304L made by directed energy deposition additive manufacturing. *Acta Materialia*, Volume 110. (2016).
- [35] H. D. Carlton, A. Haboub, G. F. Gallegos, D. Y. Parkinson, & A. A. MacDowell. Damage evolution and failure mechanisms in additively manufactured stainless steel. *Materials Science and Engineering*. Volume 651. (2016).
- [36] K. Rajasekhar, C.S. Harendranath, R. Raman, and S.D. Kulkarni, Microstructural Evolution During Solidification of Austenitic Stainless Steel Weld Metals: A Color Metallographic and Electron Microprobe Analysis Study, *Mater. Charact.*, 1997, 38, p 53–65
- [37] A. Putz, M. Althuber, A. Zelić, E. M. Westin, T. Willidal, & N. Enzinger. (2019). Methods for the measurement of ferrite content in multipass duplex stainless steel welds. *Welding in the World*, 63(4), 1075–1086.
- [38] R. Saluja and K. M. Moeed. (2012). The emphasis of phase transformations and alloying constituents on hot cracking susceptibility of type 304L and 316L stainless steel welds. *International Journal of Engineering Science and Technology*, 4(5), 2206–2216. 2012
- [39] K. Y. Shakhnazarov. (2009). Chernov's iron-carbon diagram, the structure and properties of steel. *Metal Science and Heat Treatment*, 51(1–2), 3–6.
- [40] Chapter 1 Shocks and structured waves. (n.d.).
- [41] A. E. Brown (1995). Rationale and Summary of Methods for Determining Ultrasonic Properties of Materials at Lawrence Livermore National Laboratory. 1996, Vol.1 No.03.
- [42] www.nde-ed.org. Accessed February 2021.
- [43] R. L. Whelchel, G. B. Kennedy, S. K. Dwivedi, T. H. Sanders, & N. N. Thadhani. (2013). Spall behavior of rolled aluminum 5083-H116 plate. 233506.
- [44] G. I. Kanel. (2010). Spall fracture: Methodological aspects, mechanisms and governing factors. *International Journal of Fracture*, 163(1–2), 173–191.

- [45] L. Wise *et al.*, “Comparative shock response of additively manufactured vs conventionally wrought 304L stainless steel,” *AIP Conf. Proc.*, vol. 1793, no. January 2017, 2017.
- [46] G. I. Kanel. Distortion of the Wave Profiles in an Elastoplastic. *Journal of Applied Mechanics and Technical Physics*, 42(2), 358–362. 2001.
- [47] S. Cochran and D. Banner. Spall studies in uranium. *Journal of Applied Physics*, 48(7), 2729–2737, 1977.
- [48] Laser-Based Michelson Interferometer and Interference Fringe Exploration Abstract. www.LightTrans.com/.
- [49] G. A. Swanson. (1984). Life Prediction and Constitutive Models for Engine Hot Section Anisotropic Materials. *NASA Conference Publication*, (April), 343–350.
- [50] D. J. Erskine, J. H. Eggert, P. M. Celliers, & D. G. Hicks. (2016). Ghost fringe removal techniques using Lissajous data presentation. *Review of Scientific Instruments*, 87(3), 1–9.
- [51] D. H. Dolan. (2020). Extreme measurements with Photonic Doppler Velocimetry (PDV). *The Review of Scientific Instruments*, 91(5), 051501.
- [52] A. M. Forster. (2015). Materials Testing Standards for Additive Manufacturing of Polymer Materials: State of the Art and Standards Applicability
- [53] A.B. Spierings, M. Voegtlin, T. Bauer, K. W. (2015). Mechanical properties testing for metal parts made via additive manufacturing: A review of the state of the art of mechanical property testing. *Progress in Additive Manufacturing*, 1, 9–20.
- [54] A. V. Utkin (1993) Influence of the initial damage rate on the forming spall pulse. *Journal of Applied Mechanical Technical Physics (USSR)* 34:578–584.
- [55] A. J. Godfrey, J. Simpson, D. Leonard, K. Sisco, R. R. Dehoff, & S. S. Babu. (2022). Heterogeneity and Solidification Pathways in Additively Manufactured 316L Stainless Steels. *Metallurgical and Materials Transactions A: Physical Metallurgy and Materials Science*, 53(9), 3321–3340.

- [56] T. DebRoy, H. L. Wei, J. S. Zuback, T. Mukherjee, J. W. Elmer, J. O. Milewski, ... W. Zhang. (2018). Additive manufacturing of metallic components – Process, structure and properties. *Progress in Materials Science*, 92, 112–224..
- [57] M. G. Rashed, M. Ashraf, R. A. Mines, & P. J. Hazell. (2016). Metallic microlattice materials: A current state of the art on manufacturing, mechanical properties and applications. *Materials and Design*, 95, 518–533.
- [58] E. Wycisk, A. Solbach, S. Siddique, D. Herzog, F. Walther, & C. Emmelmann. (2014). Effects of defects in laser additive manufactured Ti-6Al-4V on fatigue properties. *Physics Procedia*, 56(C), 371–378.
- [59] A. W. Prabhu, T. Vincent, A. Chaudhary, W. Zhang, & S. S. Babu. (2015). Effect of microstructure and defects on fatigue behaviour of directed energy deposited Ti-6Al-4V. *Science and Technology of Welding and Joining*, 20(8), 659–669.
- [60] T. M. Mower, & M. J. Long. (2016). Mechanical behavior of additive manufactured, powder-bed laser-fused materials. *Materials Science and Engineering A*, 651, 198–213.
- [61] T. Niendorf, S. Leuders, A. Riemer, H. A. Richard, T. Tröster, & D. Schwarze. (2013). Highly anisotropic steel processed by selective laser melting. *Metallurgical and Materials Transactions B: Process Metallurgy and Materials Processing Science*, 44(4), 794–796
- [62] D. Gu, & H. Chen. (2018). Selective laser melting of high strength and toughness stainless steel parts: The roles of laser hatch style and part placement strategy. *Materials Science and Engineering A*, 725(February), 419–427
- [63] J. Suryawanshi, K. G. Prashanth, & U. Ramamurty, “Mechanical behavior of selective laser melted 316L stainless steel,” *Mater. Sci. Eng. A*, vol. 696, no. April, pp. 113–121, 2017
- [64] W. E. Luecke, & J. A. Slotwinski. (2014). Mechanical properties of austenitic stainless steel made by additive manufacturing. *Journal of Research of the National Institute of Standards and Technology*, 119, 398–418
- [65] D. Du, A. Dong, D. Shu, G. Zhu, B. Sun, X. Li, & E. Lavernia. (2019). Influence of build orientation on microstructure, mechanical and corrosion behavior of Inconel 718 processed by selective laser melting. *Materials Science and Engineering A*, 760(May), 469–480.

- [66] H. Brodin, O. Andersson, & S. Johansson. (2013). Mechanical testing of a selective laser melted superalloy. *Proceedings of the 13th International Conference on Fracture*, 1–11.
- [67] P. H. Li, W. G. Guo, K. B. Yuan, Y. Su, J. J. Wang, X. Lin, & Y. P. Li. (2018). Effects of processing defects on the dynamic tensile mechanical behavior of laser-solid-formed Ti-6Al-4 V. *Materials Characterization*, 140(November 2017), 15–29.
- [68] N. Biswas, J. L. Ding, V. K. Balla, D. P. Field, & A. Bandyopadhyay. (2012). Deformation and fracture behavior of laser processed dense and porous Ti6Al4V alloy under static and dynamic loading. *Materials Science and Engineering A*, 549, 213–221.
- [69] M. G. Stout, & P. S. Follansbee. (1986). Strain rate sensitivity, strain hardening, and yield behavior of 304L stainless steel. *Journal of Engineering Materials and Technology, Transactions of the ASME*, 108(4), 344–353.
- [70] A. Hadadzadeh, B. S. Amirkhiz, J. Li., A. Odeshi, & M. Mohammadi. (2018). Deformation mechanism during dynamic loading of an additively manufactured AlSi10Mg_200C. *Materials Science and Engineering A*, 722(January), 263–268.
- [71] C. Hensley, K. Sisco, S. Beauchamp, A. Godfrey, H. Rezayat, T. McFalls, D. Galicki, F. List, K. Carver, C. Stover, D. W. Gandy, & S. S. Babu. (2021). Qualification pathways for additively manufactured components for nuclear applications. *Journal of Nuclear Materials*, 548, 152846.
- [72] R. Fadida, D. Rittel, & A. Shirizly. (2015). Dynamic mechanical behavior of additively manufactured Ti6Al4V with controlled voids. *Journal of Applied Mechanics, Transactions ASME*, 82(4).
- [73] S. A. Thomas, R. S. Hixson, M. C. Hawkins, and O. T. Strand, “Wave speeds in single-crystal and polycrystalline copper,” *Int. J. Impact Eng.*, vol. 139, no. January, p. 103506, 2020.
- [74] Y. Zhang, S. S. Babu, P. Zhang, E. A. Kenik, and G. S. Daehn. (n.d.). Microstructure characterisation of magnetic pulse welded AA6061-T6 by electron backscattered diffraction, 2008.
- [75] V. A. Ogorodnikov, E. Y. Borovkova, & S. V. Erunov. (2004). Strength of some grades of steel and armco iron under shock compression and rarefaction at pressures of 2 - 200 GPa.

- [76] P. E. Specht, N. N. Thadhani, and T. P. Weihs, "Configurational effects on shock wave propagation in Ni-Al multilayer composites," *J. Appl. Phys.*, vol. 111, no. 7, 2012.
- [77] T. J. Vogler, & J. D. Clayton. (2008). Heterogeneous deformation and spall of an extruded tungsten alloy: plate impact experiments and crystal plasticity modeling. *Journal of the Mechanics and Physics of Solids*, 56(2), 297–335.
- [78] D. R. Jones, S. J. Fensin, O. Diplo, R. A. Beal, V. Livescu, D. T. Martinez, C. P. Trujillo, J. N. Florando, M. Kumar, & G. T. Gray. (2016). Spall fracture in additive manufactured Ti-6Al-4V. *Journal of Applied Physics*, 120(13).
- [79] D. R. Jones, S. J. Fensin, B. G. Ndefru, D. T. Martinez, C. P. Trujillo, & G. T. Gray. (2018). Spall fracture in additive manufactured tantalum. *Journal of Applied Physics*, 124(22).
- [80] S. D. Nunn, R. R. Dehoff, and S. Simunovic. (2015). *Functionally Graded and Geometrically Ordered Titanium Composite Armor Materials*.
- [81] P. E. Specht, N. N. Thadhani, and T. P. Weihs, "Configurational effects on shock wave propagation in Ni-Al multilayer composites," *J. Appl. Phys.*, vol. 111, no. 7, 2012.
- [82] P. E. Specht, T. P. Weihs, and N. N. Thadhani, "Interfacial Effects on the Dispersion and Dissipation of Shock Waves in Ni/Al Multilayer Composites," *J. Dyn. Behav. Mater.*, vol. 2, no. 4, pp. 500–510, 2016.
- [83] Y. D. Im, K. H. Kim, K. H. Jung, Y. K. Lee, and K. H. Song, "Anisotropic Mechanical Behavior of Additive Manufactured AISI 316L Steel," *Metall. Mater. Trans. A Phys. Metall. Mater. Sci.*, vol. 50, no. 4, pp. 2014–2021, 2019.
- [84] A. T. Polonsky, W. C. Lenthe, M. P. Echlin, V. Livescu, G. T. Gray, & T. M. Pollock. (2020). Solidification-driven orientation gradients in additively manufactured stainless steel. *Acta Materialia*, 183, 249–260.
- [85] R. M. Flanagan, S. J. Fensin, and M. A. Meyers. (2022). The role of pre-existing heterogeneities in materials under shock and spall. *Applied Physics Reviews*, 9(1).
- [86] A. Fedorenko, B. Fedulov, Y. Kuzminova, S. Evlashin, O. Staroverov, M. Tretyakov, E. Lomakin, and I. Akhatov. (2021). Anisotropy of mechanical properties and residual stress in additively manufactured 316L specimens. *Materials*, 14(23), 1–17.

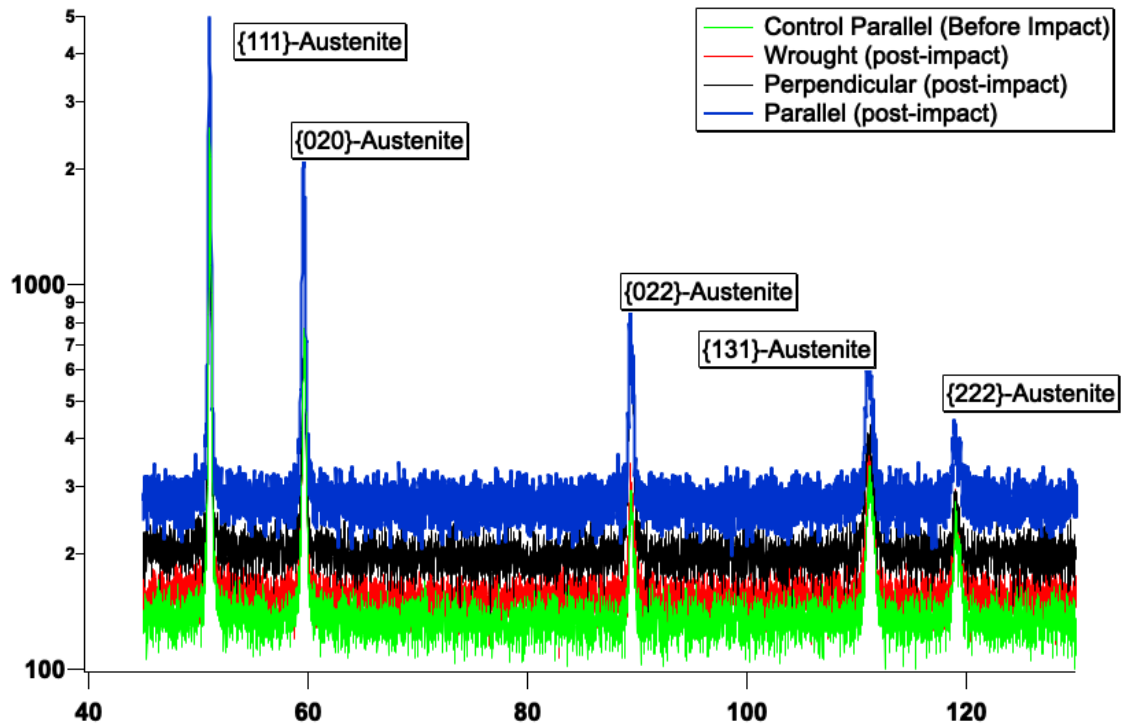
- [87] A. Charmi, R. Falkenberg, L. Ávila, G. Mohr, K. Sommer, A. Ulbricht, M. Sprengel, R. Saliwan Neumann, B. Skrotzki, and A. Evans. (2021). Mechanical anisotropy of additively manufactured stainless steel 316L: An experimental and numerical study. *Materials Science and Engineering A*, 799(August 2020), 140154.
- [88] W. Shifeng, L. Shuai, W. Qingsong, C. Yan, Z. Sheng, and S. Yusheng. Effect of molten pool boundaries on the mechanical properties of selective laser melting parts. *Journal of Materials Processing Technology*, 214(11), 2660–2667. 2014.
- [89] D. W. Galicki. (2019). *Investigation of Powder Recyclability and Liquid-Solid-Gas Interactions during Powder Bed Selective Laser Melting of Stainless Steel 316L*.
- [90] Z. Qiancheng, Y. Xiaohu, L. Peng, H. Guoyou, F. Shangsheng, S. Cheng, H. Bin, Z. Xiaohui, J. Feng, X. Feng, J. L. Tian. (2015). Bioinspired engineering of honeycomb structure – Using nature to inspire human innovation. *Progress in Materials Science*.
- [91] S. Anandan, R. M. Hussein, M. Spratt, J. Newkirk, H. Misak, & M. Walker. (2019). Failure In metal honeycombs manufactured by selective laser melting of 304 L stainless steel under compression. 2759.
- [92] J. J. Harrigan, S. R. Reid, & C. Peng. (1999). Inertia effects in impact energy absorbing materials and structures. 22, 955–979.
- [93] A. Wang, & D. L. McDowell. (2004). In-Plane Stiffness and Yield Strength of Periodic Metal. 126(April), 137–156.
- [94] B. Niu & B. Wang. (2016). Directional mechanical properties and wave propagation directionality of Kagome honeycomb structures. *European Journal of Mechanics, A/Solids*, 57, 45–58.
- [95] J. Qiao & C. Chen. (2016). In-plane crushing of a hierarchical honeycomb. *International Journal of Solids and Structures*, 85–86, 57–66.
- [96] T. Vreeland, Jr., P. Kasiraj, and R. B. Schwarz. (1984). Shock consolidation of powders – Theory and experiment. *Mat. Res. Soc. Symp. Proc.* Vol. 28.
- [97] M. A. Meyers and S. L. Wang. (1987). An improved method for shock consolidation of powders. *Acta metall.* Vol. 36, No. 4, pp. 925-936.

- [98] K. Rajasekhar, C. S. Harendranath, R. Raman, & S. D. Kulkarni. (1997). Microstructural Evolution during Solidification of Austenitic Stainless Steel Weld Metals: A Color Metallographic and Electron Microprobe Analysis Study. *Materials Characterization*, 38(2), 53–65.
- [99] H. Kasano. Ballistic Impact Performance of Composite Plate with and without Bonding. 18th International Conference on Composite Materials.
- [100] D. Hosson. (1994). Thermodynamic model of the compaction of powder materials by shock waves Thermodynamic by shock waves model of the compaction of powder materials
- [101] T. Street & C. W. Reserve. (1992). The out-of-plane properties of honeycombs. 34(6).
- [102] W. J. Sames, F. A. List, S. Pannala, R. R. Dehoff, & S. S. Babu. (2016). The metallurgy and processing science of metal additive manufacturing. *International Materials Reviews*, 61(5), 315–360.
- [103] Dieter, G.E., 1988. *Mechanical Metallurgy*. McGraw-Hill, New York.
- [104] Gibson, L. J., and M. F. Ashby. *Cellular Solids: Structure and Properties*. 2nd ed. Cambridge University Press, 1997.

Appendix

Supplementary Data: X-ray Diffraction (XRD) Results

Kevin Lamb – “Anisotropic Spalling Failures of Additively Manufactured 316 Stainless Steel”



Instrument Parameters:	
Instrument Used	Malvern PANalytical Diffractometer
Stage Used	XYZ Stage
Detector Used	PIXcel 3D Scanning Mode
<i>Collimation (Incident)</i>	
Divergence Slit [°]	0.125
Anti-scatter Slit [°]	0.25
Goniometer Radius [mm]	240
Beam Type	Co K α 1 to K α 2
Data Collection Parameters:	
Software Package	HighScore Plus v4.7
Temperature [°C]	25
Pressure	Ambient
Operating Voltage [kV]	45
Operating Current [mA]	40
<i>Goniometer Parameters</i>	
Wavelength [Å]	1.79
Scan Range [° 2 θ]	45.0 < 2 θ < 130.0
Step Size [° 2 θ]	0.013
Scan Step Time [s]	23.970

	Reitveld Refinement	Strain Refinement
Global	Specimen Displacement	Specimen Displacement
	Background	Background
	Scale Factor	Scale Factor
Phase Dependent	March-Dollase Factor	March-Dollase Factor
	Lattice Parameter, a	Lattice Parameter, a
	U	U
	W	W
	Peak Shape 1	Peak shape 1
	Peak shape 2	Peak shape 2

Your area with 5mm mask: 1.36 x 7 mm

Supplementary Information: Detailed methodology and calculation of spall plane location

Kevin Lamb – “Anisotropic Spalling Failures of Additively Manufactured 316 Stainless Steel”

Figure 7A illustrates the calculated Lagrangian distance (x) versus time (t) diagrams based on the shock velocity calculated using the empirical constants for 316L [7] and the measured elastic wave speeds and particle velocity estimated from the wave profiles captured using PDV interferometry. The x - t diagrams predict a difference in the spall plane location for the two cases of the IP and TT samples, because microstructural anisotropy influences wave speeds which in turn affect the location where the reflected release waves interact.

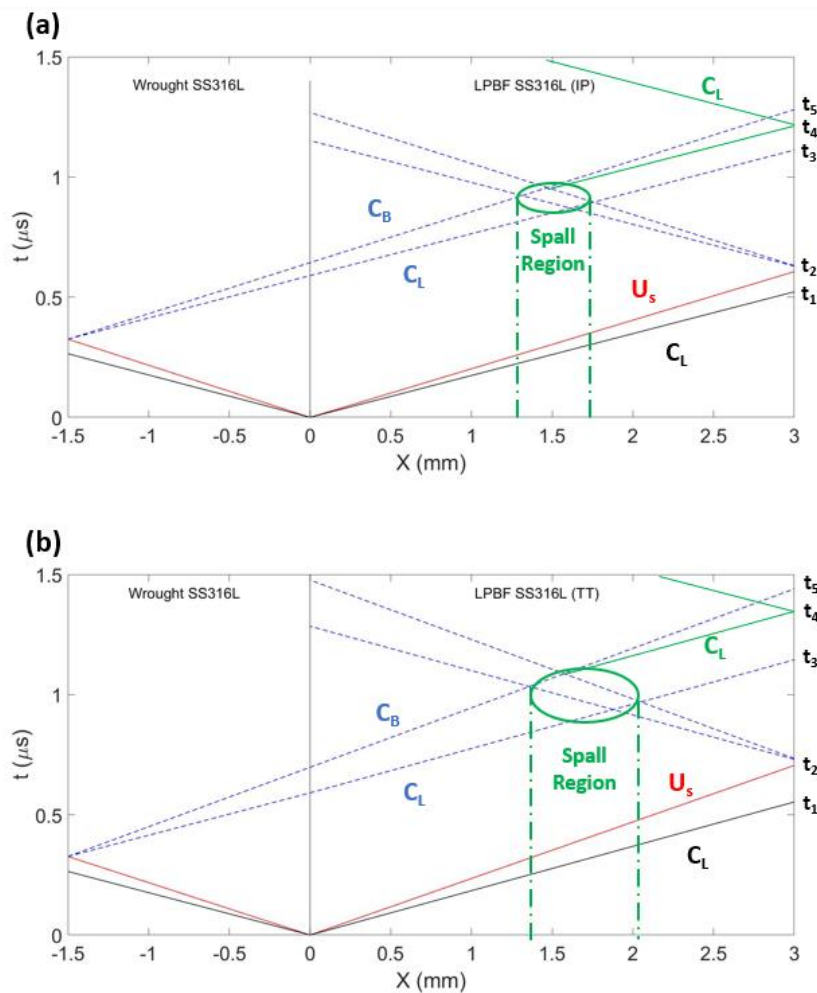


Figure 7A: Lagrangian x - t plots of (a) IP sample and (b) TT sample.

In Figure 7A, the arrival of the shock pulse at the rear free surface at t_2 and of the post-spall recoil pulse at t_4 are both directly indicated based on the velocimetry data. Between these two discrete moments the spall event occurs.

The distance from the rear free surface to the spall plane can be established using the measured wave speeds and the unknown time segments t_{2-s} (time between t_2 and spall) and t_{s-4} (time between spall and t_4).

- $X_{spall} = X_{2-s} = C_b \Delta t_{2-s}$ (X1)

- $X_{spall} = X_{s-4} = C_L \Delta t_{s-4}$ (X2)

Since this distance must indicate the same location regardless of path, a relation between the time steps can be established using the known sound wave properties. Also, the individual time steps combine to account for the known time recorded in the experiment between the free surface arrival times t_2 and t_4 .

- $\frac{C_b}{C_L} = \frac{\Delta t_{s-4}}{\Delta t_{2-s}}$ (7X3)

- $\Delta t_{2-4} = t_4 - t_2 = \Delta t_{2-s} + \Delta t_{s-4}$ (8X4)

This set of equations can then be solved for the intermediate time interval.

- $\Delta t_{2-s} = \frac{\Delta t_{2-4}}{1 + \frac{C_b}{C_L}}$ (9X5)

A simplified approach is then possible based on the time intervals available directly from the velocimetry data. As mentioned, the arrival of the shock pulse is observed at t_2 . This pulse (a) travels the full length of the sample and (b) incorporates both the elastic and plastic flow components. Since the wave propagation is considered one-dimensional, the rarefaction wave that travels from the rear free surface to the spall plane is exposed to the same conditions but across a different time interval and distance. Using the relation of the distance traveled by the shock wave (X_{target}) and the relative time intervals for shock wave arrival (t_2 from velocimetry) and spall occurrence (Equation X5), the general location of the spall plane can be determined to within a reasonable estimation.

- $X_{spall} = \frac{\Delta t_{2-s}}{t_2} X_{target}$ (X6)

Using this relation with the values for Δt_{2-s} calculated previously for TT and IP samples (0.37 μs and 0.50 μs , respectively), the spall plane distance from the rear free surface is estimated to be at 1.2 mm (for TT) and 1.5 mm (for IP). These approximations are in agreement with the locations for primary spall damage plane observed in the post-mortem optical images (Figure 4 in manuscript).

Vita

Kevin Matthew Lamb was born on April 22, 1981, in Oak Ridge, TN. He lived in nearby Oliver Springs, TN with his parents and younger brother. He graduated from Oliver Springs High School with honors in 1999.

He attended Tennessee Technological University (TTU) in Cookeville, TN from 1999 to 2004. He graduated Cum Laude from TTU in 2004 with a Bachelor of Science (BS) in Mechanical Engineering with a concentration in Energy Systems. During his time at TTU, he participated as an intern at Oak Ridge National Laboratory (ORNL) in 2001 and in the TTU cooperative education program as a student-employee at Y-12 National Security Complex in 2002-2003.

From 2004 to present, he has worked at Y-12 National Security Complex in Oak Ridge, TN. From 2004-2011, he served as a Mechanical Design Engineer with focus on mechanical flow systems and as a technical discipline lead for nuclear related procurements. From 2011-2014, he served as a Liaison to Production Operations for the Technology Applications and Deployment group within Y-12 Development. Starting in 2014, he transitioned to a Research Engineer position in the Y-12 Development Mechanical, Controls, and Sensor Systems Engineering group.

Concurrently, from 2009-2013 he participated in graduate studies at North Carolina State University (NCSU) through a distance learning program. In 2013, he earned a Master of Science (MS) in Mechanical Engineering with a concentration in Thermal/Fluid Sciences.

From 2017 to present, he has been enrolled at the University of Tennessee (UTK) as a graduate student pursuing the PhD degree in Mechanical Engineering. The area of his research is Advanced Manufacturing, with a primary focus on the dynamic behavior of additive manufactured steels. This dissertation serves to satisfy the requirement for that degree.

Publications:

K. Lamb, K. Koube, J. Kacher, T. Sloop, N. Thadhani, and S.S. Babu. Anisotropic spall failure of additively manufactured 316L stainless steel. Additive Manufacturing, Volume 66. (2023). <https://doi.org/10.1016/j.addma.2023.103464>.

K. D. Koube, T. Sloop, K. Lamb, J. Kacher, S. S. Babu, and N. N. Thadhani. An assessment of spall failure modes in laser powder bed fusion fabricated stainless steel 316L with low-volume intentional porosity. Journal of Applied Physics, Volume 133. (2023). <https://doi.org/10.1063/5.0143744>.

Presentations:

National Nuclear Security Administration (NNSA) Additive Manufacturing working group meeting: High Strain Rate Mechanical Testing of Additively Manufactured Steels (316L). January 2020.

Minerals, Metals, and Materials Society (TMS) 2020 meeting: High Strain Rate Mechanical Properties of Additively Manufactured Steels (316L). February 2020.

National Nuclear Security Administration (NNSA) Additive Manufacturing working group meeting: Anisotropic Spall Characteristics of Additively Manufactured Steels (316L). March 2022.

Minerals, Metals, and Materials Society (TMS) 2022 meeting: Anisotropic Spall Characteristics of Additively Manufactured Steels (316L). March 2022.